Ultrafast Carrier Dynamics in Organic-Inorganic Semiconductor Nanostructures

Chaw Keong Yong

St Hugh's College, Oxford

Thesis submitted in fulfilment of the requirements for the degree of Doctor of Philosophy at the University of Oxford

Michaelmas Term, 2012

Ultrafast Carrier Dynamics in Organic-Inorganic Semiconductor Nanostructures

Chaw Keong Yong, St Hugh's College, Oxford

Thesis submitted in fulfilment of the requirements for the degree of Doctor of Philosophy at the University of Oxford. Michaelmas Term, 2012

Abstract

This thesis is concerned with the influence of nanoscale boundaries and interfaces upon the electronic processes that occur within the inorganic semiconductors. Inorganic semiconductor nanowires and their blends with semiconducting polymers have been investigated using state-of-the-art ultrafast optical techniques to provide information on the sub-picosecond to nanosecond photoexcitation dynamics in these systems.

Chapters 1 and 2 introduce the theory and background behind the work and present a literature review of previous work utilising nanowires in hybrid organic photovoltaic devices, revealing the performances to date. The experimental methods used during the thesis are detailed in Chapter 3.

Chapter 4 describes the crucial roles of surface passivation on the ultrafast dynamics of exciton formation in gallium arsenide (GaAs) nanowires. By passivating the surface states of nanowires, exciton formation via the bimolecular conversion of electron-hole plasma can observed over few hundred picoseconds, in-contrast to the fast carrier trapping in 10 ps observed in the uncoated nanowires. Chapter 5 presents a novel method to passivate the surface-states of GaAs nanowires using semiconducting polymer. The carrier lifetime in the nanowires can be strongly enhanced when the ionization potential of the overcoated semiconducting polymer is smaller than the work function of the nanowires and the surface native oxide layers of nanowires are removed. Finally, Chapter 6 shows that the carrier cooling in the type-II wurtzite-zincblend InP nanowires is reduced by order-of magnitude during the spatial charge-transfer across the type-II heterojunction.

The works decribed in this thesis reveals the crucial role of surface-states and bulk defects on the carrier dynamics of semiconductor nanowires. In-addition, a novel approach to passivate the surface defect states of nanowires using semiconducting polymers was developed.

"There are grounds for cautious optimism that we may now be near the end of the search for the ultimate laws of nature."

Stephen W. Hawking

Acknowledgements

I would like to thank my supervisors, Prof. Laura M. Herz for her unwavering patience, guidance and support. I would also like to thank Dr. Michael B. Johnston and Prof. Robin J. Nicholas for invaluable discussions. This work could have not have been completed without their enthusiasm and supports.

I would like to thank everyone in the LMH, MBJ and JLH groups for enjoyable and fruitful discussions and for making the Clarendon an even more enjoyable place to work in. There are too many to name individually but I would like to particularly thank those who directly helped with work presented in this thesis – Dr. Hannah J. Joyce, Dr. Samuel D. Stranks, and Dr. James Lloyd-Hughes for the generous helps and the wonderful discussion in pub.

I have enjoyed working with several collaborators within the University. Thank you to Dr. Feliciano Giustino and Keian Noori (Department of Materials, Oxford University), and Prof. Harry L. Anderson (Department of Chemistry, Oxford University) for enjoyable and fruitful collaborations. I am also so grateful to have immense support from oversea collaborators in Australian National University for providing the nanowires samples. Thank you to Prof. Chennupati Jagadish, Dr. Qiang Gao, Dr. Jenny Wong-Leung for providing GaAs and InP nanowires samples and for the electron microscopy works.

Many thanks also to St Hugh's College, the Condensed Matter Physics Sub-Department for helping me in every step of study and research during this wonderful time. I also wish to thank Yayasan Khazanah for their full-financial support through the Merdeka Scholarship.

Last, and certainly not least, thank you to my friends and family for their unwavering support, both in Oxford and from abroad. I have met so many wonderful people during my

time in Oxford and you have certainly made my experience amongst the Spires unforgettable. Finally, thank you to my parents, Mr. Si Poh Yong and Madam Yoke Soon Tee, for their unlimited supports throughout my career. Finally, thank you to my siblings who constantly support me throughout the study and you all are wonderful.

Contents

Publications

C. K. Yong, H. J. Joyce, J. Lloyd-Hughes, Q. Gao, H. H. Tan, C. Jagadish, M. B. Johnston and L. M. Herz. Ultrafast Dynamics of Exciton Formation in Semiconductor Nanowires. *Small*, **11**:1725–1731, 2012.

J. K. Sprafke, D. V. Kondratuk, M. Wykes, A. L. Thompson, M. Hoffmann, R. Drevinskas, W-H Chen, C. K. Yong, J. Karnbratt, J. E. Bullock, M. Malfois, M. R. Wasielewski, B. Albinsson, L. M. Herz, D. Zigmantas, D. Beljonne, and H. L. Anderson. Belt-Shaped π-Systems: Relating Geometry to Electronic Structure in a Six-Porphyrin Nanoring. *Journal of the American Chemical Society*, **133**:17262-17273, 2011.

S. D. Stranks, C. K. Yong, J. A. Alexander-Webber, C. Weisspfennig, M. B. Johnston, L. M. Herz and R. J. Nicholas. Nanoengineering Coaxial Carbon Nanotube-Dual-Polymer Heterostructures. *ACS Nano*, **6**:6058-6066, 2012.

H. J. Joyce, J. Wong-Leung, C. K. Yong, C. J. Docherty, S. Paiman, Q. Gao, H. H. Tan, C.i Jagadish, J. Lloyd-Hughes, L. M. Herz, and M. B. Johnston Ultralow Surface Recombination Velocity in InP Nanowires Probed by Terahertz Spectroscopy. *Nano Letters*, **12**:5325-5330, 2012.

C. K. Yong, K. Noori, Q. Gao, H. J. Joyce, H. H. Tan, C. Jagadish, F. Giustino, M. B. Johnston and L. M. Herz. Strong Carrier Lifetime Enhancement in GaAs Nanowires Coated with Semiconducting Polymer. *Nano Letters*, **12**:6293-6301, 2012.

C. K. Yong, Jennifer Wong-Leung, H. J. Joyce, Q. Gao, H. H. Tan, C. Jagadish, J. Lloyd-Hughes, M. B. Johnston and L. M. Herz. Direct Observation of Carrier Heating in Type-II WZ-ZB InP Nanowires Heterojunctions. *Nano Letters*, **Accepted**, 2013.

Manuscripts in preparation/submitted

C. K. Yong, W-H Chen, D. V. Kondratuk, P. Parkinson, A. Stannard, A. Summerfield, J. K. Sprafke, M. O'Sullivan, P. H. Beton, H. L. Anderson, and L. M. Herz. Spatially Coherent Excitations in Synthetic Light-Harvesting Nanorings. *Manuscript submitted.*

C. K. Yong, E. Buchaca-Domingo, N. Stingelin, M. B. Johnston and L. M. Herz. Ultrafast Exciton Delocalization in Solid-state Pressesd Conjugated Polymer Film. *Manuscript in preparation.*

Prizes

David Ryan Prize for Distinguished Work as a Second Year Postgraduate Student
Condensed Matter Physics, University of Oxford, 2011.

Nicholas Kurti Prize for Distinguished Work as a Third Year Postgraduate Student
Condensed Matter Physics, University of Oxford, 2012.

Young Scientist Award
Organic and Hybrid Interfaces of Excitonic Solar Cells: From Fundamental Science to Applications, 30 Anniversary Spring Meeting of the European Materials Research Society, 2013.

Chapter 1

Introduction

1.1 Introduction and Motivation

The limited supply of energy together with the growing demands and concerns over climate change have prioritised the development of renewable energy sources. Among all, solar energy power is reliable technology with a significant potential for long-term growth in nearly all world regions. The International Energy Agency estimates that by 2050, solar photovoltaic power will provide around 11% of global electricity production and avoid 2.3 gigatonnes of CO_2 emissions per year [1]. Achieving this roadmap's vision undoubtedly requires significant and long-term efforts for optimal technology progress, cost reduction and ramp-up of industrial manufacturing for mass deployment.

However, current solar cell technologies require highly purified silicon, resulting in high costs of production, energy-intensive fabrication processes, and long pay-back periods [2]. Recently, hybrid organic photovoltaics (OPVs), using inorganic and organic semiconducting materials as active components, have attracted intensive research and industrial interests[3–7]. Unlike the conventional solar cell, hybrid OPVs devices can be processed through all-solution methods over large area at low temperature, which reduces the processing cost significantly [8]. The combination of organic and inorganic semiconductor offers several advantages that cannot be achieved by devices fabricated based on single component alone, in particular, the chemical tunability of organic semiconductor bandgap allows broad optical

absorption spectrum coverage, the high electron-mobility and charge permitivity of inorganic semiconductor and the chemical and physical stability of inorganic semiconductor.

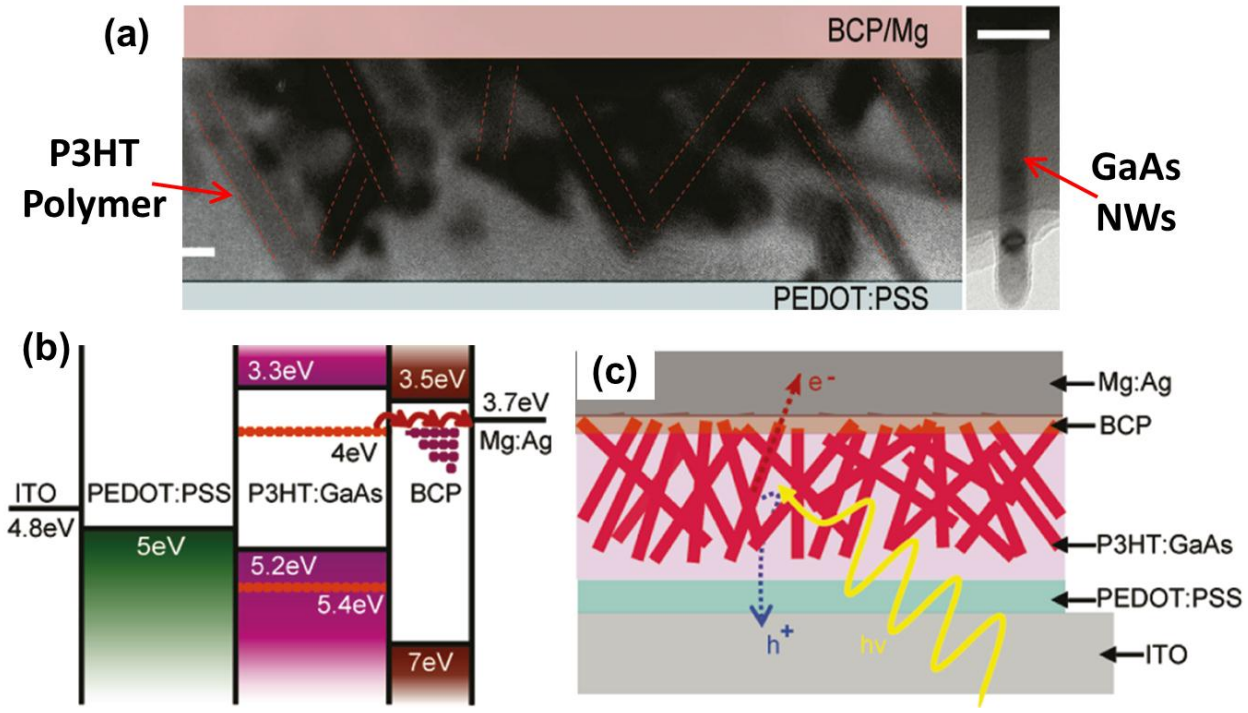

Figure 1.1: (a) The transmission electron microscopy (TEM) cross section image of hybrid OPV using P3HT and gallium arsenide (GaAs) nanowires (NWs) as electron donor and acceptor, respectively. The active materials are sandwiched between two electrodes. (b) Schematic illustration of energy level alignment across the hybrid OPV device. (c) Schematic of the poly(3,4-ethylenedioxythiophene)-poly(styrenesulfonate) (PEDOT-PSS)/P3HT-GaAs/Bathocuproine (BCP)/Magnesium-Silver device stack. Light shines through the electrodes is absorbed by the P3HT. The photoexcited electron-hole pairs are separated at the interface of P3HT/nanowires such that electron and hole transport occurs through the nanowires and P3HT, respectively, toward the corresponding electrodes. Taken from Ref. [9].

Traditional solar cells utilise materials such as silicon, gallium arsenide, and cadmium telluride where exciton binding energies are low and free electrons and holes are readily generated at built-in p-n junctions. However, organic materials have large exciton binding energies and require a second material to form type-II bulk heterojunctions for the exciton dissociation and charge generation [10, 11]. Fig. 1.1a shows a transmission electron microcscopy cross section of typical hybrid OPV device with the photo-active media formed by the P3HT and GaAs nanowires. The related energy level alignment of the device is shown in Fig. 1.1b and the charge transport is schematically illustrated in Fig. 1.1c. Here, the

type-II bulk heterojunctions are formed by P3HT and GaAs, where the excitons generated in the P3HT are dissociated at the interfaces, followed by electron and hole transport in the GaAs (electron accepting material) and P3HT (electron donating material), respectively. The details of the photoexcitation and device operation are illustrated in Fig. 1.2.

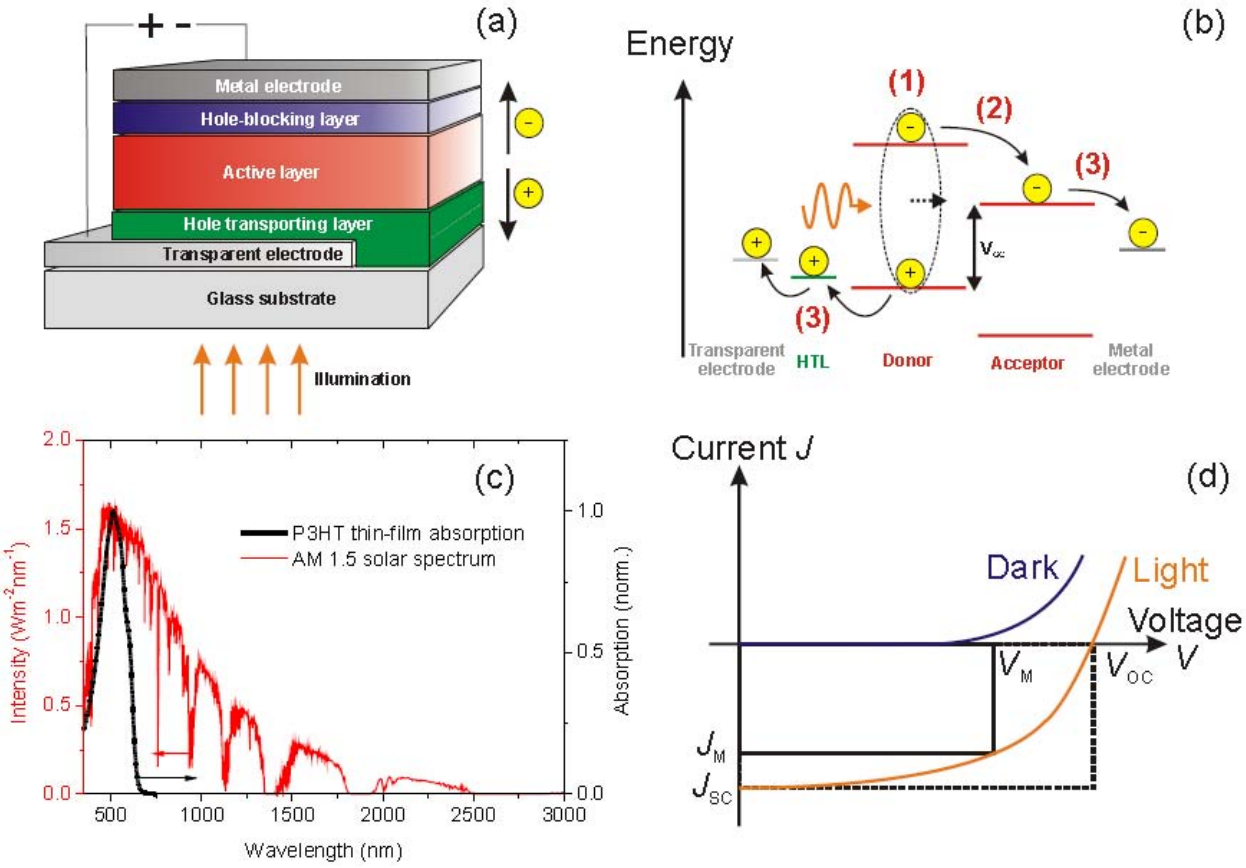

Figure 1.2: (a) Schematic diagram of a typical OPV device layered architecture. (b) Schematic energy level diagram showing the key processes occurring in an operating OPV device, as described in the text. (c) The normalised AM 1.5 solar spectrum incident on a surface tilted at 37° obtained from the model in Ref. [12]. The absorption spectrum of a thin film of the light-harvesting semiconducting polymer P3HT is also overlaid. (d) Typical *J*-*V* light and dark curves for an OPV device, with some of the key parameters labelled.

Fig. 1.2 (a) shows a typical hybrid OPV device architecture and (b) shows the electronic processes occurring. Three key steps can be identified:

(1) Photoexcitation of the donor species in the active layer, producing excitons which migrate to an interface with an acceptor.

(2) Charge transfer at the interface leading to charge-transfer states (exciplexes or polaron pairs) which can dissociate to give free polarons (*i.e.* charge separation).

(3) Charge transport and collection of electrons and holes at electrodes

Photoexcitation typically occurs through a bottom transparent electrode such as indium tin oxide (ITO). Electrons are transported through the hole and exciton blocking layer (*e.g.* bathocuproine BCP) to the metal electrode (typically aluminium), while holes are transported through the hole transporting layer (typically a PEDOT:PSS polymer blend) to the transparent electrode. The directional transport is due to the internal electric field created both by the work function difference of the electrodes and by the heterojunctions in the active layer, generating a photocurrent through the circuit. A photovoltage is also established across the terminals due to the charge imbalance, driving electrons through a load in the external circuit to do electrical work.

A normalised AM 1.5 simulated solar spectrum is shown in Fig. 1.2 (c) with the absorption spectrum of a thin film of P3HT overlaid. The overlap shows that P3HT is a good choice for a solar light-harvester. The absorption at the lower energy of the spectrum can be covered by a number of inorganic semiconductors such as silicon, gallium arsenide, indium phosphide and cadmium telluride. Furthermore, the band gap of the inorganic semiconductor can be controlled by dimension and size, which may be used to broaden the absorption range of solar spectrum, when mixed with an organic semiconductor in hybrid OPV devices.

A typical $J-V$ curve is shown in Fig. 1.2 (d) and allows the key parameters to be defined. The ***short-circuit current*** J_{SC} is the current flowing when there is no external field applied. It is determined by the charge separation efficiency, electrical transport through the materials and rate of carrier recombination during transport [11]. The ***open-circuit voltage*** V_{OC} is the external voltage when no net current flows in the device. It represents the maximum voltage that can be generated in the device and is a property of the donor-acceptor blend – the V_{OC} is given approximately by the energy difference between the donor HOMO level and acceptor LUMO level [13], as shown in Fig. 1.2 (b). The ***fill factor*** FF is the ratio of the maximum obtainable power $V_{\mathrm{M}}J_{\mathrm{M}}$ to the theoretical power at both V_{OC}

and J_{SC} together and can be interpreted as the ratio of the areas of the rectangles shown in Fig. 1.2 (d). The FF gives a measure of the quality of the solar cell and decreases in the presence of a large series resistance, corresponding to high internal losses. These parameters can be combined to give the overall power conversion efficiency η by:

$$\eta = \frac{P_{out}}{P_{in}} = \frac{V_{OC} J_{SC} FF}{P_{in}}, \quad FF = \frac{V_M J_M}{V_{OC} J_{SC}}, \tag{1.1}$$

where P_{in} is the incident light power and P_{out} is the electrical power output of the device.

To-date, the power conversion efficiency (PCE) of hybrid OPVs remains low and incompetitive to the solar cell based on the expensive silicon technology [14]. Unlike the conventional silicon solar cell, substantial photocurrents can be generated only by interpenetrating networks based on electron-donor and acceptor components that are generally used to form a so-called bulk-heterojunction (BHJ) for which ultrafast exciton dissociation and charge generation occurs primarily at the interface between the two material components [3, 15–18]. A variety of promising hybrid solar cells have been reported which use π-conjugated polymers, such as polythiophenes or polyphenylenevinylene derivatives, in conjunction with inorganic semiconductor nanostructures such as gallium arsenide (GaAs) [9], cadmium selenide (CdSe) [3, 15, 19], indium phosphide (InP) [20], zinc oxide (ZnO) [4, 21], or lead selenide (PbSe) [22]. The inorganic semiconductor nanostructures can act as both an electron transporter and a complementary photon absorber if narrower bandgap materials are used. Indeed, these polymer/nanocrystal hybrid OPVs demonstrate higher efficiency than those based on the corresponding single component films. However, the device efficiency is largely limited by the inefficency of the hopping charge transport through the discontinuous percolation pathways in the BHJ films [17]. It has been shown that higher photocurrent can be achieved by using nanorods and nanotetrapods, which was attributed to an enhanced charge hopping percolation path [23].

Recently, III-V semiconductor nanowires (NWs) with high aspect-ratio have become particularly attractive for use in hybrid solar cells because they offer direct charge pathways

to electrodes, large surface areas, high carrier mobility along the nanowires and superior physical and chemical stability of these materials [3, 5, 9, 20, 24, 25]. The high aspect ratio of nanowires further provides direct electron pathways that not just only rely on electron hopping, as generally seen in nanoparticle based BHJ devices. However, the charge transport in such nanowires has been shown to be strongly affected by the surface defect states [26–28] that act as charge traps. A number of methods have therefore been devised to passivate such traps, including overgrowing the NWs surface with a layer of large-bandgap semiconductor [26, 29] or treatment with sulfides [30].

Systematic probing of the carrier dynamics in the inorganic semiconductor nanostructures and their blend with organic semiconductor is therefore essential to identify the effect of defect states that appear in the bulk and surface of nanowires, in order to optimize the hybrid OPV device performance. However, the investigation of charge dynamics in a device can be further complicated by two major obstacles. First, the electronic processes tend to occur deep within the bulk of the active layer, as seen in the TEM cross section image in Fig. 1.1a, while the charge generation mainly occurs at the type-II interfaces formed by electron donor and acceptor in the active layer. Hence, experimental techniques requiring electrical contact to the materials are inapproprate for determining the intrinsic properties. Secondly, the charge injection across the donor-acceptor interfaces occurs on ultrafast time-scales. The photoinjected charge-carriers in most of the inorganic semiconductor nanocrystals also decay on the picosecond time-scales. The direct probing of the carrier dynamics undoubtedly requires experiments with an equally fast response time. The work presented in this thesis focuses on the ultrafast optical spectroscopy techniques that are able to investigate the electronic process on the femtosecond (10^{-15} s) to nanosecond (10^{-9} s) timescales, using a non-contact approach to investigate the carrier dynamics in the inorganic semiconductor nanowires and their blend with various semiconducting polymers and small organic molecules.

1.2 Thesis Outline

In this thesis, the charge carrier dynamics in III-V semiconductor nanowires with high aspect ratio and their blends with various conjugated polymers and small organic molecules are investigated using ultrafast photoluminescence spectroscopy. The structure of thesis is organized as follows:

Chapter 2 will introduce the electronic and optical processes in inorganic and organic semiconductor. Particularly, for inorganic semiconductor, the intraband carrier cooling, interconversion of uncorrelated electron-hole plasma into exciton, the influence of surface states on the carrier relaxation processes, and the effect of surface-passivation on the carrier dynamics are reviewed. For organic semiconductor, the nature and behaviour of photoexcitations are described, and the evolution of the resultant electronic state is examined. In-addition, the electronic processes in organic photovoltaics (OPV) and hybrid organic photovoltaics will be introduced.

Chapter 3 describes the experimental setups used to investigate nanomaterials and the analytical tools required to interpret the data. The photoluminescence up-conversion (PLUC) spectroscopy and time-correlated single-photon counting (TCSPC) system were used to obtained most of the results in this thesis is explained. In-addition, the optical-pump terahertz-probe time-domain spectroscopy (OPTP-TDS) was used to investigate the dynamical conductivity of photoinjected species in semiconductor nanowires. X-ray photoemission spectroscopy (XPS) was used to examine the chemical states of the surface of nanowires. These tools form the basis for the works presented and represent the cutting-edge of non-contact spectroscopy. Finally, the growth of nanowires will be introduced briefly.

The experimental results and discussion are presented in 3 chapters. The effect of surface passivation in nanowires on the carrier dynamics at a substrate temperature of 10 K is investigated in Chapter 4. In this research, the nanowires have a typical size of 5 μ in length by 50nm in diameter and the surface is passivated by 30 nm aluminum gallium arsenide (AlGaAs) shell layers and 5 nm GaAs skin layers. The coaxial type-I heterojunction confines

all carriers within the GaAs-core through the use of the higher bandgap AlGaAs shell layer. The resulting nearly-defect free nanowire core allows the observation of contributions to the photoemission from both free (uncorrelated) and bound charge pairs (excitons). Following non-resonant photoexcitation with a femtosecond pulse, it is shown that the nanowires photoluminescence (PL) emission reveals a fast, charge-density dependent interconversion from the initial free electron-hole plasma to a predominant exciton population over a total electron-hole charge pair density range of $1\text{–}4\times10^{16}\text{cm}^{-3}$. The gradual Mott-transition in the nanowires is attributed to the slow carrier-cooling during the bimolecular interconversion of free charge carriers into excitons and to the presence of chemical-potential fluctuations. As a control, nanowires with same dimension but without the passivating layers (i.e. in "bare" GaAs nanowires) are measured under same conditions. Both free-charge pair and excitons dynamics become dominated by rapid trapping at defect sites within a few picoseconds after excitation. The results of Chapter 4 demonstrate that the carrier dynamics in nanowires is largely dominated by the defect-trapping at the surface states.

The interfacial interactions of conjugated polymer and inorganic semiconductor nanowires are investigated in Chapter 5. GaAs nanowires are embedded in a variety of π-conjugated polymers to form type-II hybrid heterojunctions. The PL lifetime of nanowires embedded in the π-conjugated polymers can be enhanced significantly when the ionization potential (IP) of the polymer is smaller than the workfunction of the nanowires and the native oxide layers on the surface of NWs are removed. X-ray photoemission spectroscopy reveals that the surface-states of the uncoated GaAs NWs are electron-deficient in chemical character. Hence, the strong carrier lifetime enhancement is attributed to the filling of surface states in the nanowires by electron-injection from the highest-occupied molecular orbital (HOMO) of the polymer into the energetically lower-lying surface trap states of the nanowires until an equilibrium state is reached. Density-functional theory calculations performed on the GaAs/polythiophene heterojunction reveal that the polymer becomes an electron-donating reagent to give a relatively thin ($\approx 3\,\text{Å}$) "degenerate" electron-doping layer on the surface of GaAs. The results presented in Chapter 5 demonstrate that charge lifetimes in GaAs nanowires can be significantly enhanced through overcoating with an organic semiconduct-

ing material of suitable *IP* that has the dual functions of acting as a surface passivating agent and being the secondary material component in the BHJ photovoltaic material.

In Chapter 6, transient PL from the InP nanowires containing WZ-ZB polytypism along the growth axis of nanowires was used to demonstrate that while the electron-hole pairs undergo ultrafast spatial separation across the type-II heterojunction, the intraband energy loss rate of hot-carrier is reduced significantly. The crystal structure of the nanowires used in this study is predominantly wurtzite with sizeable stacking faults unevenly distributed along the growth axis of nanowires. The resulting wurtzite-zincblende heterojunctions exhibit type-II band alignment and the electrons and holes can be spatially confined in the zincblende and wurtzite segments of nanowires, respectively. Two sets of nanowires that shows different diameters and twin-defect densities were used in this study. Following a non-resonant photoexcitation with femtosecond laser pulse, the nanowires PL emission reveals a fast, injection density independent quenching in 12 ps – 33 ps, that arises from the transfer of photoelectrons from the conduction band of WZ segments into the energetically lower-lying electronic states of ZB segments. Transient photoconductivity measurements further show that the spatially separated carrier lifetime exceeds 1 ns and independent on the diameter of nanowires. The evolution of carrier temperature during the charge transfer was directly monitored from the transient PL spectra. Surprisingly, The long-term carrier temperature increases successively as the injection density and charge-transfer rate are increased. Hence, the slow carrier cooling was attributed to the buildup of non-equilibrium phonon population induced by the spatial charge transfer across the WZ-ZB type-II heterojunctions of the nanowires. During such transition, the excess energy of the charge-carriers, due to the energetic offset across the heterojunction, is released to the lattice via the phonon-emission. Since the decay of the acoustic modes is rather slow in these nanowires, the carrier cooling rate is reduced by increasing the excitation density and charge-transfer rate. The results shown in Chapter 6 demonstrate that the spatial charge transfer across the type-II interface in semiconductor nanowires reduces the intraband carrier cooling rate by order of magnitudes.

Finally, Chapter 7 provides a conclusion of the work in this thesis, along with an outlook

and future experiments that could extend the experimental fndings reported here.

Chapter 2

Electronic Processes in Inorganic and Organic Semiconductors

2.1 Basic Concepts of Inorganic Semiconductor

2.1.1 Electronic Properties

Intrinsic semiconductors are characterized by a band gap separating the occupied valence band and the empty conduction band states at low temperature. The energy band gaps range vary from very small values (less than 1 eV) for semiconductors like PbSe, HgCdTe to several eV such as for ZnS, TiO_2 and CdSe. All semiconductors can be classified either as direct gap semiconductor with the valence band maximum and conduction band minimum occuring at the same point in the Brillouin zone, or indirect semiconductor in which the extrema occur at different points in the Brillouin zone [31].

Fig. 2.1 shows the band structure of GaAs, which is a direct gap semiconductor with the extrema occurring at the same point in the Brillouin zone [31, 32]. The conduction band has subsidiary minima at higher energies near other symmetry points in the Brillouin zone. The Γ valley is spherically symmetric with a parabolic energy dispersion with wavevector (E vs k) relationship at low energies (an isotropic effective mass of $0.067\, m_e$). The electron

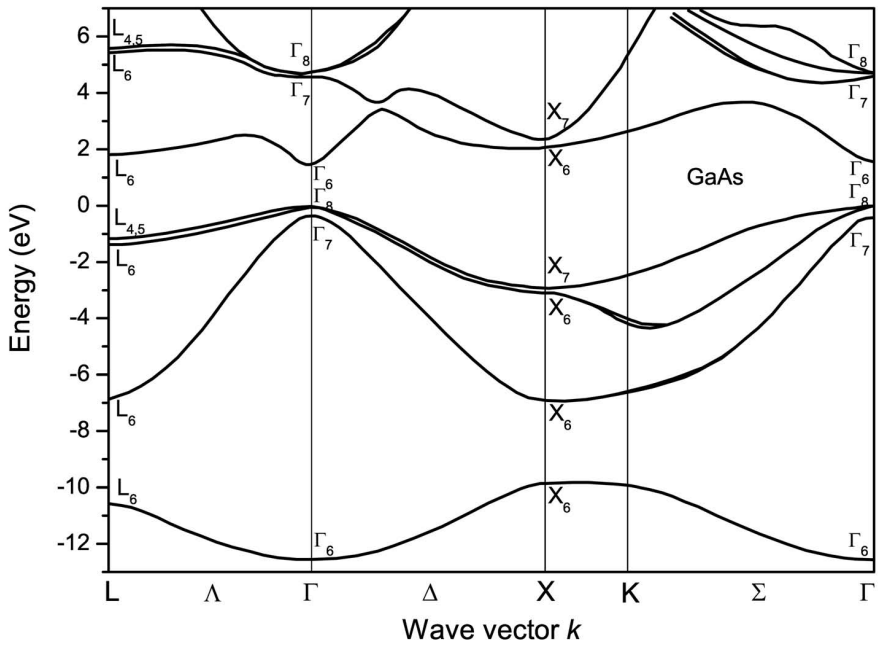

Figure 2.1: Band structure of GaAs showing the four valence band maximum and conduction band minimum occurs at the same point in the Brillouin zone (after Ref. [32]).

states in the Γ valley are two-fold degenerate (including spin) and are primarily s-like near the minimum, with an increasing admixture of p-character at higher energies. The electron band structure near the X and the L minima is highly anisotropic.

The valence band in GaAs is four-fold degenerate at the zone center and is split into the Heavy-Hole (HH) and Light-Hole (LH) band at larger k values. The degeneracy between the HH and LH bands at $k = 0$ can be lifted by perturbation such as stress or quantum confinement. The valence band states are p-like and the valance band shows anisotropy and warping. There is also a spin-split-off valence band at lower energies.

2.1.2 Density of states and Fermi-Dirac distribution

According to the Pauli exclusion principle, electrons and holes try to occupy low energy positions in the conduction and valence band and each state can only be occupied by one charge at one time, leading to build-up of occupied states with increasing energy. The available number of states N per unit energy per unit volumie is called density of states (DOS) [33]

$$g(\mathrm{E}) = \frac{2}{\mathrm{V}}\frac{d\mathrm{N}}{d\mathrm{E}} \tag{2.1}$$

The factor 2 takes into account that two electrons of opposite spin can occupy each state. Using the effective mass approximation, where the effect of the periodic potential of the crystal lattice on the electrons is treated by introducing an effective electron mass m_{e}^{*}, the density of states for a bulk semiconductor is given by [33]:

$$g^{3D}(\mathrm{E}) = \frac{1}{2\pi^2}(\frac{2\mathrm{m}_{\mathrm{e}}^{*}}{\hbar^2})^{3/2}E^{1/2} \tag{2.2}$$

Hence, well away from the band gap energies, the density of states increases with the square root of energy, as schematically illustrated in Fig. 2.2(a). In a pure semiconductor, the valence band is fully occupied and the conduction band is empty at low temperature. When the valence band is fully occupied, the electrons in these states have no available momentum to move into and hence do not contribute to the conductivity. The carriers contribute to the conduction only when excited into the conduction band via either photo or chemical-injection. Hence, the conductivity of the semiconductor can be increased by orders of magnitude via chemical doping or photo excitation [31].

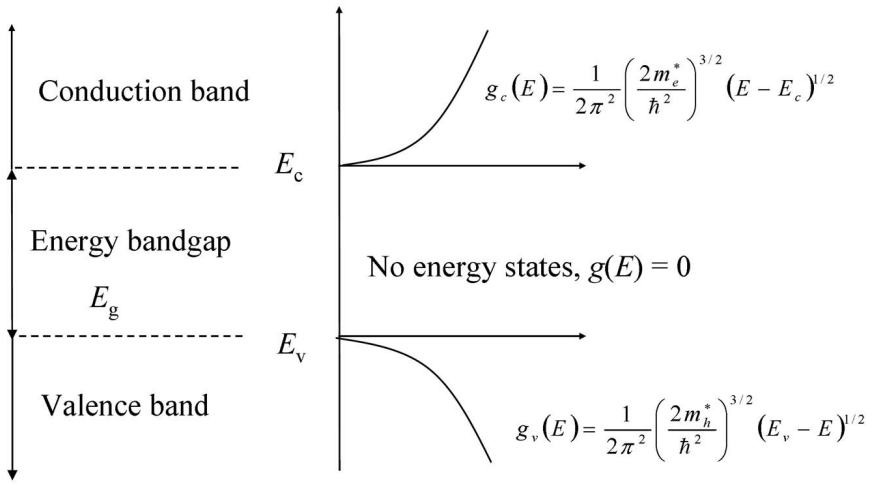

Figure 2.2: The density of states functions for a bulk semiconductor. $g_{\mathrm{c}}^{3\mathrm{D}}(\mathrm{E})$ is for the conduction band and $g_{\mathrm{v}}^{3\mathrm{D}}(\mathrm{E})$ is for the valence band. For pure semiconductor/insulator, the density of states within the energy bandgap is zero.

For low dimension semiconductor, the quantum confinement results in carrier movement in two (2D, quantum well, (QW)) and one (1D, quantum wire, (QWR)) or zero (0D, quantum dot, (QD)) direction. The density of states for QW and QWR will be considered here since it is related to the low-dimension semiconductor nanostructures studied in this thesis.

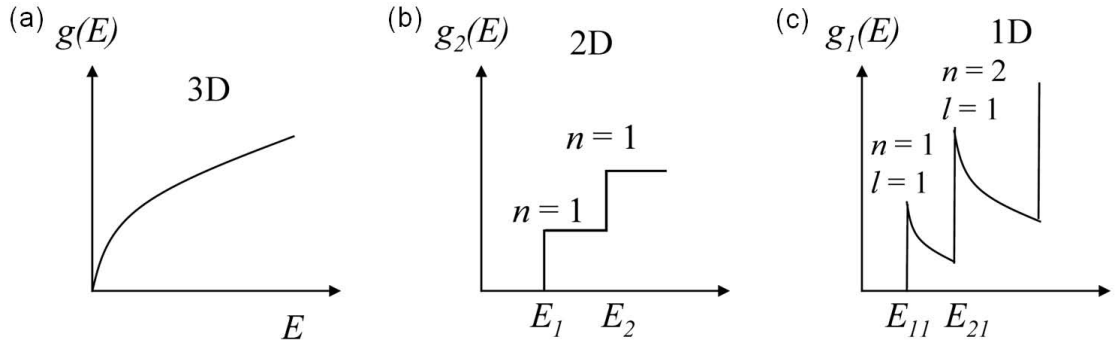

Figure 2.3: The comparison of density of states function for (a) 3D, (b) 2D and (c) 1D semiconductor.

Fig. 2.3 shows the density of states for (a) bulk, (b) QW and (c) QWR. As the dimensionality of semiconductor is reduced from bulk to 2D, the DOS becomes independent on E. In quasi-1D QWR, the DOS is inversely proportional to E.

At high temperature, the initially empty conduction band can be thermally occupied by electrons, leaving holes in the valence band. Hence, the population within the conduction band is no longer zero at high temperature. The probability a state being occupied at temperature T is described by the Fermi-Dirac function $f(\mathrm{E})$:

$$f(\mathrm{E}) = \frac{1}{1 + \exp[(E - E_\mathrm{f})/k_\mathrm{b}T]} \tag{2.3}$$

where k_b is the Boltzmann constant, and E_f is the Fermi energy. Fig. 2.4 shows the Fermi-Dirac distribution as a function of energy. At $\mathrm{T} = 0\,\mathrm{K}$, the variation of $f(\mathrm{E})$ around E_f is abrupt, indicates the full occupation of states below the Fermi energy. As the temperature is increased, the carrier distribution function smears out from the E_f and can be summarized as following: (1) For $\mathrm{E} < E_\mathrm{f}$, the $f(\mathrm{E})$ is higher than 0.5; (2) For $\mathrm{E} = E_\mathrm{f}$, $f(\mathrm{E}) = 0.5$; (3) For $\mathrm{E} > E_\mathrm{f}$, the $f(\mathrm{E})$ is lower than 0.5.

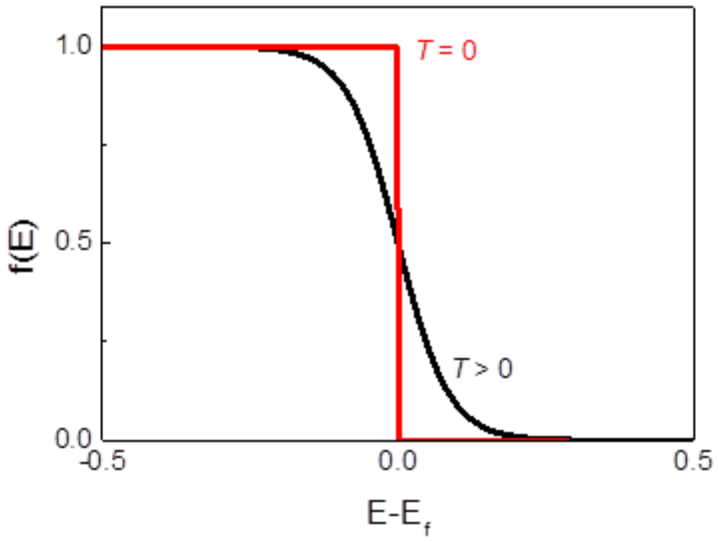

Figure 2.4: Fermi-Dirac distribution as a function of energy for T = 0 K and T > 0 K.

2.1.3 Optical Properties of Semiconductors

Illuminating light on semiconductors causes interband transition, excitonic transitions or below gap transitions. The light absorption, reflection and transmission in the semiconductors is governed by the complex frequency-dependent dielectric constant $\epsilon(\omega)$. In this thesis, the carrier dynamics in semiconductor nanowires are studied by optical probing methods. The diameter of the nanowires (d_{NW}) used in these studies are much larger than their Bohr radius (a_{B}) and hence the quantum confinement effect is negligible [34–36]. This therefore allows the band structure based on bulk semiconductor to be used when interpreting the optical data of these nanowires. The optical properties of these nanowires are mainly modulated by the dielectric confinement between the $\epsilon(\omega)$ of nanowires (denoted as ϵ_{NW}) and that for the surrounding matrix (denoted as ϵ_{s}) due to the high aspect ratio and small diameter of nanowires [37, 38]. The surrounding matrix is normally air or solution where the $\epsilon_{\mathrm{NW}}/\epsilon_{\mathrm{s}}$ is typically ≥ 10.

The main consequence of large dielectric constant mismatch is a strong polarization of light absorption and emission for these nanowires, and can be modelled by using Maxwell's equations. For cylindrical-like nanowires in an external electric field ($E_{\circ}$), the electric field

has a component parallel ($E_{\parallel}$) or perpendicular ($E_{\perp}$) to the axis of the nanowires as [39, 40]:

$$E_{\parallel} = E_{\circ}, \qquad E_{\perp} = \frac{\epsilon_{NW}}{\epsilon_{\mathrm{NW}} + \epsilon_{\mathrm{s}}} E_{\circ} \tag{2.4}$$

Hence, for $\epsilon_{\mathrm{NW}} \gg \epsilon_{\mathrm{s}}$, the perpendicular component of the field within the nanowires will be strongly suppressed to give weaker absorption and emission. For single nanowires, the absorption cross-section ($\sigma(\omega)$) of nanowires excited by photon energy far above the band edge is given by [41]:

$$\sigma(\omega) = \frac{\omega}{n_{\mathrm{s}} c}(\pi r^2 l) \left| \frac{4\epsilon_{\mathrm{NW}}}{\epsilon_{NW} + \epsilon_{\mathrm{s}}} \right| (2 n_{\mathrm{r}} k_{\mathrm{s}}) \tag{2.5}$$

where ω is the photon frequency, n_{s} is the refractive index of the surrounding matrix, $r = d/2$ the radius of nanowires, n_{r} is the refractive index of the nanowires, k_{s} is the imaginary part. This equation can be used to estimate the photoexcitation density in a single nanowire or an aligned essemble of nanowires. Accordingly, the photoluminescence from nanowires is also highly polarized in the same way as the absorption. The emitting intensity with polarization parallel ($I_{\parallel}$) and perpendicular ($I_{\perp}$) to the nanowire axis can be estimated as [39]:

$$\frac{I_{\parallel}}{I_{\perp}} = \frac{(\epsilon_{\mathrm{NW}} + \epsilon_{\mathrm{s}})^2 + 2\epsilon_{\mathrm{s}}^2}{6\epsilon_{\mathrm{s}}^2} \tag{2.6}$$

$$P_r = \frac{I_{\parallel} - I_{\perp}}{I_{\parallel} + I_{\perp}} \tag{2.7}$$

A number of photoluminescence and absorption experiments have revealed such strong anisotropic optical properties in nanowires even for nanowires with negligible quantum confiment. Wang *et al.* reported a strong optical anisotropy observed from the photoluminescence measurements of InP nanowires [40]. In these experiments, a photoluminescence polarization ratio (as defined by Eq. 2.7) of 0.96 was measured when varying the polarization of the exciting beam and fixing the detection polarization along the axis of nanowire. Similarly,

a polarization ratio of 0.92 was measured when varying the detection polarization and fixing the excitation polarization along the axis of nanowire. Indeed, Eq. 2.4 has been used to model the experimental data successfully without inclusion of any quantum confinement effects. This indicates the strong dielectric confinement effect on the optical anisotropy of nanowires. Furthermore, the photoconductivity of other nanowires such as GaAs [42], and CdSe [38] was found to be strongly polarized along the axis of the nanowires, which can be explained by the strong optical absorption along the axis of nanowires, as suggested in Eq. 2.4.

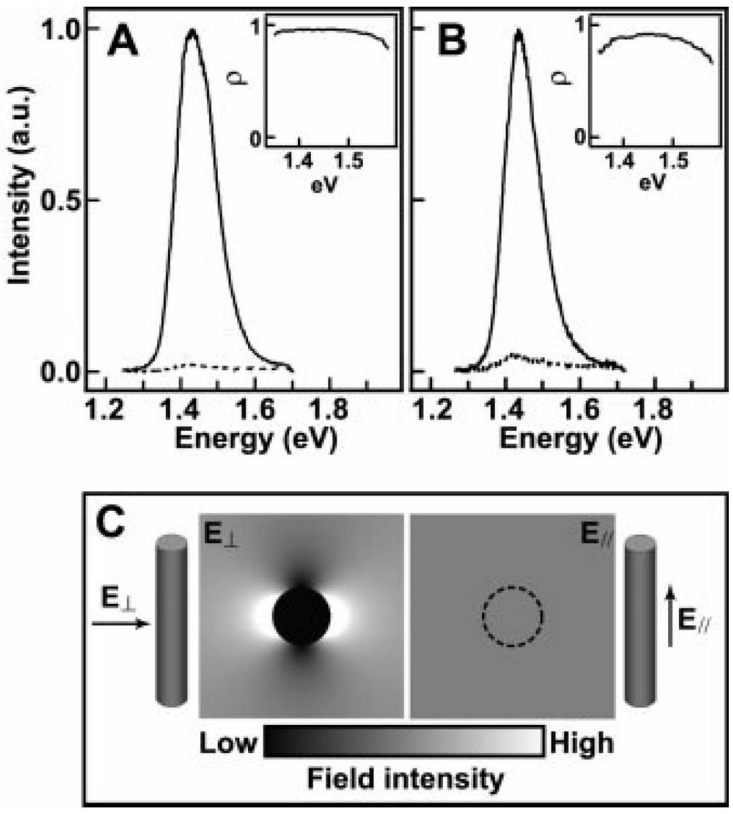

Figure 2.5: Polarized excitation and emission spectra of nanowires. (A) Excitation spectra of a 15 nm diameter InP nanowire. These spectra were recorded with the polarization of the exciting laser aligned parallel (solid line) and perpendicular (dashed line) to the wire axis. Inset plots of the polarization ratio as a function of energy. (B) Emission spectra of the same wire as in (A). These spectra were taken with the excitation parallel to the wire, while a polarizer was placed in the detection optics. Inset, plot of the polarization ratio as a function of energy. (C) Dielectric contrast model of polarization anisotropy. Adapted from Ref. [40].

Lan *et al.* further studied the effect of the dielectric medium of the surrounding matrix by

embedding CdSe nanowires into poly(methyl methacrylate) (PMMA) [38]. The polarization of photoluminescence of nanowires in the PMMA ($\epsilon_s \approx 3$) was found to be lower than those observed in air, as shown in Fig. 2.6. This is similar to the observation found in lithographically created nanowires in a semiconductor matrix and consistent with theoretical calculation [40, 43].

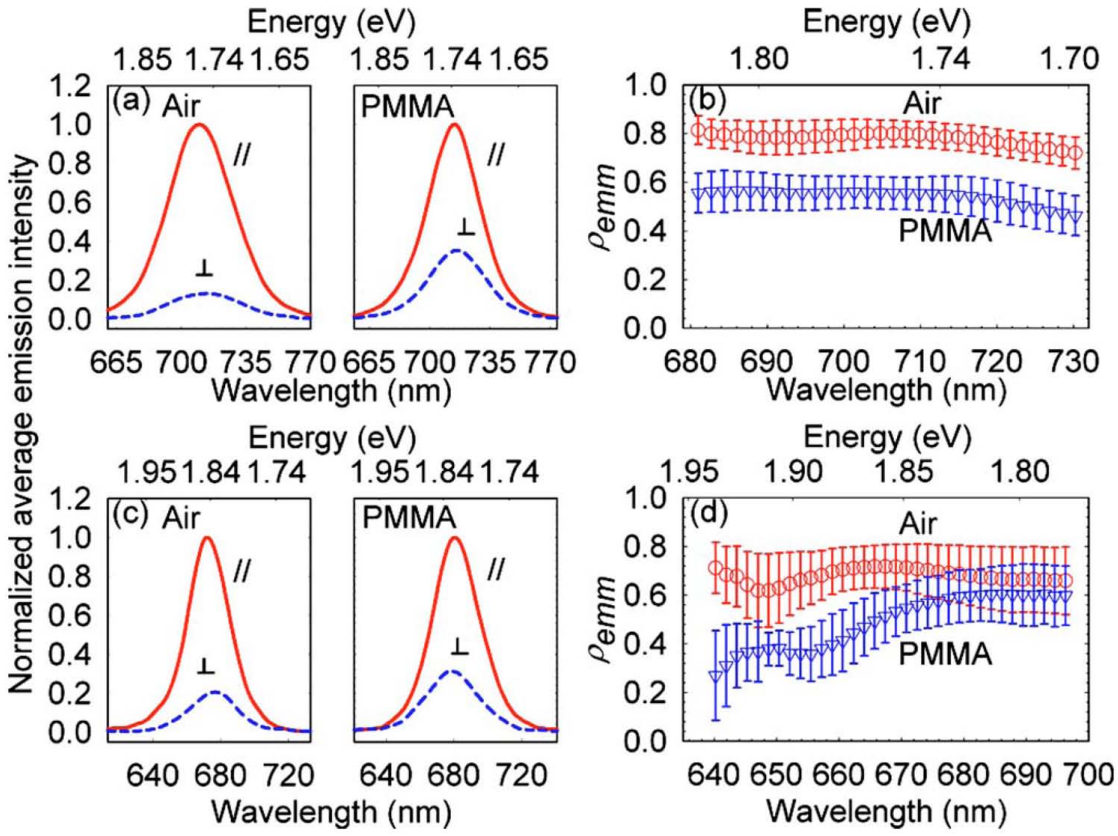

Figure 2.6: (a) The averaged emission spectrum for thick wires in air and under PMMA, with exicitation polarization parallel and perpendicular to the axis of nanowires. (b) The corresponding ensemble averaged emission polarization anisotropy as a function of emission wavelength calculated from (a). (c) The averaged emission spectrum of nanowires in air and under PMMA. (d) The corresponding ensemble averaged emission anisotropy as a function of emission wavelength calculated from (c). Adapted from Ref. [38].

Recently, Muskens *et al.* have demonstrated an enhanced absorption in semiconductor nanowires by suppression of the diffuse reflectance of the nanowires to below that of the corresponding transparent effective medium [44]. This points toward the exciting possibility of rationally designing nanowires layers to maximize the absorption for hybrid organic photovoltaics application.

2.2 Ultrafast Carrier Dynamics in Bulk Semiconductors

2.2.1 Initial Thermalization of Photoexcited Carriers

The absorption of a photon creates an electron in the conduction band and leaves behind a positive charge, termed a hole, in the valence band. When the absorbed photon energy is greater than the band gap, the distribution of the excess energy between electron (ΔE_{e}) and hole (ΔE_{h})is given by

$$\Delta E_{\mathrm{e}} = (h\nu - E_{\mathrm{g}})[1 + m_{\mathrm{e}}^{*}/m_{\mathrm{h}}^{*}]^{-1}; \tag{2.8}$$

$$\Delta E_{\mathrm{h}} = (h\nu - E_{\mathrm{g}}) - \Delta E_{\mathrm{e}} \tag{2.9}$$

where m_{e}^{*} and m_{h}^{*} are the effective mass of electrons and holes, respectively. Since m_{e}^{*} is typically much smaller than m_{h}^{*}, the excess energy gained by electrons is always higher than that of holes, as seen from Eq. 2.8. The excess energy appears in the respective charge carriers as kinetic energy and the photoexcitation produced by the absorption of photon energy larger than the band gap are far from equilibrium and the carrier temperature of electron and hole is not identical and cannot be quantified from the Maxwell-Boltzmann Statistic, as illustrated in Fig. 2.7. If photon absorption produces electrons and holes with initial excess kinetic energy at least k_{B}T above the conduction and valence bands, the initial carrier temperature (T_{c}) of both electron and hole are always above the lattice temperature. These carriers are called hot carriers. The energy distribution of the carrier population immediately after the femtosecond excitation depends on the excitation pulse profile and cannot be described by a Fermi-Dirac or Maxwell-Boltzmann distribution with a defined temperature and depends on the band structure and photon energy.

Since the nanowires used in this thesis study do not exhibit quantum confined in any dimension, their band structure can be approximated to be that of the bulk material. There-

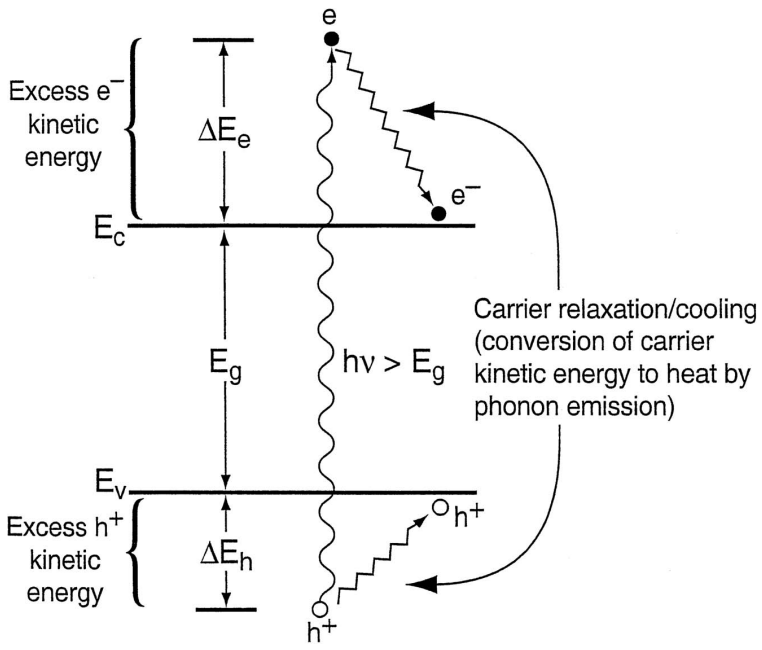

Figure 2.7: Hot carrier generation and relaxation in semiconductors.

fore, it is important to understand the temporal evolution of carriers after non-resonant excitation. In-particular, photocarrier relaxation in the incoherent regime is dominant since the phase relationship existing initially between the driving pump laser field and the photoexcited carriers persists only less than a few tens of femtoseconds before the onset of various relaxation and scattering processes [45–47], as illustrated in Fig. 2.8.

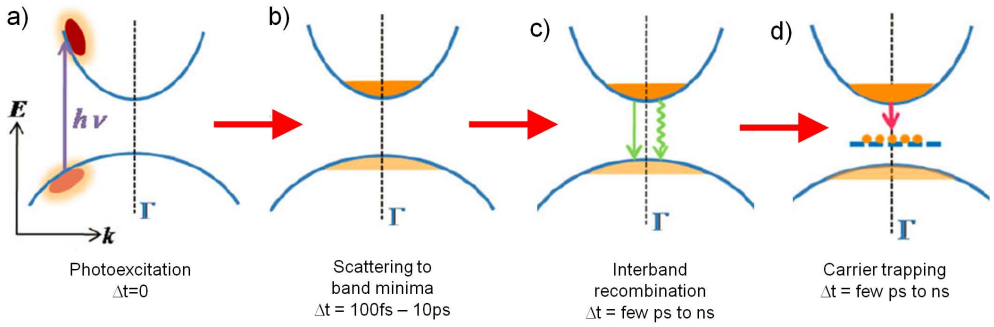

Figure 2.8: Carrier relaxation in a bulk semiconductor after ultrashort pulsed photoexcitation above the band gap.

Fig. 2.8 shows the photocarrier relaxation processes in bulk semiconductor. The first step toward establishing equilibrium is for the electrons and holes to interact among themselves through their respective collision to form a separate Boltzmann distribution of electrons

and holes. On the time scales longer than the average scattring time of the electrons and holes, which depends on the carrier density, the kinetic energy distribution always has a well-defined temperature governed by Fermi-dirac distribution or, in the limit of low density, a Maxwell-Boltzmann distribution [48, 49]. Time-resolved photoluminescence spectroscopy and transient absorption spectroscopy with temporal resolution of $\approx 100\,\mathrm{fs}$ have been widely used to probe the energy distribution of photoexcited charge carriers during the early time delay [48–54]. Elsaesser *et al.* used femtosecond luminescence spectroscopy to study the carrier thermalization in GaAs after photoexcitation at an energy of 1.93 eV. Following the non-resonant photoexcitation at densities ranging from $1.7\times10^{17}\,\mathrm{cm}^{-3}$ to $7.0\times10^{17}\,\mathrm{cm}^{-3}$, luminescence in a wide range of energies from the band gap at 1.42 eV up to 1.7 eV was observed intanstaneously within 200 fs. The broad structureless spectra observed at these early delay times give evidences for the fast redistribution of Γ valley electrons and holes within 10 fs, as confirmed by Monte Carlo simulations [51] (Fig. 2.9A).

The carrier-carrier (cc) scattering rate depends crucially on the injected charge density [48, 49]. Leitenstorfer *et al.* used transient absorption spectroscopy to show that the dynamics of ground state bleaching signal of carriers probed at an energy of 1.62 eV depends on the injection density. As the injected density increased from $1.5\times10^{15}\,\mathrm{cm}^{-3}$ to $2\times10^{16}\,\mathrm{cm}^{-3}$, the decay constant of an initial fast decay component decreases from 220 fs to 185 fs (Fig. 2.9B). Snoke *et al.* further shows that the photoinjected hot carriers remain non-thermal over 50 ps when the injected density is below $1\times10^{14}\,\mathrm{cm}^{-3}$ [49]. The results from Knox *et al.* show strikingly the increase of transmission at energies close to the excitation energies immediately after the excitation (Fig. 2.10A) , which results from the initial nonthermal distribution of photoexcited carriers in GaAs [54]. Such nonthermal distribution of carriers disappears in 200 fs (Fig. 2.10B) and confirms that carrier-carrier scattering occurs typically on the time-scale of a few tens to hundred of femtoseconds. These published works provide valueable information and summary for the initial thermalization of charge carrier via carrier-carrier scattering. It appears that at sufficiently high injection density ($10^{17}\,\mathrm{cm}^{-3}$), the thermalization occurs within 10 fs. As the carrier density is reduced, the carrier-carrier scattering rate is also decreased. At a charge carrier density below $10^{14}\,\mathrm{cm}^{-3}$,

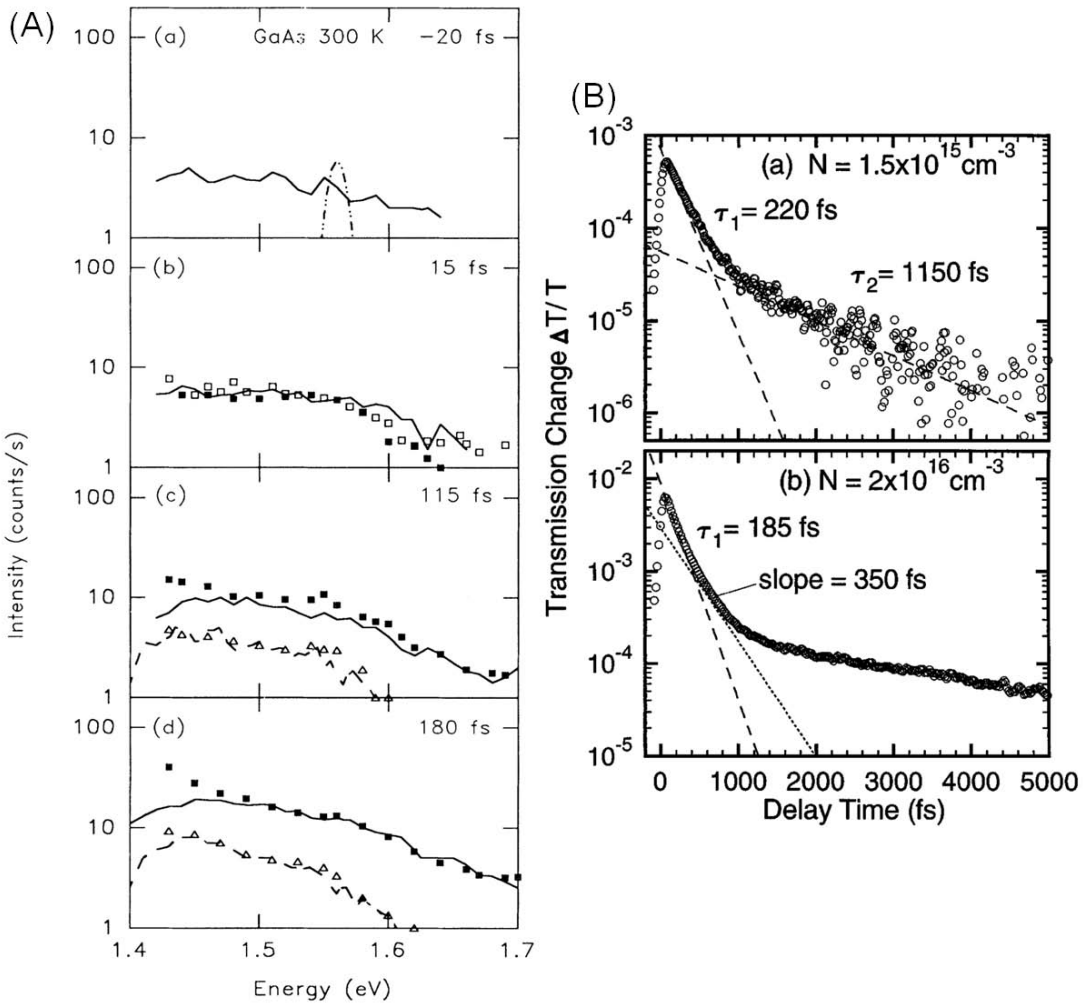

Figure 2.9: (A) Luminescence spectra of GaAs after femtosecond excitation at 1.93 eV at excitation density of $7\times10^{17}\,\mathrm{cm}^{-3}$ (solid lines) and $1.7\times10^{17}\,\mathrm{cm}^{-3}$ (dashed lines). The luminescence intensity is plotted against energy for delay times of (a) -20 fs, (b) 15 fs, (c) 115 fs, and (d) 180 fs. The solid squares and the triangles represent the spectra calculated from Monte Carlo simulation while the open squares are calculated with the molecular-dynamics model. (Adapted from Ref. [51]) (B) Transient transmission changes $\Delta T/T$ at a probing energy of 1.62 eV at an injection density of (a) $1.5\times10^{15}\,\mathrm{cm}^{-3}$ and (b) $2\times10^{16}\,\mathrm{cm}^{-3}$. (Adapted from Ref. [48])

the injected carriers remain non-thermal at longer time ($> 50\,\mathrm{ps}$) after the excitation.

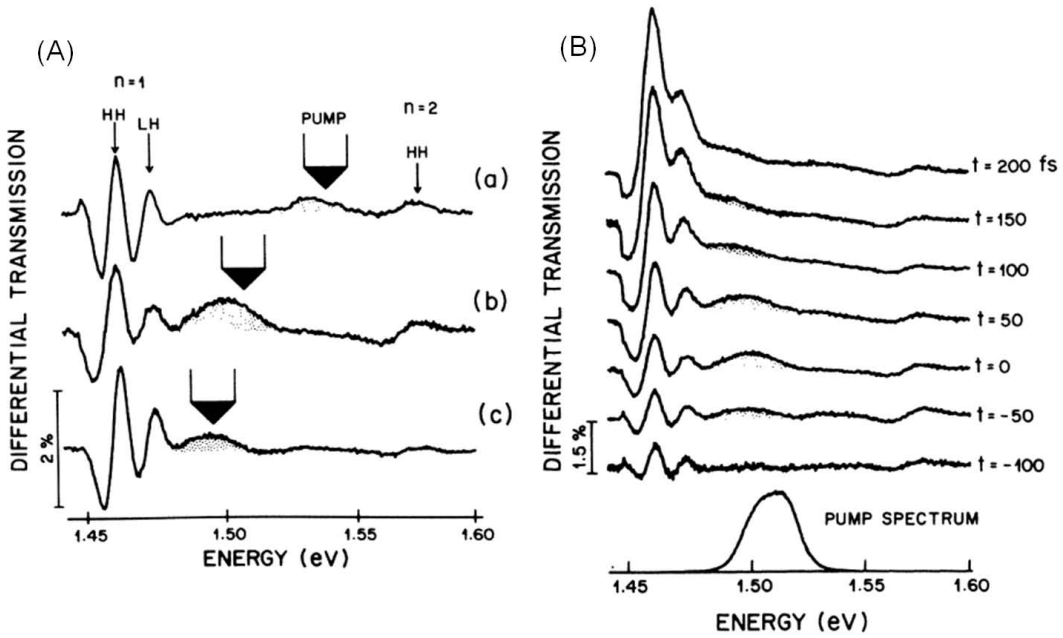

Figure 2.10: (A) Differential transmission spectra of an undoped GaAs/AlGaAs multiple quantum well sample for nominally zero delay between the excitation and the probe pulses for three different excitation photon energies. (B) Differential transmission spectra at different delays. (Adapted from Ref. [54])

2.2.2 Hot-carrier Cooling

After the carriers have become thermalized among themselves, their temperature remains higher than the lattice temperature (T_L). Equilibration of the hot carriers with the lattice is achieved through carrier-phonon interactions where the excess kinetic energy gained during the photoexcitation is transferred from carriers to phonons, allowing them to reach the bottom of the band on a time scale of a few picoseconds (Fig. 2.8). Transient PL spectroscopy has been widely used to extract the carrier temperature [55–58]. This is because the luminescence intensity for the band-to-band recombination of free carrier is proportional to the Fermi-Dirac distribution of electrons (f_e) and holes (f_h) via [55–58]:

$$I(\hbar\omega) \propto \alpha(\hbar\omega - E_\mathrm{g}) f_\mathrm{e}(\hbar\omega) f_\mathrm{h}(\hbar\omega), \tag{2.10}$$

where $\alpha(\hbar\omega - E_{\mathrm{g}})$ is the step function denoting the density of states, and $f_{\mathrm{e}}(\hbar\omega)$ and $f_{\mathrm{h}}(\hbar\omega)$ are the Fermi-Dirac distribution function of electrons and holes, respectively. For a non-degenerate system, the distribution function becomes simply a Boltzmann distribution and the intensity is reduced to

$$I(\hbar\omega) \propto \alpha(\hbar\omega - E_{\mathrm{g}}) e^{-(\hbar\omega - E_{\mathrm{g}})/k_{\mathrm{B}}T_{\mathrm{c}}} \tag{2.11}$$

Hence the slope of the PL spectrum at the high-energy edge is proportional to the carrier temperature T_{c}. For polar semiconductor, such III-V and II-VI semiconductor, the carrier-phonon interaction is dominated by the long-range Fröhlich interaction involving longitudinal optical (LO) phonons [46]. Yoon *et al.* has modelled the energy loss rate (ELR) from the transient PL spectra measurements of GaAs at different lattice temperature and concluded that the main ELR per carrier is due to LO-phonon emission in the bulk of GaAs, where [59]

$$\left\langle \frac{d\mathrm{E}}{d\mathrm{t}} \right\rangle_{\mathrm{LO}} \left(\frac{\mathrm{eV}}{s} \right) = 1.27 \times 10^{12} \left(\frac{m^*}{m_\circ} \right)^{1/2} \exp\left[-\frac{\hbar\omega_{\mathrm{LO}}}{k_{\mathrm{B}}T_{\mathrm{c}}} \right], \tag{2.12}$$

Cooling by acoustic-phonon emission occurs through deformation-potential scattering and piezoelectric scattering. Goebel *et al.* estimated the contribution from the deformation-potential scattering to be [60]:

$$\left\langle \frac{d\mathrm{E}}{d\mathrm{t}} \right\rangle_{\mathrm{dp}} \left(\frac{\mathrm{eV}}{s} \right) = 7.88 \times 10^{5} \left(\frac{m^*}{m_\circ} \right)^{5/2} \left(\frac{k_{\mathrm{B}}T_{\mathrm{c}}}{\mathrm{meV}} \right)^{3/2} \times \frac{(T_{\mathrm{c}} - T_{\mathrm{l}})}{T_{\mathrm{c}}}, \tag{2.13}$$

The piezoelectric scattering is given by

$$\left\langle \frac{d\mathrm{E}}{d\mathrm{t}} \right\rangle_{\mathrm{pz}} \left(\frac{\mathrm{eV}}{s} \right) = 1.18 \times 10^{7} \left(\frac{m^*}{m_\circ} \right)^{3/2} \left(\frac{k_{\mathrm{B}}T_{\mathrm{c}}}{\mathrm{meV}} \right)^{1/2} \times \frac{(T_{\mathrm{c}} - T_{\mathrm{l}})}{T_{\mathrm{c}}}, \tag{2.14}$$

Direct comparison of ELR based on Eq. 2.12, 2.13 and 2.14 indicates that the energy loss rate of hot-carriers in semiconductor is dominated by LO-phonon interactions. In-particular, the ELR estimated from above equations is independent on the injected carrier

density. Eq. 2.12 – 2.14 suggest that at high T_c, the cooling is dominated by LO-phonon coupling. As the T_c is reduced, the emission of LO phonons ceases and the cooling is dominated by acoustic phonon coupling. Shah *et al.* further showed that the cooling rate of photoexcited holes is higher than that of electrons, due to the presence of non-equilibrium phonons [61]. A number of studies have shown that the <ELR> decreases with increasing excitation density, due to the increasing population of non-equilibriun phonons [46, 47, 57, 58, 61, 62]. For injection density above $10^{18}\,\mathrm{cm}^{-3}$, significant build-up of non-equilibrium LO-phonon population in bulk semiconductors has been observed in Raman spectroscopy. The slow carrier cooling at high injection density has been attributed to the reabsorption of non-equilibrium phonons [62]. Klimov *et al.* further showed that the carrier cooling in II-VI semiconductors, which are more polar than III-V semiconductors, is also subjected to sizeable heating by reabsorption of non-equilibrium phonons, as the carrier density is increased (Fig. 2.11).

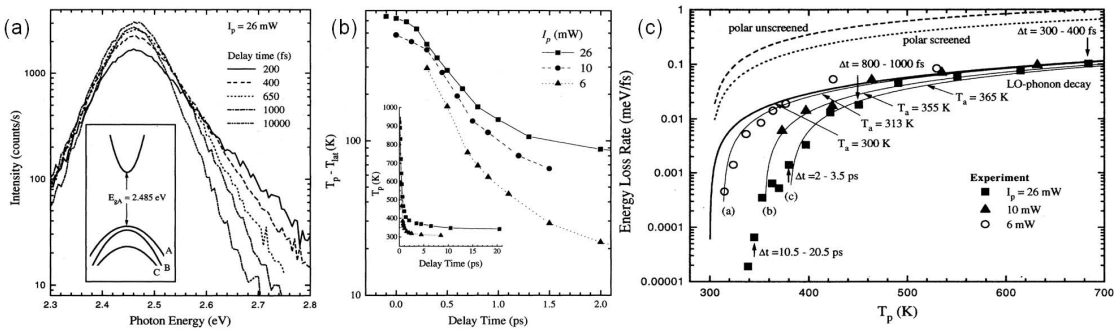

Figure 2.11: (a) Time-resolved PL spectra of CdS (at 300 K) measured at excitation intensity $I_\mathrm{p} = 26\,\mathrm{mW}$ with the inset showing the band structure of CdS in the center of the Brillouin zone. (b)Cooling curves derived from the time-resolved PL spectra at different excitation intensity. The inset shows the evolution of T_c over the first 20 ps for $I_\mathrm{p} = 26\,\mathrm{mW}$ and 6 mW. (c) Energy-loss rate per carrier found from the measured cooling curves. The solid lines are output of fitting from Eq. 2.15. (Adapted from Ref. [57])

Hence, at the high density regime, the carrier cooling is strongly related to the decay of LO phonons into acoustic phonons. To account for the non-equilibrium phonons, Klimov *et al.* have developed a semi-empirical equation for the energy-loss rate per carrier [56, 57]:

$$\left\langle \frac{d\mathrm{E}}{d\mathrm{t}} \right\rangle = \frac{3}{2}\frac{\hbar\omega_\circ}{\tau_{LO}}\left(\exp^{\hbar\omega_\circ/k_\mathrm{b}T_\mathrm{a}} - \exp^{\hbar\omega_\circ/k_\mathrm{b}T_\mathrm{c}}\right)\frac{N_\mathrm{LO}(T_\mathrm{a})}{N_\mathrm{LO}(T_\mathrm{c})}\left(\frac{k_\mathrm{b}T_\mathrm{c}}{\hbar\omega_\circ}\right)^2 \exp^{-\hbar\omega_\circ/k_\mathrm{b}T_\mathrm{c}}, \tag{2.15}$$

where τ_LO is the LO-phonon decay rate, T_a is the AC-phonon temperature and $\hbar\omega_\circ$ is the LO-phonon energy. $N_\mathrm{LO}(T)$ is the LO-phonon occupation number at temperature T. Fig. 2.11c shows the fitting from the output of Eq. 2.15. At high carrier temperature, the carrier cooling rate is independent on the injected carrier density. As the carrier temperature is reduced toward the lattice temperature, carrier cooling via the LO-phonons is reduced, as seen from Eq. 2.12. The LO-phonon population is increased as the hot-carrier temperature is reduced toward the lattice temperature. Hence, the cooling at later stage appears to be affected substantially under different excitation densities, attributed to the increase of non-equilibrium acoustic phonons population to give sizeable carrier heating.

2.2.3 Radiative Recombination

The radiative recombination of free carriers in a pure semiconductor occurs via a bimolecular recombination route where the PL intensity I_PL is proportional to the carrier density n via the bimolecular recombination constant B, $I_\mathrm{PL} = Bn^2$ [64–66]. For a bulk semiconductor, B is related to the carrier temperature via:

$$B = \frac{2\sqrt{\pi}n_\mathrm{r}e^2hE_\mathrm{g}}{m_\mathrm{o}c^3[(m_\mathrm{e}+m_\mathrm{h})k_\mathrm{b}T_\mathrm{e}]^{1.5}}\frac{E_\mathrm{p}}{3}; \tag{2.16}$$

where E_p is the interband transition matrix element, m_e and m_h are the effective masses of the electron and the hole, E_g is the bandgap energy and n_r is the refractive index [64]. The calculated B value for GaAs is shown in Fig. 2.12a, which plots the B as a function of carrier density at different temperature [63]. At low temperature, B depends on the injection density and increases as the carrier density is reduced. This is mainly attributed to the Coulomb binding of electron-hole pairs. At high temperature, B is independent of the

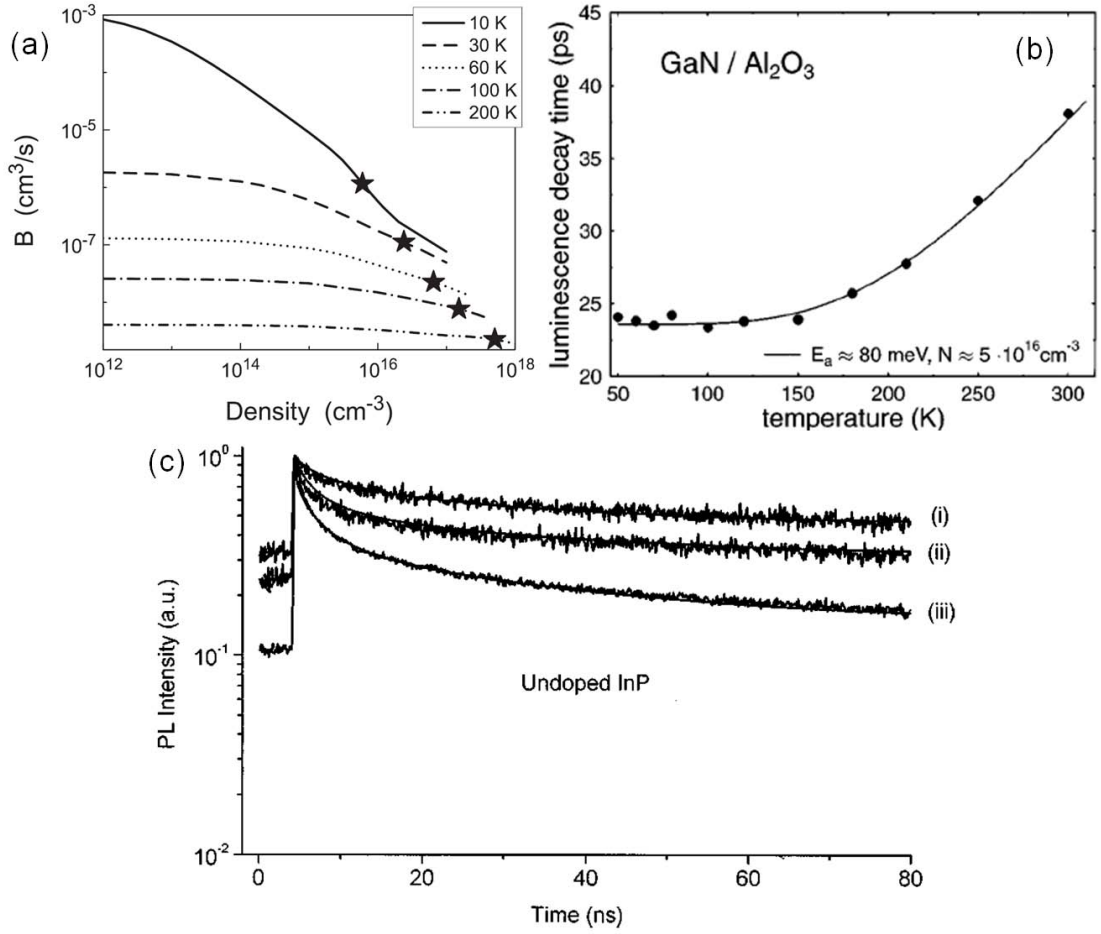

Figure 2.12: (a) The density-dependent radiative recombination coefficient for various temperatures. The optimal cooling density is marked with a star for each temperature (Adapted from Ref. [63]). (b) Radiative lifetime of free carriers measured at different lattice temperature. At low temperature, the recombination is dominated by exciton recombination (Adapted from Ref. [64]). (c) Transient PL decau curves of single crystal InP under injection densities of (i) $1\times10^{15}\,\mathrm{cm}^{-3}$, (ii) $1\times10^{17}\,\mathrm{cm}^{-3}$, (iii) $1\times10^{18}\,\mathrm{cm}^{-3}$ (Adapted from Ref. [65]).

injection density, suggesting that recombination is dominated by the uncorrelated electron-hole pairs. The temperature dependence of B also seen in other semiconductors, such as GaN [64], as shown in Fig. 2.12b.

Fig. 2.12 shows how the radiative lifetime of free carrier increases with increasing temperature. This result appears when the interband transition is dominated by radiative processes, such as in GaN [64] and InP [65, 67]. Since the probability of such radiative recombination processes depends on the carrier density, increasing the carrier density is expected to increase the radiative recombination rate.

2.2.4 Exciton and Many-body Effects

Optical excitation of a semiconductor promotes electrons from the valence band to the conduction band. The Coulomb interaction between the electron and its associated hole is strong enough to enable binding. For thermal energy lower than the binding energy (E_{B}), the resulting quasi-particle is called an exciton [31]. The lowest binding energy of the lowest state is given by $E_{\mathrm{B}} \propto \mu/(m_{\circ}\epsilon^2)\mathrm{Ry}$, where ϵ is the reduced electron-hole pair mass, ϵ the dielectric constant, $m_{\circ}$ the bare electron mass and 1 Ry $\approx$13.6 eV the hydrogen atom Rydberg energy. The small effective masses and large dielectric constant of semiconductors result in E_{B} of barely a few meV, orders of magnitude below the bandgap energy. Unlike the radiative recombination of free electron-hole pairs, the strong electron-hole correlation means that excitons have a high radiative recombination probability. The high luminescence yield of excitonic materials makes them important building blocks of many optoelectronics devices, especially in optical displays and light emitting diodes (LEDs).

Two limiting cases of excitons have been particularly well-studied. Frenkel excitons correspond to strong electron-hole attraction, as found in ionic crystals (i.e., CuCl), and organic semiconductor (as will be addressed in later section 2.3), the electron and the hole are tightly bound to each other within the same or nearest-neighbour unit cells [68]. The distance between the correlated electron-hole pair, the Bohr radius (a_{B}), is comparable to the lattice constant of the semiconductor, as schematically shown in Fig. 2.13. Wannier-Mott excitons, or simply Wannier excitons, corresponds to weak electron-hole attraction, as occurs in most inorganic semiconductors. They result from the strong screening of Coulomb interaction by the valence electrons via the dielectric constant.

Like the hydrogen atom, the exciton has a series of states $n = 1, 2, 3$, etc., as schematically shown in Fig. 2.13b. In bulk semiconductors, their binding energy scales as $E_{\mathrm{B}} = E_{\circ}/n^2$. Hence, the near bandgap absorption spctrum consists of a series of sharp excitonic transitions of diminishing strength and decreasing spacing, merging into the continuum band-to-band absorption which is also modified by the Coulomb interaction between electrons and holes, as first discussed by Elliot [70]. Such exciton absorption can be clearly observed only for samples

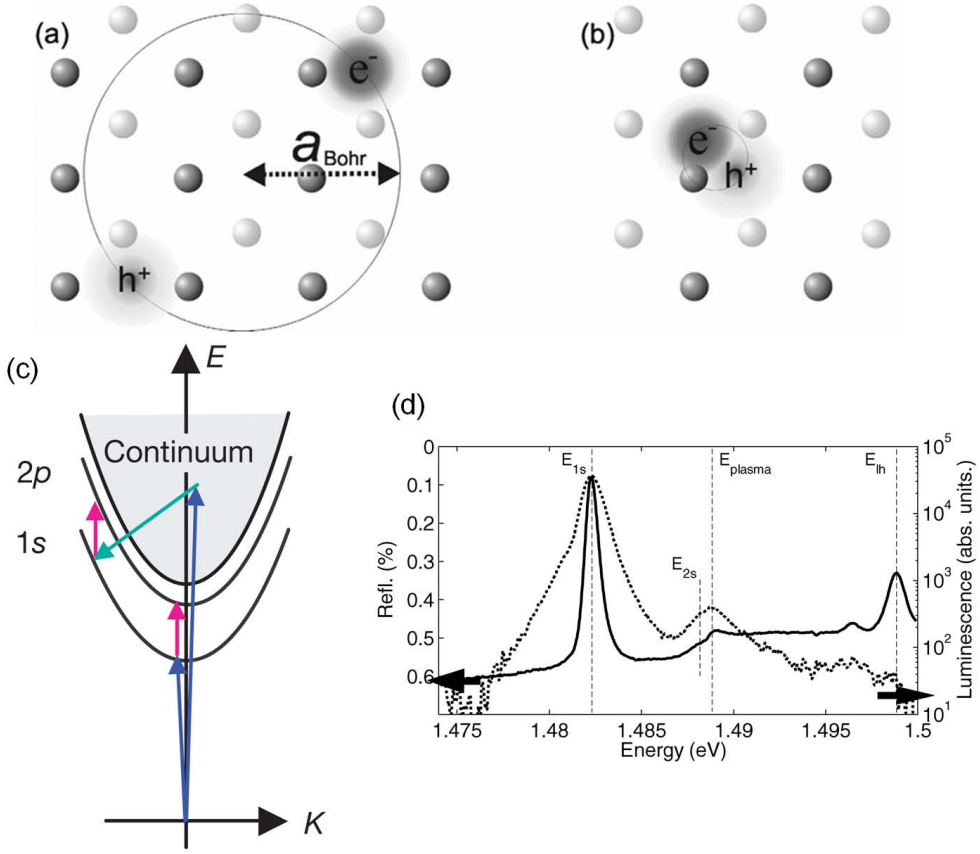

Figure 2.13: (a) Schematic illustration of (a) Wannier excitons (weakly bound, with the a_B larger than the lattice spacing) and (b) Frenkel excitons (strongly bound, with the a_B comparable to the lattice spacing). (c) Exciton-energy levels as a function of total wavevector and the exciton principle quantum number n. (d) Adsorption (1 - reflectivity) and time-resolved PL spectra integrated over 1300 ps for InGaAs QW. (Adapted from Ref. [69]).

with low impurity, where the spectral broadening induced by chemical contamination near the bandgap is minimal [69].

At low excitation levels, the optical absorption spectrum near the direct band gap in semiconductors is dominated by optical transitions involving correlated electron-hole pairs, with clear exciton resonances existing in many such materials at low temperature [71]. In 1968 Keldysh suggested that excitons might condense to a metallic phase at sufficiently high pair densities [72]. According to Mott, excitons become unstable at an electron-hole pair density (n_M) where the corresponding plasma screening length is comparable to the excitonic Bohr radius a_B [73, 74]. Since then, the Mott-transition in semiconductors has been widely debated [34, 46, 74–77] Fehrenbach *et al.* provides direct evidence from transient absorption

spectra of GaAs under conditions of *resonant* optical excitation that an excitonic resonance persists up to pair densities two orders of magnitude above the theoretical calculated Mott density ($2\times 10^{14}\,\mathrm{cm}^{-3}$ at $T_l = 0$) [78] (Fig. 2.14a). This is arguably due to the relatively weak self-screening of discrete excitons [79]. The relatively broad excitonic emission in the optically thin sample is attributed to the increasing contribution of inhomogeneity arising from the surface of GaAs.

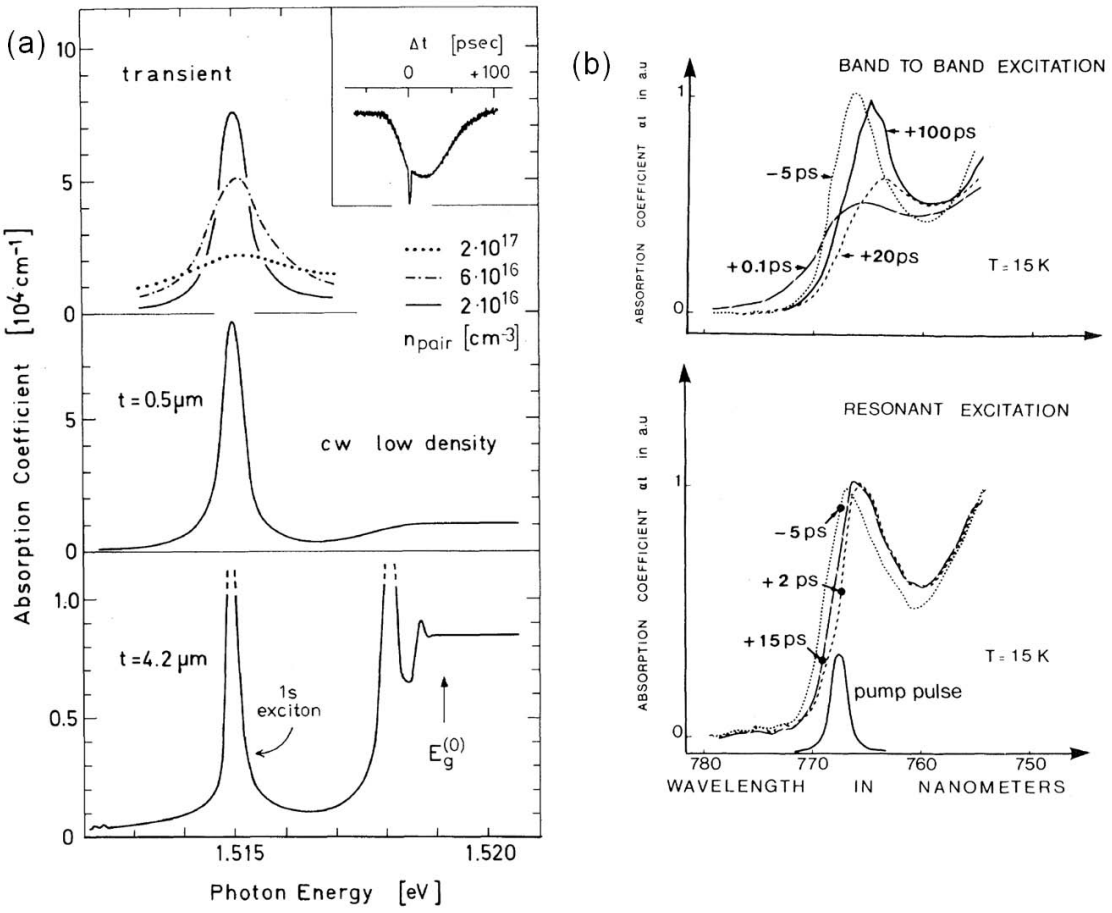

Figure 2.14: (a) Transient optical absorption spectrum of GaAs under conditions of resonant excitation collected at time delay of 8 ps after the excitation pulse. The inset shows the temporal behavior of the probe-beam absorption coefficient for fixed photon energy 1.515 eV after deposition of $6\times 10^{16}\,\mathrm{cm}^{-3}$ pair density by the excitation pulse. The width of the sharp spike at time delay = 0 indicates the coherence time of the laser pulse. The corresponding continuous wave are shown for the same sample (middle) and an "optically-thick" sample of the GaAs (bottom). The relatively broad excitonic emission in the optically thin sample is attributed to the increasing contribution of inhomogeneity arise from the surface of GaAs (Adapted from Ref. [78]). (B) Time-resolved absorption of GaAs-$Al_{0.3}Ga_{0.7}As$ multiple-quantum-wells after non-resonant (top) and resonant (bottom) photoexcitation. (Adapted from Ref. [80]).

Time-resolved optical spectroscopy has been widely used to study the conducting-to-insulating transition and optical properties of semiconductors. At sufficiently low temperature, resonant excitation of a semiconductor results in formation of excitons as the dominant species. Exciton-exciton screening becomes increasingly important at higher excitation densities and leads to a renormalization of the exciton self-energy that blue-shift the exciton resonance in $< 1\,\mathrm{ps}$ [80]. Similar experiments were conducted under non-resonant excitation conditions, which shows a higher blue-shift of exciton resonance at identical injection density. Hulin *et al.* further showed that such excitonic energy renormalization depends on the well-width in quasi-2D quantum well and attributed their origin to the decreasing Coulomb screening in low dimensions [81]. These results explains the early obervation by Fehrenbach *et al.* which showed the high exciton resonance effect at injection densities far above the "theoretical" limit under steady-state, resonant excitation conditions [78]. At higher temperature, the photogenerated exciton becomes unstable and can be quickly ionized into uncorrelated free carriers by phonon absorption. Knox *et al.* performed femtosecond transient absorption measurements on GaAs quantum wells and showed that exciton ionization occurs within 300 fs at 220 K, where the resulting free carriers produce Coulomb screening for the excitonic absorption [82].

Under non-resonant photoexcitation, an uncorrelated electron-hole plasma is first generated, followed by cooling toward the band edge via interaction with phonons, as described in Section 2.2.2. The conducting-to-insulating phase transition has been studied extensively both in bulk and two-dimensional semiconductors [34, 74, 80, 83–85] since the original concept was developed by Mott [73]. At sufficiently low lattice temperature and low injection densities, where both the phonon population and Coulomb screening remains low, excitons are formed over a wide range of energies during the carrier cooling via interaction with LO-phonons [46]. These non-thermal excitons interact among themselves to form a thermalized hot-exciton gas whose temperature may be higher than the lattice temperature [46, 69].

The optical spectroscopic evidence of such conducting-to-insulating transition is shown in Fig. 2.14b, which compares the situation under resonant and non-resonant excitation [80].

For non-resonant excitation, the transition is first dominated by the band-to-band recombination of free carriers. The broadened transition energy below the band gap indicates that band gap renormalization arises from many-body interactions of charge carriers. The excitonic transition appears slowly as the carrier density is reduced. At longer time delay, the transition is dominated by excitonic recombination. For resonant excitation, the transition is dominated by the excitonic recombination immediately after the excitation. The initial blue-shift is attributed to exciton-exciton screening effects. However, such blue-shifts arising from excitons is rather smaller than those that arise from the charge carriers, as seen in Fig. 2.14b.

Since excitons are formed indirectly from the Coulomb binding of free carriers, the exciton ionization and formation rates are high enough that an equilibrium between excitons and free carriers is established, which is described by the well-known Saha equation [46, 76, 86], under low injection conditions. The observation of the luminescence arising from the recombination of excitons and free carriers suggests that the two species are in thermodynamic equilibrium. The relationship between the exciton population and free carrier population is given by

$$[e] + [h] \overset{E_{\mathrm{B}}}{\leftrightarrow} [X]\,, \tag{2.17}$$

where $[e]$, $[h]$ and $[X]$ are the electron (n_{e}), hole (n_{h}) and exciton (X) densities, respectively, and E_{B} is the exciton binding energy. The densities are related through a temperature-dependent equilibrium constant K as follows:

$$\frac{n_{\mathrm{e}} n_{\mathrm{h}}}{X} = K, \tag{2.18}$$

and K is related to the carrier temperature T_{c} and E_{B} via [87]

$$K\left(T_{\mathrm{c}}\right) = 2\left(\frac{\mu_x k_{\mathrm{B}} T_{\mathrm{c}}}{2\pi\hbar^2}\right)^{3/2} \exp\left(\frac{-E_{\mathrm{B}}}{k_{\mathrm{B}} T_{\mathrm{c}}}\right), \tag{2.19}$$

Eq. 2.19 implies that the ratio of exciton and free carrier population is constant. A paradoxical predictions of this equation is that at low carrier densities the thermodynamic equilibrium is dominated by free carriers while at higher carrier densities it is the excitons that dominate. However, the opposite scenario has been observed experimentally [88–91], which can be attributed to the increasing contribution of Coulomb screening. Hence, such relationship is valid only under low-excitation limits, where the Coulomb screening effect can be neglected [88].

At high excitation density, excitons are ionized into uncorrelated free electron-hole pairs. In other words, excitons are not formed under high injection limits in both resonant and non-resonant excitation conditions until the total electron-hole pair density is reduced below the Mott limits [34, 73]. At a high excitation density situation, the luminescence spectrum is characterized by the recombination of unbound electron-hole pairs with Fermi-energy that shows significant occupation at high energy and bandgap renormalization (BGR) caused by exchange and correlation effects [34]. The former shows increasing luminescence at the high energy edge of spectra while the later shows a red-shift of PL emission energy, as seen in Fig. 2.15a. The many body and correlation effects have been discussed extensively [34, 46, 90, 91]. Since the Pauli principle forbids two electrons with parallel spin from sitting in the same unit cell, the exchange energy increases the average distance between electrons with parallel spin and subsequently reduces their total repulsive Coulomb energy. The correlation energy is spin independent and describes the fact that the electron-hole pair energy is further reduced by the "residual" Coulomb attraction.

The BGR induced by exchange and correlation effects has been studied in various semiconductor materials. Tränkle *et al.* has shown that the BGR depends critically on the dimensionality of semiconductor [92, 93]. The distance between the carriers is always characterized by a dimensionless unit r_{s}, in which the volume occupied by a carrier pair in the plasma is compared with the volume of an exciton:

$$r_{\mathrm{s}} = \left(\frac{4\pi a_{\mathrm{B}}^3}{3} n_{\mathrm{p}} \right)^{-1/3}, \tag{2.20}$$

Fig. 2.15b shows that the BGR unit, after normalized with the excitonic Rydberg energies, is smaller in 2D than in 3D structures, which suggests a reduced efficiency of screening in two dimensions. It should be noted that the absolute BGR is higher in 2D than in 3D, as a results of higher excitonic correlation found in low dimension. A reduced Coulomb screening effect has been recently observed in quasi-1D quantum wires, where the excitonic emission is dominant even at injection density far above the expected Mott limits [88].

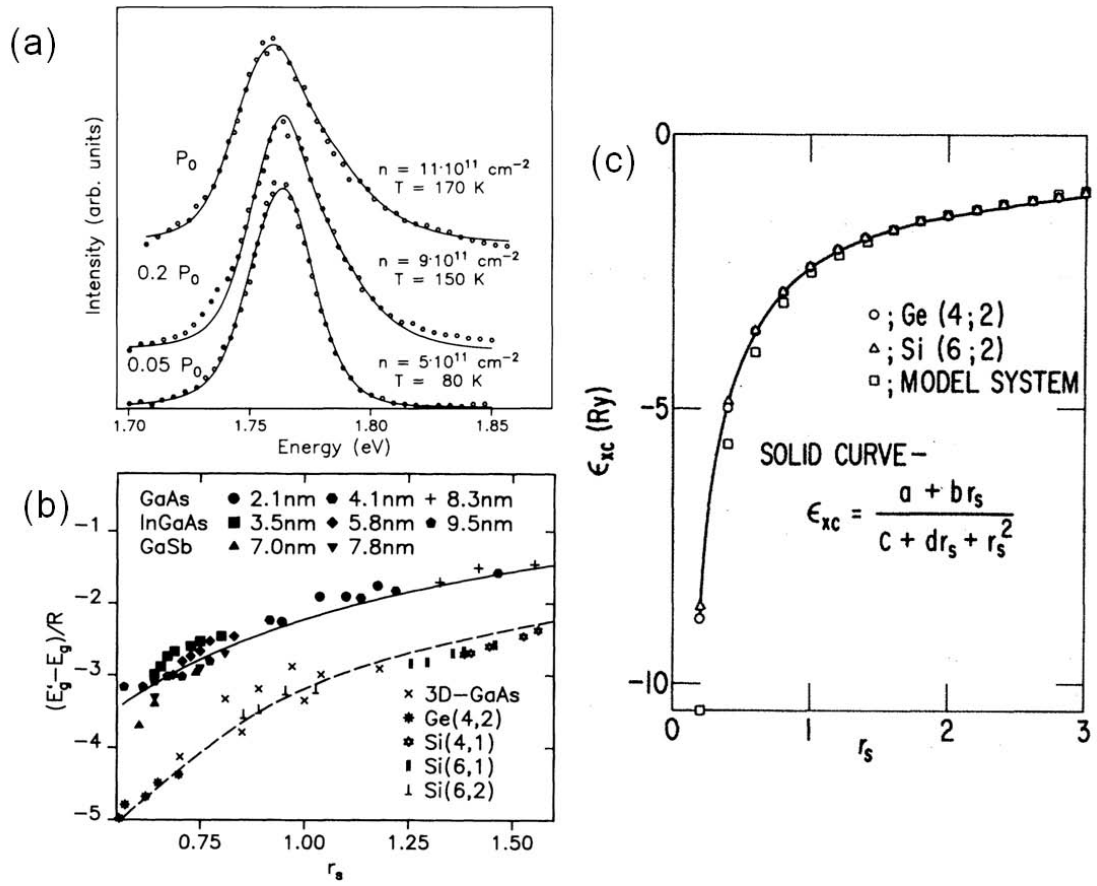

Figure 2.15: (a) The luminescence spectra of GaAs quantum well (width = 57 $\mathring{A}$. (b) Band gap renormalization scaled by the 2D and 3D Rydberg energies (R) vs the dimensionless interparticle distance r_s for 2D and 3D structure (Adapted from Ref. [93]). (c) The sum of exchange and correlation energies in units of Rydberg energy as a function of r_s (Adapted from Ref. [94]).

The general trend of BGR vs. r_s observed in Fig. 2.15b further suggests the BGR is independent on the choice of materials. Indeed, Vashishta and Kalia have shown that the BGR induced by the exchange and correlation in semiconductors can be well-approximated by the following [94]:

$$\Delta_{BGR} = \frac{-\mathrm{E_b}(-4.8316 - 5.0879\mathrm{r_s})}{(0.0152 + 3.0426\mathrm{r_s} + \mathrm{r_s^2})} \tag{2.21}$$

Fig. 2.15c shows the fit of Eq. 2.21 to the BGR observed in various semiconductors at different densities. The good fitting confirms the universal behavior of exchange and correlation energy in semiconductors. Hence, following non-resonant excitation, the PL of a semiconductor with direct bandgap is first characterised by the recombination of unbound electron-hole pairs with Fermi-energy that shows significant occupation at high energy and BGR caused by exchange and correlation effects. As the pair density reduces, excitonic emission subsequently begins to dominate the PL spectra as the BGR becomes comparable to the E_B [34]. Despite initial expectations, Mott transitions have often been found to be smooth crossovers across a range of electron-hole pair densities for both bulk semiconductors [74, 95] and two-dimensional semiconductor quantum wells [75, 86].

Fig. 2.16a shows the PL spectra of high purity InGaAs quantum wells integrated between 130 ps and 180 ps after the excitation at different densities. At high injection densities, the PL is dominated by the emission from the band-to-band recombination of free electron-hole pairs at energy higher than the exciton emission energy. The excitonic emission appears only as the injection density is reduced. Fig. 2.16b shows the normalized transient PL decay curves of the total integrated intensity, following non-resonant excitation at various densities. At low density, the PL transient is characterized by a slow rise and decay, attributable to the slow exciton formation via the bimolecular recombination of unbound electron-hole pairs [69, 76]. Increasing the excitation density results in a decrease of the PL lifetime due to the increased exciton formation efficiency and the increasing fraction of excitons with respect to the total pair population (as governed by the Saha equation). Once the exciton formation rate is considerably stronger than the radiative recombination rate of the exciton, the PL lifetime remains approximately constant in a large interval of densities. This is due to the predominantly excitonic population [75]. At the highest injection density situation, a fast radiative decay is observed during the early time delay, which was assigned to the fast radiative decay of degenerate electron-hole plasma via the bimolecular recombination route.

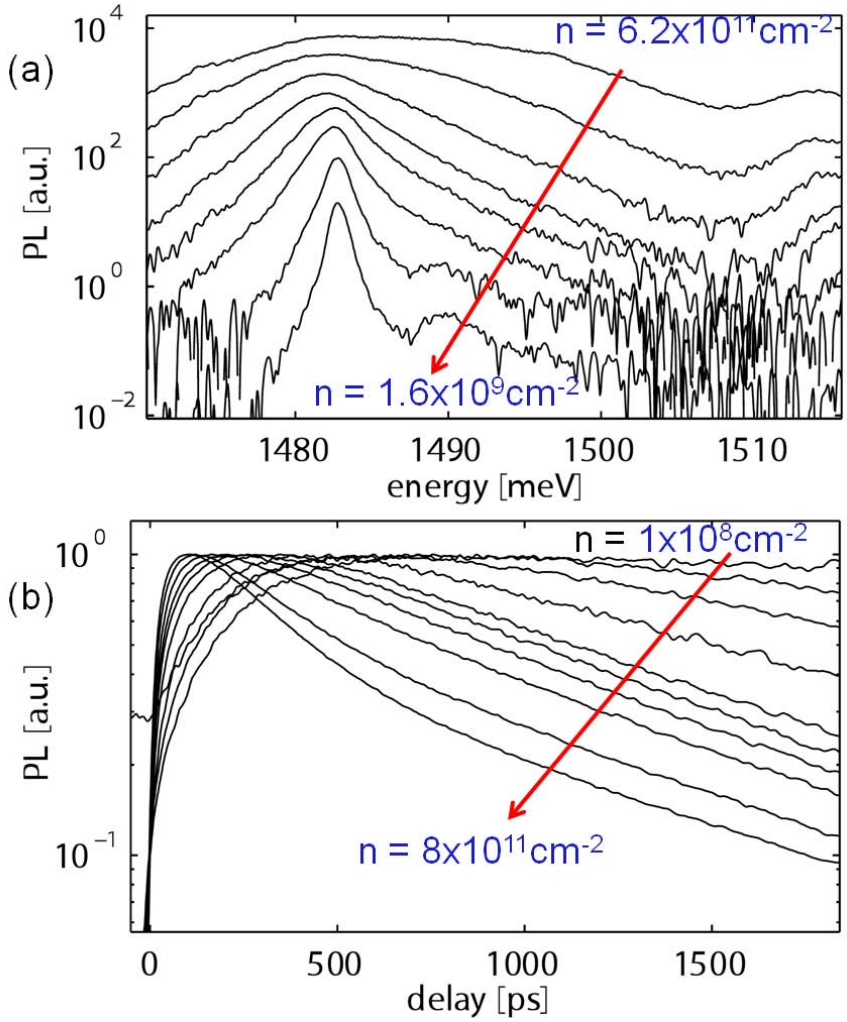

Figure 2.16: (a) PL spectra of high purity InGaAs quantum wells integrated between 130 ps and 180 ps after the excitation at different densities. (b) Normalized decay curves of the total integrated intensity as a function of delay time for various excitation densities. (Adapted from Ref. [75]).

2.2.5 Ultrafast Carrier Dynamics in Semiconductor Nanostructures

Quantum confinement occurs on the nanometre scale, and the behavior of quantum objects such as zero-dimensional quantum dots, one-dimensional quantum rods, or two-dimensional quantum wells are well studied. The carrier recombination in strongly confined nanostructures is dominated by Auger recombination due to the strongly overlapping electron and hole wavefunctions [41, 96, 97]. During the Auger recombination process, the interband recombination energy is transferred to the third particle, to give sizeable carrier heating [56].

Furthermore, the recombination rate depends crucially on the crystal dimension [97]. The carrier recombination rate increases with increasing injection density.

The ultrafast carrier dynamics in non-quantum confined (or intermediate regime) nanostructured materials are less well-investigated. This class of materials has been widely used as nanosized building blocks for various optoelectronic devices. In-particular, semiconductor nanowires have attracted intense research interest in the past decade. A wide range of nanowire-based electronic and photonic devices have already been developed, including nanowire solar cells [5, 98, 99], photodetectors [40, 100], light-emitting diodes [101, 102], lasers [103–105], single-electron transistors [106, 107], and highly sensitive biological and chemical sensors [108, 109]. A good review of the synthesis, microscopy and material characteristics of nanowires is given in Ref. [110].

The large surface-area to volume ratio of nanowires leads to many novel effects and the carrier dynamics become highly sensitive to the presence of surface states on the nanowires. Parkinson *et al.* have shown that the carrier lifetime and photoconductivity in GaAs nanowires is increased significantly as the surface of nanowires is overcoated with a semiconductor shell layer that has a larger bandgap semiconductor layer, such as AlGaAs [26, 113], to form the core-shell heterojunction, as seen at Fig. 2.17a. The carrier recombination becomes slower as the injection carrier density is increased. This is attributed to the dominant role of carrier trapping at the surface states [26]. The presence of surface states not only reduces the PL quantum efficiency of nanowires (Fig. 2.17b) [111] but also broadens the PL spectral linewidth inhomogeneously [114]. As the dimension of nanowires is reduced, the carrier recombination becomes faster, as a result of the increasing role of surface-trapping as the surface-area to volume ratio of nanowires is increased (see Fig. 2.17c) [112].

Most semiconductors are known to exhibit a depletion space charge layer near the surface [115] which in nanowires can be on the order of the wire diameter. In most of the semiconductor nanowires, this is known to result in trapping of electrons at the surface-states to give strong Fermi-level pinning [26, 116, 117]. The resulting negative electric field at the surface bends the conduction and valence bands upward in energy, causing holes to

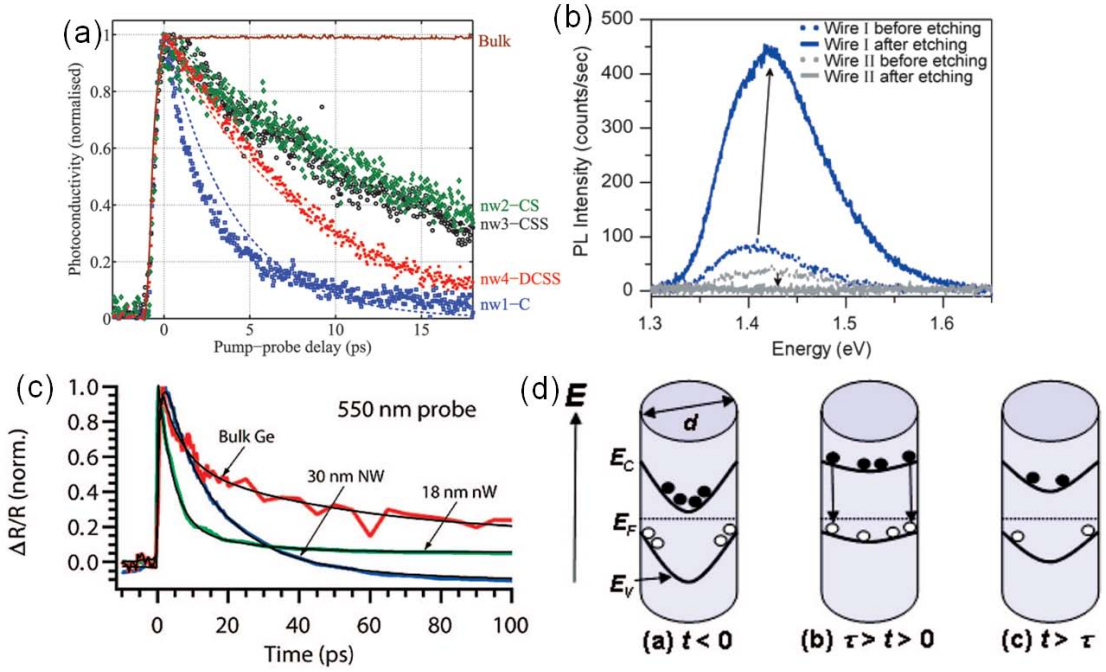

Figure 2.17: (a) Normalized photoconductivity of four types of nanowires and bulk GaAs as a function of time after photoexcitation. The data from the different samples are distinguished by the following labels and colors: Bulk GaAs (Bulk, brown), GaAs-AlGaAs core-shell NWs ([nw2-CS], green), GaAs-AlGaAs-GaAs core-shell-skin NWs ([nw3-CSS], black), GaAs-AlGaAs-GaAs core-shell-skin NWs with high density of twin defects ([nw4-DCSS], red), and GaAs core only NWs ([nw1-C], blue). (Adapted from Ref. [26]). (b) Steady state PL spectra of InP nanowires before and after surface photoetching process (Adapted from Ref. [111]). (c) Optical pump-probe measurements of Ge nanowires with different diameters probing at the transition energy corresponds to the indirect band gap of Ge (Adapted from Ref. [112]). (d) Schematic depicting the influence of nanowires surface properties on carrier dynamics at different time domains.

accumulate near the surface to maintain charge neutrality [115], as schematically depicted in Fig. 2.17d. This spatially separates the electron and hole populations in the nanowires, with holes near the surface and electrons accumulating at the center of the nanowires. Hence, as the dimension of the nanowires is reduced, photoinjected carriers can be driven to surface states more rapidly than carriers injected into nanowires with larger diameter.

2.2.6 Surface passivation in semiconductor nanostructures

The theory of recombination of conduction band charges at bulk traps was developed by Shockley and Read in 1957 [118]. Additionally, non-radiative trapping centres can arise at

the surface of semiconductors due to the atomic arrangement of ions at the surfaces, presence of impurities, in turn depending on the chemical origin of the surface atoms. The direct correlation of carrier recombination with the surface chemistry of semiconductor nanostructures is beyond the scope of this thesis and Ref. [119] covers some of the issues involved. The impact of surface states are discussed here. In particular, the presence of surface states in GaAs nanowires have resulted in ultrafast carrier trapping within 10 ps after the photoexcitation [26, 42, 113].

Spicer's group in Stanford presented the advanced unified defect model (AUDM) and pointed to the important role of As antisite (As_{Ga}) on the surface of GaAs [120]. The presence of excess As on the surface of GaAs has been identified by various group to be the origin of double donor-states in GaAs, which results in Fermi-level pinning at $\approx 0.5\,\text{eV}$ – $0.75\,\text{eV}$ above the valence band maxima [120–123]. Pashley *et al.* further showed that the passivation of surface states via bulk-doping in high-purity n-type GaAs is compensated by the formation of kinks in the dimer-vacancy rows of the $(2\times4)/c(2\times8)$ surface reconstruction. As a result, the Fermi-level pinning persists at the donor-states of GaAs, which hampers the modulation of Schottky-barrier height [123].

Surface passivation in semiconductors is essential to reduce the carrier trapping at the surface states of semiconductors. Parkinson *et al.* have shown that surface passivation in GaAs nanowires via overcoating with large bandgap semiconductor layer, such as AlGaAs, is essential to increase the carrier lifetime and photocarrier mobility [26]. Alternatively, surface passivation using organic small molecules has been demonstrated, in-particular, sulfide- and thiol-based treatments have been shown to improved the photoluminescence quantum yield, photocarrier lifetime and electrical properties of GaAs [30, 124–127]. Lunt *et al.* conducted one of the few systematic studies of a broad range of organic- and inorganic-thiol treatment on the surface of GaAs [30]. Fig. 2.18 summarizes the PL intensity of 1 μm thick epilayer (100) n-GaAs samples after various treatments. Their results revealed that the surface passivation using "sulfur-donors" can effectively increase the PL intensity by reducing the surface trapping states. Numerous studies further show the effectiveness of surface pas-

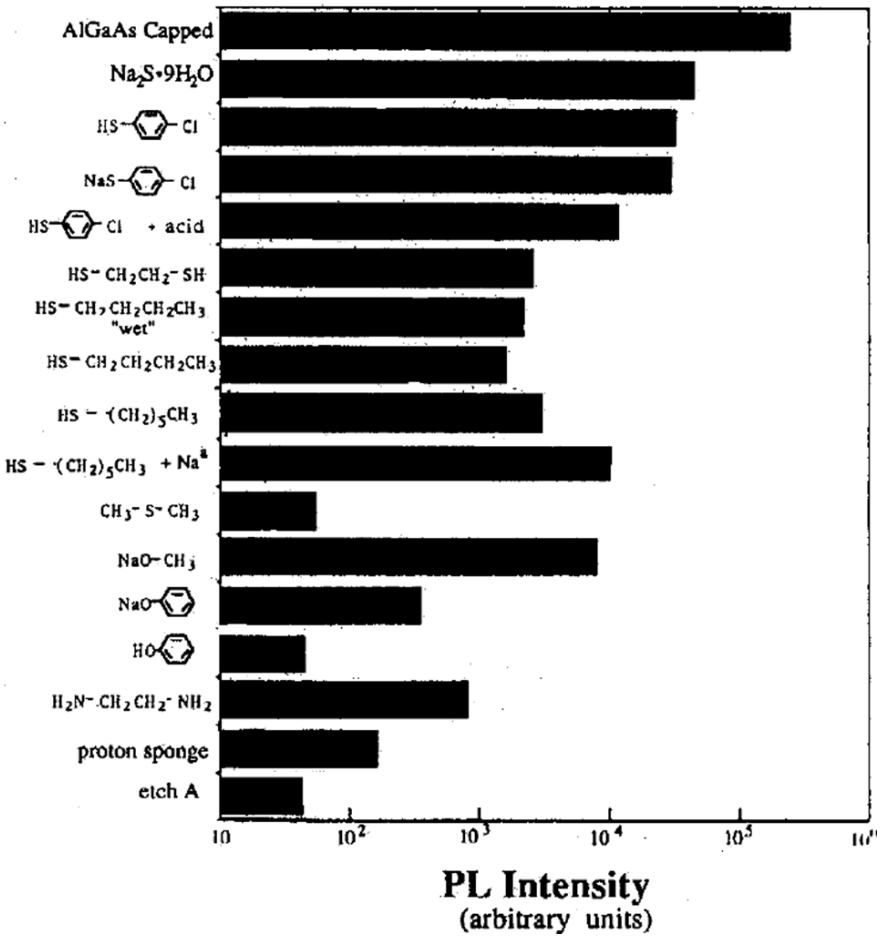

Figure 2.18: Bar graph of steady-state PL intensity at 874 nm for 1 μm thick epilayer (100) n-GaAs samples after exposure to various nonaqueous solutions. For the highest PL intensity sample, the term "AlGaAs capped" refers to a structure whose terminating topmost layer has a composition of $Al_{0.4}Ga_{0.6}As$. Additional experimental details are given in Ref. [30], from which this graph is reprinted.

sivation using selenium and sulfur treatments, which shows that reducing the donor states near the mid gap of GaAs is crucial to increasing their PL lifetime. Related to this is an ultrahigh vacuum (UHV) - scanning tunneling microscopy (STM) study by Pashley *et al.* of the n-GaAs (100) surface treated with elemental selenides [123]. Evidence is provided for Se-induced removal of kinks in the dimer vacancy rows of the GaAs (100) - (2×4) surfaces. Surface states arising from such kinks are believed to contribute to Fermi level pinning on the (100) surface of n-type GaAs material. High-resolution photoemission spectroscopy further reveals the formation of gallium-based selenides appearing as dominant species at the surface of GaAs [128]. The semiconductor surface treatment has extensive impact on

the device performance. He *et al.* showed that the surface conductance of silicon can be modulated by controlling the polarity of the attached ligands to modulate the surface-state filling [129]. These results indicate that carrier dynamics in semiconductor nanostructures can be controlled by modulating the surface properties.

2.3 Semiconducting Polymers

In year 2000, Alan Heeger, Alan MacDiarmid and Hideki Shirakawa were awarded the 2000 Nobel Prize in Chemistry for "the discovery and development of conductive polymers". The unique of this class of material can be seen as a new revolution where plastic material can be used in many electronic devices not as insulator but active conducting building-block. The carbon atoms comprising the backbone can be in an sp^3-hybridised form, termed saturated polymers, in which the four valence electrons are confined to be stationary in σ-bonds and no interesting electronic or optical properties arise [11]. Alternatively, the carbon atoms can be in an sp^2- (or sp-) hybridisation form in which one electron (π-electron) resides in a p_z-orbital which can be considered decoupled from the backbone σ-orbitals. These π-electrons can be delocalised along the chain and the resulting polymers are referred to as π-conjugated polymers.

2.3.1 Electronic Band Structure

The electronic band structure of semiconducting polymers is illustrated here using *trans*-polyacetylene as an example, whose structure is shown in Fig. 2.19 (a). Since each π-bond can accommodate up to two electrons, the π-band is half-filled around the Fermi level which would suggest that *trans*-polyacetylene would have metallic conductivity (*i.e.* the dispersion relation follows that of a 1-dimensional free-electron gas model) with a unit cell length of $a = 0.12\,\text{nm}$. However, 'real' polyacetylene has alternating single and double bonds with respectively longer and shorter lengths than equilibrium C-C bond lengths due to electron-phonon coupling [11]. The unit cell length is doubled due to the two degenerate configu-

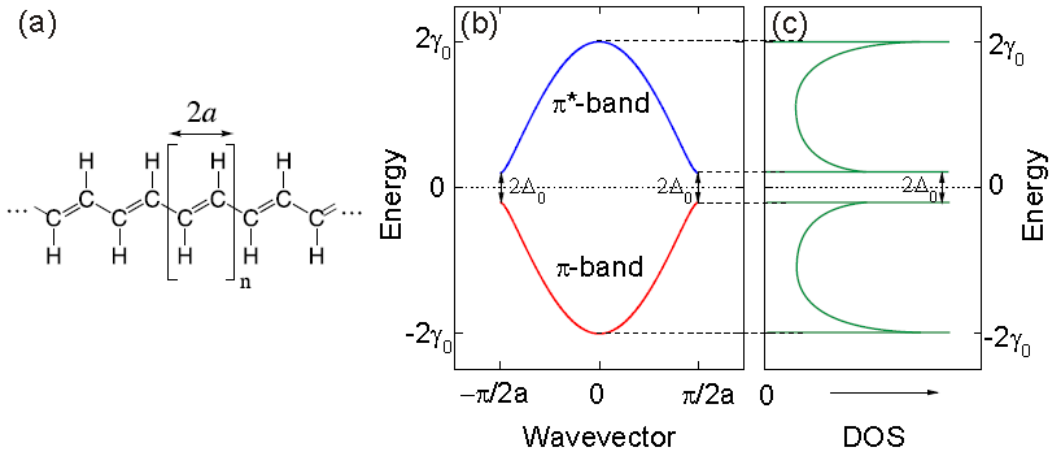

Figure 2.19: (a) Chemical structure of *trans*-polyacetylene, with the dimerised unit cell indicated. (b) The band structure of *trans*-polyacetylene in the first Brillouin zone given by Eq. 2.22, where the bandgap is given by $E_g = 2\Delta_0$. (c) The *trans*-polyacetylene DOS arising from the band structure.

rations arising from swapping the double and single bonds. This is known as dimerisation, which leads to an effective doubling of the real-space extent of a unit cell. This perturbation can be considered to be a Peierls instability[1] of a 1-dimensional metal and the two degenerate states at the Fermi level split into one above and one below, effectively opening up a bandgap (Peierls gap) given by $E_g = 2\Delta_0$ [11]. The overall effect of this process turns the *trans*-polyacetylene into an insulator, or - depending on the size of the band gap - a semiconductor.

Hückel molecular orbital theory (HMO) was developed by E. Hückel, presents a mathematical method to treat the properties of hydrocarbons with alternating single and double bonds [11]. It is equivalent to the Tight-binding (TB) model used in the field of inorganic semiconductors. The wavefunctions are treated to be linear combinations of p_z-orbitals, contributions from other atomic orbitals are neglected and the transfer integral term, γ_0, is used to describe how an electron is transferred to its nearest neighbours. A detailed derivation of the dispersion relation is not provided here but the interested reader is directed to Ref. [11]. The Schrödinger Equation is solved using the Su-Schrieffer-Heeger (SSH) Hamiltonian in the

[1]According to Peierls' Theorem, a one-dimensional equally spaced chain with one electron per ion is unstable with respect to a static lattice deformation of wavevector $G = 2k_F$. Such deformation creates a energy gap at the Fermi surface, thereby lowering the energy of electrons below the energy gap. [33]

dimerised form [130], which gives the dispersion relation in terms of the wavenumber k as:

$$E(k) = \pm\sqrt{\epsilon(k)^2 + \Delta_0^2}, \quad \epsilon(k) = 2t_0 \cos ka \tag{2.22}$$

The dispersion relation in the first Brillouin zone is plotted in Fig. 2.19 (b) and the corresponding DOS in Fig. 2.19 (c). The degenerate states split into the lower energy valence (π) and higher energy conduction (π^*) bands, separated by $E_g = 2\Delta_0$. All states in the π-band are filled but all states in the π^*-band are empty.

The band structure has been presented here for the simplest π-conjugated polymer *trans*-polyacetylene, which contains 2 carbon atoms in the repeating unit (unit cell) and subsequently 2 π-bands. However, the theory can be extended to other conjugated polymers with larger and more complex repeat units. In general, a conjugated polymer with n atoms in the main chain of the repeat unit will have n π-bands further split into $n/2$ π-subbands and $n/2$ π^*-subbands [11]. The highest energy π-subband that is occupied is referred to as the HOMO (Highest Occupied Molecular Orbital) and the lowest energy π^*-band that is empty is referred to as the LUMO (Lowest Unoccupied Molecular Orbital) [68].

2.3.2 Optical Properties

When a polymer absorbs a photon, an electron is promoted from the valence π-band to the conduction π^*-band, leaving a hole behind. The lack of intrinsic free carriers leads to a low level of Coulomb screening (typically $\epsilon_r \sim$2–4 [131]), and allows the creation of a Coulombically bound exciton, rather than free carriers. In a conjugated polymer, the strong binding of electron-hole pairs results in Frenkel excitons with small radii that are largely localized within the molecular chain alone with a diffusion length of <10 nm [11]. Photoluminescence polarization studies by Raucher *et al.* have shown that the primary photoexcitation species in conjugated polymers are indeed excitons, rather than free carriers [132]. Hence, the neutral excitations – excitons, can be seen as fundamental energy carrier in most conjugated polymers. The definition of exciton binding energy in organic semiconductors is rather more

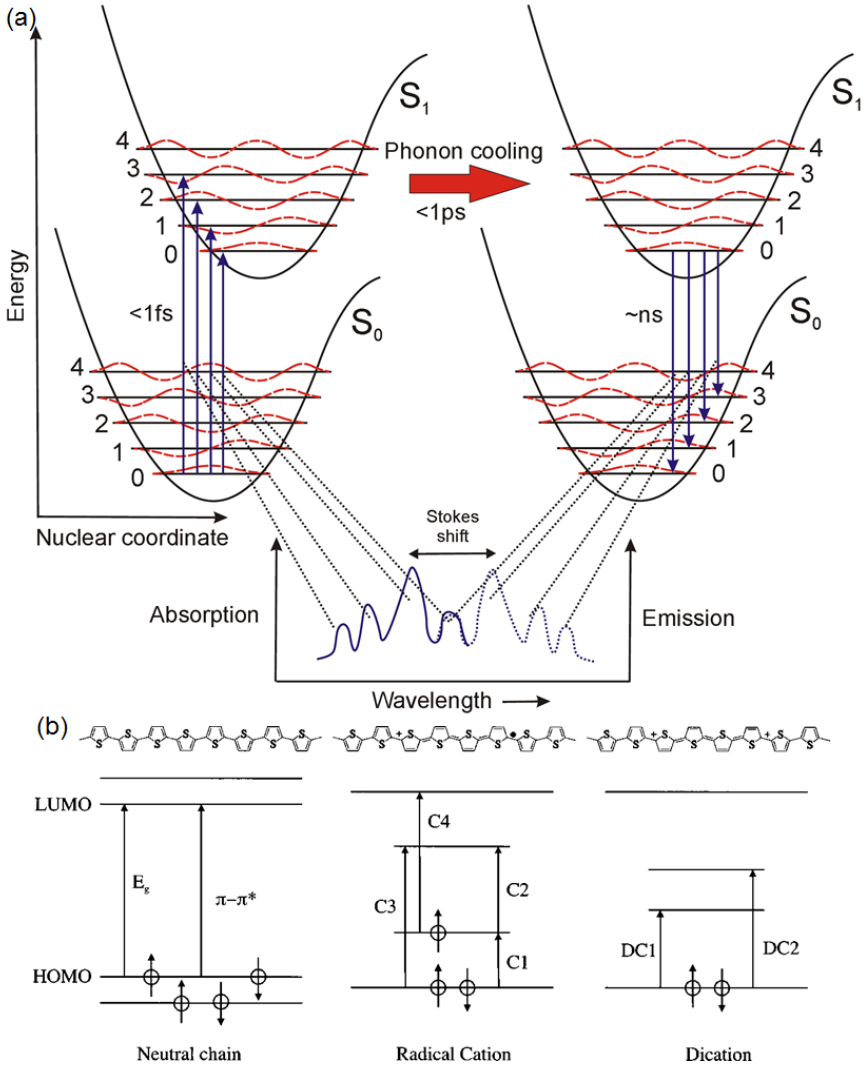

Figure 2.20: (a) Schematic diagram to illustrate the Franck-Condon Principle and the Stokes shift between absorption and emission progressions. (b) Molecular energy levels of a 1D thiophene chain for neutral (exciton), singly charged (polaron) and doubly charged (bipolaron) species. The C1 and DC1 transitions corresponds to the polaron and bipolaron relaxation energies, respectively. Transitions C3, C4 and DC2 are symmetry-forbidden in isolated chains.

complicated than that of their inorganic counterpart, due to the strong coupling between the polymer backbone goemetry and excitonic state. Brédas *et al.* suggest that the binding energy is the difference in energy between creating the excitonic state, and the creation of two oppositely charged, spatially separated and geometrically relaxed polarons [133]. The binding energy of Frenkel-type excitons in organic semiconductor varies significantly, with binding energies ranging from <100 meV for the polyvinylenes and polythiophenes to ∼400 meV for the polyfluorenes and even larger values for other conjugated polymer systems have been reported [11]. Typically, a distribution of exciton binding energies will exist in a polymeric system, due to the combined effects of strong carrier-phonon coupling and distribution of conjugated segments with specific electronic properties.

The lowest energy optical transition is the HOMO-LUMO (π-π^*) transition and corresponds to a singlet S_0 to singlet S_1 electronic transition in which the electron spins remain antiparallel. The creation of a mobile exciton could lead to removal of a π-conjugated electron from the backbone and result in creation of saturated bond. Hence, the polymer backbone is expected to undergo conformational change. Conjugated polymers exhibit strong electron-lattice coupling and each electronic S_i energy level is further split into vibrational energy levels approximated by the energy levels of the harmonic oscillator. These levels are illustrated schematically in Fig. 2.20 under the Born-Oppenheimer approximation, which states that the electronic transitions and nuclear motions (*e.g.* vibrations) are independent. The Franck-Condon Principle follows directly from this; the lighter electrons are excited on a much faster time scale (sub-fs) than the motion of the heavier nuclei (∼100 fs) and hence electronic transitions in Fig. 2.20 are represented by vertical lines. When an electron is promoted from the S_0 to the S_1 state it will generally be in a higher vibronic state. Rapid relaxation (sub-ps) occurs to the lowest S_1 vibrational state by phonon cooling and a transition occurs back to the S_0 state (∼ns), again to an excited vibrational state, with emission of a photon (fluorescence) [68]. Further vibrational relaxation returns the electron to the ground state. The intensities of the transitions are given by the overlap of the wavefunctions of the initial and final states in this Franck-Condon approximation [68].

Fig. 2.20a shows the chain of processes and reveals that the emission spectra are mirror images of the absorption spectra but with a red-shift. The difference between the 0-phonon absorption band edge and 0-phonon emission line is called the Stokes shift [11], which is typically ∼50 meV for semiconducting polymers [11, 134] and maybe negligible for the more rigid and ordered carbon nanotubes, in which excitons couple more weakly to nuclear motions [135].

Whether in absorption or emission, the probability of an electronic transition between two states is related to the overlap of their vibrational states. This dependence is expressed by the Huang-Rhys parameter S. If a single phonon dominates the electron-phonon coupling, the intensity of the nth peak in the vibronic progression of the absorption or emission spectrum is related to the intensity $I_\circ$ of the 0-0 peak (transition between the two vibrational ground states) by the following equation [136, 137]:

$$\frac{I_{0\to n}}{I_\circ} = \frac{S^n e^{-S}}{n!} \tag{2.23}$$

The change in configurational coordinate upon photoexcition, such as the electron-phonon coupling to form the polarons, bipolarons or excitons, is responsible for the localization of the excited states on the polymer chains, as shown in Fig. 2.20b [136]. In practice, absorption and emission spectra of π-conjugated polymers are significantly broadened [11] due to inhomogeneities in exciton energies arising from distributions in polymer conjugation length, effects caused by the chemical state of the polymer, torsional vibration leading to closely spaced replica, and lifetime-limiting effects, such as collisions in solution. Furthermore, the emission spectrum is usually narrower than the absorption spectrum. This phenomenon is due to exciton migration. The photogenerated exciton diffuses and becomes trapped in the low-energy portions of the polymer film prior to radiative recombination, a phenomenon called spectral diffusion [136, 137].

2.3.3 Polymer Aggregation and Chain Coupling

The simple Franck-Condon progression described previously holds for free and isolated polymer chains, such as when the polymer is dissolved in a 'good' solvent where the chains repel each other, resulting in well separated, stretched configurations. However, upon film formation, conjugated polymer chains tend to aggregate, forming ordered structures because of strong van der Waals interactions (π-π stacking) between chains. In general, formation of aggregates increases the effective conjugation length of the system and leads to optical red-shifts because the chains extend and planarise and the electronic coupling of parallel transition dipole moments also leads to significant reductions in PL quantum efficiencies [138].

According to Kasha's exciton model, excitons on polymer chains can be considered as point dipoles [139]. The interaction between these dipoles is crucial in aggregated systems and determines the oscillator strengths for transitions. Fig. 2.21 (a) shows a transition between the energy levels for an isolated polymer chain corresponding to a 0-0 transition. The excitations are intra-chain only and the regular Franck-Condon progression is observed. However, parallel chains form *weakly interacting* H-aggregates [140] and the corresponding dipoles can couple in such a high symmetry ensemble state, effectively delocalizing the excitation partly onto another chain. Parallel dipoles reinforce but antiparallel dipoles cancel, leading to a splitting of the energy levels into lower and higher energy components, respectively [139]. The transition dipole strength depends on the sum of the dipole vectors and hence the lowest energy transition, corresponding to the 0-0 transition, is forbidden[2]. By contrast, this symmetry is broken in higher vibronic states and the usual Franck-Condon progression is observed [141]. The net effect with increasing aggregation is an overall red-shift of all transitions, a reduction in PL intensities and a suppression of the 0-0 peak relative to the higher vibronic transitions [142].

The self-aggregation of polymers to form H-aggregate has been always directly associated with the marked changes in the emission spectral line shape. A particularly important

[2]H-aggregates are so called because the coupling described here leads to a forbidden lower energy transition, giving an effective *hypsochromic* (*i.e.* blue) shift in their electronic transitions.

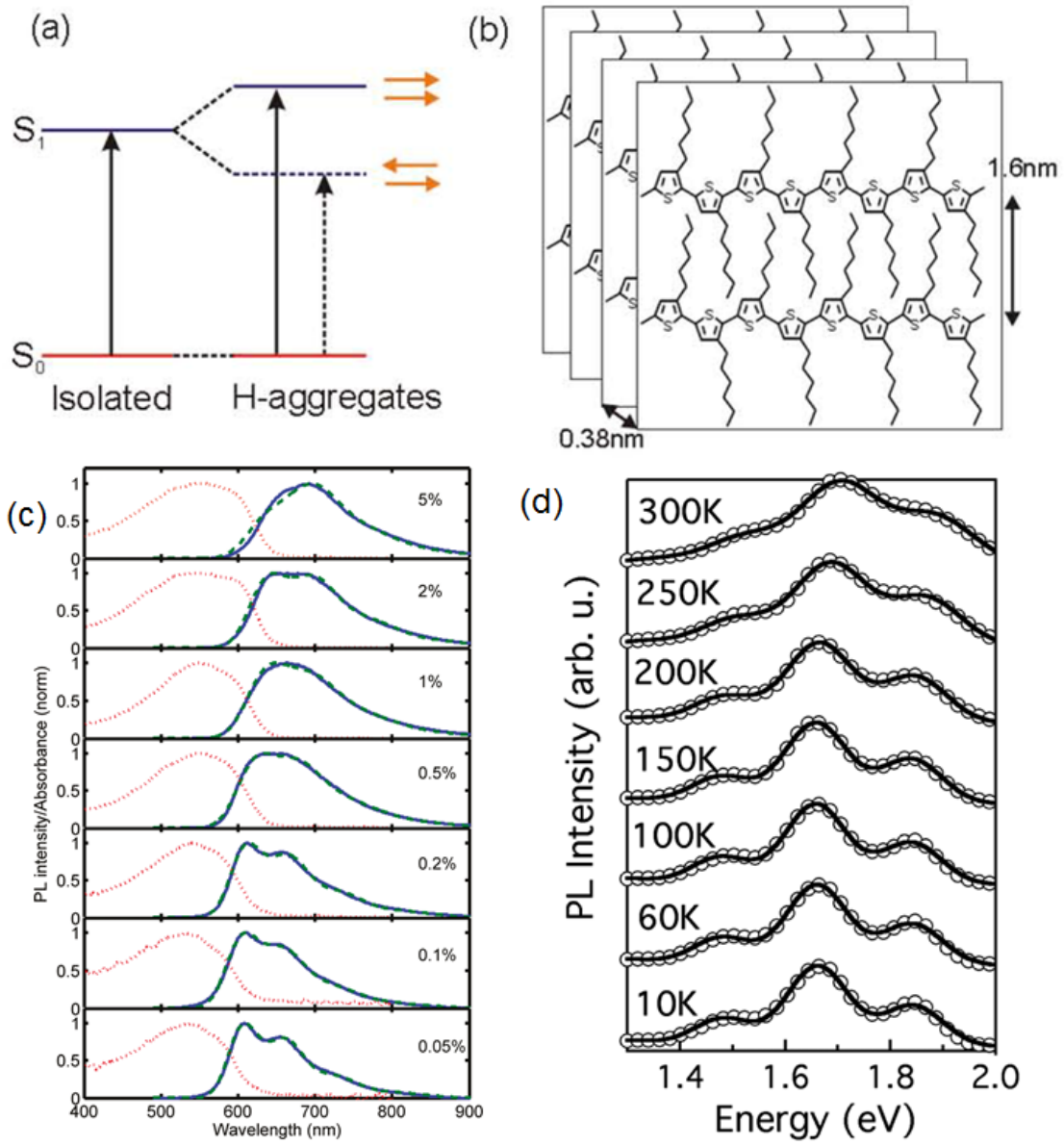

Figure 2.21: (a) Schematic energy diagram to show the splitting of the excitonic levels corresponding to the 0-0 transition due to chain-chain coupling, leading to a forbidden transition (dashed line). (b) Schematic diagram of P3HT lamellar aggregates showing the dimensions of interchain distances within and between π-stacks [143]. (c) Adapted from Ref [144]. PL (solid blue; green dashed shows fit using model proposed in Ref. [142]) and absorption spectra (red dotted) for samples progressing from isolated (0.05wt%) to aggregated (5wt%) P3HT suspended in an inert polyethylene matrix. (d) Temperature dependent PL spectra of film spun from chloroform solution (Adapted from Ref [142]).

polymer system that demonstrates this behaviour is regioregular poly(3-hexylthiophene) (P3HT). The regioregular alternating alkyl side-chain geometry leads to the polymer chains forming 2-dimensional, highly ordered lamellar structures, as shown in Fig. 2.21(b). The lamellae form by π-stacking of the conjugated backbones and the alkyl chains interdigitate within sheets. The dominant interactions are between the π-stacks due to the shorter stacking distance, and the aggregates can therefore be considered as H-type [141]. P3HT has been studied using grazing-angle X-ray diffraction (GIXRD) and Near-edge X-ray absorption fine-structure (NEXAFS) spectroscopy, which reveal the high crstallinity and existence of cofacial π-π stackings [145, 146]. Fig. 2.21(c) compares the absorption and emission spectra obtained by Parkinson *et al.* from P3HT suspended in a matrix of inert polyethylene at low and high concentrations (*i.e.* isolated and aggregated chains, respectively) [144]. At low concentration (i.e., well-separated polymer chains), the 0-0 emission is comparable to that of the 0-1 emission. As the concentration is increased, the 0-0 peak is suppressed while the higher vibronic peaks follow the usual Frank-Condon progression, with an overall underlying red-shift. Clark *et al.* further confirm that the emissions at the 0-0 and 0-1 peaks origin from the vibronic coupling and cannot be attributed to the presence of two uncorrelated species [142]. In organic solid film, the 0-0 emission strength can be increased by the torsional effect associated with the thermal relaxation [142]. Fig. 2.21 (d) shows the temperature dependent PL emission spectra. As the temperature is increased, the 0-0 emission strength is increased, as a result of thermal disorder.

In practice, the presence of disorder in the film relaxes the selection rule and allows the observation of such transition with lower intensity than expected from a simple Frank-Condon progression [142]. Hence, the spectroscopic signatures of the H-aggregates of P3HT is highly dependent on the processing conditions and the 0-0 to 0-1 peak intensity was used as a measure of the disorder in the film, which is related to the device performance. From the ratio of the 0-0 to the 0-1 absorption peaks, the free exciton band width $\mathbf{W}$, which is related to the strength of the intermolecular coupling J in the π-π stacking direction ($\mathbf{W} = 4J$ in the weak coupling regime [141, 141, 142]). It has been shown that the exciton bandwidth is related to the organic semiconductor transistor action. Sharper turn-on current was ob-

served in transistors using P3HT with smaller W, indicating the presence of H-aggregates with longer conjugation lengths and narrower distribution of traps near the valence-band edge [147]. In general, the H-aggregates responsible for the luminescence spectra are distinct from those responsible for absorption [148]. The emitting aggregates were found to have on average larger exciton band width (i.e., shorter conjugation lengths) than the absorbing aggregates. However, the red-shift due to aggregation is much larger than the blue-shift due to the reduced conjugation length, therefore the emission from the film remains red-shifted compared to the absorption.

2.3.4 Polarons in Organic Semiconductors

A free charged particle (electron or hole) moving on a conducting polymer will deform the lattice structure [11]. The charge plus its associated polarisation field can be considered as a quasi-particle called a polaron. In a conjugated molecule such as polyacetylene or P3HT, the dimerisation of the two configurations of alternating double and single bonds is perturbed at the point of the polaron [136]. The relaxation of the bond dimerisation and lattice structure leads to two localised states in the HOMO-LUMO gap, resulting in two optical polaronic transitions. This is shown in Fig. 2.22 (a) for a hole confined to a 1D polymer chain, called a localised polaron P^+. Their spectroscopic signatures appear therefore as sub-gap absorption bands. Chemical doping is the easiest way to introduce charges in the polymers [149]. Polarons can be generated in a semiconductor via chemical doping, electrical injection, and selective trapping of electrons or holes [150]. The later results in quenching of exciton emission, which is generally observed in organic photovoltaics formed by electron donating and accepting materials. More details about exciton quenching in organic photovoltaic will be discussed in Section 2.4.2.

In a 2D polymer stucture, such as the lamellar networks formed by P3HT, the neighbouring chains are coupled and this causes a reduction of the HOMO-LUMO gap by an amount 2Δ, due to increased conjugation, and a splitting of each of the polaronic levels by the same amount [150]. The polaron can be considered as delocalised across several chains

and is referred to as a delocalised polaron, shown in Fig. 2.22 (b) for the case of a hole (DP^+). The relaxation energy of polarons was found to be smaller in highly regioregular P3HT compared to low regioregular P3HT [150]. The dynamical motion of polarons differs significantly from that of excitons, due primarily to the non-zero electronic charge. The formation of delocalized polarons in regioregular P3HT, which is attributed to the increased π-π stacking in the film, is also associated with higher carrier mobility, as compared with the mobility of polarons in other polymers. Mobility values as high as $0.1\,\mathrm{cm^2V^{-1}s^{-1}}$ can be achieved in highly ordered networks of polymer such as in the lamellar structures formed by P3HT [151].

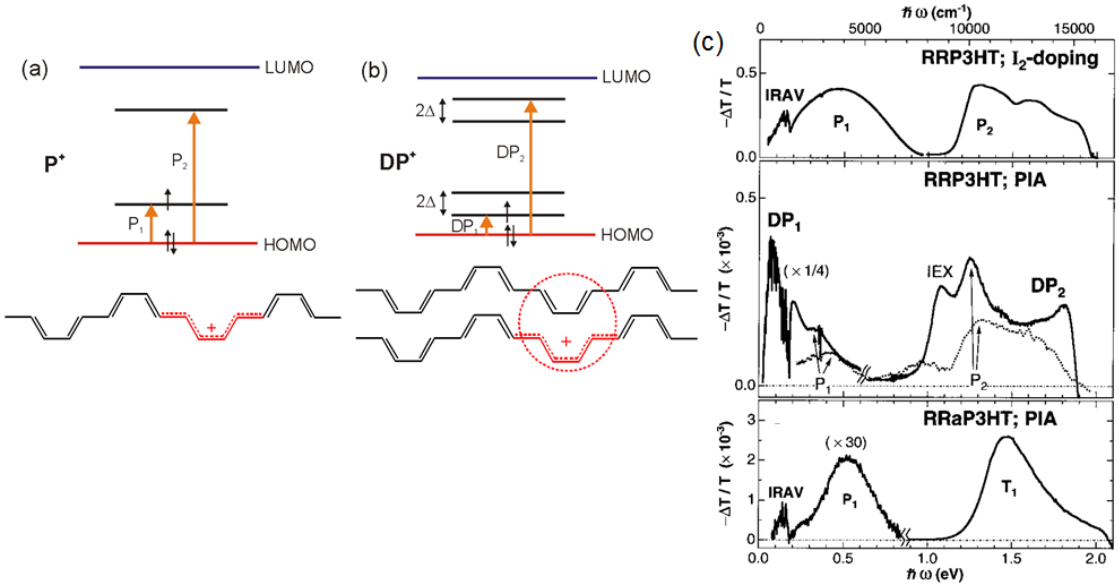

Figure 2.22: (a) A free hole on a 1D conjugated polymer chain backbone is a localised polaron P^+ and leads to two mid-gap states. (b) Coupling between adjacent chains in a 2D lamellar structure allows the hole to be delocalised across several chains, corresponding to a delocalised polaron DP^+ in which the polaronic states are themselves split. (c) The PIA bands of regioregular P3HT (RRP3HT) film doped with I_2 (above), PIA band in regioregular (medium) and regiorandom (RRaP3HT, bottom) films, collected at 80 K. IEX and T_1 are related to interchain singlet exciton and intrachain triplet exciton, respectively, whereas IRAV are IR-active vibrations associated with the 1D polarons. After Ref. [150].

Photoinduced absorption (PIA) spectroscopy is conceptually the simplest way of studying the presence of new absorption bands due to excited states. In non-degenerate ground state polymers, photoexcitation generates polarons, bound polarons and excitons (Fig. 2.21b). In MEH-PPV, PIAs at 0.6 and 1.6 eV have been attributed to bipolaron transitions [149].

The assignments of PIA is always compared with the chemically doped samples. The band disappears in more ordered material, and thus confirming that bipolarons are stablized by disorder. Fig. 2.22c displays the PIA induced by chemical doping and photoexcitation in regioregular and regiorandom P3HT. The band assignment in PIA spectra is in accordance with the absorption spectrum obtained after chemical doping. Polarons in highly ordered polymer matrix appear to have lower relaxation energy (DP1 and DP2) as compared with polarons localized by disorder (P1 and P2) [150].

2.4 Organic Photovoltaics (OPVs)

2.4.1 Exciton Migration - Energy Transfer Processes

In organic semiconductor, excitons tend to hop from spectroscopic units of higher energy to those of lower energy. This effect has been experimentally observed from time-resolved photoluminescence spectroscopy. The photoluminescence spectra gradually red-shift with increasing time [152, 153]. The lowest energy state is generally the section of polymer backbone with the longest conjugation length. However, in a polymer blend consisting of two organic semiconductors with different band gaps, the exciton can be spatially hopping from the polymer with larger band gap (donor) to another polymer associated with smaller band gap (acceptor). For polymer blends consisting of suitable donor and acceptor materials, a type-I heterojunction, shown in Fig. 2.23 (a), forms when the HOMO-LUMO gap of the acceptor lies between the gap of the donor. In this case, the photoexcited exciton on the donor can transfer non-radiatively to the acceptor in a process called ***energy transfer***. The exciton on the acceptor can then recombine radiatively (or non-radiatively).

The energy transfer generally occurs via the Förster Resonance Energy Transfer (FRET) mechanism, which is non-radiative, Coulomb-mediated interaction. The transfer involves the coupling of electric dipoles on the donor and acceptor [154]. The transfer rate k_{FRET} can be derived from Fermi's Golden rule and is given by:

$$k_{\mathrm{FRET}} = \frac{1}{\tau_{\mathrm{D}}} \left(\frac{R_0}{R} \right)^6, \tag{2.24}$$

where τ_{D} is the donor radiative decay time constant and R is the distance between the donor and acceptor. Eq. 2.24 suggests that the energy transfer efficiency depends critically on the physical distance between the donor and acceptor. This is characterized by the Förster radius R_0, representing the distance at which the efficiency of energy transfer is 50%, and is given by:

$$R_0^6 = \frac{9\kappa^2 \phi_D}{128\pi^6 n^4} J, \quad J = \int \frac{f_D(\nu)\sigma_A(\nu)}{\nu^4} d\nu. \tag{2.25}$$

Here n is the refractive index of the medium between the donor and acceptor, ϕ_D is the PL quantum efficiency of the donor, κ is the orientation factor between donor and acceptor, and the integral term J represents the spectral overlap between the donor emission f_D and the acceptor absorption (cross-section) σ_A weighted with a factor involving the wavenumber of light ν [154, 155]. Typical Förster radii are 1–10 nm and the transfer rate drops significantly at larger distances because of the R^{-6} dependence in Eq. 2.24 [154].

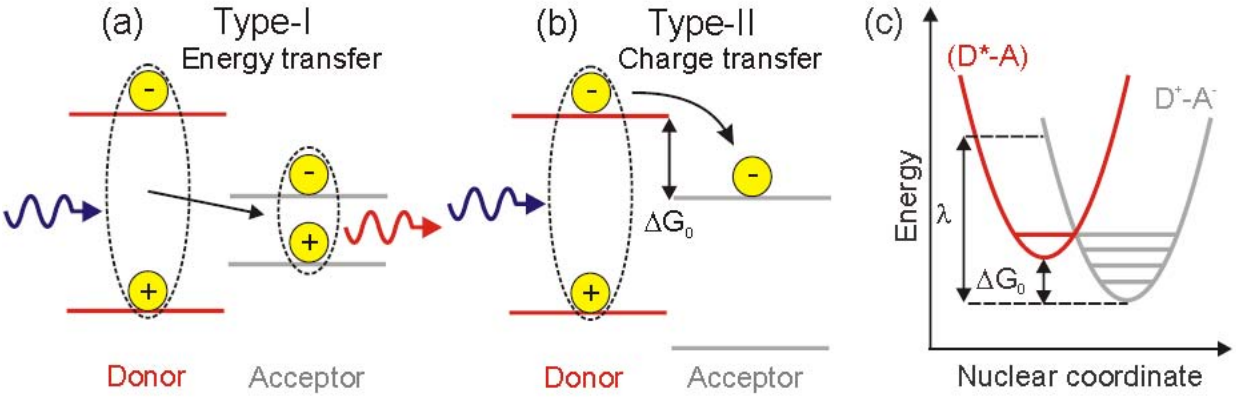

Figure 2.23: A donor-acceptor blend forming a type-I (a) and type-II (b) heterojunction interface at which energy and charge transfer occur, respectively. (c) Charge transfer between a photoexcited donor D^* and acceptor A is governed by semi-classical Marcus theory. The rate is determined by the overlap of the vibrational wavefunctions of the acceptor with those of the ground vibrational state of the donor and the reduction in free energy ΔG_0 relative to the total reorganisation energy λ.

In some cases, the strong overlapping of wavefunctions in the donor and acceptor leads to exciton tunneling between polymer strands via intermolecular orbital overlap. This process occurs typically at very short distances between the donor and acceptor ($R < 1\,\text{nm}$) [156]. Dexter extended the Förster theory to include higher order multipoles and wavefunction overlap [157]. This leads to an electron exchange mechanism (Dexter exchange) whereby energy transfer occurs by simultaneous transfer of an electron from the donor to the acceptor LUMO and another from the acceptor to the donor HOMO. The rate of Dexter transfer k_{Dexter} is given by:

$$k_{\text{Dexter}} \propto J' e^{-2R/L}, \tag{2.26}$$

where J' is the same spectral overlap integral as in Eq. 2.25 except without the ν^4 weighting, L is an effective average Bohr radius for the excited and unexcited states of the donor and acceptor and the exponential term arises from the wavefunction overlap. The exchange mechanism can only occur over a very short distance, typically an order of magnitude less than a Förster mechanism [157].

2.4.2 Charge Transfer and Charge Separation Processes

When the energy level alignment between the donor and acceptor exhibits staggered alignment, a type-II heterojunction is formed, as shown in Fig. 2.23b. Photoinduced charge transfer can occur across the materials provided there is a significant driving force that can overcome the binding energy of the exciton on the donor [11]. The driving force is given by the difference between the LUMOs of the donor and acceptor ΔG_0, as labelled on Fig. 2.23b. However, energy transfer can be favorable when the band gap of the donor is larger than that of the acceptor. This process is similar to the scenarios described for a type-I heterojunction (Fig. 2.23a), except that the energy transfer is competing with the charge-transfer. In a type-II heterojunction, the charge transfer is controlled by the staggered alignment across the heterojunctions. The energy barriers present at the interface allows the transfer of elec-

trons but not holes, from the donor to the acceptor. As will be discussed in Section 2.4.3, this process is crucial for charge generation in OPV devices. Efficient device performance relies upon the photogenerated exciton moving to a donor/acceptor interface so that exciton dissociation can occur. Due to their electrical neutrality, the motion of excitons is not affected by electric fields, and thus, they diffuse through the blend randomly. This diffusion is typically described as a Förster-type incoherent energy transfer process, which can be either intramolecular or intermolecular and usually acts to lower the energy of the exciton.

The charge transfer process can be described by considering the overlap between the lowest vibrational state in the donor's excited state with an acceptor vibrational state of similar energy, as shown in Fig. 2.23 (c). Although there is a reduction in free energy driven by the energy difference ΔG_0 (driving force), there is a barrier to transfer in the form of a reorganisation energy λ, which incorporates components from the change in molecular shape (λ_0) and the reorientation of dipoles due to the placement of the transferred charge [158]. The rate of charge transfer between conjugated systems satisfying the Franck-Condon principle is given by the semi-classical Marcus theory [158–161] as:

$$k_{\mathrm{CT}} = \frac{2\pi}{\hbar} H^2 \left(\frac{1}{4\pi\lambda_0 kT} \right)^2 (FC), \quad \text{where} \tag{2.27}$$

$$(FC) = \sum_{n=0}^{\infty} \exp(-S) \frac{S^n}{n!} \exp\left(\frac{-(\lambda_0 + n\hbar\omega + \Delta G_0)^2}{4\lambda_0 kT} \right). \tag{2.28}$$

Here, the first factor (H^2) is the coupling matrix element between the donor and acceptor electronic states and the second factor arises from the classical density of states. The Franck-Condon (FC) factor is a sum over all possible vibrational overlap integrals between the initial 0-th vibrational donor level and the n-th vibrational level of the acceptor, where the exponential factor $\exp(-S)$ accounts for the effective electron-phonon coupling S and $S^n/n!$ describes the population probability of the acceptor's vibrational states with harmonic oscillator vibration frequency ω. The final exponential factor is a Boltzmann term describing the probability of the transfer, showing that the rate is maximised if there is a close

match between the energy released ΔG_0 and the sum of the acceptor vibrational energy and reorganisation energy λ_0 [158]. Equation 2.28 predicts that as the ΔG_0 increases, so does the electron transfer rate, until the maximum rate is reached when $\lambda_0 = \Delta G_0$ [162]. At this point, the reaction has no activation barrier and further increases in -ΔG_0 will decrease the reaction rate. This is called the Marcus inverted region and has indeed been observed expermentally [163–165].

The spatially separated electron-hole pairs bound at the interfaces of donor-acceptor, due to the weak Coulomb screening in organic semiconductor. The charge-transfer species is referred to as a ***polaron pair***. Ultrafast PIA spectroscopy has revealed the formation of such species appears at the interface of organic donor-acceptor. Their dissociation into free carriers is rather slow and occurs over a few microseconds [166–168]. Recent experiments based on optical pump-push-probe spectroscopy further confirms that the binding energy of such "cold" interface bound states is typically 300–500 meV [169]. In organic solar cells, one of the loss mechanism has been identified to be due to the geminate recombination of electron-hole pairs Coulombically bound at the interface between donors and acceptors [160]. The long-term recombination of electron-hole pairs is mainly dominated by the non-geminate recombination via the bimolecular recombination route [167]. The various charge recombination processes are summarized in Fig. 2.24.

The geminate recombination of electron-hole pairs that are Coulombically bound is first described by Onsager [170] and later modified by Braun to account for the finite lifetime of the Coulombically bound electron-hole pairs [171]. In this revised Onsager-Braun model, it is assumed that the dissociation of the bound pairs into free charge carriers is a reversible process and competes with the recombination of this charge pair. The dissociation rate is given by:

$$k_{\text{diss}} = k_R \frac{3}{4\pi a^3} e^{-E_B/kT} \left[1 + b + \frac{b^2}{3} + \frac{b^3}{18} + \ldots\right], \quad b = e^3 E / 8\pi\epsilon_0\epsilon_r k^2 T^2, \tag{2.29}$$

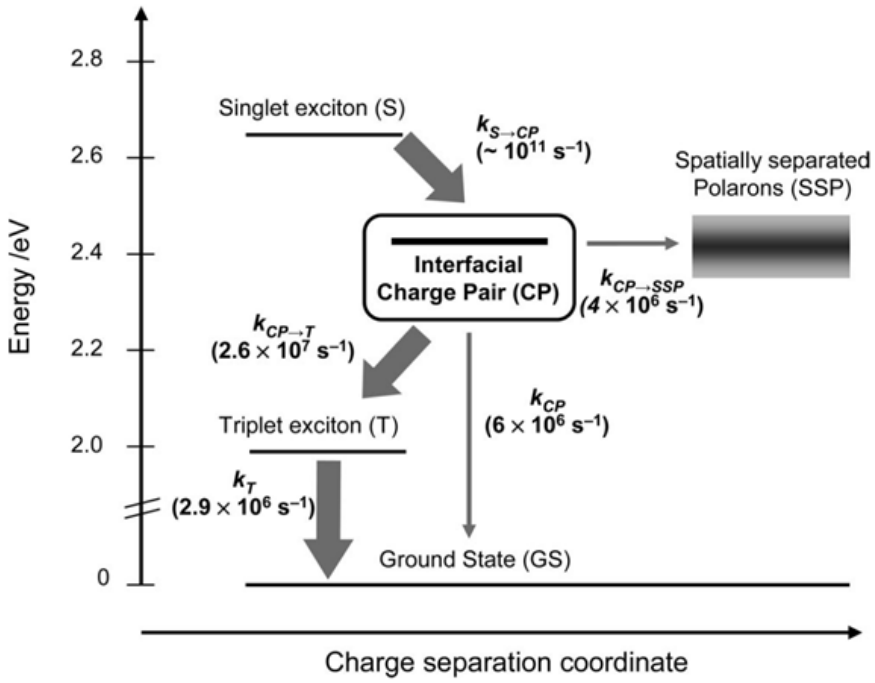

Figure 2.24: Charge recombination mechanism at the polymer-polymer heterojunction. After Ref. [167].

where k_R is the recombination rate of the dissociated charges, a is the separation of the charges, E_B is the polaron-pair binding energy, T is the temperature and E is an external or built-in electric field across the blend.

There is currently debate over the mechanism for dissociation of the polaron pairs. Tachiya *et al.* noted that Onsager's theory was no longer applicable when materials with very high electron mobility are used since the model assumed describes the Brownian motion of a particle only when its mean free path is negligibly short compared to the length scales used in the equation [172]. More recently, ultrafast spectroscopy evidence shows that the excess energy gained from the charge transfer across the type-II interface with energetic offset higher than the binding energy of exciton is transferred to the kinetic energy of polarons that assists the dissociation into free charge carriers [173, 174]. While the free charge carrier generation in organic semiconductor is yet to be resolved, the Cambridge group has revealed that such dissociation involves excess energy of the order of few hundred meV to excite the "cold" polaron into the uncorrelated HOMO-LUMO states of donor and acceptor [169].

2.4.3 Bulk Heterojunction Solar Cells

The first investigation of OPV cells came as early as 1959, at which the antracene single crystal was used as photo-active media. The cell exhibited a photovoltage of 200 mV with efficiency lower than 0.1 % [175]. A significant breakthrough was made by Tang *et al.* in 1986 where the OPV cells were made in a donor-acceptor bilayer structure, which resulted in an efficiency of ∼1 % [10]. The energy level alignment of such devices exhibit staggered type-II band alignment, where excitons generated in the proximity of donor-acceptor interface can be dissociated to form charge-carriers. However, the device architecture based on bilayer donor-acceptor heterostructures set the limit for the thickness of the active layer, since the exciton diffusion length in organic semiconductor is typically < 10 nm [176, 177] and exciton recombination can occur prior to their dissociation at the donor-acceptor interface. Reducing the film thickness will resolve this issue. However, the film might be too thin to absorb sufficient incident photons. In mid-1990, OPV devices based on bulk heterojunctions that have a nanostructured phase-separated morphology in which each of the two components self-assemble to form a continuous interpenetrating networks was demonstrated [178]. This effectively reduces the exciton decay processes at which the length scale of blends is comparable to the exciton diffusion length in the bulk and exciton dissociation can take place in the proximity of exciton generation prior to their self-decay process [11, 179], as shown schematically in Fig. 2.25c, d. In 2001, bulk-heterojunction photovoltaics based on conjugated polymers poly(2-methoxy-5-(3,7-dimethyloctyloxy)-p-phenylene vinylene) (MDMO-PPV) and ((6,6)-phenyl-C61-butyric acid methyl ester) (PCBM) blend yielded a power conversion efficiency of 2.5 % [180]. By further optimizing the nanoscale morphology, it was shown that the efficiency of organic PV could reach 6 % when regio-regular poly(3-hexylthiophene) (P3HT) and PCBM were used as photo-active media [181, 182]. This shows the importance of nanoscale morphologies, energy alignment and composition of the blend on the efficiencies of the OPV devices [182, 183]. The Forrest group further shows the potential application of copper-phthalocyanine (CuPc) as electron donor and absorbing layer, which when blended with fullerene gives an efficiency of 6 % [184, 185].

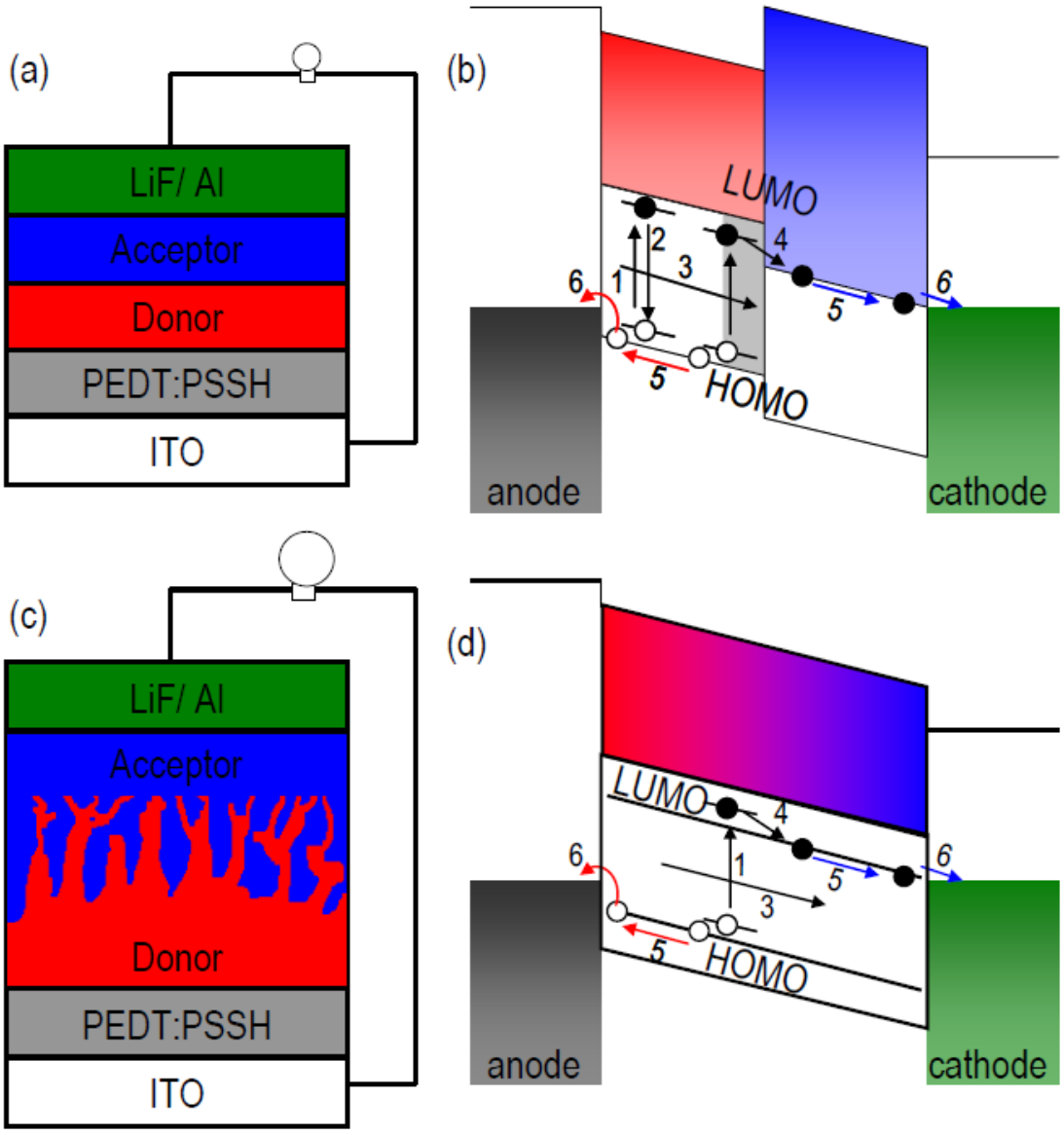

Figure 2.25: Schematic structure and energy alignment diagram of bilayer (a, b) and bulk heterojunctions (c, d). The number refer to the operation processes as follow: 1. exciton generation; 2. exciton recombination; 3. exciton diffusion; 4. exciton dissociation and interface charge transfer to form Coulombically bound polarons; 5. dissociation of polaron pairs at the interface to generate free carriers and charge transport in the respective donor and acceptor phases for holes and electrons; 6. charge collection at the electrode-semiconductor interfaces.

The current benchmark organic solar cells utilise polymers as donors blended with substituted fullerenes as electron acceptors [183]. As mentioned in Chapter 1, the majority of the semiconducting polymers only absorb sunlight near the visible region, leaving the photon at below the infrared regime largely wasted. By using recently synthesised low bandgap polymers as donors, efficiencies have reached 5-8 %, with internal quantum efficiencies approaching unity (*i.e.* nearly all absorbed photons are converted into free polarons that are collected at the electrodes) [186–188], and a commercial market has recently emerged [183]. The most heavily investigated system consists of regioregular P3HT blended with phenyl-C_{61}-butyric acid methyl ester (PCBM), a fullerene with a solubilising side group. The success of this blend can be attributed to two key factors. First, the P3HT and PCBM components segregate into crystalline phases upon thermal annealing, providing separate and continuous networks to transport the electrons and holes to respective electrodes [183]. Second, PCBM has a very deep LUMO level (*i.e.* high electron affinity), leading to a very large driving force ($\Delta G_0 \sim$1 eV) for charge transfer from P3HT. The relatively large polaron pair binding energies are thought to be overcome by the excess energy from the charge transfer process (hot polaron pairs) [173], the large local mobilities in the crystalline regions [189] or, perhaps most significantly, the delocalisation of charge carriers within conjugated segments of the polymer chain [190].

There are a few main challenges remaining in the are of OPV devices based on polymer–polymer blends. The morphology of the photoactive layer is difficult to control to give well-formed of percolation paths for the separated charges to travel within the material toward the electrods [191–193]. As mentioned in Section 2.4.2, the separated electron-hole pairs at the interface between donors and acceptors remains largely bound to form charge-transfer states, where the pairs undergo geminate recombination within a few nanoseconds which competes directly with the full dissociation into free carriers [194].

2.4.4 Hybrid Organic Solar Cells

Solar cells made with organic and inorganic materials have been demonstrated recently by several groups. Most hybrid devices comprise an interpenetrating networks of electron donor and acceptor materials[3–7]. P3HT, MEH-PPV have been widely used as electron donor to blend with inorganic semiconductors, such as silicon, gallium arsenide, cadmium selenide, cadmium telluride, and metal oxide [3, 4, 9, 15, 19–22]. The key advantages of using inorganic semiconductor components in these excitonic solar cells include a higher dielectric constant, higher carrier mobility, direct band gap for optical absorption, chemical and physical stability and control over the band gap energy via dimension and size of nanostructures [3, 5, 9, 20, 24, 25]. Furthermore, the inorganic components in the hybrid organic solar cells are superior electron transporter and dominate the photocurrent generation in the solar cells [5, 195, 196].

These cells have much higher efficiencies than those based on single-component polymer films, but the device performance can be limited by the inefficient charge transport due to discontinuous percolation pathways [4, 5]. Since the exciton diffusion length in the polymer matrix is typically few nanometers [197], the morphologies of the bulk heterojunctions play important roles for the device efficiencies. Regioregular P3HT has been widely used as electron donor which acts as both photon absorber and hole-transporter in the devices. This is mainly due to the higher hole mobility in the regioregular P3HT, as compared with other polymers. Herrmann *et al.* have been shown that the loss mechanism in regioregular P3HT based hybrid solar cells is mainly due to the bimolecular recombination of free carriers occuring on time scale above a few hundred microseconds [198]. However, switching from regioregular P3HT to regiorandom P3HT has resulted in loss mechanisms dominated by the geminate recombination of charge carriers at the interfaces of organic-inorganic semiconductors. Single crystalline nanowires, on the other hand, provide superior carrier transport along their growth axis [20, 26, 199]. It has been recently shown that hybrid solar cells employing nanowires with high aspect ratio give higher short circuit current and lower series resistance [20, 200, 201]. The distance between the nanowires is also crucial, and should remains comparable to the exciton diffusion length of the organic semiconductor surrounding

them [4, 5, 9].

As mentioned in section 2.4.2, the type-II heterojunction at the organic-inorganic heterojunction leads to ultrafast charge transfer and separation [5, 15, 198]. The PL emission is a direct probe of exciton dissociation at the interface, since its intensity is proportional to the product of electron and hole densities in the same **k** space [46]. However, the exciton dissociation in these devices has been found to be much slower [202] than in the fastest polymer bulk heterojunctions [203–205], and is limited by the potential barriers at the interface and the nonideal overlap of the densities of states of the polymer and the inorganic phase [206, 207]. Furthermore, steric effects arising from the polymer side-chains may inhibit the charge-transfer process across the interfaces [16]. Electron transport and recombination rates, on the other hand, are extremely sensitive to the nanoparticle morphology, with directional and elongated nanorod structures showing significantly improved cell efficiencies [3, 23, 202, 208].

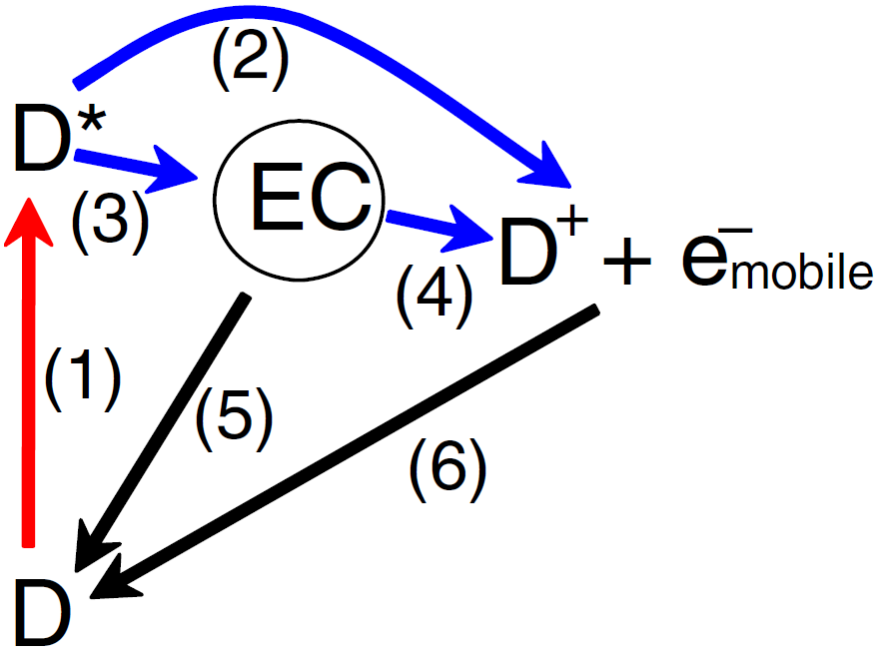

Figure 2.26: Scheme of the processes in dye-sensitized semiconductors. (1) Dye excitation, (2) direct electron injection, (3) formation of an electron-cation (EC) complex, (4) dissociation of EC complex, (5) recombination of EC complex and (6) charge recombination.

The free-charge generation in organic solar cells is rather slow, due to the strong Coulomb binding of electron-hole pairs at the donor-acceptor interfaces, and competing directly with

the geminate recombination. The higher electronic permitivity in inorganic semiconductors could give faster charge separation and has been subjected to a wide debate in both ultrafast spectroscopy and organic photovoltaic communities. In-particular, hybrid photovoltaic devices show very moderate performance [195, 209, 210]. Using ultrafast laser spectroscopy, a number of research groups have shown the influence of the electronic permitivity on the free-carrier generation at inorganic-organic semiconductor interfaces. Their findings suggest that the spatially separated electron-hole pair at the organic-inorganic interfaces is still subjected to sizeable Coulomb interactions [18, 195, 209–213]. Němec and co-workers studied the free-carriers injection from the organic dyes to the TiO_2 and ZnO nanostructures [18]. The dielectric constant of TiO_2 is nearly 20 times higher than the dielectric constant of ZnO [18, 210]. The various photoinjection processes are summarized in Fig. 2.26. For charge-injection from the dye to ZnO, the free carrier generation is associated with the interaction betweeen the injected electrons and dye cations at the organic-inorganic interfaces over a few hundred picoseconds. This leads to the formation of an electron-cation complex, which causes fast charge recombination at the interface and dramatically decreases the electron mobility. For dye-sensitized TiO_2, the free carriers generation is almost instantaneous and no such electron-cation complex is detectable at the interfaces, attributable to the high permittivity efficiently screening the charges.

The formation of bound states at the interfaces of organic-inorganic interfaces has been further demonstrated by the Cambridge group using optical pump-push-probe techniques [212]. Using this technique, the bound charge pair formed at the interface of polymer-ZnO is "pushed" back to their "hot" state to form free charges in the polymer and ZnO [169, 212]. Their results show that the bound charge pairs are quickly formed within a few picoseconds after photoexcitation. The dissociation of these bound charge pairs requires "re-excitation" energy of a few hundreds meV, indicates the formation of tightly bound of electron-hole pairs is still possible even at the polymer-metal oxide interface. The formation of such bound charge pairs reduces the free carrier generation due to the geminate recombination process. The formation of bound charge pairs can be reduced by terminating the surface of semiconductor with a self-assembled monolayer, without reducing the injection of carriers

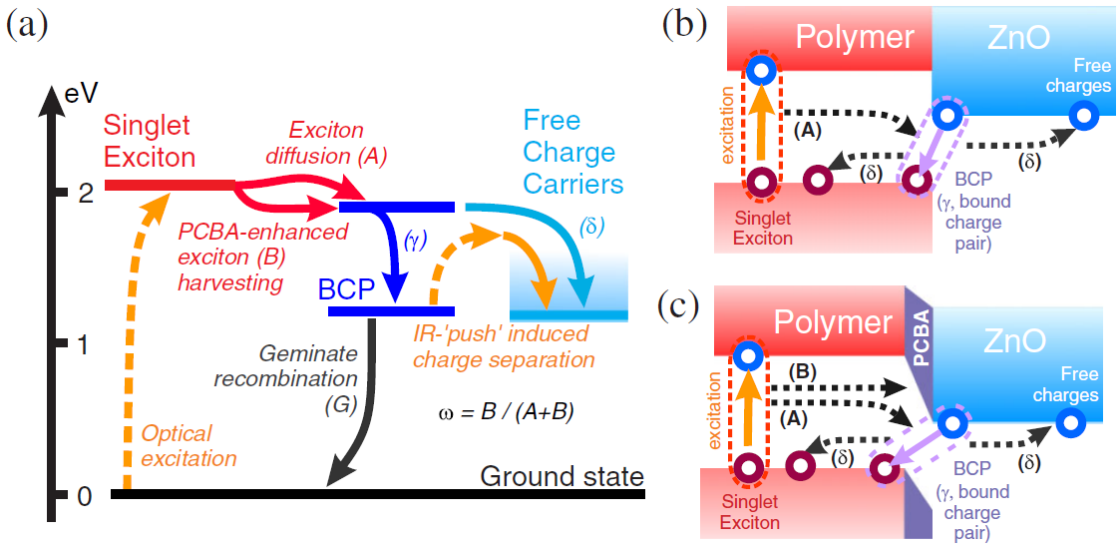

Figure 2.27: (a) The state model of charge separation. Dashed arrows represent optical transitions driven by pump and push pulses. A and B are two channels of exciton transfer to the organic-inorganic interface. A is exciton diffusion and B is additional exciton harvesting promited by the phenyl-C61-butyric acid (PCBA) modification of the interface. γ and δ represent the relative amount of bound charge pair (BCP) and free charges, respectively. (b), (c) Band diagram of photoconversion in hybrid photovoltaic devices. Dashed arrows illustrate the processes described by the model in (a). From Ref. [212]

from the polymer to the inorganic semiconductor [214]. The injected carrier mobility has been found to be affected by the dielectric constant of the inorganic semiconductor component used in the hybrid structures.

2.5 Summary

- Inorganic Semiconductors
  - The quantum confinement of nanowires used in this thesis is negligible since their diameter is typically 50 nm. Their band structure can be well-described by the bulk-model. However, the high aspect ratio of this nanowires results in significant dielectric confinement, so that their optical and electrical properties are strongly anisotropic.
  - The thermalization of initially photoinjected carriers occurs via carrier-carrier

scattering within 100 fs, where their distribution can be described by the Maxwell-Boltzmann distribution. The carrier-lattice thermalization is dominated by LO-phonon coupling. While the carriers relax toward the band edge via phonon-coupling, the carrier temperature normally remains higher than the initial lattice temperature. Under high-injection densities situations, the carrier cooling is further reduced by the presence of the non-equilibrium phonon.

- The radiative recombination of free carriers occurs via the bimolecular recombination route where the recombination rate depends on the carrier density and carrier temperature.
- At sufficiently low injection density and low lattice temperature conditions, excitons can be formed immediately after resonant photoexcitation into the exciton band. The Coulomb screening by excitons reduces the correlation of electron-hole pairs and blue-shifts the excitonic emission. Increasing the injection density results in ionization of excitons, as a result of increasing Coulomb screening.
- Under non-resonant excitation, excitons are formed indirectly from the uncorrelated electron-hole pairs and mediated by LO-phonon coupling. The equilibrium between excitons and free carriers is established by the law of mass-action at low-injection limits. For excitation far above the Mott-limits, the PL is dominated by the emission of the uncorrelated electron-hole plasma at energies above the exciton emission energy. Many-body interactions result in band gap renormalization and Fermi-filling. Excitons are observed only as the density of electron-hole pairs is reduced and the band gap renormalization is reduced below the exciton binding energy.
- The carrier dynamics in semiconductor nanostructures are dominated by the presence of surface states due to the large surface-area to volume ratio. Surface passivation is necessary to improve the photoconductivity, carrier lifetime and quantum yield of photoluminescence.

- Semiconducting Polymers

  - Conjugated polymers are 1-dimensional systems with bandgaps from Peierls instabilities. The lowest optical transition corresponds to the HOMO-LUMO gap.
  - Absorption and emission spectra show Franck-Condon progressions with a Stokes shift. Aggregated samples exhibit altered progressions due to chain coupling.
  - Free charges on conjugated polymers distort the lattice and are quasi-particles called polarons.

- Organic Photovoltaics (OPVs)
  - Excitons migrate from the spectroscopic unit of higher energy to those of lower energy. In polymer blends consisting of two polymers with different band gaps, excitons migrate from the polymer with larger band gap to the polymer with lower band gap, normally through the Förster Resonance Energy Transfer route. When the wavefunctions of donors and acceptors are strongly overlapping, energy transfer occurs via electron exchange across the donor-acceptor interfaces.
  - An OPV device requires a type-II heterojunction between a donor and acceptor blend to dissociate donor excitons and transfer electrons to the acceptor. The electron and hole remain bound as a charge-transfer state but can further dissociate to produce free polarons, resulting in charge separation. The charges are transported and collected at respective electrodes.
  - Semiconducting polymers with lower band gap energy have potential to improve the device efficiency. These materials have potential to capture the sunlight near the infrared regimes.
  - For hybrid OPV devices formed by organic and inorganic semiconductor nanostructures, the Coulomb interaction of spatially separated electron-hole pairs can be screened when using inorganic semiconductors with higher dielectric constant.

Chapter 3

Experimental Methods

The experimental studies in Chapters 4, 5 and 6 rely a variety of spectroscopic techniques that can be broadly divided into steady-state and time-resolved techniques. The steady state techniques includes time-integrated PL measurements and X-ray photoemission spectroscopy (XPS). These two techniques provide a wealth of spectroscopic information about the electronic processes in semiconductor samples and their surface properties. Particularly, XPS is a powerful technique that provides useful information about the material characteristics from the top-most surface ($\approx 2\,\mathrm{nm}$). The time-resolved techniques are based on photoluminescence upconversion spectroscopy (PLUCS) and time-correlated single-photon counting (TCSPC). While TCSPC relies on the electronic-gating system that is commercially available, PLUCS is an optical-gated techniques that relies on non-linear optical effects and ultrafast laser pulses. Hence, the important topics of non-linear optics will be introduced, followed by the experimental details and a description of setup associated with PLUCS used in these studies. The electron microscopy used in these studies to image the nanostructures will be briefly covered. Finally, the growth of nanowires and the preparation of polymer thin films will be introduced.

3.1 Time-Resolved Spectroscopy

Time-resolved spectroscopy provides useful information about the evolution of a system that has been perturbed from its equilibrium state, typically by a short optical pulse. Normally, the detection utilizes high-speed electronics, which are easy to implement, to detect the PL emission from the samples as a function of time. However, the fundamental limit for resolution is set by the speed of the electronics within the detection devices, and the ultimate resolution is set by the clock rate of the data acquisition circuit. This means that the temporal resolution of the detection is order-of-magnitudes longer than the femtosecond to picosecond range, which are characteristic of various electronic processes in semiconductors, such as carrier-cooling [48, 51, 56], defect-trapping [26, 29, 42], torsional relaxation in organic semiconductors [152, 215], and charge-transfer at the closely-packed donor-acceptor interfaces [216]. To overcome this limitation, *optically*-gated techniques are essential, which provide the temporal resolution that is limited fundamentally by the duration of the laser pulse. This will allow us to gain the insights of various electronic processes that occurs within the sub-picosecond to tens of picosecond range after excitation.

3.1.1 Non-Linear Optics

In most instances, it is assumed that optical properties of materials, such as refractive indices and absorption coefficients, are independent of the optical power. However, in the case of laser systems where high powers are achieved, the assumption becomes invalid and the formulation must be generalised to include *non-linear* optics [68]. This regime gives rise to important effects such as frequency-mixing, exploited in the experimental techniques described later.

The various optical properties of materials are derived from the electric susceptibility, χ. In linear optics, it is assumed that the polarisation $\mathbf{P}$ of the medium has a linear relationship with the electric field $\mathbf{E}$ of the light, such that:

$$\mathbf{P} = \epsilon_0 \chi \mathbf{E}, \tag{3.1}$$

where ϵ_0 is the vacuum permittivity. However, in the non-linear optics regime the expression in Eqn. 3.1 must be generalised. This is done by first considering a non-linear medium in which the polarisation is parallel to the electric field and the polarisation P and electric field E can be treated as scalar quantities. The generalised non-linear polarisation is then written as the sum of components of increasing order, that is:

$$\mathrm{P}_{\mathrm{non-linear}} = \mathrm{P}_1 + \mathrm{P}_2 + \mathrm{P}_3 + \ldots = \epsilon_0(\chi_1 \mathrm{E} + \chi_2 \mathrm{E}^2 + \chi_3 \mathrm{E}^3 + \ldots), \tag{3.2}$$

where E is the magnitude of the electric field, and P_n and χ_n are the n-th order non-linear polarisations and susceptibilities, respectively, and χ_1 is the normal linear susceptibility. In general, each susceptibility order component will be a tensor quantity because the non-linear response of the medium will depend on the directions of the applied fields and they will not necessarily be parallel.

Non-Linear Frequency Mixing

The majority of phenomena of interest are attributed to either the second- or third-order terms, χ_2 or χ_3, but the discussion here will be limited to second-order effects. If two incident sinusoidal waves with frequency ω_i of the form $\mathrm{E}_i(t) = \mathrm{E}_i \cos \omega_i t$ are considered and, again, χ_2 is considered as a scalar component, the second-order non-linear polarisation will take the form:

$$\begin{aligned} \mathrm{P}_2(t) &= \epsilon_0 \chi_2 (\mathrm{E}_1(t) \times \mathrm{E}_2(t)) && (3.3) \\ &= \epsilon_0 \chi_2 \mathrm{E}_1 \mathrm{E}_2 \frac{1}{2} \left[\cos(\omega_1 + \omega_2)t + \cos(\omega_1 - \omega_2)t\right]. && (3.4) \end{aligned}$$

The non-linear response at second-order generates polarisation waves at both the sum $\omega_1+\omega_2$ and difference $\omega_1-\omega_2$ frequencies of the incident light and this effect is called *non-linear frequency mixing*. To ensure a high conversion efficiency from these weak processes, the phases of the non-linear waves generated throughout the medium need to add together coherently. This is called *phase matching* and is achieved by applying conservation of momentum, $\mathbf{k} = \mathbf{k_1} + \mathbf{k_2}$, where the wavevector $\mathbf{k}$ is generated by mixing two photons with wave vectors $\mathbf{k_1}$ and $\mathbf{k_2}$. This phase-matching condition becomes a constraint on the refractive indices n_{ω_i} of the material for each frequency and polarisation and is often satisfied by exploiting the birefringent properties of the non-linear crystal medium. In practice, the condition can only be achieved if the crystal is oriented in a very precise direction.

A common application of non-linear frequency mixing is *frequency-doubling*, where the incident directions of propagation are co-linear in a non-linear crystal and $\omega_1 = \omega_2$ such that the emitted light has a frequency of 2ω. This is particularly useful for generating the frequencies required to excite organic semiconductors from a Ti:Sapphire laser system and will be utilised in the techniques described later. To satisfy the phase matching condition, the fundamental wave is polarised perpendicular to the crystal optical axis in order to propagate with constant refractive index n_o. The frequency-doubled waves have components both parallel and perpendicular to the optical axis with a refractive index depending on the angle between the propagation direction and optical axis. A crystal angle can therefore be found to satisfy the phase matching condition, namely $n_\omega = n_{2\omega} = n_o$ [68].

Another application is found in the *photoluminescence up-conversion* (PLUC) process and this is demonstrated in Fig. 3.1. Here, the photoluminescence photons from a sample $\omega_1 = \omega_{\mathrm{PL}}$ are added to those from a suitably delayed gate laser pulse $\omega_2 = \omega_{\mathrm{gate}}$ to produce 'up-converted' photons of frequency $\omega_{\mathrm{PL}} + \omega_{\mathrm{gate}}$. The sum-frequency signal is generated only during the gating laser pulse and this provides an all-optical method of temporally resolving the photoluminescence [46]. Moreover, inspection of Eq. 3.4 shows that the up-converted signal intensity is proportional to the photoluminescence as a function of time after the initial sample excitation $\mathrm{E}_1(t)$ because the gating laser E_2 is fixed [217]. The crystal angle to

satisfy the phase matching condition will be specific to the energy of the PL photons under investigation and thus only these photons will be detected.

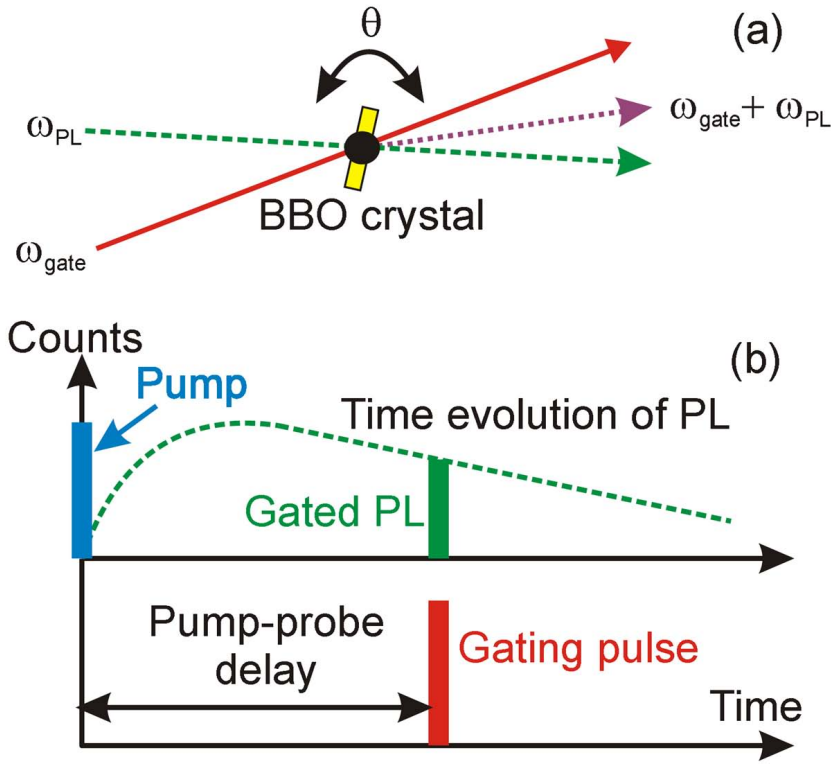

Figure 3.1: Schematic diagram to represent the processes involved in the PLUC technique. After photoexcitation of the sample, PL photons of frequency ω_{PL} are made to overlap spatially and temporally with gate photons of frequency ω_{gate} in a non-linear crystal, producing up-converted photons of frequency $\omega_{\mathrm{PL}} + \omega_{\mathrm{gate}}$. The lower plots illustrate how sum frequency generation acts as a gate, where the up-converted photons used to detect the PL are only produced during the gating laser pulse [46].

In order to observe second-order non-linear processes, a non-centrosymmetric crystal must be used because otherwise $\chi_2 = 0$ [68]. In addition, it is desirable that the crystal has a high χ_2 value and low absorption in the incident and generated photon range to ensure an adequate generation efficiency [217]. In the experimental setups presented here, the non-linear processes described above were achieved using beta barium borate (β-BaB_2O_2; BBO) crystals because of the high value of χ_2 =1.28 pmV^{-1} and low absorption at wavelength above 200 nm [218].

3.1.2 Experimental setup: Photoluminescence Up-Conversion Spectroscopy (PLUC)

PLUC is an optically-gated technique to measure the time-resolved photoluminescence of a sample by utilising a non-linear crystal. The technique has low sensitivity due to the weak second-order nature of the process. However, a very high time resolution of 220 fs could be achieved in the setup described here.

Figure 3.2 displays the details of the PLUC system used in this study. The output from the pumped Ti:Sapphire laser consists of laser pulses of 100 fs duration, a repetition rate of 80 MHz, tuneable centre wavelength between ∼710–950 nm, and typical pulse energies of 11 nJ. Here, the Ti:sapphire laser is pumped by a Nd-YAG pump laser at 532 nm, 5.5 W (Spectra-Physics, Millennia). The output laser pulse first passes through the polarising beam splitter (BS1) to be split into two paths with the intensity ratio controlled by the half-wave plate (P1). One of the beam is used as "excitation beam" to excite the sample while the other beam is used as "gate" beam. The semiconductor nanowires are photoexcited at photon energy of 1.68 eV where the excitation density and polarization can be adjusted from the combination of half-wave plate (P4) and Glan-Thompson polariser (G2). To excite semiconducting polymer at a photon energy of 3.06 eV, the laser output at a photon energy of 1.53 eV was focused by lens L1 onto a BBO crystal (B1, cutting angle of 35°) to generate frequency-doubled laser pulses. A Glan-Thomson polarizer (G1) and a band-pass filter (F1) were used to block the residual fundamental beam. The excitation beam is incident on the front of the sample with a small angle $\approx 13°$. For measurements conducted at low temperature, the sample was maintained in a liquid-helium flow cryostat, where the temperature was controlled by the heater attached to the cold-finger. For measurements conducted at room temperature, the sample was mounted in a home-made holder connected to a dynamic vacuum pump. The PL emission was collected by a pair of off-axis parabolic mirrors (O1 and O2) and focused onto a BBO crystal (B2) mounted on a rotation stage.

The intense vertically-polarised "gate" beam passing through a reflecting mirror pair mounted on a mechanical, micro-controlled delay stage (S2) and arriving at the BBO crystal

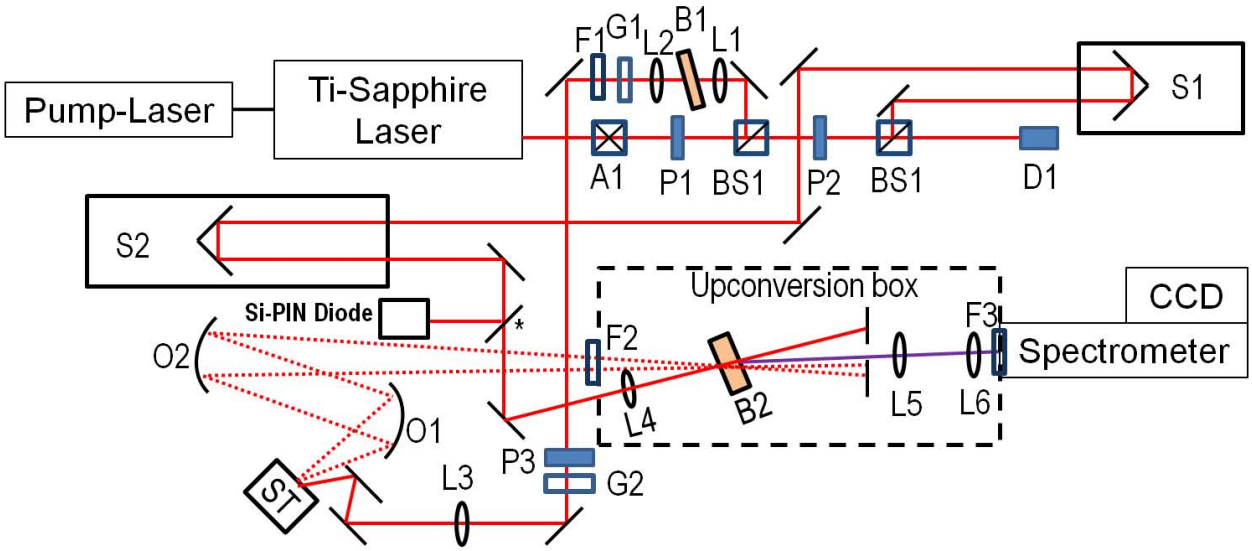

Figure 3.2: Schematic diagram of the experimental setup used for PLUC and TCSPC measurements in this work. The general beam paths and key components are described in the text. The starred mirror is only present in the TCSPC setup.

(B2) at adjustable time delays was used to up-convert the PL signal. The mixing angle between the "gate" beam and the collected luminescence cone at the crystal was set at 12°. The crystal was mounted on a rotation stage and a careful calibration of optimal crystal angle for each wavelength allowed the correct crystal angle to be set. The up-converted photons were focused by a pair of lenses (L5 and L6), onto the entrance slit of a spectrometer (Jobin Yvon: Triax90) where they were dispersed, and then detected by a low noise, liquid-nitrogen cooled CCD (Jobin Yvon: Symphony). The time-resolved PL decay curves at a given photon energy can be mapped out by using automated software to vary the delay stage across the desired pump-probe delay range. To measure time-resolved spectra at a delayed time, the BBO crystal is rotated to map the spectrum, in-accordance with the crystal angle calibration map (discussed in the next section). To obtain clear up-conversion signal, suitably long CCD integration time is required. The background noise is normally due to the stray light from the "gate beam" and its second harmonic generated at the BBO crystal. To reduce the background noise, all appropriate long-pass filter and band-pass filter were placed at F2 and F3 position, respectively. The temporal resolution of this UCPL setup was determined from the cross-correlation of the gate beam and the excitation light scattered from the sample

Equipment	details
pump laser	Nd-Yag laser
Ti:sapphire laser	Spectra-Physics, Tsunami
A1	periscope
P1, P2, P3	half-wave plate
BS1, BS2	cube beam-splitters
D1	Ocean Optics spectrometer
S1, S2	mechanical moving stage
L1, L2, L3, L4, L5, L6	Focusing lens
B1, B2	BBO crystals
G1, G2	Glan-Thompson Polarizer
O1, O2	off-axis parabolic mirrors
ST	sample stage
F1, F2, F3	F1: BG39 band-pass filter F2: long-pass filter F3: UG11 or BG39 band-pass filter

Table 3.1: List of items used in PLUC spectroscopy

surface to be $\approx 300\,\text{fs}$. The entance slit width of spectrometer was set to $1000\,\mu\text{m}$. The spectral resolution is typically 32 meV using a 600 grid/mm grating in the monochromater.

The same setup was also used to measure the steady-state visible-NIR PL of the sample except with the up-conversion crystal removed, and the gate beam blocked. The slit width was set to $38\,\mu\text{m}$. The spectral resolution is typically 4 meV using a 300 grid/mm grating in the monochromater.

3.1.3 Time-Correlated Single Photon Counting (TCSPC)

While PLUC is an optically-gated technique, TCSPC utilises electronic gating and therefore gives a lower temporal resolution ($\sim$120 ps on the system described here). However, it offers high sensitivity and can achieve a dynamic range of up to five decades [219].

The principles of the technique are illustrated in Fig. 3.3. A pump pulse photoexcites the sample synchronously with a trigger pulse on a Si-PIN Diode, defining the start of a measurement period. The sample photoluminesces and either the detection of a PL photon or the next laser pulse ($\sim$12 ns later) defines the end of the measurement period. After

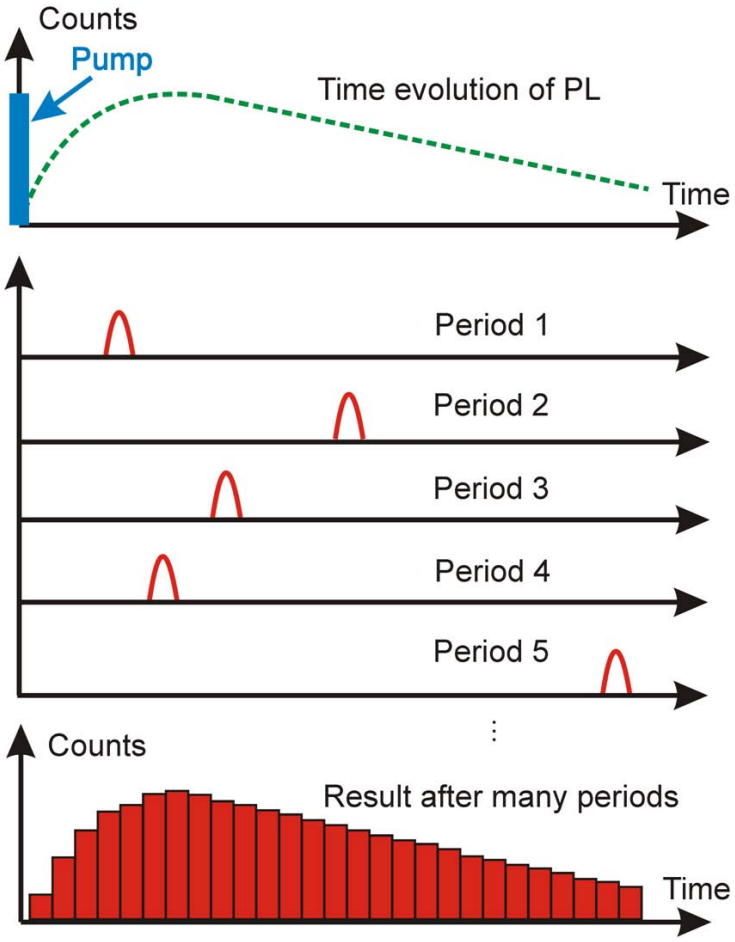

Figure 3.3: Schematic diagram to illustrate the principles of the TCSPC technique. During each signal period, at most one photon is detected. After many signal periods, a histogram of arrival times is acquired and traces the actual PL profile shown in the top curve.

many signal periods, a histogram of photon arrival times is built up and a PL decay curve is obtained. For low level, high repetition rate signals, the light intensity is low enough that the probability of detecting a photon during one signal period is much less than one [219].

The setup for TCSPC used the same overall schematic layout as for the PLUC shown in Fig. 3.2, except for a few key differences. First, the starred mirror in the figure was inserted and directed the gate beam onto a Si-PIN Diode. This provided the trigger pulse for a signal period for the measurements. Meanwhile, the BBO (B2) crystal was removed and the PL was directed into the spectrometer and onto a photomultiplier tube (PMT) with use of appropriate filters.

3.2 X-ray Photoemission Spectroscopy (XPS)

X-ray photoemission spectroscopy (XPS), also known as Electron Spectroscopy for Chemical Analysis (ESCA), provides detailed information about the chemical states of the surface of materials. It was first developed in the mid-1960s by Kai Siegbahn and his research group in Uppsala University, Sweden. Although the X-ray photon penetrates deeply into the materials, the useful photoelectron signals mainly originate near to the top-most surface, as a result of limited inelastic mean free path (IMFP) of photoelectrons escaped from the surface, as seen in Figure 3.4. This makes XPS a unique surface-sensitive technique for chemical analysis.

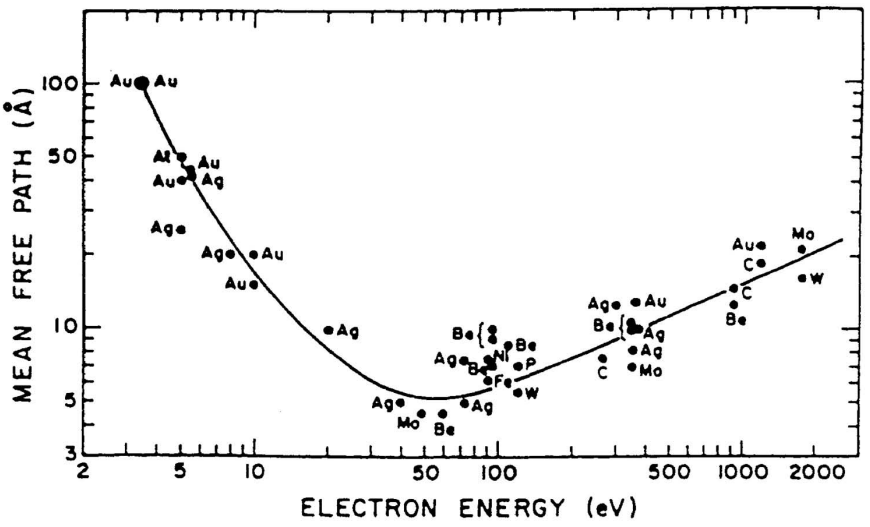

Figure 3.4: Universal curve of the inelastic mean free path (IMPF) for electrons based on experimental data for various materials. Taken from Ref. [220].

In general, X-ray photon sources, such as Al-$K\alpha$ ($h\nu$ = 1486.6 eV) or Mg-$K\alpha$ ($h\nu$ = 1253.6 eV) are used in lab-based experiments. Alternatively, synchrotron-radiation with tunable energy for different photoelectron cross-sections has been widely used for studies of the electronic structure of materials. Figure 3.5 shows the photoemission process. The photoelectrons escaped from the surface are detected by an electrostatic analyzer or a retarding-field analyzer by which the photoelectrons are filtered electrostatically to reach the channeltrons via the hemispherical analyzer and amplified by channeltrons at the end to generate an analog signal. The scan-control unit (SCU) converts the analog signal to a

digital signal which is transferred to a computer.

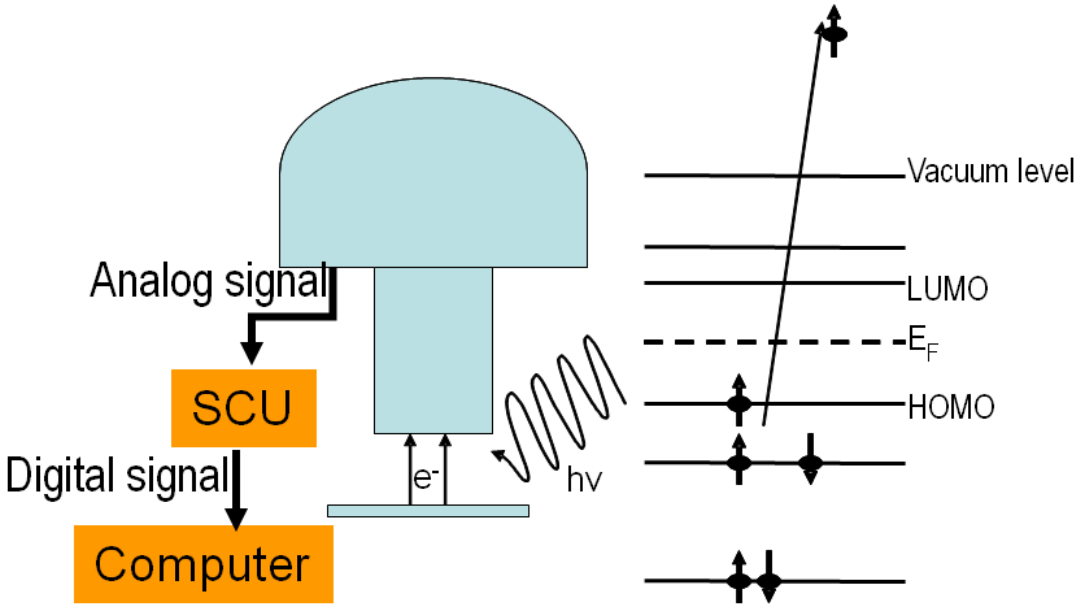

Figure 3.5: Schematic diagram for photoemission process.

While the kinetic energy E_K of the emitted electrons varies with the energy of the incoming X-rays $h\nu$, the binding energy E_B stays constant for electrons from a certain element in a certain chemical state. The X-ray photoemission spectrum is conventionally plotted with the intensities of emitted electrons versus their binding energies, which can be calculated from the conventional photoelectric equation as:

$$E_B = h\nu - E_B - \phi_m, \tag{3.5}$$

where ϕ_m is the work function of the energy analyzer. Therefore, the Fermi energy (E_F) of a metal in the spectrum is defined as $E_B = 0$. An X-ray photoemission spectrum is formed by electrons which leave the surface without energy loss, while the electrons that undergo inelastic loss processes before emerging from the surface form the background. The binding energy for a certain core level of element is sensitive to the chemical states. In-particular, the chemical oxidation of the surface increases the binding energy of photoelectrons due to the increased nuclear charge on the valence electrons[220, 221].

A three-step model has been proposed for the photoemission process [222]: (i) the prob-

ability of excitation in the solid; (ii) the probability of scattering of the excited electron on its path to the surface by the atoms, and (iii) the probability of transmission through the surface to the detector. Hence, special care must be taken when probing the surface of insulating or semiconducting materials to avoid surface charging.

The chemical composition of GaAs nanowires was investigated by high-resolution X-ray photoelectron spectroscopy (XPS) at Daresbury National Centre for Electron Spectroscopy and Surface Analysis. A Scienta ESCA300 spectrometer with a rotating anode Al-$K\alpha$ ($h\nu$ = 1486.6 eV) X-ray source, a seven crystal X-ray monochromator and a 300 mm mean radius spherical sector electron energy analyzer with parallel electron detection system was used. The X-ray source was run with 100 mA emission current and 14 kV anode biases, while the analyzer was operated at 150 eV pass energy with 0.8 mm slits. Gaussian convolution of the analyzer resolution with a linewidth of 260 meV for the X-ray source gives an effective instrument resolution of 0.1 eV. The instrument is calibrated regularly with the gold reference. The GaAs nanowires were inserted via a quick-entry load lock into the ultrahigh vacuum (UHV) chamber and kept at a base pressure of $< 10^{-9}$ mbar. The photoelectrons emitted along a trajectory 35° off of the surface were collected by a hemispherical analyzer with a energy resolution of 100 meV. Before analyzing the data, a Shirley background was calculated and subtracted from the original spectra.

3.3 Microscopy

To resolve structures with dimensions on the order of the wavelength of visible light (nano to micrometers), optical microscopy is insufficient. Instead, techniques such as electron microscopy need to be utilised and these images can yield rich information about nanostructures.

3.3.1 Scanning Electron Microscopy (SEM)

In SEM, a focused beam of electrons raster scans across the sample surfaces and the signals generated are used for imaging. SEM uses secondary electrons and back-scattered electrons for imaging. Many secondary electrons are reabsorbed by the sample and only electrons produced near the surface (up to 50 nm below the surface) can escape from the surface to reach the detector. The number of secondary electrons emitted from the region of surface depends on the topography. In general, the number is lowest when the incident electron beam is perpendicular to the sample surface. In other words, the number increases with increasing the angle between the surface normal and the incident electron beam. Thus, protrusions produce higher count of secondary electrons than the flat surface, which makes these features brighter. Special care must be taken to avoid surface charging that can damage the surface.

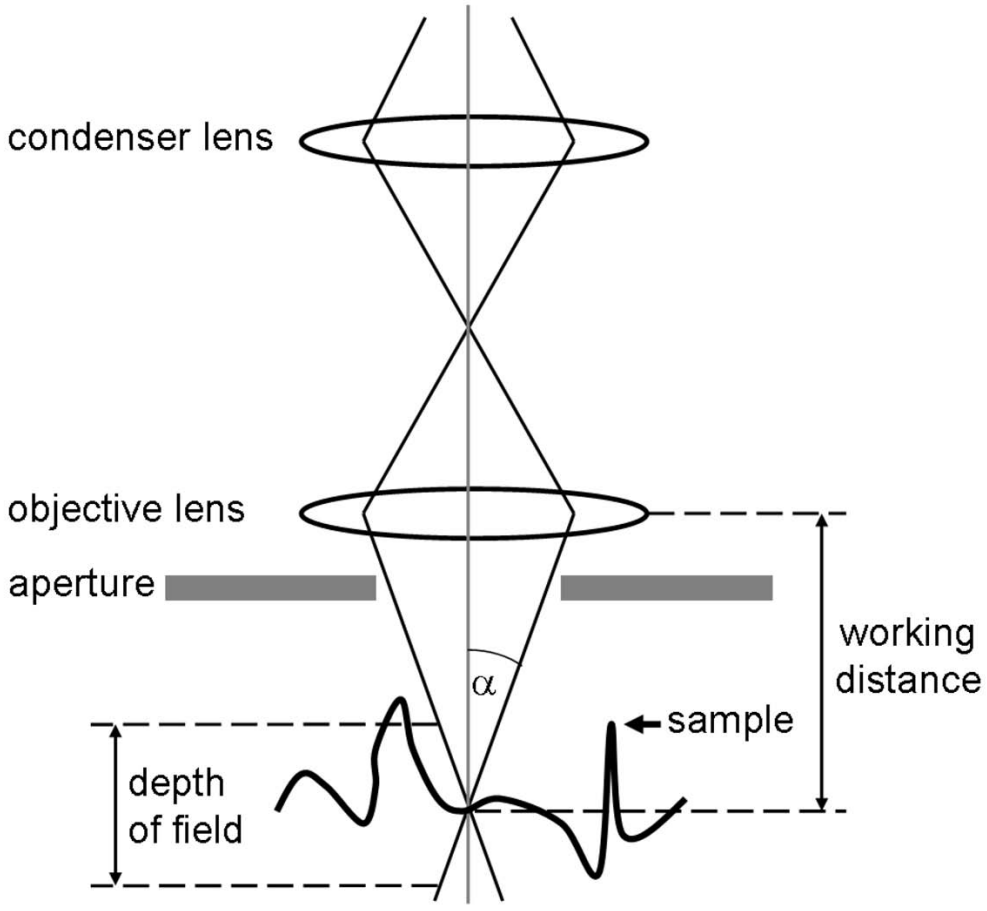

Figure 3.6: Schematic diagram of SEM showing the depth of field and working distance.

Figure 3.6 show the schematic diagram of SEM. When imaging nanowires, the major parameters are depth of field, beam diameter and signal strength. The beam diameter define the image resolution and smaller beam diameter produces images with greater resolution. This can be achieved by reducing the working distance. To obtain sharp images, the depth of field can be increased by narrowing the aperture or increasing the working distance. Narrowing the aperture could reduce the signal strength and the image resolution might be reduced. Hence, compromise between image resolution and depth of field must be made.

The SEM imaging of nanowires used in this thesis were performed by Dr. Hannah J. Joyce (Department of Physics, Oxford University) on a Hitachi S4300 field emission scanning electron microscopy (FESEM).

3.3.2 High resolution Transmission Electron Microscopy (HRTEM)

Transmission electron microscopy (TEM) is a technique to obtain images from transmitted electron beams that have interacted with a sample. High-resolution TEM (HRTEM) is an imaging mode of TEM that allows the crystallographic structure of a sample to be imaged on an atomic scale [223]. The images are formed by phase contrast, where the phases of electron waves differ after interaction within the sample. The HRTEM images presented in the following chapters were obtained by Dr Jennifer Wong-Leung (Department of Electronic Materials Engineering, Australian National University) on a Philips CM300 at an accelerating voltage of 300 kV. All nanowires examined had diameters less than 300 nm and consequently met the requirement of electron transparency and no thinning or polishing process is required. The samples were prepared by either ultrasonication or direct mechanical transfer to holey carbon grid.

3.4 Growth of III-V Semiconductor Nanowires

All III-V nanowires used in this thesis were grown by metal-organic chemical vapour deposition (MOCVD), using Au nanoparticles to drive the nanowire growth. The underlying nanowire growth mechanism is closely related to the vapor-liquid-solid (VLS) wire growth mechanism proposed by Wagner and Ellis [224], to explain the anisotropic growth of Si wires catalyzed by the metallic Au particles. Fig. 3.7 illustrates the VLS mechanism. The Si precursor species were supplied in the vapour phase. At growth temperature, the metallic Au particles formed a liquid eutectic alloy with the Si. With further supply of Si this Au-Si alloy particle became supersaturated with Si, and the Si precipitated at the particle semiconductor interface to form a solid crystalline Si wire. Wagner and Ellis proposed two possibilities to explain nanowire growth. First, that due to the high accommodation coefficient of the liquid phase, the liquid particles are favourable collection sites for the vapour phase reaction species, and thus assist nanowire growth. The second possibility is that the metallic particle is a chemical catalyst which lowers the activation energy barriers to enhance the decomposition of the gas-phase precursors. Following this work on Si wires, the VLS mechanism was then applied to III-V semiconductor nanowire growth, using Au nanoparticle [225].

Similar procedures were applied for the growth of III-V semiconductor nanowires used in this study [26, 226]. Au nanoparticles were deposited on a semiconductor substrate surface. To initiate growth, vapour phase group III and group V precursors are provided to the reaction chamber. The Au nanoparticles alloy with specific reactant elements to form a liquid or solid alloy, for instance Au-Ga. Deposition of III-V material occurs preferentially at the nanoparticle-substrate interface, so that nanowire nucleation takes place. With continual supply of group III and V reactants, deposition of III-V material continues at the nanoparticle-nanowire interface. Thus the nanoparticle, located at the growing tip of the nanowire, drives highly anisotropic nanowire growth. The diameter at the tip of the grown nanowire is defined by the diameter of the Au nanoparticle. This is essentially a bottom-up fabrication technique, which offers high controllability in nanoscale dimensions not possible by the top-down techniques.

The nanowires used in this thesis were grown by Dr. Qiang Gao (Department of Electronic Materials Engineering, Australian National University), using the MOCVD method, with gold nanoparticles as catalyst.

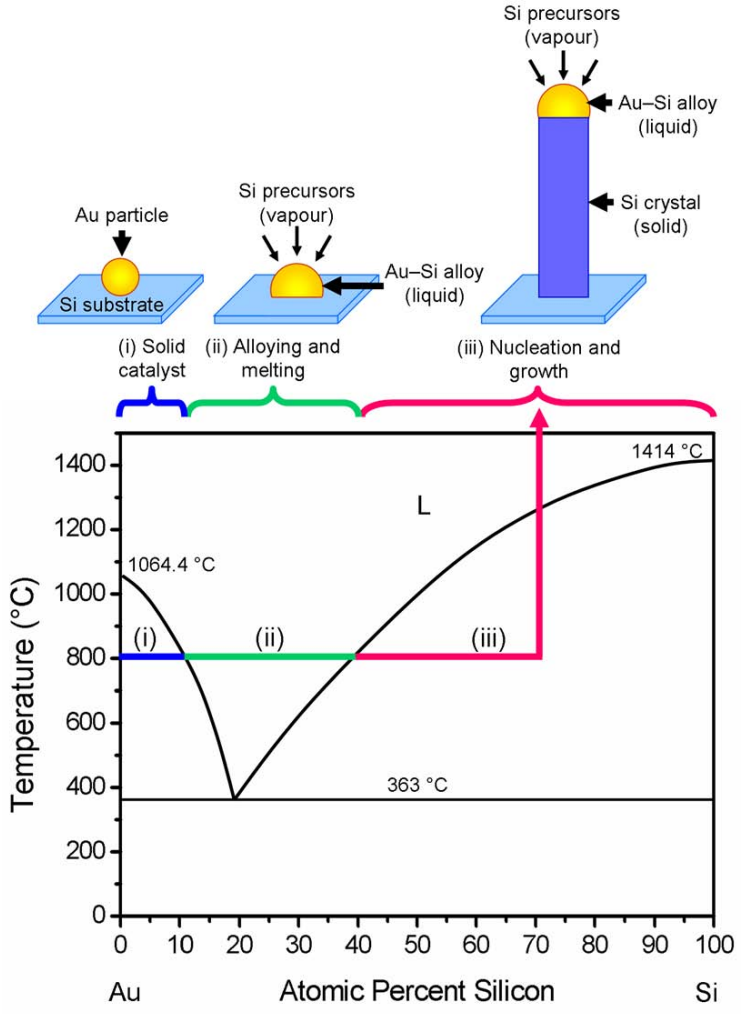

Figure 3.7: Schematic illustration of the VLS growth of Si wires using a Au catalyst particle. The Au-Si binary phase diagram illustrated in the lower portion indicates the various phases the Au-Si particle can adopt under different temperatures and in different composition ranges. Labels (i), (ii) and (iii) illustrate the different stages of nanowire growth for a growth temperature of 800°C, and the corresponding state of the Au-Si particle.

3.5 Summary

The experimental techniques used in this thesis are summarised below:

- Photoluminescence Up-Conversion (PLUC) Spectroscopy is a pump-probe technique using frequency-mixing to optically gate the PL from a photoexcited sample. A high temporal resolution (∼220 fs here) is achieved, allowing observation of ultrafast processes.

- Time-Correlated Single Photon Counting (TCSPC) is another technique to detect time-resolved PL from a photoexcited sample. A histogram of arrival times of photons is built up and an electronic gate is used in the detection system. As such, TCSPC is a lower resolution technique (∼120 ps here) but has a greater sensitivity than PLUC and allows the long time behaviour to be examined.

- X-ray Photoemission spectroscopy (XPS) is complementary technique to characterize the surface states of GaAs nanowires with results described in Chapter 6.

- High-Resolution Transmission Electron Microscopy (HRTEM) and Scanning Electron Microscopy (SEM) are complementary imaging techniques to characterise nanostructures with resolutions on the atomic scale.

- The nanowires used in this thesis are grown using the MOCVD method, with gold nanoparticles as catalyst.

Chapter 4

Ultrafast Dynamics of Exciton Formation in Semiconductor Nanowires

As explained in Chapter 1, the carrier recombination in nanostructured inorganic semiconductors is dominated by trapping at the surface-defect states. In this chapter, the ultrafast carrier dynamics in GaAs nanowires are reported. To obtain high-quality nanowires, it is often preferable to use a growth technique such as metal-organic chemical vapour deposition (MOCVD) to grow the nanowires. In-particular, the GaAs nanowires used in this study were grown via a two-temperature growth procedure to minimize the formation of twin-defects [226]. To passivate the surface-defect states, a 30 nm aluminum gallium arsenide (AlGaAs) layer was grown coaxially on the surface of GaAs nanowires, followed by termination of 5 nm GaAs layer. The carrier dynamics in the nanowires were investigated using femtosecond transient photoluminescence spectroscopy at a substrate temperature of 10 K. The exciton lifetime in the resulting defect-free nanowires is long-lived and bimolecular interconversion of the initially generated electron-hole plasma into an exciton population was observed. This conducting-to-insulating transition appears to occur gradually over electron-hole charge pair densities of 2–4$\times 10^{16}$cm^{-3}. The smoothness of the Mott transition is quali-

tatively attributed to the slow carrier-cooling during the bimolecular interconversion of free charge carriers into excitons and to the presence of chemical-potential fluctuations leading to inhomogeneous spectral characteristics. Without the surface-passivation, the photoluminescence of the nanowires is quickly quenched in 10 ps, and surface-trapping mechanisms are suggested to be dominant trapping channels in the GaAs nanowires.

4.1 Introduction and Background

The successful incorporation of semiconductor nanowires (NWs) into opto-electronic and photovoltaic devices as both elements and interconnects has sparked intense interest in the nature of carrier dynamics in such nano-scale materials [40, 109, 227–230]. Optical probing of ultrafast carrier dynamics in these materials has provided valuable insights here into both the quantum confined and surface mediated behavior of carriers [28, 67, 231, 232]. For nanowires with diameter much larger than the exciton Bohr radius, the carrier relaxation is strongly affected by unsaturated surface defects, which also increase the non-radiative recombination rate of excitons [113, 233, 234]. It has been shown previously that by overgrowing the NW surface with a layer of large-bandgap semiconductor, the surface defect density can be reduced tremendously resulting in strong increases of charge carrier lifetimes towards their intrinsic bulk values [26, 42, 235].

The conducting-to-insulating phase transition has been studied extensively both in bulk and two-dimensional semiconductors [34, 74, 80, 83–85] since the original concept was developed by Mott [73]. In a semiconductor, such transitions result from screening of the attractive Coulomb interaction between an electron and a hole by the surrounding bound or free charge pairs, which increases with pair density. Following non-resonant excitation, the photoluminescence (PL) of a semiconductor with direct bandgap is first characterised by the recombination of unbound electron-hole pairs with Fermi-energy that shows significant occupation at high energy and bandgap renormalization (BGR) caused by exchange and correlation effects. As the pair density reduces, excitonic emission subsequently begins

to dominate the PL spectra. Despite initial expectations, Mott transitions have often been found to be smooth crossovers across a range of electron-hole pair densities for both bulk semiconductors [74, 95] and two-dimensional semiconductor quantum wells [75, 86].

In this chapter, the transition from an initial hot electron-hole plasma to a relaxed exciton density in high-quality GaAs-AlGaAs-GaAs core-shell-skin (CSS) NWs at substrate temperatures of 10 K was conducted using femto-second time-resolved photoluminescence spectroscopy. The coaxial type-I heterojunction confines all carriers within the GaAs-core through the use of the higher bandgap AlGaAs shell layer. The resulting nearly-defect free NW core allows the observation of contributions to the photoemission from both free (uncorrelated) and bound charge pairs (excitons). Following non-resonant excitation with a femtosecond pulse, the NW emission reveals a fast, charge-density dependent interconversion from the initial free electron-hole plasma to a predominant exciton population. The time-evolution of this conducting-to-insulating transition was quantified through the use of a coupled rate equation model that accounts for the bimolecular formation of excitons from the plasma, exciton-carrier ionization and radiative recombination. In-addition, the line width of the PL spectra reduces gradually, while the PL peak becomes centered at the exciton energy and band gap renormalisation effects are reduced below the exciton binding energy. All three markers indicate that the Mott transition in high-quality NWs occurs gradually with decreasing charge pair density around a range of $2–4\times10^{16}\mathrm{cm}^{-3}$. The origin of the smooth transition was qualitatively attributed to the slow carrier-cooling during the bimolecular interconversion of free charge carriers into excitons and to the presence of chemical-potential fluctuations leading to inhomogeneous spectral characteristics. Without the surface-passivation (i.e. in "bare" GaAs core NWs), both free-charge pair and exciton dynamics become dominated by rapid trapping at surface-defect sites within a few picoseconds after excitation.

4.2 Sample Preparation and Experiments

4.2.1 Growth of GaAs-AlGaAs-GaAs core-shell-skin nanowires

GaAs-CSS NWs were grown on semi-insulating GaAs (111)B substrates with a 50 nm gold-colloid seeded vapor-liquid-solid metal-organic chemical vapor deposition technique. Trimethyl-gallium and AsH_3 were used as precursors. The nanowires were grown via a two-temperature growth procedure to minimize the formation of twin-defects. [226] The growth was initiated with a nucleation step at high temperature (450°C) and rapidly ramped down to the subsequent growth temperature (375°C). Fig. 4.1a shows the TEM image of as-grown GaAs nanowires. The nanowires sidewall is smooth with minimal tapering effect. The AlGaAs shell layer was grown at higher temperature (650°C) to obtain compositional and structural uniformity, as confirmed in a representative SEM image shown in Fig. 4.1b. The nanowires used in this study were grown by Dr. Hannah J. Joyce (Department of Physics, University of Oxford) and Dr. Qiang Gao (Department of Electronic Materials Engineering, Australian National University). To eliminate the otherwise dominant photoluminescence signal from the GaAs substrate, the NWs were then transferred from the as-grown substrate to a z-cut quartz substrate by gently touching the two substrates together.

4.2.2 Time-Integrated and Time-Resolved PL Measurements

For time-integrated and time-resolved PL measurements, the sample was maintained at a temperature of 10 K in a liquid-helium flow cryostat. Time-resolved PL measurements were performed using a PL up-conversion set-up described in Chapter 3. The sample was excited at a photon energy of 1.68 eV with the output from a mode-locked Ti:Sapphire laser oscillator supplying 100-fs pulses at 82 MHz repetition rate.

The initial carrier density (n_0) immediately after photoexcitation (t=0) can be calculated from the density of absorbed photons. For the case of the samples under investigation, the nanowires of diameter d=50 nm were dispersed lying flat on the substrate. The optical

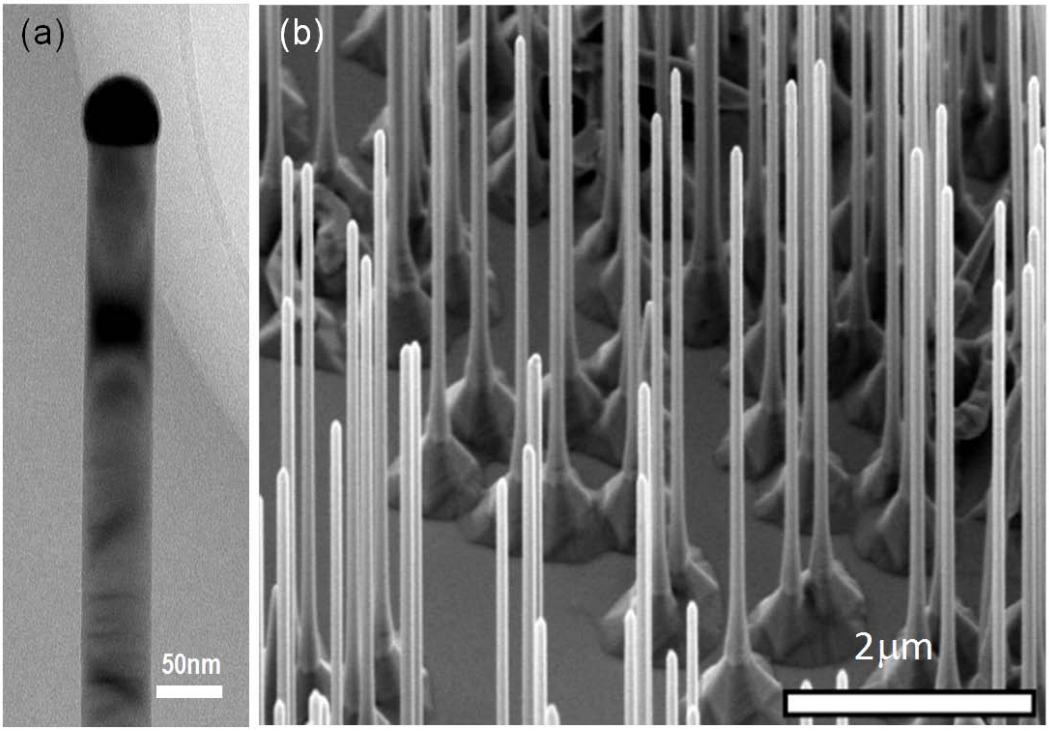

Figure 4.1: (a) The TEM image of as-grown GaAs nanowires. (b) The SEM image of as-grown GaAs-CSS nanowires on a GaAs(111)B surface.

absorption coefficient α at the excitation energy of E_{photon}=1.68 eV is taken from literature values[236–238] at 10 K to be 18000 cm^{-1}. The sample is therefore optically thin (i.e. αd=0.09) resulting in the generation of a homogeneous initial carrier density n_0 throughout each individual nanowire given by:

$$n_0 = \frac{f_0}{E_{\text{photon}}} \times \alpha(1 - R) \tag{4.1}$$

Here f_0 is the initial excitation pulse fluence incident on the nanowire and R accounts for the reflection losses occurred at the GaAs interface, given by $R = (n_{\text{r}} - 1)^2/(n_{\text{r}} + 1)^2 \sim 0.33$ with n_{r}=3.72[238].

The initial excitation fluence f_0 experienced by the nanowires is given by that at the very centre of the Gaussian excitation spot profile because of the experimental conditions used, as described in the following. The excitation spot on the sample had a full-width-at-half maximum of w=240 μm, which generated emission that was imaged with two off-axis

parabolic mirrors onto the nonlinear crystal with a magnification ratio of 4.1. The PL image of 1 mm diameter was then optically gated with a gate beam of 80 μm diameter. Therefore, this set-up probes an excitation area of diameter only $0.08w$ with respect to the overall excitation spot. The probed emission as a result is highly homogeneous as it is generated by the fluence f_0 at the very centre of the Gaussian excitation spot, given by:

$$f_0 = \frac{\sqrt{2}P}{\pi\left(\frac{w}{2}\right)^2} r_{\text{rep}}, \tag{4.2}$$

where P is the time-averaged total excitation power incident on the sample surface and r_{rep}=82 MHz is the pulse repetition rate of the excitation laser. Overall, this system of measurement therefore ensures that a well-defined and uniform volume density of carriers is generated in the ensemble of nanowires probed.

4.3 Results and Discussion

4.3.1 Time-Integrated PL from GaAs-CSS Nanowires

Previous study based on optical-pump terahertz probe spectroscopy has shown that the the surface passivation by AlGaAs layer reduces the surface defect-density [26]. At low-temperature, strong PL emission from the GaAs-CSS nanowires was observed. Fig. 4.2a shows the normalized time-integrated PL (TIPL) spectra measured for these NWs for a range of excitation fluences. At low excitation fluence, the PL spectrum is dominated by free exciton recombination (sharp peak at 1.521 eV) and also displays a weaker defect-mediated exciton recombination (peak at 1.50 eV). These defect trapping sites saturate quickly and free-exciton recombination is found to dominate the PL spectrum for excitation fluences above $\sim$0.2 μJcm^{-2}, indicating the high-quality nanowires obtained from such growth mechanism. As the excitation fluence is increased further, a high-energy tail begins to emerge above the exciton energy, which can be ascribed to an increasing contribution of band-to-band plasma recombination to the emission. Fig. 4.2a further reveals that the peak of

the PL remains fixed at the exciton emission energy of the NWs while the intensity of the higher-energy electron-hole plasma emission increases successively with the excitation density. Fig. 4.2b demonstrates a gradual increase of the full-width at half-maximum (FWHM) of the overall PL, as the excitation density is increased. These data therefore suggests that as the non-resonant excitation density is increased, the formation of excitons from initially created unbound free-carrier is weakened, which can be attributed to increasing charge-carrier screening effects [34].

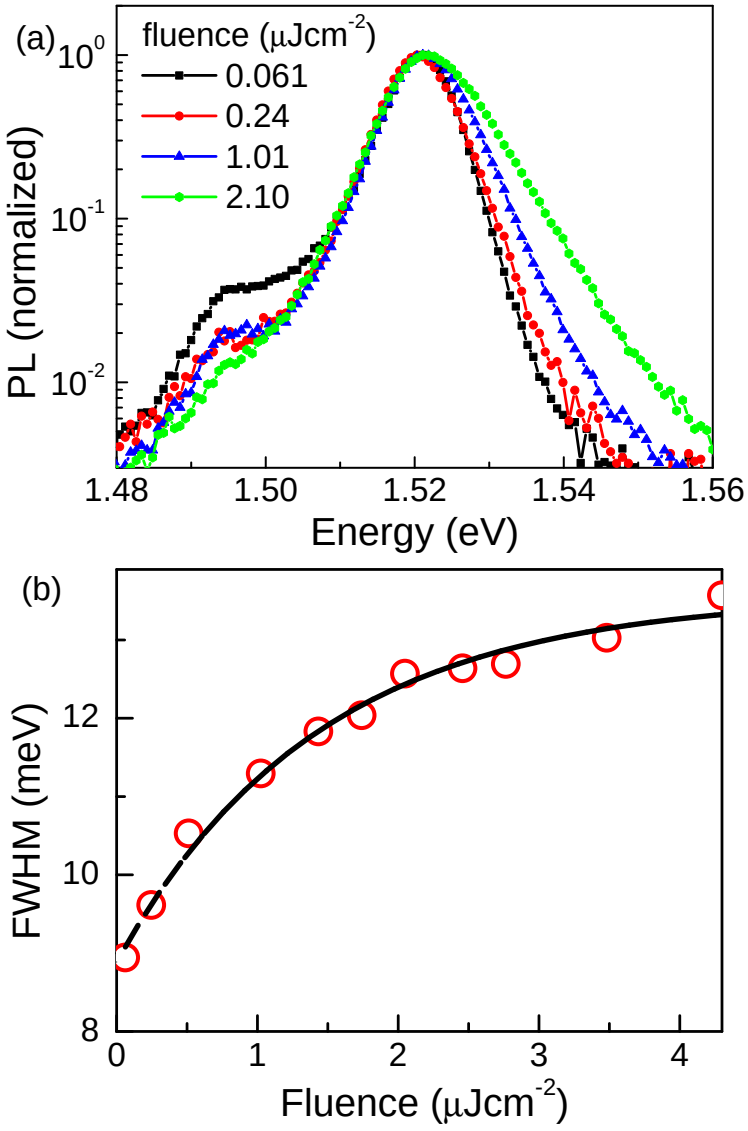

Figure 4.2: (a) Normalized time-integrated PL spectra of GaAs core-shell-skin nanowires at 10 K for a range of excitation fluences. (b) The full-width at half-maximum (FWHM) of the full PL spectra as a function of excitation fluence. The solid-line is a guide-to-the eye. The spectral resolution is 4 meV.

4.3.2 Time-Resolved PL Transients of GaAs-CSS Nanowires

In order to probe the dynamic exchange between such exciton and electron-hole plasma populations, time-resolved PL (TRPL) measurements were conducted on the GaAs-CSS nanowires at a substrate temperature of 10 K. The dynamics of the exciton population were recorded at the exciton emission peak (E_{x}=1.52 eV) and the electron-hole radiative plasma recombination was monitored at suitably higher energy (E_{eh}=1.55 eV) in order to avoid overlapping signals. In addition, the excitation fluence range was kept low ($\leq$1 μJcm^{-2}) in order to ensure that at the exciton emission energy contaminating contributions from the plasma emission were negligible.

Fig. 4.3 shows the normalized emission transients measured for exciton recombination (a) and electron-hole plasma recombination (b). With increasing injected charge carrier density, the excitonic PL rises increasingly fast and decays increasingly quickly. This fast initial rise of the excitonic PL is matched by a corresponding decay of the electron-hole plasma recombination, both of which exhibit a fast ($\approx$ 5 ps) and a slow component ($\approx$ 150 ps). These dynamics suggest that excitons in high-quality NWs are formed via bimolecular recombination of the uncorrelated electron-hole plasma, which may be mediated by interaction of carriers with longitudinal optical (LO) and acoustic (AC) phonons [239]. Such mechanisms have previously been observed for two-dimensional quantum wells [240]: with increasing carrier density, the increased probability of binding an electron to a hole through phonon interaction was found to lead to an increase in the exciton formation rate. Remarkably, high-quality GaAs nanowires can also exhibit such slow, bi-molecular exciton formation from an initially generated uncorrelated electron-hole plasma.

Some alternative explanations for the observed dynamics, such as charge trapping or bimolecular exciton-exciton annihilation can be ruled-out for the following reasons. Charge carrier trapping e.g. at surface defects should lead to increasing excitonic emission lifetimes with increasing fluence near the trap saturation regime[26] or neglible fluence-dependence significantly below it, which is contrary to the dynamics observed in Fig. 4.3. Exciton-exciton annihilation processes are also unlikely to be of any influence here, because in bulk

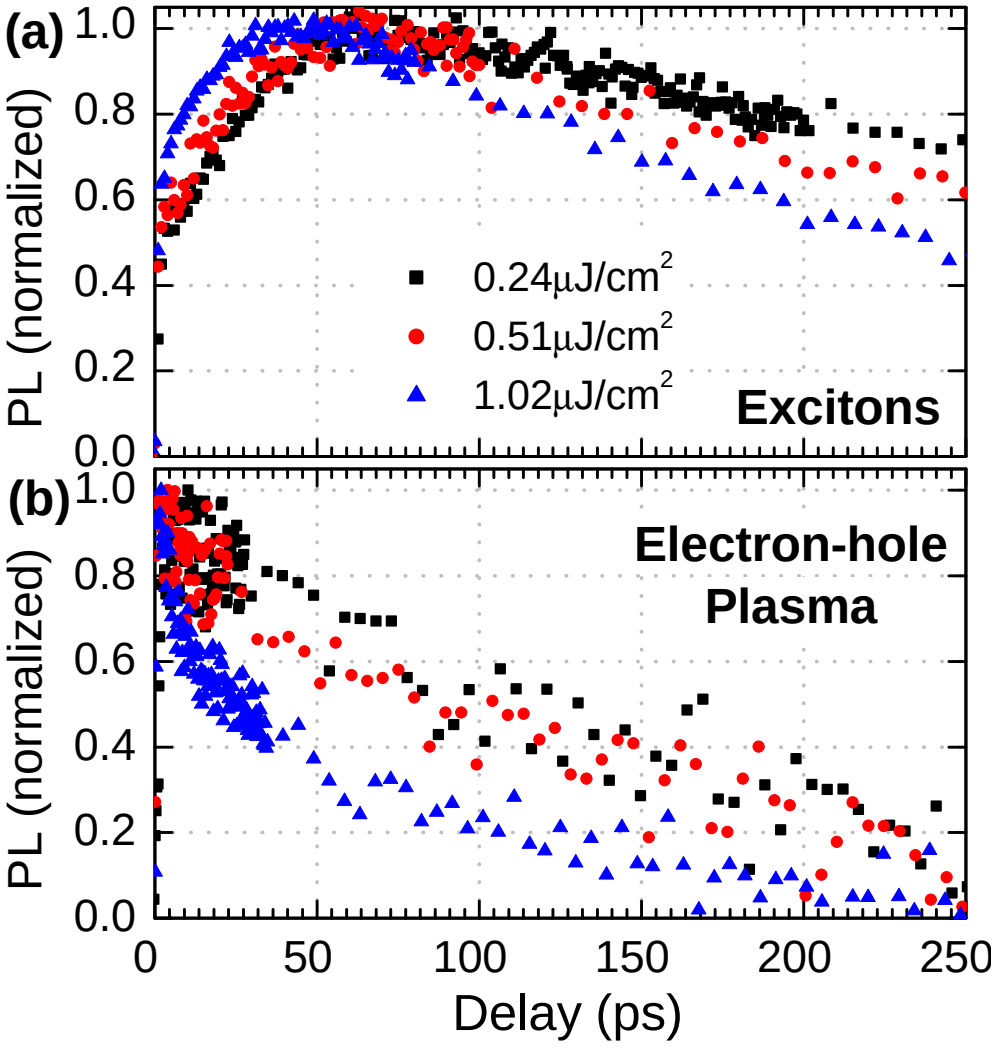

Figure 4.3: (a) Normalized PL transients of GaAs-CSS NWs measured at the emission energy of the exciton at 1.52 eV for a range of excitation fluences. (b) Normalized radiative plasma decay traces measured at 1.55 eV. The solid lines are guide to the eye.

semiconductors they are restricted by energy and momentum conservation requirements [241] and even in quantum wires, where such restrictions are lifted, these processes operate at charge densities that are over two orders of magnitude higher [241, 242] than those employed here.

4.3.3 Numerical Simulation from Coupled-Rate Equations

To gain further insight into the dynamics of exciton formation from free carriers, a model based on coupled rate equations that includes carrier-exciton interconversion as well as ra-

diative and non-radiative recombination of excitons and free carriers was constructed. Here, the exciton formation constant C governs the bimolecular formation of excitons with density X from an electron-hole plasma with charge density n. Recombination within the uncorrelated electron-hole plasma is governed by both radiative, bimolecular mechanisms (plasma constant B) or non-radiative, defect-mediated mechanisms (τ_{nr}) while exciton recombination is a monomolecular process with lifetime τ_{NW}:

$$\begin{aligned} \frac{\mathrm{d}n}{\mathrm{d}t} &= -Cn^2 + Cn_{\mathrm{eq}}^2 - \frac{n}{\tau_{\mathrm{nr}}} - Bn^2, \quad n(0) = n_i; \\ \frac{\mathrm{d}X}{\mathrm{d}t} &= Cn^2 - Cn_{\mathrm{eq}}^2 - \frac{X}{\tau_{\mathrm{NW}}}, \quad X(0) = 0. \end{aligned} \tag{4.3}$$

The recombination lifetime of excitons, τ_{NW}, can be directly determined from the excitonic emission at long times after excitation, for which free-charge inter-conversion into excitons has been completed. For this purpose, the transient PL measurements at the excitonic emission energy were further extended to long (1.5 ns) delay times using time-correlated single photon counting (TCSPC) system. The details of the system were described in Chapter 3. Fig. 4.4 shows a fusion of these TCSPC data (for times >500 ps) with those obtained from PL upconversion spectroscopy (shown for times <500 ps). The excitonic PL at a long time after non-resonant excitation exhibits a monoexponential decay with the decay rate independent on the excitation fluence. Hence, the exciton recombination lifetime of τ_{NW}=420 ps can be extracted from single-exponential fitting. Furthermore, the extracted exciton recombination rate is independent on the excitation density at the low excitation fluences used, which supports the notion of a low defect density in these high quality nanowires. The non-radiative free-charge recombination constant is therefore set to a large value of τ_{nr}=1000 ps, to reflect that such defect-mediated processes are unlikely to have any significant effect on the free-charge plasma decay. The radiative plasma recombination constant B is taken from the Ref. 63 to be the value for bulk GaAs, $B \approx 6.9{\times}10^{-19}\,\mathrm{cm^3ps^{-1}}$, given that the nanowires investigated here exhibits negligible quantum confinement.

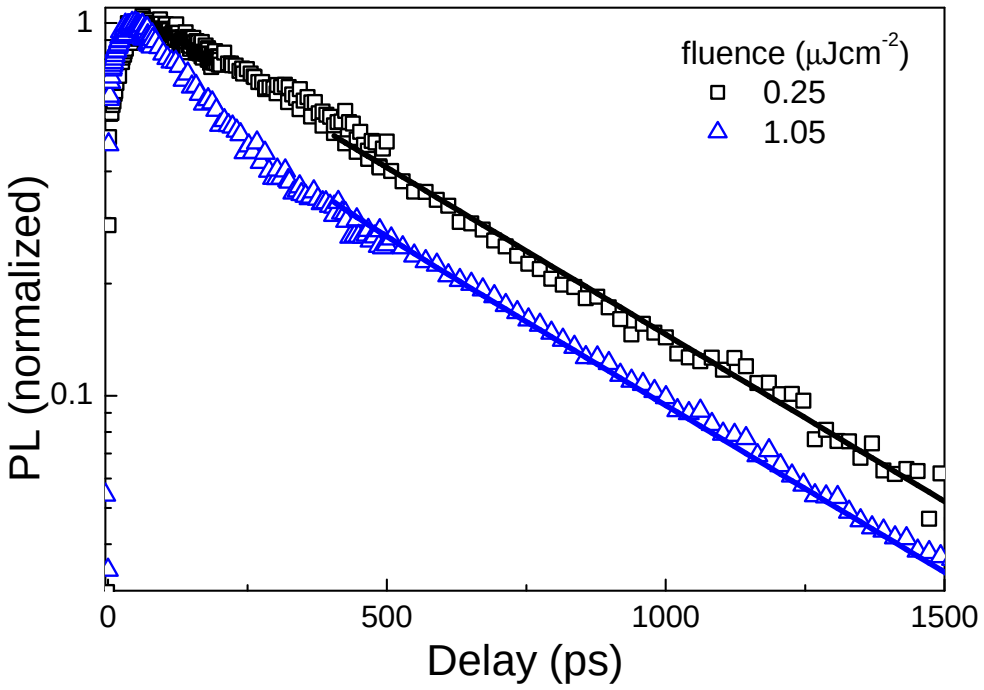

Figure 4.4: Normalized PL transients of GaAs CSS-NWs measured at the emission energy of the exciton (1.52 eV) for two different fluences. The short-term PL dynamics (≤500 ps) was measured using the PLUC technique, while the long-term emission was measured using TCSPC. Solid lines are mono-exponentials with decay time of 420 ps.

As shown by Piermarocchi *et al.*, C can be further divided into contributions arising from both acoustic (C_{AC}) and optical (C_{LO}) phonons, both of which mediate the exciton formation process [239]. The contribution arising from LO-phonon coupling given by an exponential dependence on an activation energy of ($E_{\mathrm{LO}} - E_{\mathrm{b}}$) where E_{LO} is the LO-phonon energy and E_{b} is the exciton binding energy. The AC-phonon coupling component, on the other hand, was found to be fairly constant with carrier temperature. The bimolecular exciton formation coefficient can therefore be related to the charge carrier temperature T_{C} via:

$$C = C_{\mathrm{LO}} \exp\left(-\frac{E_{\mathrm{LO}} - E_{\mathrm{b}}}{k_{\mathrm{b}} T_{\mathrm{e}}}\right) + C_{\mathrm{AC}}; \tag{4.4}$$

For non-resonant excitation, it has been shown that the average carrier cooling rate of a hot carrier at low substrate temperature (T_{l}) is dominated by LO-phonon emission at high carrier temperature (T_{C}) and AC-phonon emission when the excess energy becomes lower than the LO-phonon energy [243]. The main average cooling rates $\langle \mathrm{d}T/\mathrm{dt} \rangle$ (in units of K/ps)

per electron in a Maxwellian distribution of temperature are given by: [243]

$$\langle\frac{\mathrm{d}T_\mathrm{C}}{\mathrm{d}t}\rangle_\mathrm{OP} = 3240.319\,\left[\exp\left(-\frac{E_\mathrm{LO}}{kT_\mathrm{C}}\right) - \exp\left(-\frac{E_\mathrm{LO}}{kT_\mathrm{l}}\right)\right]; \tag{4.5}$$

$$\langle\frac{\mathrm{d}T_\mathrm{C}}{\mathrm{d}t}\rangle_\mathrm{AD} = 3.1423\times10^{-5}\,T_\mathrm{C}^{3/2}\left(\frac{T_\mathrm{C}-T_\mathrm{l}}{T_\mathrm{C}}\right); \tag{4.6}$$

$$\langle\frac{\mathrm{d}T_\mathrm{C}}{\mathrm{d}t}\rangle_\mathrm{AP} = 12.134\times10^{-3}\,T_\mathrm{C}^{1/2}\left(\frac{T_\mathrm{C}-T_\mathrm{l}}{T_\mathrm{C}}\right); \tag{4.7}$$

where the subscripts OP, AD and AP to the average cooling rates denote the different cooling mechanisms arising from optical phonon, acoustic-deformation-potential and acoustic-piezoelectric scattering, respectively. Given the large diameter of the GaAs-CSS nanowires, it is reasonably to consider the bulk GaAs value for the LO phonon energy (E_LO=36 meV). The evolution of the carrier cooling in the nanowires is deduced by calculation of their average energy lost per electron-hole pair $\langle\mathrm{d}T_\mathrm{C}/\mathrm{dt}\rangle \approx \langle\mathrm{d}E/\mathrm{dt}\rangle$ with the variation in temperature extracted from:

$$T_\mathrm{C}(t) = T_\circ - \int_0^t \langle\frac{\mathrm{d}T_\mathrm{C}}{\mathrm{d}t'}\rangle\mathrm{d}t' \tag{4.8}$$

where $T_\circ$ is given by the excess energy of carriers during initial excitation. The output of the numerical simulation is shown in Fig. 4.5.

Finally, $\mathrm{n_{eq}}$(n, X, T) in Eq. 4.3 describes the equilibrium free carrier concentration given by the law of mass-action[244, 245], for which the three-dimensional (bulk) version was chosen[87]:

$$\frac{\mathrm{n_{eq}^2}}{\mathrm{X}} = \mathrm{K(T_C)} = 2\left(\frac{\mu_\mathrm{x}\mathrm{k_B}\mathrm{T_C}}{2\pi\hbar^2}\right)^{3/2}\exp\left(\frac{-\mathrm{E_b}}{\mathrm{k_B}\mathrm{T_C}}\right), \tag{4.9}$$

where μ_x is the reduced exciton mass and $\mathrm{E_b}$ is the exciton binding energy (taken to be the GaAs bulk values of $0.0546\,m_e$ and 4.6 meV [34], respectively) and K is the equilibrium constant which depends on the carrier temperature T_C. The term Cn_{eq}^2 therefore describes

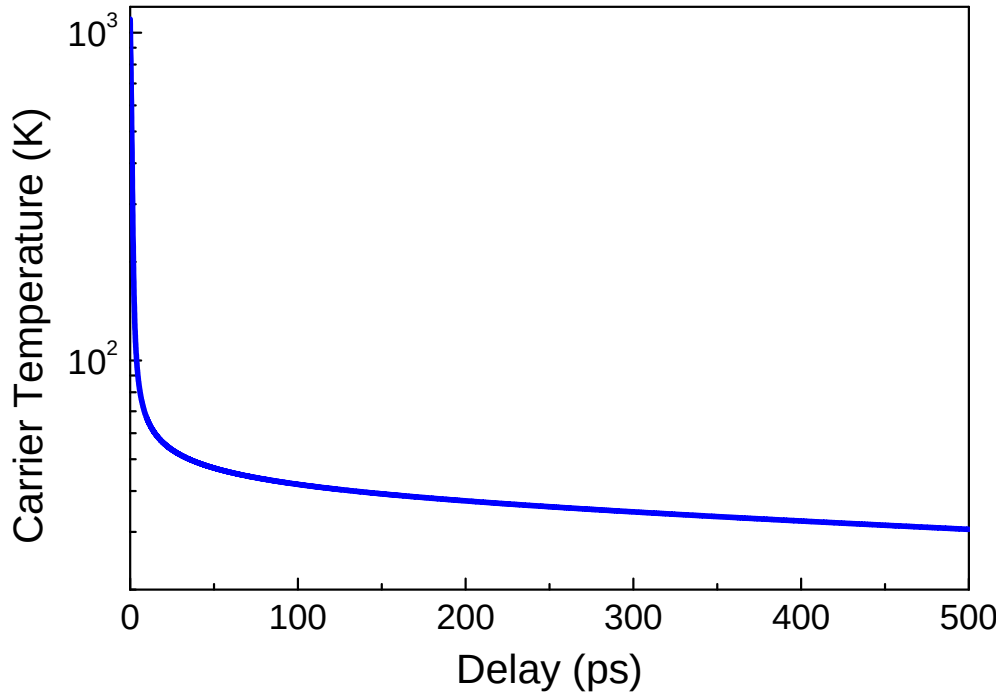

Figure 4.5: Charge carrier temperature T_C in the GaAs-CSS nanowires (black line), as extracted from the calculations based on Eq. 4.7.

the exciton ionization rate[245].

The photoluminescence data shown in Fig. 4.3 directly link to the exciton density X and free-carrier density n that are the solutions to Eq. 4.3. First, the emission transients taken at the exciton emission energy (Fig. 4.3a) are directly proportional to $X(\mathrm{t})$. Second, the free-charge density $n(\mathrm{t})$ can be computed from the measured plasma emission I_{plasma} (Fig. 4.3b) using their direct relationship, $n \propto \sqrt{I_{\mathrm{plasma}} T_{rmC}^{1.5}}$. The carrier population n was obtained from the plasma emission normalized to its initial (t=0) value, i.e. $I_{\mathrm{plasma}}/\ I_0$, through:

$$n = n_0 \sqrt{\frac{I_{\mathrm{plasma}}}{I_0} \frac{T_C^{1.5}}{T_0^{1.5}}} \tag{4.10}$$

where the initial carrier density (n_0) immediately after photoexcitation ($t = 0$) can then be calculated from the density of absorbed photons, as described in Section 4.2.

Fig. 4.6 a, and b show the best fits to the free-carrier and exciton densities data obtained through the solution of the coupled rate Eq. 4.3, with C_{AC}, and C_{LO} being the only free pa-

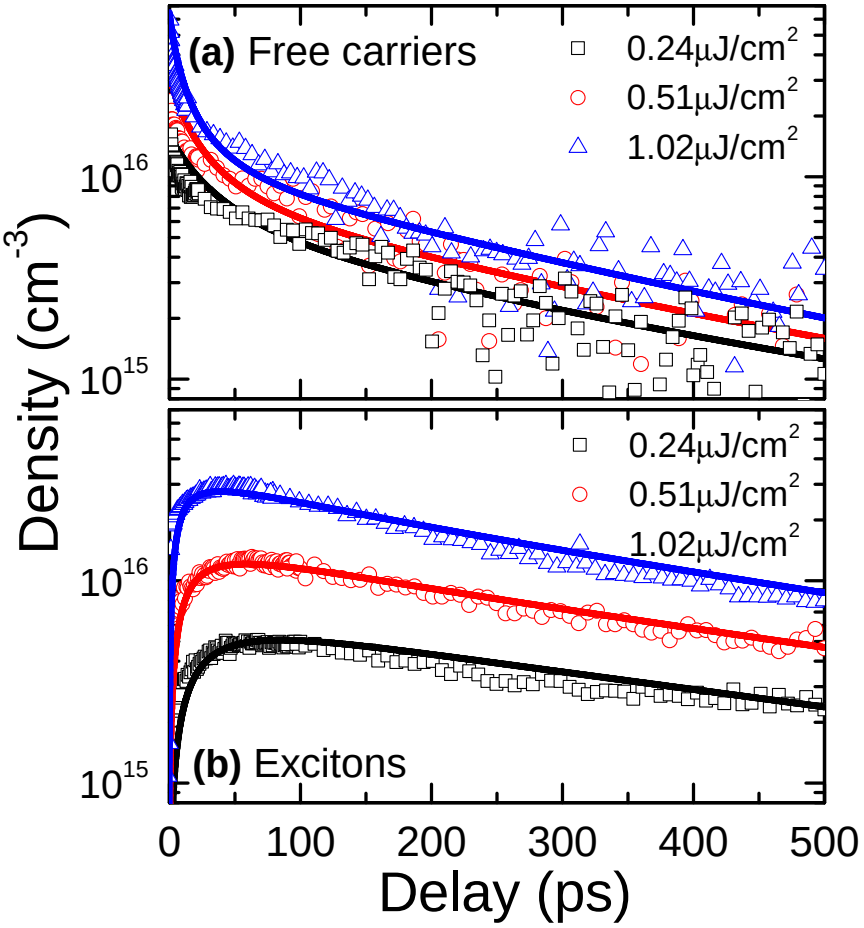

Figure 4.6: (a) Free carrier density n and (b) exciton density X in the GaAs-CSS NWs as a function of time after excitation for three different excitation fluences. Open symbols are data points while solid lines are fits based on the coupled-rate equation model described in the text. The experimental data for the free carrier density were converted from the decay traces of the radiative plasma emission shown in Fig. 4.3b using the method described in the text.

rameters, which were extracted from fits to be $1.16\times10^{-18}\,\mathrm{cm^3ps^{-1}}$ and $2.61\times10^{-18}\,\mathrm{cm^3ps^{-1}}$, respectively. The excellent agreement between the data and the model confirms the occurrence of a gradual conducting-to-insulating transition in the nanowires, i.e. excitons are formed over time through a bimolecular process from unbound free carriers. The faster decay of excitonic PL at higher excitation density is therefore attributable to the faster exciton generation. Here, the contribution of band-to-band recombination of unbound free-charge-carrier becomes dominant at increasing excitation density and competes directly with the exciton formation at early time delay. The transition from conducting-to-insulating phase occurs at later times after excitation, as a result of the decreasing screening efficiency of

charge-carriers in the nanowires [83, 84].

4.3.4 Time-Resolved PL Transients of Bare GaAs Nanowires

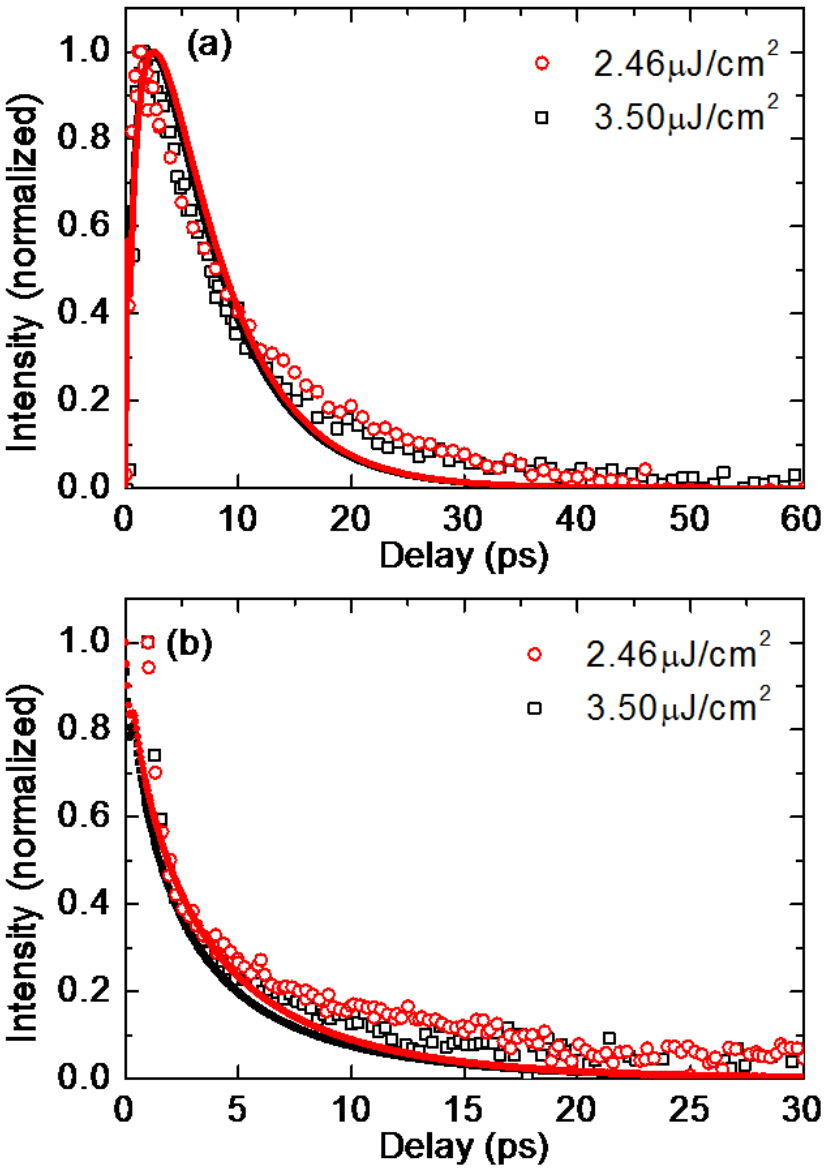

Figure 4.7: (a) Normalized PL transients of bare GaAs NWs measured at the emission energy of the exciton at 1.52 eV for different fluences (open symbols) along with the output of the numerical model (solid-line, as described in text). (b) Normalized free-carrier density decay for bare GaAs NWs . The data are obtained by normalizing the radiative plasma emission measured at 1.55 eV with T_e, as described in the text.

The PL dynamics of "bare" GaAs nanowires, for which no additional over-coating with higher-band-gap material, was measured under identical conditions. The carrier dynamics

in bare GaAs nanowires has been shown previously to be dominated by trapping at surface-defect states[26]. Fig. 4.7 shows that the PL of bare GaAs NWs at 10 K is short-lived and dominated by fast charge trapping. The evolution of exciton and free-carrier densities was simulated from the model described in Section 4.3.3 using the same parameters as for the GaAs-CSS NWs, with the exception of τ_{NW} and τ_{nr} which were allowed to vary. Good agreement was obtained between fits and data for τ_{NW}=6 ps and τ_{nr}=6 ps, as shown in Fig. 4.7. The short lifetimes and the lack of a discernable delayed rise in the exciton density with time after excitation demonstrate that fast trapping of the electron-hole plasma sets a short time window for exciton formation and thus dominates the overall time evolution of the exciton and charge densities. These results show that effective defect passivation must be achieved in order for semiconductor nanowires to display intrinsic excitonic and charge properties.

4.3.5 Spectral evolution of the nanowire emission

To gain further insights into the conducting-to-insulating transition, time-evolution of the PL spectra for GaAs-CSS nanowires under different excitation fluences were conducted. Two representative sets of time-resolved PL spectra measured at excitation fluences of $0.5\mu\mathrm{Jcm}^{-2}$ and $1\mu\mathrm{Jcm}^{-2}$ are shown in Fig. 4.8. At early time delay, the PL is blue-shifted from the exciton energy and spectral broadening can be observed, with Fermi-filling[74, 75] causing charge recombination above the band edge. At longer time-delay, the PL spectra shift to centre at the exciton peak energy and spectrally narrow. These changes occur as the free-carrier density is depleted by band-to-band recombination and exciton formation until a predominantly excitonic phase has formed [67, 74].

4.3.6 Mott Density

For a more quantitative analysis, Fig. 4.9 plots the peak position of the PL spectra as a function of time, together with the total electron-hole pair density ($N = n + X$) extracted

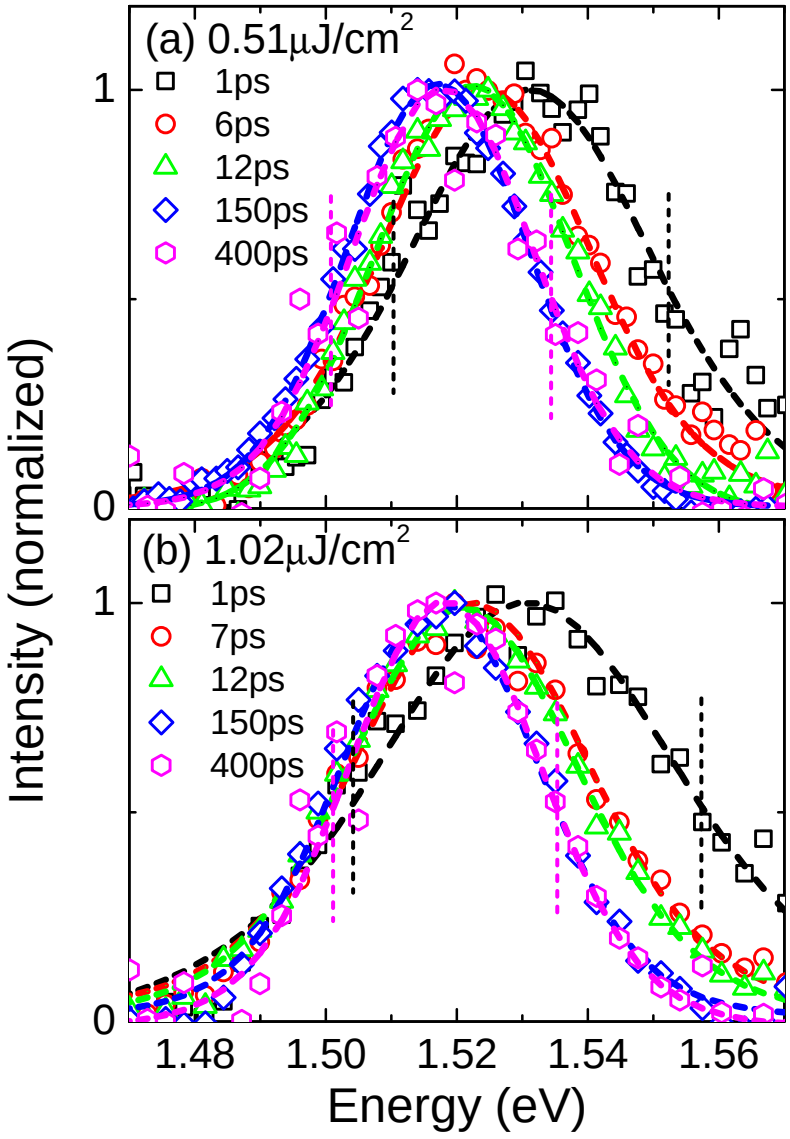

Figure 4.8: PL spectra obtained at various times after pulsed excitation with fluences of (a) 0.51 μJcm^{-2} and (b) 1.02 μJcm^{-2} for GaAs-CSS NWs. At early times, both high-energy emission from the electron-hole plasma and excitonic emission are observable, while at late times the PL converges towards predominantly excitonic emission. The pairs of vertical dashed lines indicate the spectral linewidths at half maximum for early (1 ps) and late (400 ps) time-delays. At later times after excitation, the predominantly excitonic spectra are broadened by both the spectral resolution of the system (32 meV, as limited by the high time resolution) and nanowire inhomogeneities.

from the model as described above. For PL spectra collected under initial excitation fluence of $0.5\,\mu\mathrm{Jcm}^{-2}$, the PL peak centres at the exciton emission energy at a time delay of $\approx 30\,\mathrm{ps}$. This occurs at longer time delay of $\approx 150\,\mathrm{ps}$, when the excitation fluence is increased to $1\,\mu\mathrm{Jcm}^{-2}$. These observations confirm that an increasing contribution to the total PL comes from the radiative recombination of free carriers as the fluence is increased, consistent with the TIPL measurements shown in Fig. 4.2. In theoretical support of this argument, the bandgap renormalization energy (BGR) induced by the exchange and correlation of electron-hole pairs in the nanowires was calculated. It has been established that an excitonic phase appears when the BGR is comparable to the excitonic binding energy (E_b). Vashishta and Kalia[94] showed that the sum of the exchange and correlation energies is independent of the band structure and can be determined from the electron-hole pair density and exciton binding energy as:

$$\Delta_{BGR} = \frac{-\mathrm{E_b}(-4.8316 - 5.0879\mathrm{r_s})}{(0.0152 + 3.0426\mathrm{r_s} + \mathrm{r_s^2})} \tag{4.11}$$

where r_s is a dimensionless quantity defined by the volume occupied by a carrier pair in the plasma compared with that for an exciton of radius a_b, that is, $\mathrm{r}_s = (4/3n\pi a_b^3)^{-1/3}$ [92, 94]. By taking the uncorrelated plasma density n from the fits to the emission transients as described above, the theoretically expected value ($E_{eh} - \Delta_\mathrm{BGR}$) of the low-energy emission edge (red line) was plotted in Fig. 4.9, together with the overall electron-hole pair density $N = n + X$ (blue line) and PL peak position (green diamonds). Fig. 4.9 shows that the PL peak gradually shifts to become centered at the exciton emission energy, simultaneously with the band edge $E_\mathrm{eh} - \Delta_\mathrm{BGR}$ (red line) crossing the exciton line (dashed black line). At this point the Coulomb screening becomes effectively weaker than the exciton binding [34] which therefore marks the commencement of the excitonic phase. This transition appears to be smooth and gradual and occurs when the total electron-hole pair density is reduced to ≈ 2–$4\times10^{16}\,\mathrm{cm}^{-3}$. These data also show again that as the excitation density is increased, the free-carrier-to-exciton interconversion is weakened by the presence of Coulomb screening, resulting in delayed commencement of the excitonic phase and enhanced carrier

recombination via direct band-to-band transitions. These observations therefore support the model described above and are consistent with the time-integrated emission spectra shown in Fig. 4.2.

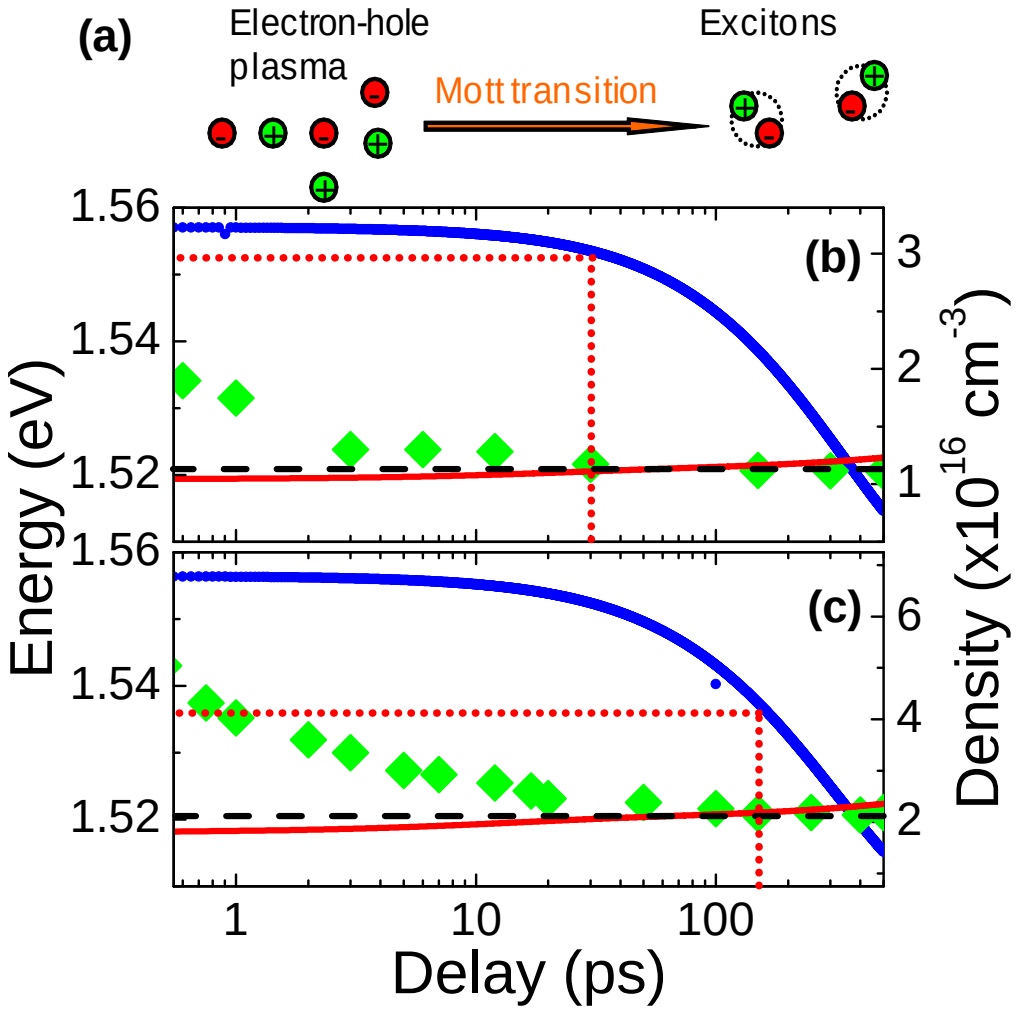

Figure 4.9: The evolution of peak energy of the total emission spectrum including plasma and excitonic contributions (green diamond) and the calculated band edge position (red solid line) and total electron-hole pair density (blue solid line) for excitation fluences of (a) $0.51\mu\text{Jcm}^{-2}$ and (b) $1.02\mu\text{Jcm}^{-2}$. The exciton emission energy is indicated as dashed-black line while the dotted red lines are guide to the eye where the Mott-transition commence.

4.3.7 Discussion

Such smooth transitions from an excitonic to a free charge plasma phase have been found previously to occur for both bulk semiconductors[95] and quantum wells[69, 75]. Two main

reasons were discussed for why a gradual transition may also be observed for the GaAs nanowires investigated here. First, it is well-established that the carrier cooling is to be rather slow in GaAs due to the weak acoustic phonon coupling[243] and hence the carrier temperature is higher than the lattice temperature over the 500 ps observation window, as seen in the simulation result shown in Fig. 4.5. For thermal lattice energies smaller than the exciton binding energy, the Mott criterion depends on the charge carrier temperature T_c[34], and therefore evolves with time following non-resonant excitation. In particular, the bimolecular interconversion of free charge carriers into excitons in the nanowires occurs concomitantly with the slow carrier cooling which can induce a broadening of the observed transition from an electron-hole plasma to and excitonic phase. The Mott density N_{M} denotes the electron-hole pair density at which the Debye-Hückel screening length ($\mathrm{K_D}$) becomes comparable to the exciton Bohr radius ($\mathrm{a_B}$), which yields:[34]

$$N_{\mathrm{M}} = (1.19)^2 \frac{\varepsilon_{\mathrm{r}} \varepsilon_o k_{\mathrm{B}} T_c}{e^2 a_{\mathrm{B}}^2} \tag{4.12}$$

where ε_r is the dielectric constant. Fig. 4.10 plots the calculated Mott density from Eqn. 4.12 using the simulated carrier temperature shown in Fig. 4.5. Following initial fast carrier cooling within the first 10 ps after excitation, N_{M} declines from $\sim 4\times10^{16}\,\mathrm{cm^{-3}}$ to $2\times10^{16}\,\mathrm{cm^{-3}}$ over the next 500 ps. These values are in excellent agreement with the experimental spectral features shown in Fig. 4.9. At excitation fluences significantly higher than those employed in these transient PL measurements, the Mott limit will be exceeded. Indeed, a distinct quenching of the excitonic emission and increase in plasma contribution to the time-integrated PL spectra for excitation fluences exceeding $\sim 1.5\,\mu\mathrm{Jcm^{-2}}$ were observed in Fig. 4.2.

A second plausible cause for the observed gradual Mott transition is the existence of inhomogeneities in the material. The presence of charge carrier density gradients in the nanowires can be safely ruled-out since the experimental conditions were carefully chosen to avoid these, as discussed in previous section. However, the TIPL spectra of the nanowires show an exciton linewidth that is much larger than thermal broadening effects to be expected at 10 K, as seen in Fig. 4.2. This suggests that carriers within the nanowires experience chem-

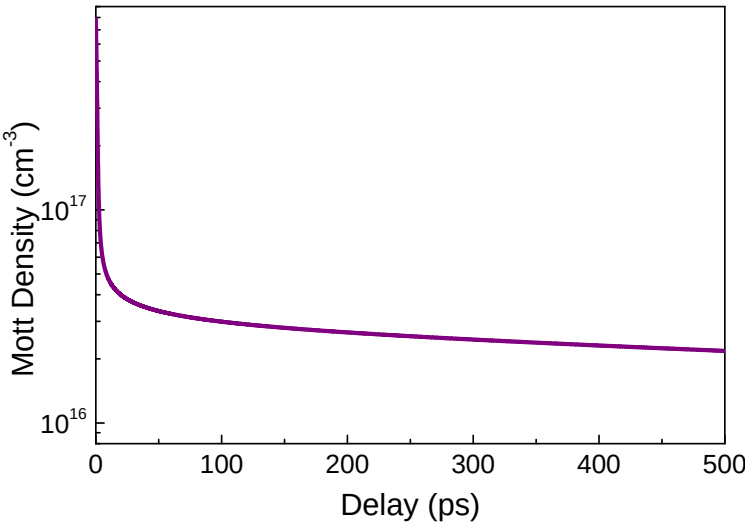

Figure 4.10: Mott transition density $N_{\mathrm{M}}(T_{\mathrm{c}})$ extracted from Eq. 4.12 and shown as a function of time after excitation.

ical potential fluctuations which may also affect their confinement and Coulomb interaction energies, leading to partially overlapping emission features from excitons and free-carriers. Such variations can possibly arise from composition gradients, nanowire diameter fluctuation or unexpected doping near the core-shell interfaces during the growth. Previous TIPL measurements on single GaAs nanowires produced from similar growth techniques have shown linewidth broadening of 23 meV at 10 K, attributed to strain and compositional non-uniformities[42]. It should be stressed that the measurements presented here were carried out on nanowire ensembles and hence further broadening is to be expected. SEM images show that both nanowire-to-nanowire diameter changes ($\pm$ 5 nm) and slight ($<$ 3 nm per micrometer length) tapering of individual nanowires occur in these materials. Variations in lateral width are common features even in high quality semiconductor nanostructures and have been investigated in detail for two-dimensional heterostructures[246] and more recently for tetrapod nanostructures[247].

4.4 Conclusion

In conclusion, the carrier dynamics in GaAs nanowires overcoated with AlGaAs/GaAs shell-skin layer have been investigated at 10 K using time-resolved PL spectroscopy. The non-resonant excitation of nearly-defect-free semiconductor nanowires is followed by bimolecular interconversion of the initially generated free electron-hole plasma into an exciton population. An increased excitation fluence leads to faster initial exciton formation, while at long times and low charge-pair densities a reduction of the exciton formation rate presents an obstacle to the system attaining thermal equilibrium. Analysis of the emission lineshape showed that the conducting-to-insulating transition occurs gradually over total electron-hole charge pair density of 2–4$\times 10^{16}$cm^{-3}. The gradual Mott-transition is attributed to the slow carrier cooling during the bimolecular interconversion of free charge carriers into excitons and the presence of chemical-potential fluctuations. For "bare" GaAs core NWs for which the passivating shell layer was absent, both free-charge and exciton dynamics are dominated by rapid trapping at defect sites within a few picoseconds after excitation and thus a clear Mott transition cannot be observed. For nanowires the surface-to-volume ratio is inherently high, which results in optoelectronic properties highly sensitive to surface defect states. The results presented in this chapter show that surface-passivation is essential to enhance the carrier lifetime and fundamental for the application in various optoelectronic devices.

Chapter 5

Strong Carrier Lifetime Enhancement in GaAs Nanowires Coated with Semiconducting Polymer

Charge generation at the interface of hybrid OPV is crucial for the device performance. For hybrid OPV using semiconductor nanostructures, the charge carriers are rapidly trapped at the surface states of nanostructures, as discussed in Chapters 4. In this chapter, the ultrafast charge carrier dynamics in GaAs/conjugated polymer type-II heterojunctions were investigated using time-resolved photoluminescence spectroscopy at 10 K. By probing the photoluminescence at the band edge of GaAs, strong carrier lifetime enhancement for nanowires blended with semiconducting polymers is observed. The enhancement is found to depend crucially on the ionization potential of the polymers with respect to the Fermi Energy level at the surface of the GaAs nanowires. These effects are attributed to the electron doping by the polymer which reduces the unsaturated surface-state density in GaAs. As a result, the electron-injection across the interface is greatly reduced and such surface-doping is absent when the surface of nanowires is terminated by native oxide. The results suggest that surface engineering via π-conjugated polymers can substantially improve the carrier lifetime in nanowire hybrid heterojunctions with applications in photovoltaics and nano-scale

photodetectors.

5.1 Introduction and Background

Solution processable, nanostructured hybrid materials consisting of organic and inorganic semiconducting components are highly attractive for the production of low-cost and high-efficiency solar cells.[3–7] To obtain substantial photocurrents, interpenetrating networks based on electron-donor and acceptor components are generally used to form a so-called bulk-heterojunction (BHJ) for which ultrafast exciton dissociation and charge generation occurs primarily at the interface between the two material components [3, 15–18]. A variety of promising hybrid solar cells have been reported which use π-conjugated polymers, such as polythiophenes or polyphenylenevinylene derivatives, in conjunction with inorganic nanomaterials such as gallium arsenide (GaAs) [9], cadmium selenide (CdSe) [3, 15, 19], indium phosphide (InP) [20], zinc oxide (ZnO) [4, 21], or lead selenide (PbSe) [22]. Semiconductor nanowires (NWs) with high aspect-ratio are particularly attractive for use in hybrid solar cells because they offer direct charge pathways to electrodes, large surface areas, high carrier mobility along the nanowires and chemical and physical stability [3, 5, 9, 20, 24, 25]. However, the charge transport in such nanowires has been shown to be strongly affected by the presence of surface defect states [26–28] that act as charge traps. A number of methods have therefore been devised to passivate such traps, including overgrowing the NWs surface with a layer of large-bandgap semiconductor [26, 29] or treatment with sulfides [30]. However, such overcoats may also form a barrier to charge generation at the interface of the nanowires when these are embedded in a π-conjugated polymer as part of a photovoltaic device structure. An excellent solution to this problem can be provided if conjugated polymers are to be found that provide both a BHJ interface with the nanowires but also effectively passivate the nanowire surface defects upon contact.

This chapter demonstrates how charge carrier lifetimes in GaAs nanowires are affected when the nanowires are embedded in a variety of π-conjugated polymers to form type-II

hybrid heterojunction. The PL lifetime of NWs embedded in the π-conjugated polymers is enhanced significantly when the ionization potential (IP) of the polymer is smaller than the workfunction of the NWs and the native oxide layers on the surface of NWs are removed. X-ray photoemission spectroscopy reveals that the surface-states of the uncoated GaAs NWs are electron-deficient in chemical character. Hence, the strong carrier lifetime enhancement is attributed to the filling of surface states in the nanowires by electron-injection from the highest-occupied molecular orbital (HOMO) of the polymer into the energetically lower-lying surface trap states of the nanowires until an equilibrium state is reached. Density-functional theory calculations performed on the GaAs/polythiophene heterojunction reveal that the polymer becomes an electron-donating reagent to give a relatively thin ($\approx 3\,\text{Å}$) "degenerate" electron-doping layer on the surface of GaAs. Our results demonstrate that charge lifetimes in GaAs nanowires can be significantly enhanced through overcoating with an organic semiconducting material of suitable IP that has the dual functions of acting as a surface passivating agent and being the secondary material component in the BHJ photovoltaic material.

5.2 Sample Preparation and Experiments

5.2.1 Growth of GaAs Nanowires

GaAs NWs were grown on semi-insulating GaAs (111)B substrates with a 50 nm gold-colloid seeded vapor-liquid-solid metal-organic chemical vapor deposition technique. Trimethyl-gallium and AsH_3 were used as precursors. The NWs were grown via a two-temperature growth procedure to minimize the formation of twin-defects. [226] The growth was initiated with a nucleation step at high temperature (450°C) and rapidly ramped down to the subsequent growth temperature (375°C). This procedure yielded GaAs nanowires of core diameter 50–60 nm and of 4–5 μm in length. The GaAs nanowire side facets are predominantly {112} oriented, resulting in a hexagonal nanowire cross-section [248]. For control samples, GaAs/AlGaAs core-shell nanowires were grown for which the GaAs nanowire core

was covered by an additional ≈30 nm-thick layer of AlGaAs. To achieve uniform, conformal deposition of the AlGaAs shells, a high growth temperature (650°C) was used.

5.2.2 Surface Etching of GaAs Nanowires and X-ray Photoemission Measurements

The native oxide typically present on the surface of GaAs can be removed by established HCl-solution etching methods [125]. In this study, as-grown GaAs nanowires on GaAs(111) substrate were dipped into a 1M HCl solution for 30 s and rinsed with DI-water for 10 s before being dried in a nitrogen gas stream. The chemical nature of the surface states present in both as-grown and etched GaAs NWs were examined by performing X-ray photoemission spectroscopy (XPS) measurements at the Daresbury National Centre for Electron Spectroscopy and Surface Analysis, as described in Section 3.2.

5.2.3 Fabrication of GaAs Nanowires/Polymer Blend Films

Fig. 5.1a shows the SEM image of the as-grwon GaAs nanowires. The GaAs NWs were subsequently embedded in BHJ thin films of various organic semiconducting materials, such as poly(3-hexylthiophene) (P3HT), poly(2-methoxy-5-(2-ethyl-hexyloxy)-1,4-phenylene-vinylene) (MEH-PPV), poly(2,5-bis(3-decylthiophen-2-yl)thieno(2,3-b)thiophene) (G2), [6,6]-phenyl-C61-butyric acid methyl ester (PCBM) and poly[(9,9-di-n-octylfluorenyl-2,7-diyl)-alt-(benzo [2,1,3]thiadiazol-4,8-diyl)] (F8BT). These materials have been widely used by others for a range of organic and hybrid organic-inorganic optoelectronic devices [7, 9, 15, 249, 250]. All polymers were purchased from American Dye Source, except G2, which was synthesized by Merck Chemicals, as described in Ref. [249].

Fig. 5.1b – f display the chemical structure of the organic semiconducting molecules used in this study. In addition, a schematic of the relevant energy levels of bulk GaAs and the organic semiconductors are shown for aligned vacuum levels (E_{VAC}). Type-II heterojunctions are expected to form at the hybrid interface when GaAs NWs are blended with P3HT, MEH-

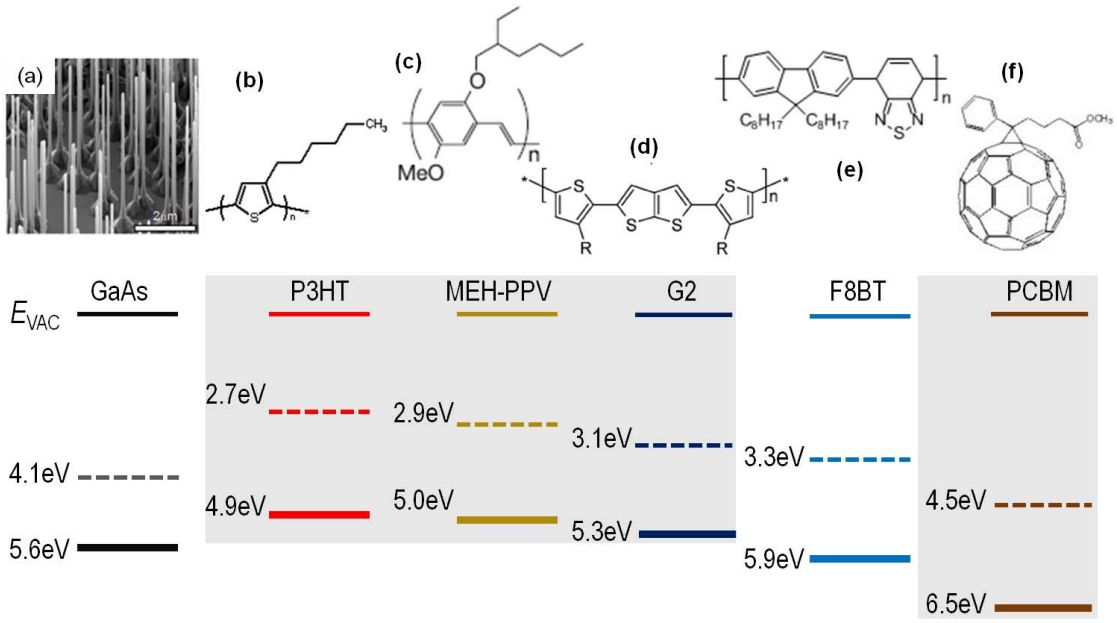

Figure 5.1: (a) Top: SEM image of GaAs nanowires as grown on an GaAs(111) substrate. Bottom: VBM and CBM energetic positions for bulk GaAs at 10 K, taken from Ref. [238]. Note that due to their large diameter, these GaAs NWs experience negligible quantum confinement effects and a bulk description is therefore appropriate here. [29] Molecular structure (top) and HOMO/LUMO energy levels of (b) P3HT, (c) MEH-PPV, (d) G2, (e) F8BT, and (f) PCBM. The energetic levels of polymers are cited from Refs. [251] and [249]. The shaded areas indicate the formation of type-II heterojunctions when GaAs nanowires are blended with P3HT, MEH-PPV, G2 or PCBM. For F8BT/GaAs nanowire blends a type-I heterojunction is expected to form.

PPV, G2 or PCBM. Specifically, hole injection from GaAs NWs into P3HT, MEH-PPV and G2 should be favorable upon photoexcitation since the valence band maximum (VBM) and conduction band minimum (CBM) of GaAs is deeper than the highest occupied molecular orbital (HOMO) and lowest unoccupied molecular orbital (LUMO) levels of these polymers. For GaAs NWs/PCBM type-II heterojunctions, on the other hand, electron injection from GaAs NWs into PCBM should follow photoexcitation, in accordance with the energetic offset at the interface shown in 5.1. As a control sample, GaAs NWs were blended with F8BT for which an interfacial type-I heterojunction ought to form at which photo-carriers are confined in the GaAs NWs by the surrounding higher-bandgap F8BT material.

The GaAs NWs/polymer blend films investigated in this study were prepared in an inert N_2 atmosphere as follows. First, a z-cut quartz substrate was spin-coated with a thin film of the organic semiconducting material, which had been dissolved in 1,2 dichloro-benzene (1,2-

DCB) at a concentration of 0.2 mg/ml. To transfer the nanowires from their GaAs substrates onto these film-coated quartz substrates, the two substrates were gently touched together. This was then followed by drop-casting 30 μl of organic semiconductor solution onto the NWs distribution deposited on the initial films. Finally the samples were dried on a hot-plate at 70°C for 3 hours. The slow drying and annealing processes employed when the hybrid films were produced generally induce arrangement of chains into more ordered domains [145, 146, 252–254]. Films of P3HT produced under such conditions have been shown to exhibit large domains of lamellar structure and a high crystallinity [145, 252, 253], and those of PCBM also exhibit crystalline domains [255]. For MEH-PPV, on the other hand, X-ray diffraction (XRD) profiles were shown to remain featureless even at high temperature [256] and the films thus can be considered to be amorphous.

5.2.4 Time-resolved PL measurements

For time-integrated and time-resolved photoluminescence (PL) measurements, the sample was maintained at a temperature of 10 K in a liquid-helium flow cryostat. Time-resolved PL measurements were performed using a PL up-conversion set-up that has already been described in detail in Chapter 3.1.2. In this study the sample was excited at a photon energy of 1.68 eV with the output from a mode-locked Ti:Sapphire laser oscillator supplying 100 fs pulses at 82 MHz repetition rate. The PL was gated optically in a β-barium borate crystal using a split-off part of the laser output that was subjected to an adjustable time delay with respect to the excitation pulse. Time-resolved and time-integrated PL spectra were recorded with a liquid-nitrogen cooled CCD detector connected to a spectrometer, and corrected for the spectral response of the apparatus. The spectral resolution of the time-resolved and time-integrated PL systems at the selected detection wavelengths was 32 meV and 4 meV, respectively, and the former system had a time-resolution of 200 fs.

5.2.5 Modeling a GaAs/P3HT Interface *via* Density-Functional Theory

Density-functional theory (DFT) calculations within the local-density approximation (LDA) [257] were performed by Keian Noori in the Guistino's group (Department of Materials, Oxford University) using the `Quantum ESPRESSO` software package [258], to investigate the interfacial interaction of GaAs/P3HT heterojunctions. t is currently beyond available computational power to incorporate into the DFT calculations the complexities of the realistic interfaces, which include surface states, non-stoichiometry, oxidation in the NWs and a certain degree of packing disorder in the polymer. However, it will be insightful to assess the extent to which charge exchange occurs at the perfectly ordered and defect-free NW/P3HT interfaces simulated here. Ultrasoft [259] (H, C, S) and norm-conserving [260] (Ga, As) pseudopotentials were used to account for the core-valence interaction. Valence electronic wavefunctions and charge density were described using plane wave basis sets with kinetic energy cutoffs of 70 Ry and 350 Ry, respectively. The lattice parameters of bulk wurtzite GaAs were optimized using a 8×8×8 Brillouin Zone (BZ) grid, yielding values (a = 3.99 Å, c = 6.58 Å) in agreement with experiment [261] and theory [262]. The structure of bulk P3HT was optimized as described in Ref. [263]. Structural relaxations of the interface were carried out with sampling of the BZ at the Γ point.

GaAs nanowires exhibit both zinc blende and wurtzite structures [261, 264, 265]. Since the wurtzite $(10\bar{1}0)$ surface is crystallographically parallel to the zinc blende {112} face, it is therefore comparable. In this study, the GaAs/P3HT interface was simulated using a wurtzite GaAs$(10\bar{1}0)$ surface, with the conformation similar to the previous work on the related ZnO/P3HT interface [263]. The atomistic model of the GaAs/P3HT interface consists of 428 atoms. Four layers of GaAs were used, with the bottom two layers held fixed in order to mimic bulk GaAs. All other atoms were allowed to relax. The transverse area of the GaAs slab is 15.96 Å,× 13.16 Å, and periodic images of the slabs were separated by 8 Å of vacuum.

The electronic charge redistribution upon formation of the interface was determined by

calculating $\Delta n(\mathbf{r}) = n_{\mathrm{GaAs/P3HT}}(\mathbf{r}) - [n_{\mathrm{GaAs}}(\mathbf{r}) + n_{\mathrm{P3HT}}(\mathbf{r})]$. In this expression $\mathbf{r}$ represents the position vector within the computational cell, $\mathrm{n_{GaAs/P3HT}}$ the ground state charge density of the GaAs/P3HT interface, $\mathrm{n_{GaAs}}$ the charge density of the GaAs slab without the P3HT layers in the same computational cell, and $\mathrm{n_{P3HT}}$ the charge density of the P3HT layers without the GaAs slab. The electrostatic potential offset is calculated by integrating, using Poisson's equation, the planar average charge of $\Delta n(\mathbf{r})$ from the middle of the GaAs slab to the middle of P3HT layer.

5.3 Results and Discussion

5.3.1 Surface States of GaAs Nanowires

Fig. 5.2 shows the XPS spectra of GaAs NWs detected for the $\mathrm{Ga_{GaAs}}$ 3d, $\mathrm{As_{GaAs}}$ 3d and O 1s core level regions. Previous studies by Joyce *et al.* have shown that the surface of the as-grown GaAs nanowires was terminated by an amorphous native oxdide layer with thickness of $\approx 1\,\mathrm{nm}$ [226]. Since the XPS technique probes a region of $\approx 2\,\mathrm{nm}$ below the NW surface, such native oxide layers ought to leave a clear fingerprint in the XPS spectra. Accordingly, Fig. 5.2a shows that the photoemission signal from as-grown GaAs NWs at a binding energy of $\approx 1.5\,\mathrm{eV}$ above the $\mathrm{Ga_{GaAs}}$ 3d that can be assigned to the existence of $\mathrm{Ga_2O_3}$. Similarly, the photoemission signal at a binding energy of $\approx 3.5\,\mathrm{eV}$ above the $\mathrm{As_{GaAs}}$ 3d core level is attributed to the formation of $\mathrm{As_2O_3}$ [266]. In comparison, for XPS spectra of GaAs nanowires treated with HCl-solution, both $\mathrm{Ga_2O_3}$ and $\mathrm{As_2O_3}$ signals are reduced tremendously with the small remaining signal probably caused by renewed oxidation during sample transfer through ambient atmosphere. Fig. 5.2c further shows that the O 1s signal is reduced tremendously after the HCl-solution treatment. These spectra hence demonstrate that the HCl solution treatment is highly effective in removing the native oxide layer present on the surface of as-grown nanowires. For clarification, the untreated (as grown) and HCl-solution treated GaAs NWs were referred as *o*-GaAs NWs and *e*-GaAs NWs, respectively.

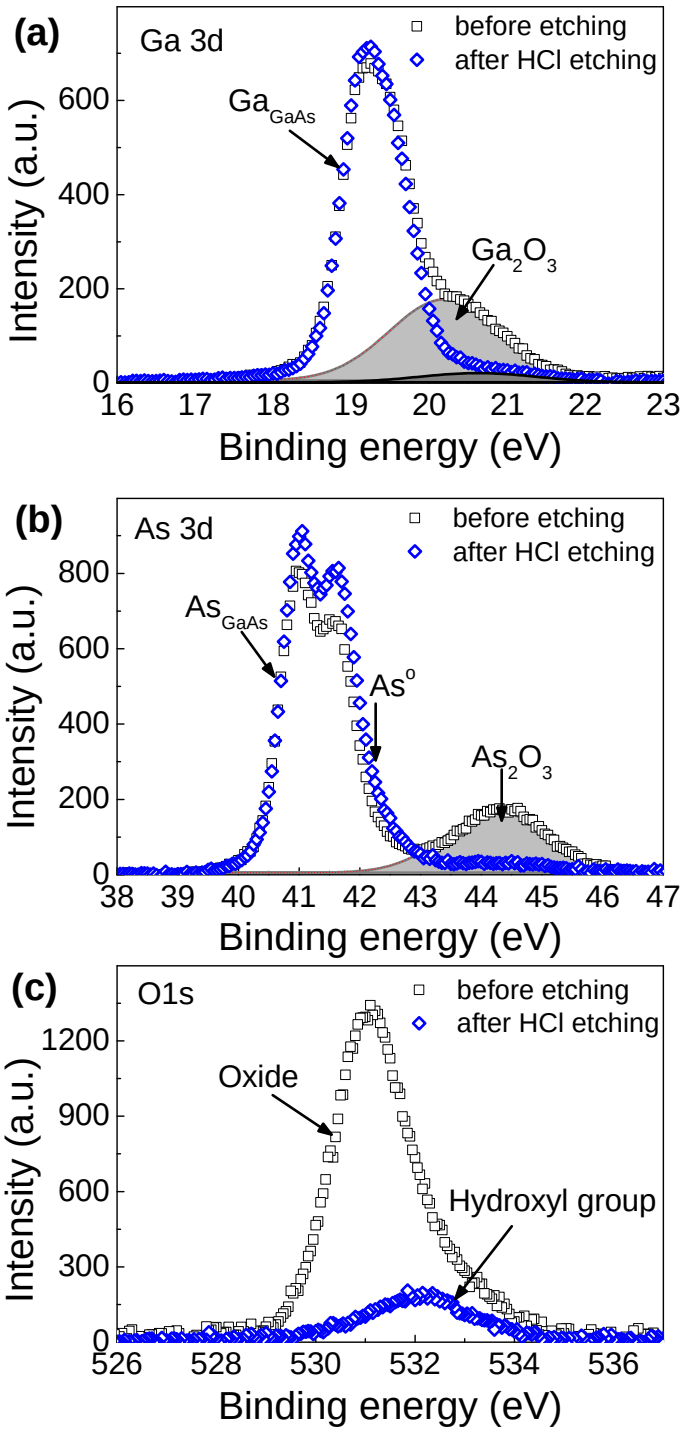

Figure 5.2: XPS spectra of GaAs nanowires before (as grown) and after etching with HCl solution, detected at the binding energy corresponding to (a) Ga 3d, (b) As 3d and (c) O 1s core energy levels. All XPS measurements were taken at a base pressure of $< 10^{-9}$ mbar and at room temperature.

In further analysis, the ratio of the integrated emission intensities of the As_{GaAs} 3d and Ga_{GaAs} 3d peaks was extracted. This ratio was found to increase by 8% after the HCl-solution treatment. In addition, the As_{GaAs} 3d signal is broadened at the high binding energy edge, which can be attributed to the presence of elemental As° on the surface of nanowires [266].

5.3.2 Fermi-level Position at the Surface of GaAs Nanowires

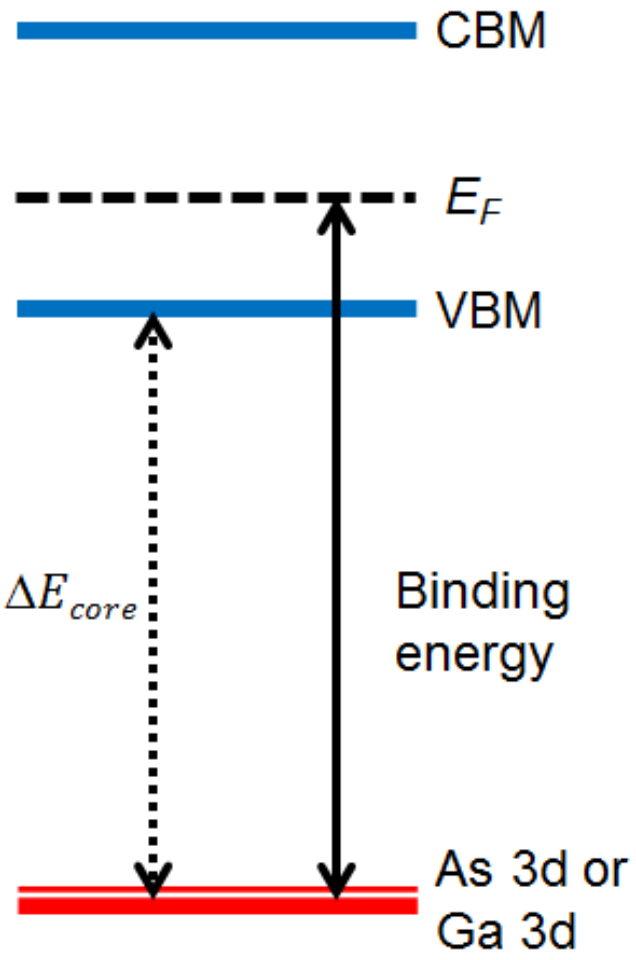

Figure 5.3: Schematic diagram illustration of the energetic level position of core level, VBM, E_F and CBM.

The Fermi-level (E_F) position near the surface of the GaAs nanowires can be calculated from XPS spectra. Here, the Ga_{GaAs} 3d and As_{GaAs} 3d core level regions recorded probe the surface of the wires to a depth of ≈ 2 nm. It has been shown that the binding energy

difference (ΔE_{core}) between Ga_{GaAs} 3d (As_{GaAs} 3d) and the VBM is 18.8 eV (40.7 eV) [267]. The binding energy of Ga_{GaAs} 3d and As_{GaAs} 3d levels for both as-grown (*o*-GaAs) and etched (*e*-GaAs) nanowires were measured to be 19.3 eV and 41.2 eV respectively, as seen in Fig. 5.2. Since the binding energy of the photoelectrons is a measure of the gap between the core level and E_F. The difference between the binding energy and ΔE_{core} is therefore equivalent to Fermi-level E_F, as schematically shown in Fig. 5.3. This suggests the E_F position at the nanowire surface is located ≈ 0.5 eV above the VBM.

Hence, the active surface-sites of GaAs NWs are electron-deficient in chemical character. It should be noted that the peak positions of Ga_{GaAs} 3d and As_{GaAs} 3d do not change after the surface treatment, suggesting the E_F-pinning near the surface remains unchanged after the HCl-solution treatment, as previously observed [268]. Such E_F-pinning below the midgap in GaAs has been attributed to the formation of donor states across the bandgap caused by the presence of excess As and an oxide layer [120, 269]. Since the nanowires under investigation here were grown under As-rich conditions [226], such surface-defect states are highly likely to be present near the nanowire surface. Therefore, the nanowires under investigation are characterized by the presence of chemical surface defects that render the NW surface *p*-type and present a significant trapping cross section to charge carriers.

5.3.3 Ultrafast PL Dynamics in GaAs Nanowires

In order to investigate the charge carrier dynamics in GaAs nanowires, time-resolved PL measurements were conducted at a substrate temperature of 10 K. The samples were excited at a photon energy of 1.68 eV and the PL emission dynamics were monitored near the band edge of the GaAs NWs ($E_g = 1.52$ eV). The excitation density (1.61×10^{17} cm^{-3}) was kept low in order to prevent PL quenching via carrier-carrier annihilation [29]. While the exciting photon energy is far below the bandgap energy of the polymers used in this study, photoexcitations may still be generated in the polymer to some extent by weak two-photon absorption processes.

However, the PL signal originating from such two-photon transitions in the polymer

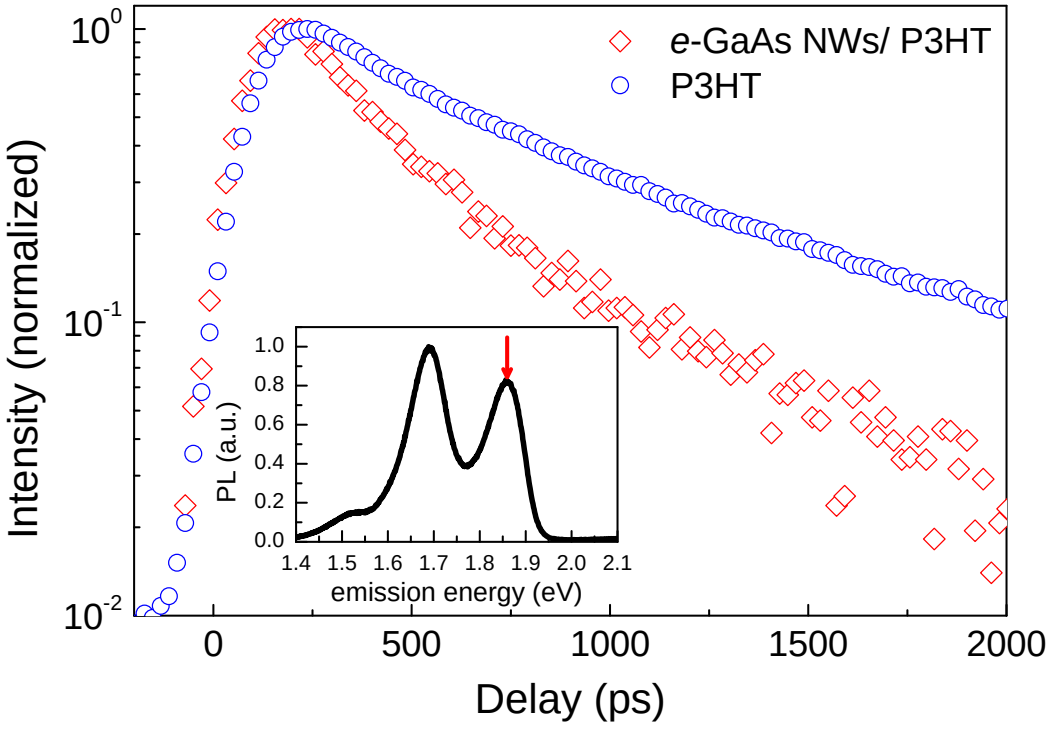

Figure 5.4: Time-resolved PL recombination of P3HT (blue circle) and *e*-GaAs NWs/P3HT (red diamond) measured at the emission energy of 1.87 eV, following an excitation at energy 1.68 eV. The substrate temperature is held at 10 K. These data were detected with a photomultiplier coupled to a Becker & Hickl time-correlated single photon (TCSPC) card, which gave an overall time resolution of about 200 ps. The inset shows the PL spectrum of a P3HT film excited at an energy of 3.1 eV. The red arrow indicates the energy at which the time-resolved PL was probed.

is rather weak, as compared with the PL emerging from direct excitation of GaAs NWs, and further quenched in the presence of GaAs NWs, as seen in Fig. 5.4. The quenching of PL decay is attributable to the exciton migration and dissocation at the interface of GaAs/P3HT. However, the non-optimized thickness of the polymer film renders the PL quenching to be rather slow [216, 270].

Fig. 5.5a shows the time-resolved PL spectra collected for *e*-GaAs NWs following excitation at 1.68 eV. At early time after excitation, the spectra are blue-shifted and broadened, compared with the spectra collected at later time delay, due to hot-carrier cooling toward the band edge of GaAs, as shown in Chapter 4. Emission spectra collected from the *e*-GaAs NWs/P3HT sample are identical to those collected from bare (uncoated) *e*-GaAs NWs, as seen in Fig. 5.5b. The PL for the *e*-GaAs NWs/P3HT sample is thus mainly dominated by

GaAs NWs and no significant contribution to the photoluminescence originates from P3HT within the spectral region of the GaAs emission (≈1.45–1.57 eV). This observation clearly suggests that the PL spectra from NW/polymer blends are dominated by emission from the GaAs nanowires at energies below 1.60 eV and the PL signal recorded at the photon energy of 1.52 eV hence corresponds to the GaAs NWs band edge emission.

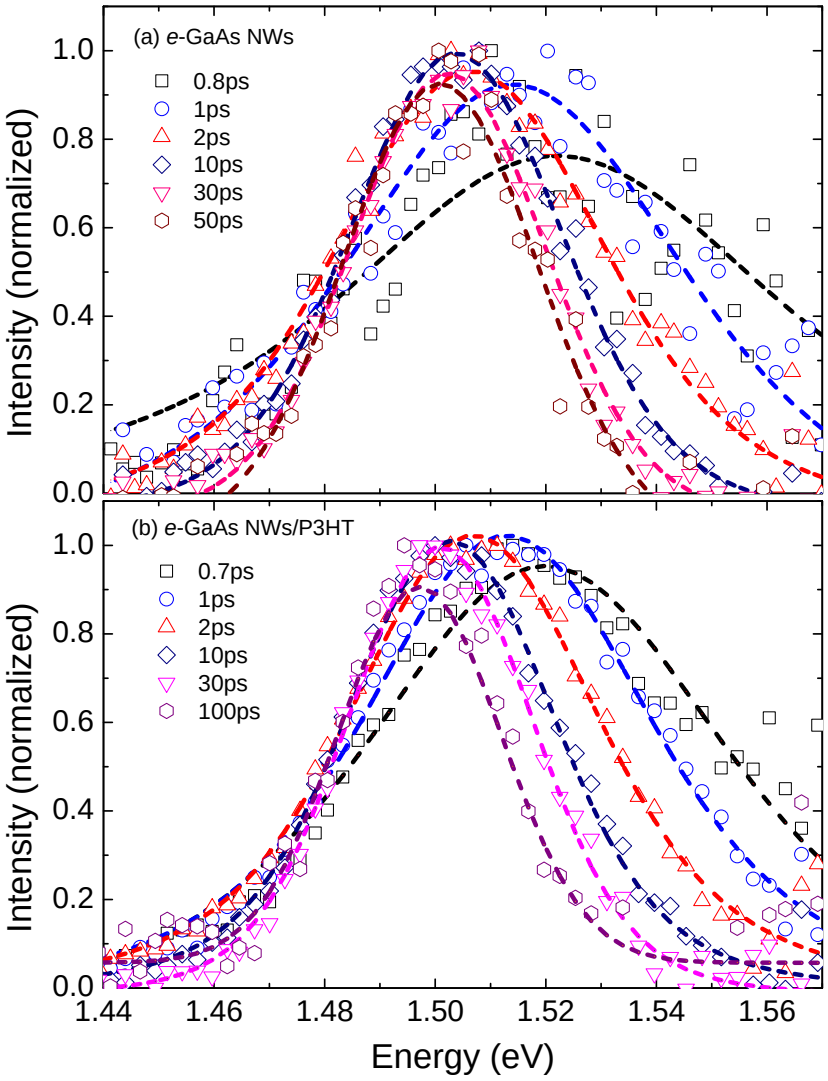

Figure 5.5: Time-resolved PL spectra of (a) *e*-GaAs NWs and (b) *e*-GaAs NWs/P3HT following excitation at 1.68 eV. At later times after excitation, the PL spectra are broadened by the spectral resolution of the system (32 meV, as limited by the high time resolution) and nanowires inhomogeneities.

Fig. 5.6 shows the transient PL of untreated *o*-GaAs NWs. The PL lifetime was extracted from a single exponential fit to be 46.5 ps for *o*-GaAs NWs. The short PL lifetime in bare (uncoated) GaAs nanowires is caused by a dominant non-radiative decay channel originating

from charge trapping at surface-defect states [26, 29], as also discussed in detail in Chapter 4. Following chemical etching which removes the surface native oxide, the PL lifetime of the *e*-GaAs NWs shows a marginal increase (52.1 ps), as displayed in Fig. 5.6. This suggests that for etched GaAs NWs, charge-carrier dynamics are still largely dominated by surface-defect states, in agreement with the observation from XPS measurements that the Fermi level near the surface remains unchanged upon etching.

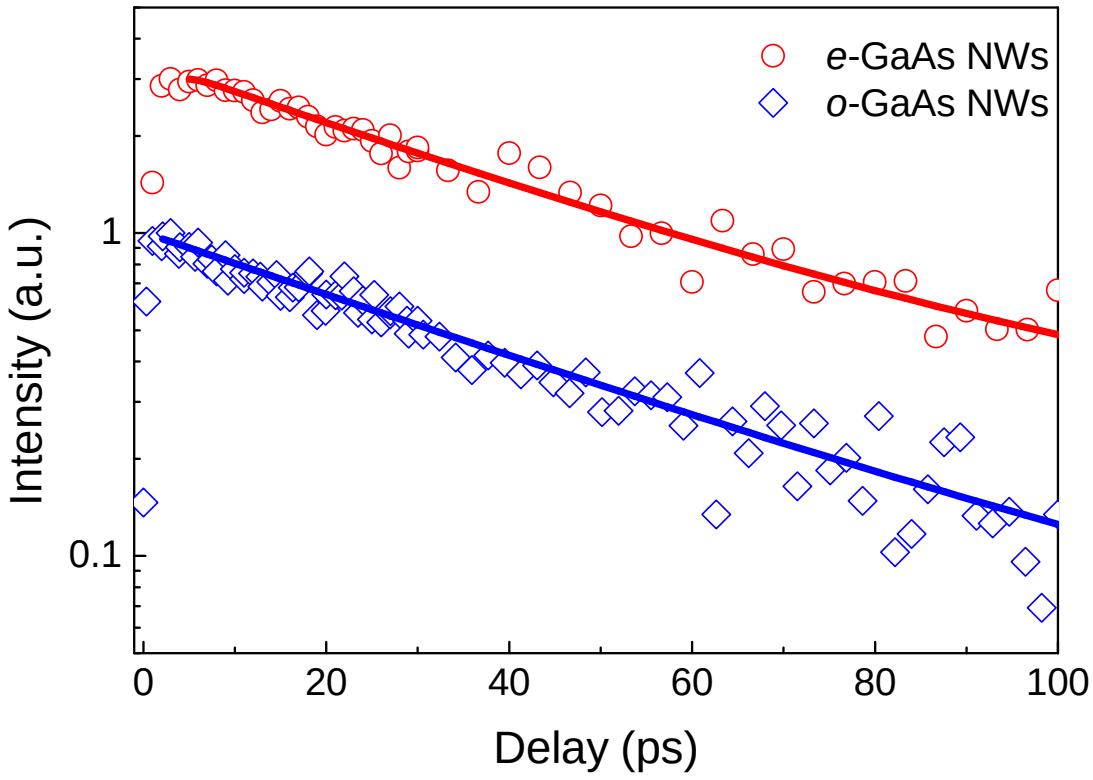

Figure 5.6: PL transients of untreated (*o*-) and etched (*e*-) GaAs NWs measured at the emission energy of 1.52 eV, close to the band edge of GaAs at 10 K. The solid lines are the output of fitting these data with single-exponential decay functions.

For a control experiment, the *e*-GaAs NWs were blended with F8BT to form a hybrid type-I heterojunction (Fig. 5.1). In this case, charge-injection from GaAs NWs into F8BT should be blocked by the higher bandgap and type-I band alignment with respect to F8BT. Fig. 5.7 shows the transient PL decay traces of *e*-GaAs NWs and *e*-GaAs NWs/F8BT film samples. The initial slow rise observed in *e*-GaAs NWs/F8BT can be attributed to the ultrafast energy transfer from F8BT to the nanowires owing to its higher bandgap. However, the long-term emission rate of *e*-GaAs NWs in the F8BT matrix is similar to that in the bare

(uncoated) *e*-GaAs NWs. This suggests that in presence of an F8BT overcoat, charge-carrier recombination is still dominated by ultrafast trapping at surface defect states.

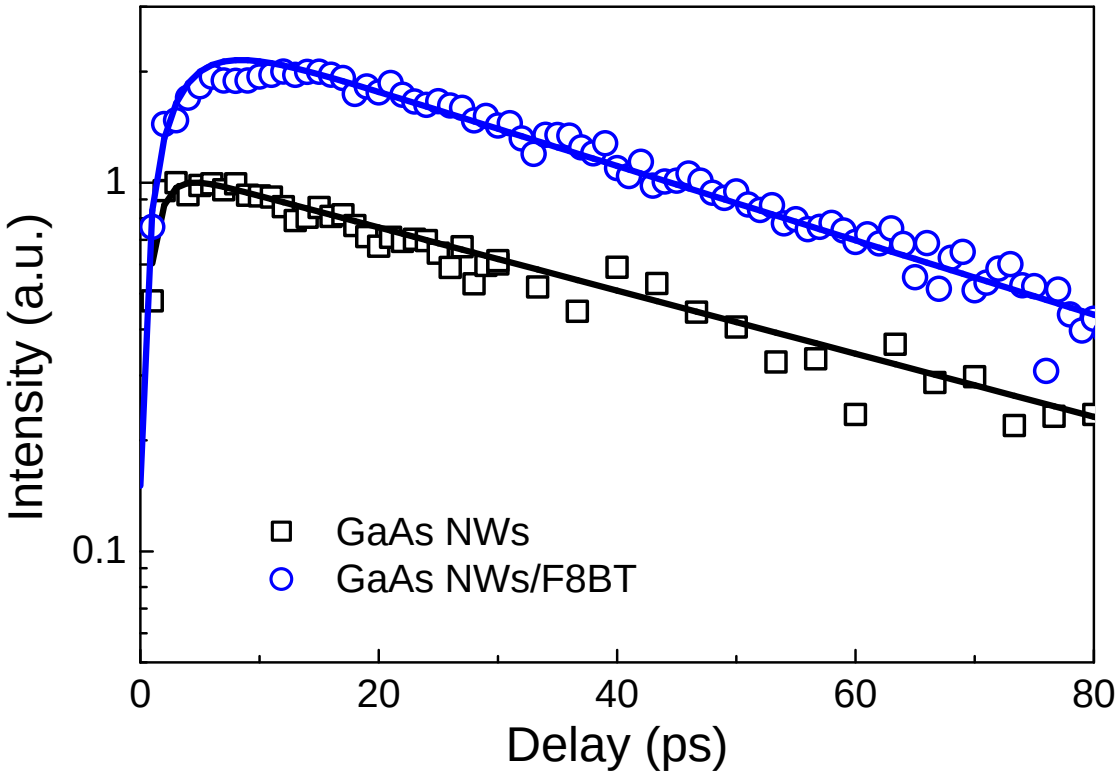

Figure 5.7: Transient PL decay traces of *e*-GaAs NWs and *e*-GaAs NWs/F8BT following excitation at an energy of 1.68 eV at 10 K. The PL transients are measured at the emission energy of 1.52 eV, which corresponds to the bandgap of the GaAs NWs.

To investigate the carrier dynamics at a range of type-II heterojunctions, the GaAs nanowires were blended with P3HT, MEH-PPV, G2 or PCBM. It has been generally observed that charge-transfer across the interface of type-II heterojunctions reduces the PL lifetime of the charge-donating material [16, 17, 216]. Fig. 5.8a shows the PL dynamics observed in *o*-GaAs NWs/polymer heterojunction blends. Fast PL quenching is observed when *o*-GaAs NWs are blended with P3HT, MEH-PPV and G2. This is attributable to hole transfer from GaAs NWs to the adjacent polymer layers, in accordance with their energetic level alignment shown in Fig. 5.1. However, when these untreated nanowires are blended with PCBM, the PL recombination rate remains essentially unchanged from the PL observed in bare *o*-GaAs NWs. These data demonstrate that electron transfer from untreated GaAs NWs into the surrounding organic semiconductor is significantly slower than hole-transfer.

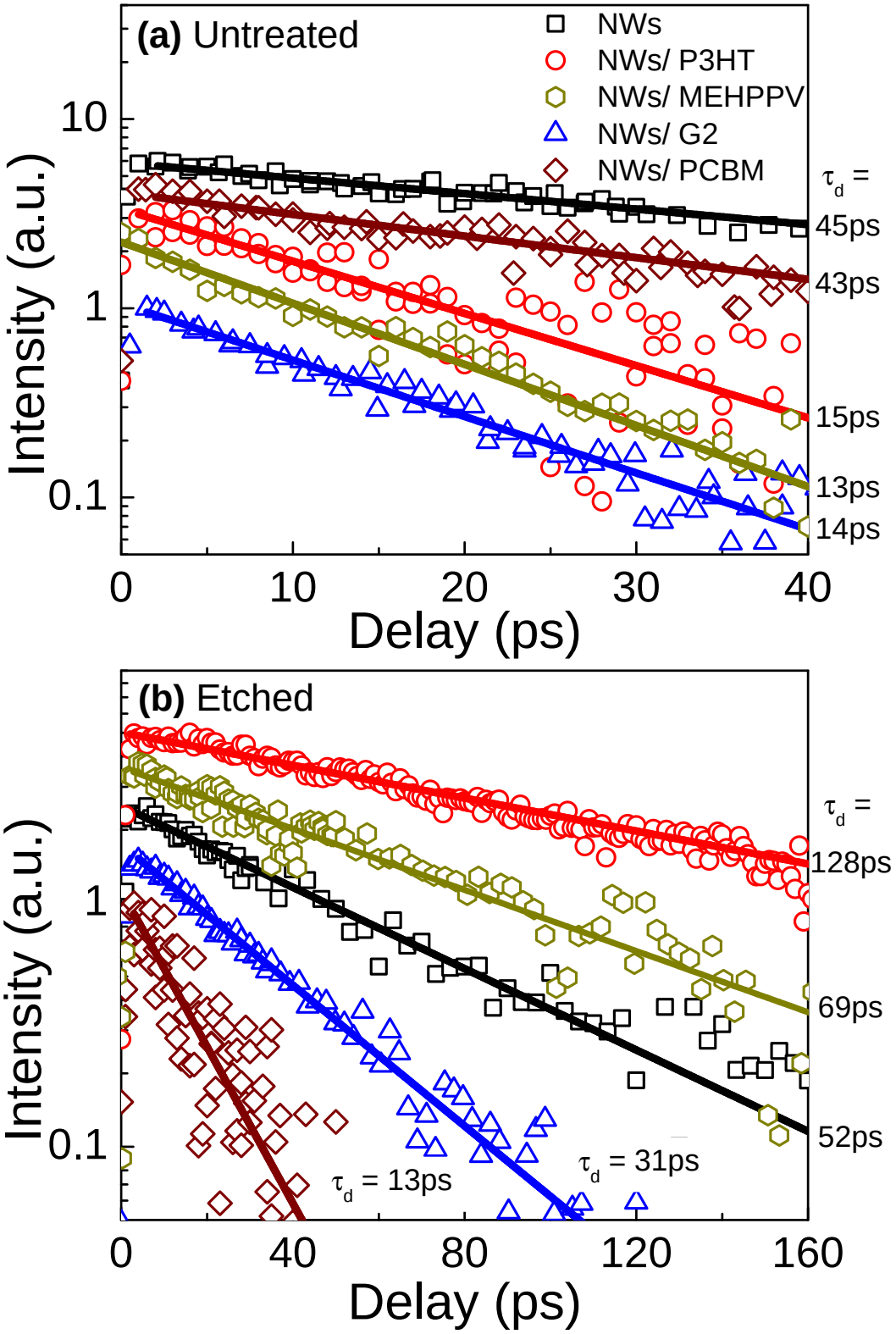

Figure 5.8: PL transients of (a) untreated (*o*-) and (b) etched (*e*-) GaAs NWs and their blends with a range of organic semiconductors, measured at the emission energy of 1.52 eV, close to the band edge of GaAs at 10 K. The solid lines are the output of fitting these data with single-exponential decay lifetime (τ_d).

Fig. 5.8b shows the contrasting PL dynamics for GaAs NWs that have been etched with HCl solution prior to being embedded in the same series of organic semiconductors. The PL dynamics appear more complex and are strikingly different from those observed for NWs covered in a native oxide layer. For *e*-GaAs NWs/PCBM heterojunction, nanowire PL quenching is now observed in accordance with efficient electron transfer from the NWs into PCBM. This result is to be expected given that the removal of the native oxide layer on the surface of the nanowires ought to facilitate charge transfer across the NW/PCBM interface. Surprisingly however, the PL decay becomes slower following etching for *e*-GaAs NWs blended with G2, MEH-PPV or P3HT. Fig. 5.8b reveals that charge pair lifetimes in *e*-GaAs NWs blended with P3HT and MEH-PPV are even longer than those for bare (uncoated) *e*-GaAs NWs. Interestingly, the greatest PL lifetime enhancement is observed for the *e*-GaAs NWs blended with P3HT, which has the lowest *IP* of the polymers use in this study. These data suggest that following the removal of the native oxide layer, charge transfer across the *e*-GaAs NWs/polymer type-II heterojunctions becomes strongly dependent on the alignment between the relevant energy levels in the polymer and the NWs.

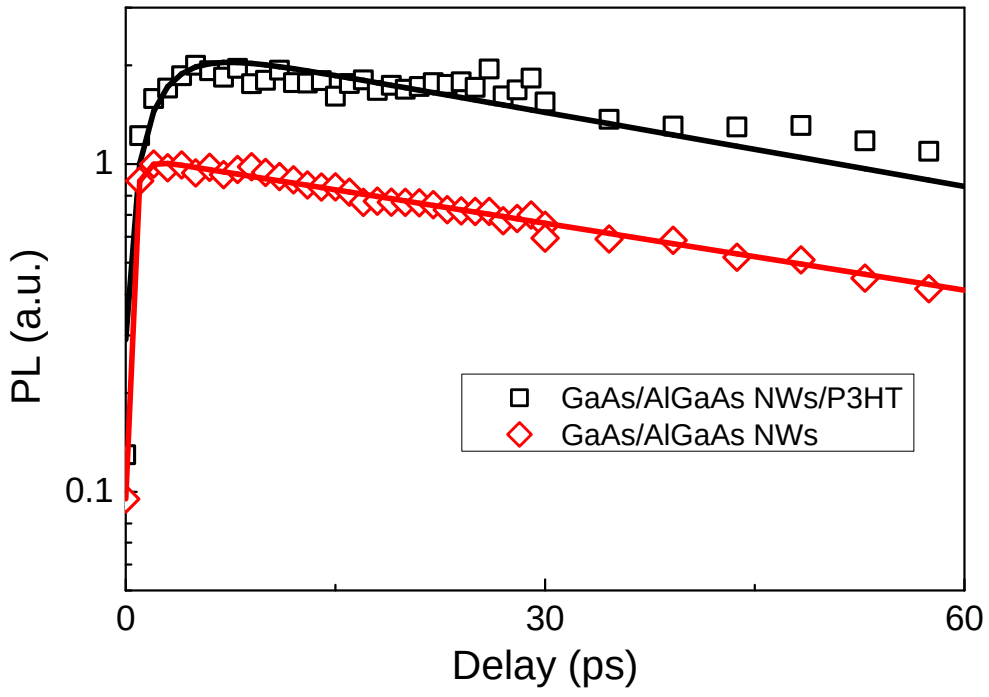

Figure 5.9: Transient PL decay traces of core-shell GaAs/AlGaAs NWs and GaAs/AlGaAs NWs/P3HT following excitation at 1.68 eV, measured at 10 K. The PL is detected at an emission energy of 1.52 eV, which corresponds to the bandgap of GaAs.

As a further control experiment Fig. 5.9 shows the transient PL of GaAs NWs overcoated with a 30 nm-thick AlGaAs layer in the absence (GaAs/AlGaAs NWs) and presence (GaAs/AlGaAs NWs/P3HT) of a P3HT overcoat. The PL decay rate remains unchanged upon coating these core-shell nanowires with P3HT, i.e. the carrier trapping in GaAs/AlGaAs NWs is not affected by the presence of the polymer. The thick overcoat of AlGaAs hence appears to suppress charge doping and surface passivation by the polymer, as well as any photoinduced charge separation.

5.3.4 Surface State Filling Effects

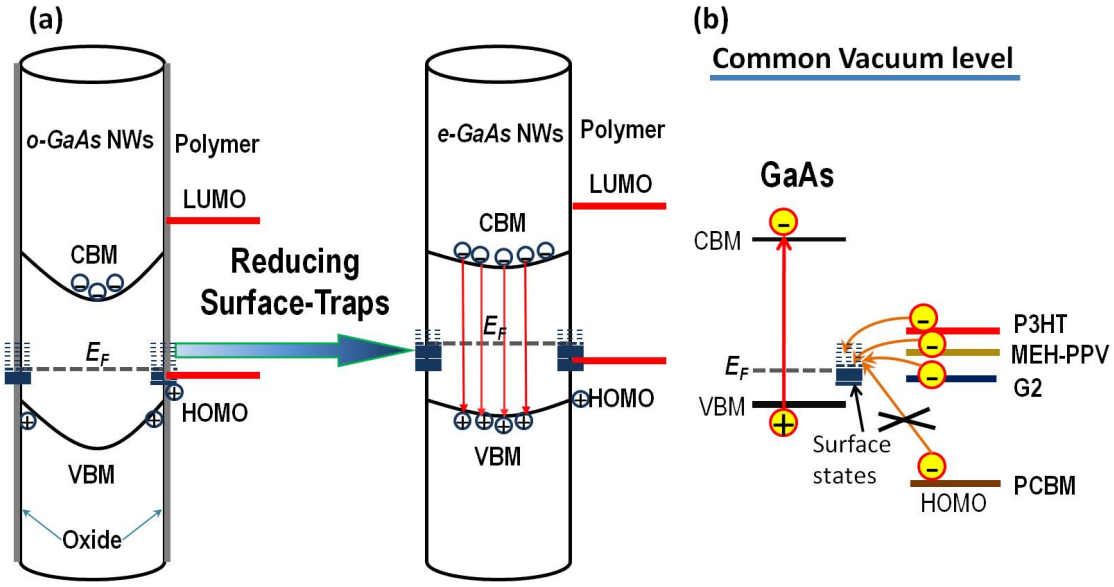

Figure 5.10: Schematic diagram illustrating the energy level alignment at the GaAs NW/organic semiconductor interface: (a) Schematic depicting band-bending effects across the nanowire cross section for *o*-GaAs NWs/polymer (left) and *e*-GaAs NWs/polymer (right) heterojunctions. For oxidized *o*-GaAs NWs the unpassivated surface leaves a p-doped surface that results in bending of the conduction (CB) and valence (VB) bands, while for *e*-GaAs NWs, charge injection from the polymers effectively passivates surface defects which leads to a flattening of the bands. (b) Common vacuum level picture indicating the passivation of NW surface states through electron transfer from the HOMO levels of P3HT, MEH-PPV or G2.

The complex charge carrier dynamics observed for the NW/organic semiconductor blends can be directly related to the modification of surface states density in the NWs by the organic semiconductor overcoating. The charge lifetime in the nanowires is altered by the surround-

ing organic semiconductor through two distinct mechanisms. First, the organic semiconductor offers a charge transfer pathway to photoexcitations generated in the nanowires, and second, it may passivate surface defect states in the GaAs NWs and hence eliminate charge trapping. The resulting changes in charge carrier lifetime in the nanowires can hence be understood quantitatively considering the surface band-bending in the NWs, as illustrated in Fig. 5.10a and explained in the following. XPS measurements reveal that the surface defect states in the uncoated nanowires are electron-deficient in chemical character and give E_F-pinning below the midgap of GaAs. The resulting negative electric field at the surface bends the conduction and valence bands upward in energy, which spatially separates the electron and hole populations in the nanowires with holes accumulating near the surface and electrons near the center of the nanowires to maintain charge neutrality [120, 124, 271]. Under low intensity photoexcitation, holes can be driven to the surface of the nanowires by the built-in electric field while the electrons remain in the bulk of the nanowires, as illustrated in Fig. 5.10a (left). Hence, the transfer of holes from the NWs into a surrounding material is expected to be much faster than the transfer of electrons which are inhibited by the surface potential barrier from reaching the surface. This scenario appears to be entirely consistent with the charge carrier dynamics observed in oxidized GaAs NW embedded in organic semiconductors (Fig. 5.8a). In the presence of $\approx 1\,\text{nm}$ thick layer of native oxide, electron transfer from the *o*-GaAs NWs to PCBM is undetectably slow, while hole transfer to the MEH-PPV, G2 or P3HT polymers is fairly rapid. Consequently, the photoinduced charge transfer dynamics across the interface between the oxidized GaAs NWs and an organic semiconductor is governed by band-bending effects and cannot be portrayed within the simple picture of energetic offset across the interface under flat-band conditions.

However, once the surface of the GaAs NWs has been etched in order to remove the native oxide layer, significant changes are found to occur in the observed NW PL dynamics. Fig. 5.8b demonstrates that removal of the NW surface oxide results in increased electron injection into PCBM and decreased hole injection into the polymers MEH-PPV, G2 or P3HT surrounding the NWs. The increased electron injection rate into PCBM is clearly expected given that an insulating oxide barrier has now been removed between the GaAs

NW and the PCBM overcoat. However, following overcoating with conjugated polymers, contrary to expectation, a lengthening of charge carrier lifetimes is now observed in etched NWs in comparison to overcoated oxidized NWs. In particular, embedding the etched NWs in semiconducting polymers with the lowest ionization potential (e.g. P3HT and MEH-PPV) is found to increase the lifetime of the PL emitted from the NWs with respect to that in uncoated NWs (Fig. 5.8b). Chapter 4 has demonstrated that the PL dynamics from GaAs NWs is governed by strong charge trapping effects that have been shown to result from the presence of a high density of surface defects in the GaAs NWs. [26, 29] Such charge trapping at surface states effectively competes with charge transfer from the nanowires into the organic semiconductor coating. Hence, the PL lifetime enhancement observed in GaAs NWs, as shown in Fig. 5.8b, demonstrates that once the native oxide layers on the surface of NWs have been removed, the direct contact between the semiconducting polymer and the NWs must have reduced the surface states available for charge-trapping. Such surface-defect passivation will reduce the extent of surface band bending as the Fermi energy near the surface is lifted towards the VBM of GaAs [120, 124, 271, 272]. This scenario is illustrated schematically in Fig. 5.10b: bringing an organic semiconductor with suitable *IP* into contact with the etched nanowire will lead to an initial electron injection into the NW until equilibrium is reached. This process leads to a reduction of charge trapping at surface states and a flattening of the bands, which in turn modifies the transfer of charges photogenerated inside the nanowires into the surrounding semiconductor. In particular, data in Fig. 5.8b suggest that photoexcited holes in the etched nanowires experience slower transfer across the interface than in the absence of surface passivation. This is most likely so because holes are now to a lesser degree confined near the nanowire surface, however, the modification of the available density of states in the polymer following charge injection into NW surface states may also be a significant contributing factor.

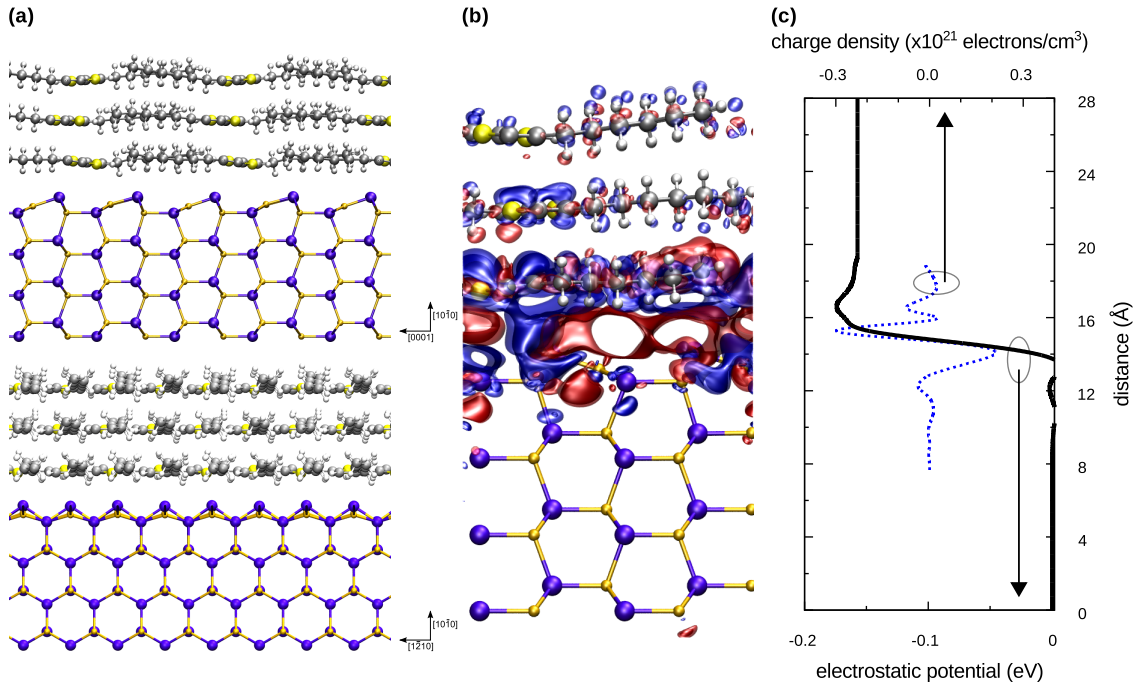

Figure 5.11: Density-functional theory modeling of the charge transfer at an idealized GaAs-P3HT interface. (a) Side views of the optimized and relaxed GaAs/P3HT interface with the P3HT backbone (top) and alkyl side chains (bottom) perpendicular to the page. The model comprises 4 layers of GaAs and 3 layers of P3HT (428 atoms). Atomic color code: Ga(violet), As(gold), O(red), S(yellow), C(grey) and H(white). (b) The isosurface of charge redistribution upon formation of the interface (isovalue: $\pm 6.75 \text{x} 10^{-3}$ electrons/Å^3 for red/blue), calculated as $n_{\text{GaAs/P3HT}} - [n_{\text{GaAs}} + n_{\text{P3HT}}]$, $n(\mathbf{r})$ being the electron density at the position $\mathbf{r}$. (c) Planar average of the charge redistribution (dotted black line) and corresponding electrostatic potential profile across the interface (solid blue line), as obtained by integrating Poisson's equation. See 5.2.5 for a detailed description of the computational methods used.

5.3.5 Density-Functional Theory Calculation

The emission lifetime enhancement observed upon overcoating the etched GaAs NWs with conjugated polymers suggests that this method is highly effective at passivating surface defects. To understand the interfacial charge transfer between GaAs NWs and polymers that induces this passivation, DFT calculations based on idealized GaAs/P3HT heterojunctions was performed by Keian Noori in the Guistino's group (Department of Materials, Oxford University). Fig. 5.11a shows the obtained optimized atomistic configuration of the P3HT layers on the GaAs surface. The observed degree of P3HT interdigitation is in line with both bulk values and calculated values reported for ZnO/P3HT interface [263]. Fig. 5.11b shows the isosurfaces of the charge-carrier re-distributions upon formation of the GaAs/P3HT in-

terface, with red (blue) regions indicating an increase (decrease) in electron density upon contact between the two materials. The GaAs/P3HT interface formation is followed by an overall electron transfer from P3HT to GaAs that is spread across a surprisingly narrow region around the interface. Fig. 5.11c shows the planar average of charge density re-distributions across the interface, which are found to be largely localized within $\approx 3\,\text{Å}$ of that interface. Integration of these planar charge density profiles via Poisson's equation reveals that the charge redistribution results in an electrostatic potential offset of $\approx 0.2\,\text{eV}$ within the $3\,\text{Å}$ around the interface. Such strong charge localization at the interface is consistent with previous experimental findings for materials with low electron permittivity, for which charge carrier interactions at the interface are predominantly electrostatic [18]. From the calculated charge redistribution, it appears that the surface of GaAs is degenerately doped at a charge carrier density of $\approx 1.2\times10^{13}\text{cm}^{-2}$, which corresponds to 0.07 holes per thiophene-ring on P3HT for the simulated chain arrangement shown in Fig. 5.11a. These results clearly suggest the feasibility of a δ-electron doping layer forming on the surface of GaAs after it has been coated with P3HT.

5.3.6 Discussion

Surface-doping has previously been demonstrated in both organic and inorganic semiconductors through the use of surface functionalization with polar molecules, which allow controlled enhancement of the charge conductivity near the surface [273–276]. For GaAs surfaces, monolayer coverage with electron-donating reagents [30] or polar molecules [124] has been shown to effectively reduce the surface recombination velocity via charge-transfer to the unsaturated surface-states [271]. In contrast, bulk doping of GaAs has been found to be fairly ineffective for passivating surface-defect states, in particular for high-quality n-doped GaAs, because of the formation of surface acceptor states by a self-compensation mechanism [123]. The results show that functional conjugated polymers, such as P3HT, can be highly effective electron-donating reagents for inorganic semiconductors as they appear to induce a δ-electron doping layer on the surface of GaAs. Since the active surface-states of

the nanowires investigated here are electron-deficient in chemical character, electron-doping will be essential to reduce the unsaturated surface-states density.

To quantify the extent to which surface-defect passivation occurs for the different organic semiconductors used as overcoats, PL recombination rates (k_{d}) of the GaAs NW emission were extracted from the data shown in Fig. 5.8. The results of single-exponential fitting procedures are shown in Fig. 5.12 which displays the extracted decay rate constants as a function of energy level alignment parameter Δ_{IB} and *IP* for bare-GaAs NWs and for GaAs NWs blended with P3HT, MEH-PPV and G2. Here, Δ_{IB} is the difference between the nominal valence band maximum VBM_{GaAs} of bulk GaAs (5.6 eV) and the HOMO level of the surrounding polymer when aligning their vacuum level.

For heterojunctions formed between oxidized *o*-GaAs NWs and polymers, the PL recombination rate k_{d} falls into the range of $0.065 - 0.071\,\mathrm{ps}^{-1}$ and shows no dependence on Δ_{IB}. This result is thus in accordance with the 1 nm-thick layer of native GaAs oxide preventing charge exchange between the two materials upon contact, leaving the surface traps on the GaAs NWs unpassivated. As a result, the PL recombination dynamics are governed by charge trapping at surface sites as previously observed[29] and additional photoinduced injection of holes localized near the NW surface into the polymer (see Fig. 5.10b, left) as discussed above. However, such photoinduced hole transfer appears to be independent of Δ_{IB}, which is expected given the large energetic offset at the interface (compared with the exciton binding energy of 4.5 meV in GaAs), the band-bending near the surface of nanowires that favors the hole-transport to the interface (Fig. 5.10a) and the large variety of hole acceptor states available in the polymers [277].

In marked contrast, the PL recombination rate k_{d} for *e*-GaAs NWs coated with conjugated polymer is significantly lower than that observed in *o*-GaAs NWs/polymer heterojunctions and decreases concomitantly with the increase of Δ_{IB} across the heterojunctions. Strikingly, the emission lifetime for *e*-GaAs NWs increases (lower k_{d}) when these nanowires are coated with either P3HT or MEH-PPV in accordance with effective passivation of NW surface trap states. Linear extraploation of the data (see dashed line in Fig. 5.12) reveals

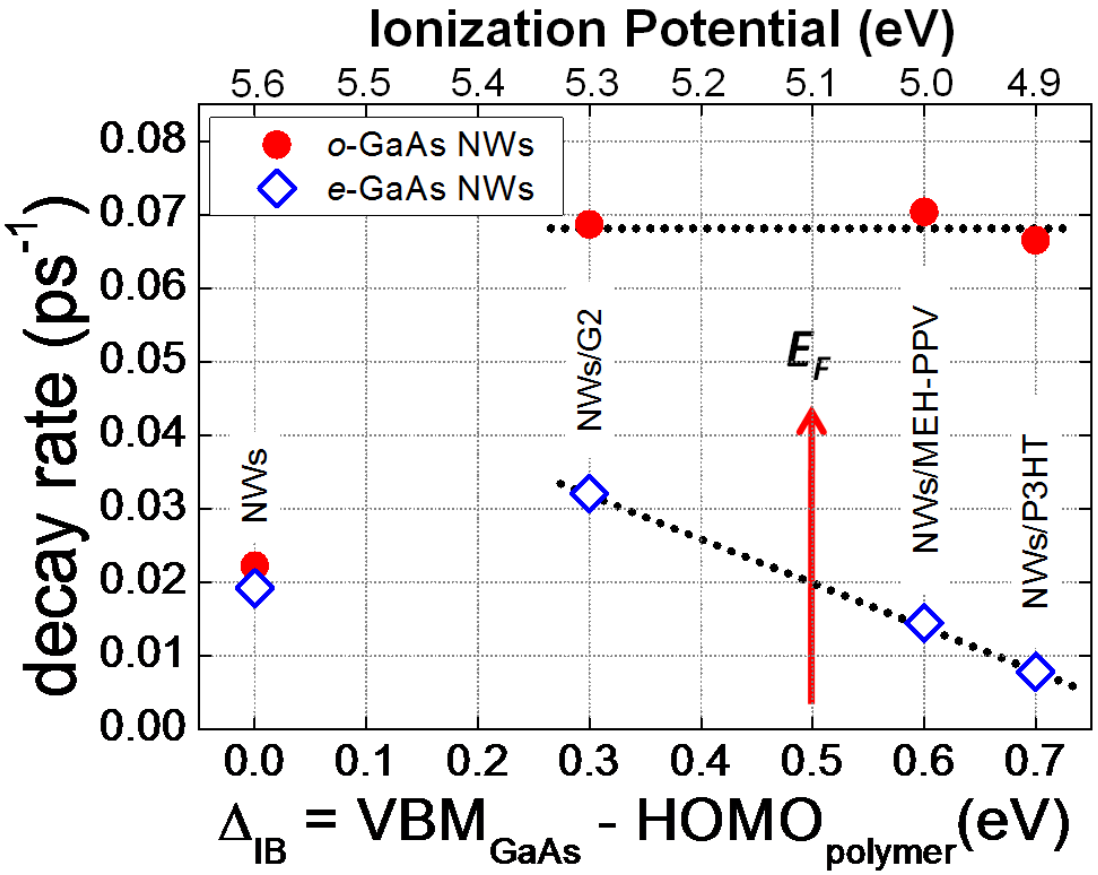

Figure 5.12: The PL recombination rate (k_{d}) of *o*-GaAs NWs (full circles) and *e*-GaAs NWs (empty diamonds), uncoated or as part of a heterojunction with different polymers, as extracted by mono-exponential fitting to the corresponding PL decay traces shown in Fig. 5.8. k_{d} values are shown as a function of the ionization potential *IP* (top axis), where the *IP* for the polymer is used for NW/polymer heterojunctions and the *IP* of bulk GaAs is used for bare (uncoated) NWs. The bottom axis (Δ_{IB}) shows the same scale as the top axis, but with the *IP* of bulk GaAs (5.6 eV) subtracted in order to indicate the dependence of (k_{d}) on the *IP* offset between the two materials, as expected from common vacuum level considerations. The red-arrow indicates the Fermi level E_F position on the surface of bare NWs (5.1 eV) as inferred from XPS measurements. The dotted-lines are guide-to-the eyes.

that, for $\Delta_{\mathrm{IB}} > 0.5\,\mathrm{eV}$ (corresponding to a polymer $IP < 5.1\,\mathrm{eV}$), the recombination rate of these type-II heterojunction falls below the recombination rate observed in bare NWs. Interestingly, this value also corresponds to the Fermi level position E_F near the surface of the GaAs NWs, which XPS measurements showed to lie 0.5 eV above the the VBM_{GaAs} (VBM_{GaAs}=5.6 eV for bulk GaAs at 10 K [238]). This plot therefore confirms that the carrier lifetime enhancement observed in *e*-GaAs NWs/polymer heterojunctions is directly related to the filling of unsaturated nanowires surface states via electron doping from the HOMO of the π-conjugated polymer with the efficacy of the mechanism depending on the *IP* of the polymer, as shown in Fig. 5.10b. In accordance with DFT calculations, an interface dipole is formed concomitantly to lower the HOMO level of the polymer until the system attains equilibrium and further charge flow across the interface ceases. Hence, the semiconducting polymer with the lowest *IP* should give the highest surface-state-filling, which is consistent with the data shown in Fig. 5.12. Furthermore, the calculations suggest that this δ-electron doping layer is largely localized in the close vicinity of the interface ($\approx 3\,\text{Å}$). Accordingly, the presence of $\approx 1\,\mathrm{nm}$ native oxide on the surface of the nanowires is sufficient to prevent such passivation of defect-states, as is the deposition of a 30 nm-thick layer of AlGaAs on top of the GaAs nanowire core prior to polymer coating (see Fig. 5.9). Effective defect passivation of inorganic semiconductors with conjugated polymers thus requires both the correct choice of ionization potentials and sufficiently barrier-free interfaces to allow charge equilibration between the two components.

Such observations raise the question of how surface doping and sample morphology affect the expected photovoltaic device performance. The strong localization of such doping effects near the interface, with most changes in the polymer occurring within the first monolayer at the interface, and the clear correlation with polymer *IP*, suggest that energy level alignment is the dominant factor in determining the interfacial charge dynamics for this system. The extent of molecular ordering in the organic semiconductor, which varies strongly between the investigated materials[145, 146, 252–256], hence appears to play a less important role. However, molecular ordering is likely to have significant effects on the initial exciton diffusion and subsequent charge collection through the organic semiconductor, which is not

investigated here but has a strong impact on the overall device performance of hybrid photovoltaic cells.[252]. As far as the overall light-harvesting is concerned, this study shows that surface doping prolongs the lifetime of excitations in the nanowires, but it also appears to slow charge transfer across the hybrid interface, possibly due to a combination of reduced band-bending and changes in the density of states in the charge-injecting organic. For use of these materials in photovoltaic devices, this means that the change in overall charge injection efficiency from nanowires into the organic may be small. However, such reduced charge transfer across the interface will also reduce recombination at a later stage. In addition, the reduction in charge trapping will allow better charge collection along the nanowires. Hence, the overall effect is likely to enhance the device efficiency and further investigations of charge transport and recombination dynamics based on complete hybrid photovoltaic devices are needed to explore such effects in the future.

5.4 Conclusion

In conclusion, this study provides direct evidence for an effective passivation of surface defect states in GaAs nanowires through overcoating with conjugated polymers that establish a type-II heterojunction. Upon removing the native oxide layer from the surface of the nanowires, strong carrier lifetime enhancement for GaAs NWs overcoated with certain π-conjugated polymers was clearly observed from time-resolved PL measurements. This effect is attributed to δ-electron-doping from the polymers to the surface of GaAs NWs, which reduces the unsaturated surface-state density. Quantitative analysis of the PL decay traces for all investigated heterojunctions reveals that the carrier-lifetime enhancement depends critically on the *IP* of the polymers: PL lifetime enhancement is only observed for nanowires blended with conjugated polymers whose *IP* is lower than the workfunction of the nanowires. These observations suggest that electron-injection from the HOMO of the polymer into the energetically lower lying surface states of the GaAs nanowires readily occurs during the formation of a hybrid type-II heterojunction until the system comes to an equilibrium. While the picture that emerges superficially resembles that of a metal-semiconductor

Schottky-contact [120], a fundamental difference is the strong localization of passivating dopant carriers near the GaAs/polymer surface: DFT calculations reveal that such doping is predominantly limited to the top-most layers near the surface ($\approx 3\,\text{Å}$) and an interface dipole is formed concomitantly to lower the HOMO level of the π-conjugated polymer until the system attains equilibrium. Hence, when the surface of nanowires is covered by native oxide layer of thickness $\approx 1\,\text{nm}$, such surface doping of the nanowires becomes inhibited. The result of this chapter thus demonstrates that in nanowire/conjugated polymers type-II hybrid blends, the polymer can perform the dual function of hole transporter and nanowire surface passivating agent. The removal of native oxide on the surface of the nanowires and the use of polymers with sufficiently small *IP* are essential in order for effective trap passivation to occur. These findings are important for the design and implementation of new blend materials for hybrid photovoltaic devices and nanoscale photodetectors.

Chapter 6

Direct Observation of Carrier Heating in Type-II WZ-ZB InP Nanowire Heterojunctions

Carrier cooling after non-resonant photoexcitation in semiconductor nanowires is crucial for practical nanodevices. In-particular, semiconductor type-II heterojunctions have been widely constructed in various optoelectronic devices. Here, time-resolved photoluminescene measurements were conducted to understand the carrier cooling dynamics in InP nanowires containing wurtzite and zinc-blende phases that form type-II heterojunctions along the growth axis of the nanowires. Following non-resonant photoexcitation, the photoluminescence measurements reveal that while the photoinjected electron-hole pairs are rapidly separated across the wurtzite-zinc blende type-II heterojunctions in 12 ps – 33 ps, the intraband carrier cooling is reduced by orders of magnitude during the spatial charge transfer. Pump-intensity-dependence studies demonstrate that the carrier cooling rate is reduced as the injection density and charge transfer rate are increased. These effects are attributed to the buildup of non-equilibrium phonons induced by the spatial charge transfer across the WZ-ZB type-II heterojunction with sizeable energetic offset where the excess energy of the charge carrier is released via the phonon emission. The results demonstrate that the intraband relaxation

of hot carriers in the type-II WZ-ZB InP nanowires depends crucially on the dynamics of spatial charge transfer within the bulk of nanowires.

6.1 Introduction and Background

The successful incorporation of III-V semiconductor nanowires (NWs) into opto-electronic and photovoltaic devices as both elements and interconnects has sparked intense interest in the nature of charge carrier dynamics in such nanostructured materials [40, 227, 230]. In particular, InP NWs are promising for applications ranging from high-speed, and power optoelectronic devices [278] to photovoltaic cells [20], and sensitive photodetectors [40]. It has been shown that the crystal structure of InP NWs can be formed preferentially in either the zincblende (ZB) [67, 279] or wurtzite (WZ) phase [280, 281], depending on the growth conditions. Moreover, the existence of a polytypism phase due to stacking faults along the growth axis of nanowires has been demonstrated recently to have significant implication for the band alignment and electronic transitions [282–285]. Both theoretical [286] and experimental results [285, 287] have shown that the band gap energy of InP differs by $\approx 80\,\mathrm{meV}$ between the WZ and ZB crystal structures and staggered type-II band alignment is formed at their interface with the conduction band minima (CBM) and valence band maxima (VBM) in ZB $\approx 129\,\mathrm{meV}$ and $\approx 40\,\mathrm{meV}$ below that in WZ. Recent optical studies further show that for nanowires with predominant WZ crystal structure, a short ZB layer sandwiched between two WZ segments can form a quantum well (QW), for which the subband energy depends on the thickness of the ZB segments [282, 284, 285, 287]. The spatial separation of holes in the WZ phase and electrons in the QWs further reduces the photoluminescence (PL) recombination rate observed in the nanowires, due to the restrictions imposed by the momentum and energy conservation in semiconductors [284–286].

Carrier cooling in semiconductors has been extensively studied both in bulk and nanostructures [56, 57, 59, 288, 289]. It has been shown that, following non-resonant excitation, hot-carrier cooling is dominated by the interaction with longitudinal-optical (LO) phonons,

where the carrier cooling is mainly due to the emission of LO-phonons. As the carrier temperature (T_c) is approaching the nominal lattice temperature (T_L), the intraband energy relaxation is mainly controlled by the slow cooling of acoustic phonons (acoustic-phonon-bottleneck). At high injection density situations, the carrier cooling rate can be further reduced by the filling of non-equilibrium acoustic phonon states [57, 62, 290]. The presence of an energetic offset across the type-II heterojunction in the semiconductor further implies the charge transfer across the heterojunction is also associated with the transfer of excess energy to the lattice and electronic system. However, no such systematic study has so far been performed to investigate the effect of charge transfer across the type-II heterojunction on the intraband energy-loss rate of hot-carriers in semiconducting nanowires.

In this Chapter, the effects of charge-transfer across type-II heterojunction on the carrier cooling dynamics in semiconductor nanowires were investigated for the first time. Transient PL from the InP nanowires containing WZ-ZB polytypism along the growth axis of the nanowires was used to demonstrate that while the PL is rapidly quenched by the interfacial charge transfer across the type-II heterojunction, the intraband energy loss rate of hot-carriers is reduced significantly. The crystal structure of the nanowires used in this study is predominantly WZ and containing high density of stacking faults. The resulting WZ-ZB heterojunctions exhibit type-II band alignment and the electrons and holes can be spatially confined in the ZB and WZ segments of nanowires, respectively. Two sets of nanowires that show different diameter distributions and twin-defect densities were used to identify the effects of diameter of nanowires and spatial charge-separation rate across the WZ-ZB type-II heterojunctions on the intraband carrier cooling. Following a non-resonant photoexcitation with a femtosecond laser pulse, the PL emission and photoconductivity measurements show that the long-lived photoexcited electron-hole pairs undergo ultrafast spatial separation in 12 ps – 33 ps. The evolution of the carrier temperature during the spatial charge transfer was directly monitored from the transient PL spectra. Surprisingly, the intraband energy relaxation of the hot carriers was found to have slowed down significantly during the charge-transfer across the WZ-ZB type-II heterojunction of the nanowires. The carrier cooling rate at time delay ≥ 2 ps is lower in the nanowires where the spatial charge-transfer rate is higher.

The slow carrier cooling observed in these nanowires is attributed to the buildup of non-equilibrium phonon induced by the spatial charge-transfer across the WZ-ZB type-II heterojunction in the InP NWs. During such spatial charge-transfer, the excess energy of the charge carriers, due to the presence of energetic offset across the WZ-ZB type-II heterojunction, is released to the lattice via the phonon emissions. Since the carrier cooling rate decreases with increasing the non-equilibrium phonon population, and the decay of acoustic phonon modes persists over few hundred picoseconds, the buildup of non-equilibrium phonon population is therefore dominated by the dynamics of spatial charge-transfer across the WZ-ZB type-II heterojunction. Hence, the carrier cooling rate is reduced in the nanowires where the spatial charge-transfer rate is higher. This is further confirmed from the quantitative analysis of the carrier temperature and charge-transfer dynamics, which reveals that the long-term carrier temperature increases successively as the injection density and charge-transfer rate are increased, and is not affected by the diameter of the nanowires. These results demonstrate that while the diameter of the nanowires plays a negligible role on the carrier cooling, the spatial charge transfer across the type-II interface in semiconductor nanowires reduces the intraband carrier cooling rate by orders of magnitudes.

6.2 Sample Preparation and Experiments

6.2.1 Growth of InP Nanowires

The InP nanowires used in this study were fabricated on poly-L-lysine treated InP (111)B substrates using a metal-organic chemical vapor deposition (MOCVD) technique. Two sets of nanowires were used in this study where their diameter is controlled by the size of colloidal Au nanoparticles (20, or 80 nm) that served as catalyst. The nanowires were grown at a pressure of 100 mbar and a total gas flow rate of 15 slm. Growth was performed at 420°C for 20 minutes using trimethylindium and phosphine precursors with a V/III ratio of 700. The nanowires used in this Chapter were fabricated by Dr. Paiman Suriati (Department of Electronic Materials Engineering, Australian National University)

6.2.2 Electron Microscopy and Calculation of Average Nanowire Diameters

Field emission scanning electron microscopy (FESEM) was carried out using a Hitachi S4300 FESEM at an accelerating voltage of 5 kV. For transmission electron microscopy (TEM) investigations, nanowires were first mechanically transferred to holey carbon grids. TEM was performed using a Phillips CM300 TEM operated at 300 kV. At least 5 nanowires were examined from each sample. Nanowires were examined for crystal structure and stacking faults over their entire length. Fig. 6.1a shows a representative SEM image of the nanowires. The high-resolution transmission electron microscopy (TEM) image is presented in Fig. 6.1b. While the crystal structure of the nanowires is predominantly WZ, a considerably high volume fraction of ZB can be clearly identified from the TEM image. This suggests the presence of a high density of stacking faults in the nanowires [282, 284, 285]. The ZB sections vary in thickness between one bilayer (a single stacking fault) and up to few bilayers and they are unevenly distributed along the growth axis of nanowires.

To determine the cross section of each sample, at least 50 individual nanowires were examined in the SEM. For each individual nanowire, measurements of nanowire diameter were taken at approximately 250 nm intervals along the entire nanowire length. Using these data an average diameter was calculated for each nanowire. Each nanowire was binned according to its average diameter. The histograms were constructed by plotting the percentage of nanowires in each bin. The total nanowire length was also measured for each nanowire. The average diameter, $\bar{d}$, for each sample was then calculated using the formula:

$$\bar{d} = \frac{\sum d_i l_i}{\sum l_i}, \tag{6.1}$$

where d_{i} is the average diameter of nanowire i and l_i is its length.

Fig. 6.2 shows that the nanowires can be characterized by an average diameter of $<d>$ of 50 nm and 160 nm for nanowires growth seeded by Au colloids with diameter of 20 nm and

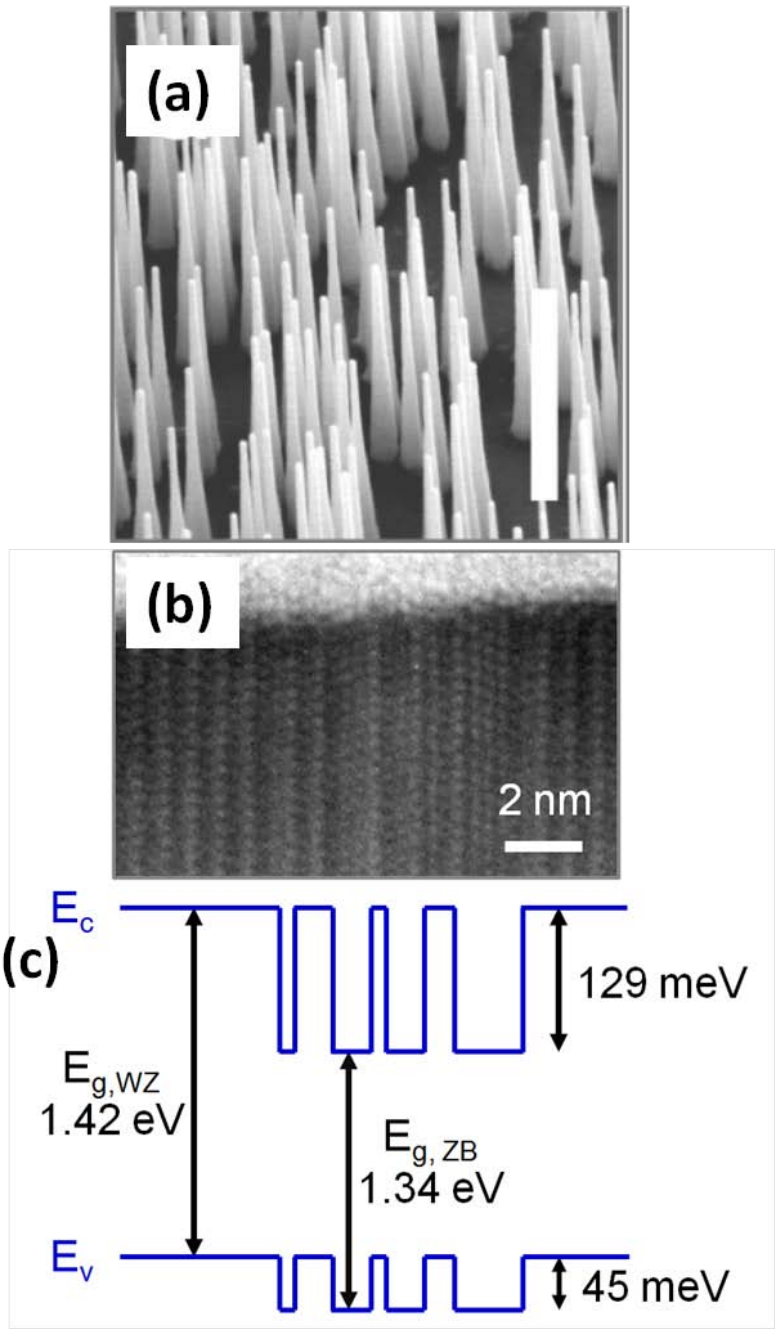

Figure 6.1: (a) Scanning electron microscopy image of InP nanowires as-grown on InP substrates at a tilt of 40°. (b) High-resolution transmission electron microscopy image of a typical InP nanowire featuring predominantly WZ structure with stacking faults. (c) The corresponding band diagrams at room temperature. These band diagrams were constructed from published experimental and theoretical data for band gaps and band offsets [285–287].

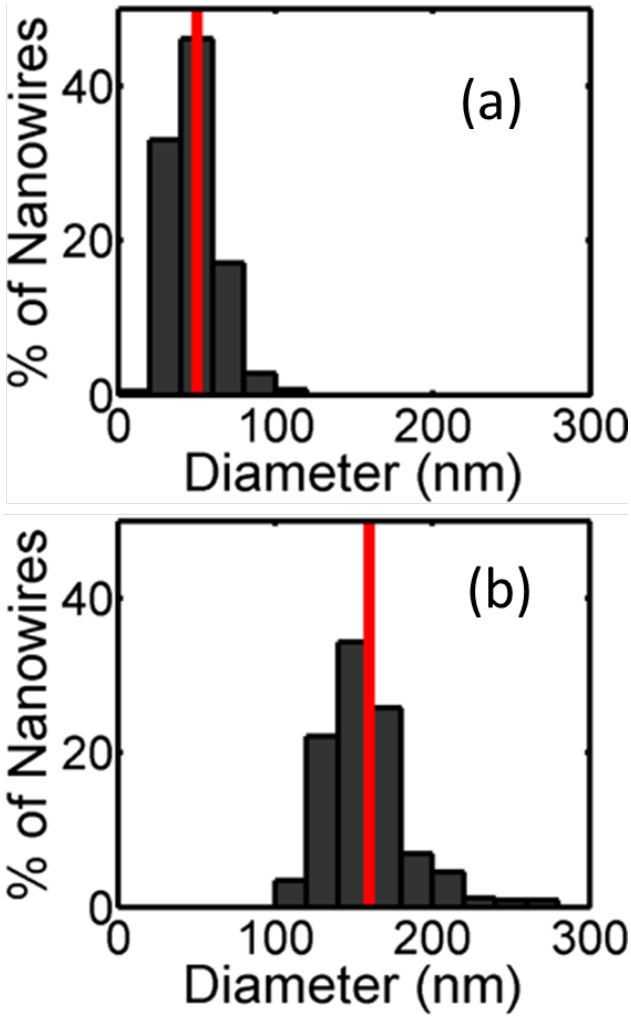

Figure 6.2: Histograms of the diameters of (a) 50nm-InP NWs and (b) 160nm-InP NWs on quartz.

80 nm, respectively. Hereafter, the nanowires with $<d>$ of 50 nm and 160 nm were referred as 50 nm-NWs and 160 nm-NWs, respectively. The SEM characterization was performed by Dr. Hannah Joyce (Department of Physics, Oxford University).

6.2.3 Time-resolved and Time-integrated PL measurements

To understand the underlying carrier dynamics in these nanowires, time-integrated PL and time-resolved PL measurements were conducted on these nanowires. For time-integrated PL measurements, the sample was maintained at a temperature of 77 K in a liquid-nitrogen flow cryostat. The time-resolved PL measurements were performed at room temperature using a PL up-conversion set-up described in Section 3.1.2. Here, the sample was excited at a photon energy of 1.68 eV with the output from a mode-locked Ti:Sapphire laser oscillator supplying 100 fs pulses at 82 MHz repetition rate. The PL was gated optically in a β-barium borate crystal using a split-off part of the laser output that was subjected to an adjustable time delay with respect to the excitation pulse. Time-resolved and time-integrated PL spectra were recorded with a liquid-nitrogen cooled CCD detector connected to a spectrometer, and corrected for the spectral response of the apparatus. The spectral resolution of the time-resolved and time-integrated PL systems at the selected detection wavelengths was 32 meV and 4 meV, respectively, and the former system had a time-resolution of 200 fs. The excitation density was calculated using the method described in Section 4.2.2.

6.2.4 Terahertz Time-Domain Spectroscopy

The optical pump terahertz probe (OPTP) measurements were conducted on the experimental setup that has been described previously [26]. An amplified Ti:Sapphire laser with 4 W average power was used to generate 35 fs pulses centred at 800 nm at a 5 kHz repetition rate. Each pulse was split into three paths: approximately 590 μJ/pulse was used as the optical pump to photoexcite the sample, 200 μJ/pulse was used to generate the terahertz (THZ) probe pulse via optical rectification in a 2 mm GaP crystal, and 1.6 μJ/pulse was

used as a gate for electro-optic detection of the transmitted THz pulse with a 200 mm GaP crystal. The optical pump beam was attenuated using neutral density filters to produce sample photoexcitation fluences between 1 and 160 μJ/cm^2. At the sample, the optical pump beamwidth had a full width at half maximum (FWHM) of 13 mm, whereas the THz probe FWHM was only 1.3 mm. Therefore the terahertz probe measured an area of approximately constant photoexcited carrier density. The THz electric field, E, was detected using a balanced photodiode circuit, and the signal was extracted using a lock-in amplifier referenced to a 2.5 kHz chopper in the THz generation beam. A second lock-in amplifier was used to detect the optical pump-induced change in terahertz electric field, ΔE, by referencing to a 125 Hz chopper in the optical pump beam. Varying the delay between the optical pump, terahertz probe and optical gate pulse produced a two-dimensional map of the THz spectral response of the material as a function of time after photoexcitation. The measurements were performed at room temperature with the entire terahertz beam path under vacuum, to avoid absorption of the terahertz radiation by atmospheric water vapour. The terahertz spectroscopy measurements were conducted by Dr. Hannah Joyce (Department of Physics, Oxford University).

6.3 Results and Discussion

6.3.1 Time-integrated PL measurements from InP Nanowires

Fig. 6.1c illustrates the band diagram that results using the known band gaps and offsets for ZB and WZ InP, where the spatial localization of photoexcited electrons in the ZB and holes in the WZ segments is energetically favorable [284–287, 291]. The WZ-ZB-WZ interfaces can define quantum wells (QWs) with the confinement energy depending on the thickness of the ZB [282, 284, 285, 287]. It has been shown previously from low temperature PL measurements that the PL emission arising from the spatially separated electron-hole pairs is rather slow, due to the restrictions imposed by the momentum and energy conservation in bulk semiconductors, and the emission energy is lower than the band gap energy of

WZ [284, 285].

To reveal the emission arising from such spatially separated electron-hole pair, time-integrated PL (TIPL) emission measurements of these nanowires were conducted at a substrate temperature of 77 K. Fig. 6.3a,b show the false-colour image spectral maps for 50 nm-InP NWs and 160 nm-InP NWs, respectively, where the vertical axis shows the emission energy and the horizontal axis shows the corresponding excitation density (on a logarithmic scale). Fig. 6.3c shows the individual normalized spectra extracted from the density-dependent PL maps for both nanowires, displaying the evolution of the PL spectra as the injection densities are increased from $1\times 10^{16}\,\mathrm{cm}^{-3}$ to $1.1\times 10^{18}\,\mathrm{cm}^{-3}$. For low injection density, the PL emission energy is centered below the band edge of WZ, consistent with the emission from the spatially separated electron-hole pairs with electrons and holes located in the ZB and WZ segments of the nanowires, respectively [284, 285]. The broad spectral linewidth may arise from an uneven distribution of ZB thickness in the nanowires, which results in a distribution of quantum confined states [282, 284, 285, 287]. By increasing the excitation density, the PL emission energy blue-shifts and gradually centers at the energy corresponding to the band gap of WZ. The spectral linewidth also reduces with increasing excitation density. These features indicate the increasing contribution of PL from the direct band-to-band recombination of electron-hole pairs within the WZ, as compared with the radiative recombination of the spatially separated electron-hole pairs in the nanowires, as the excitation density is increased. Such behaviour is expected since the PL emission yield arising from the spatially separated electron-hole pairs is intrinsically low, due to the restrictions imposed by the energy and momentum conservation in bulk semiconductors [285, 286]. However, Fig. 6.3 shows that the PL intensity ratio between the red energy edge of the spectra and the bandgap of WZ remains essentially unchanged when the injection density is above $10^{18}\,\mathrm{cm}^{-3}$. This suggests that the electronic states in the ZB segments remain highly unsaturated even at high injection density situations. Furthermore, the PL spectral linewidth of the 50 nm-InP NWs is broader than those found in 160 nm-InP NWs throughout all the injection densities, and the peak energy remains red-shifted from the band gap of WZ even when the injection density is above $10^{18}\,\mathrm{cm}^{-3}$. Since the emission at energy below

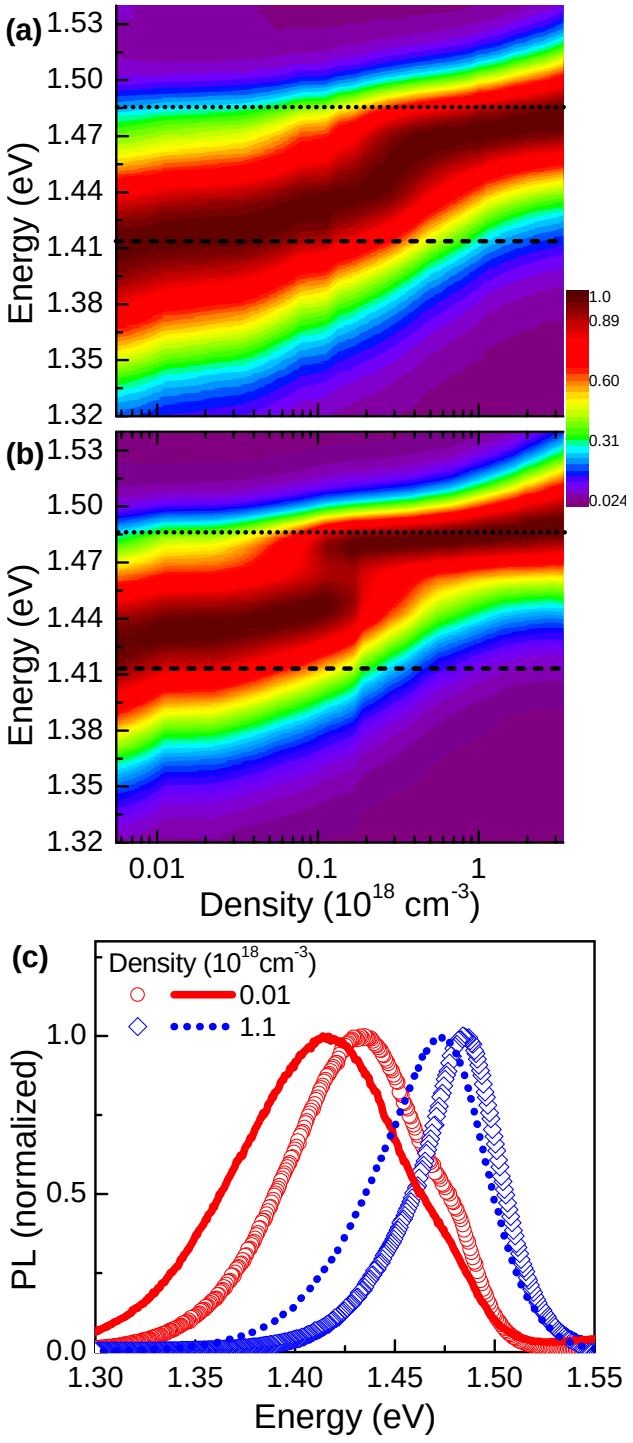

Figure 6.3: The density-dependent TIPL spectra maps for (a) 50 nm-InP NWs and (b) 160 nm-InP NWs. The intensity (on a linear false colour scale) vs excitation power (horizontal scale) and energy (vertical scale) is displayed. For clarity, all spectra were normalized to their maximum intensity. The dotted and dashed lines indicate the bandgap energy of WZ phase and ZB phase at 77 K, respectively. (c) Individual TIPL spectra for 50 nm-InP NWs (dotted and dotted lines) and 160 nm-InP NWs (circles and diamonds), displaying the evolution of PL spectra as the density is increased from 1×10^{16} cm^{-3} to 1.1×10^{18} cm^{-3}.

the bandgap of WZ is mainly due to the radiative recombination of the spatially separated electron-hole pairs across the WZ-ZB segments, these observations therefore suggest the presence of a higher density of defect states arises from the stacking-faults in the 50 nm-InP NWs, as compared with that in the 160 nm-InP NWs.

6.3.2 Ultrafast PL Dynamics in InP Nanowires

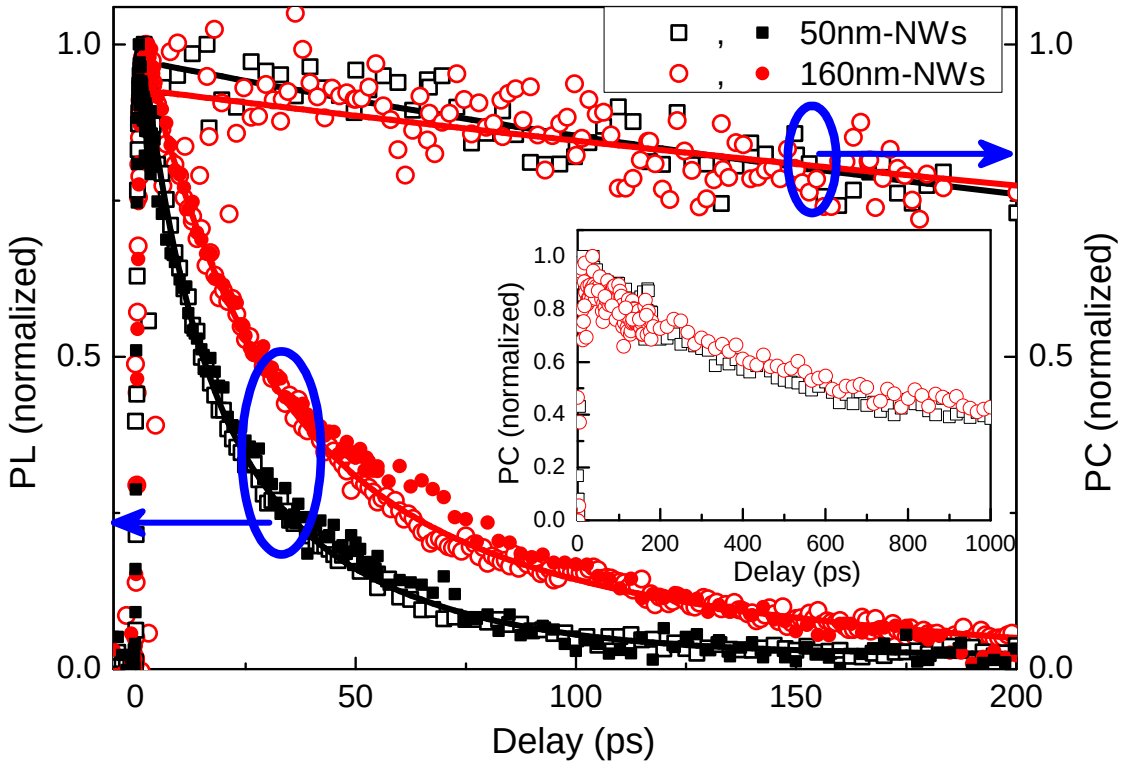

Figure 6.4: Transient photoluminescence (PL) and photoconductivity (PC) of InP NWs measured at 300 K. For transient PL measurements, the nanowires were excited at photon energy of 1.68 eV at densities of 1.4×10^{18} cm^{-3} (empty symbols) and 0.7×10^{18} cm^{-3} (solid symbols). The PL emission was detected at the energy corresponds to the bandgap of WZ phase (1.44 eV). For photoconductivity measurements, the samples were excited at photon energy of 1.56 eV at an excitation density of 1.4×10^{18} cm^{-3}. The inset shows the transient photoconductivity of 50 nm-InP NWs and 160 nm-InP NWs extended over 1000 ps.

For practical nanodevices, it is essential to understand the ultrafast carrier dynamics at room temperature (300 K). In-particular, the conduction band offset appears at the WZ-ZB type-II interface suggests that the photoexcited electron-hole pairs can be quickly separated into the WZ and ZB segments. To measure the carrier dynamics of these InP NWs on a

picosecond time scale, PL upconversion measurements were conducted on these nanowires at room temperature with a temporal resolution of 200 fs. The nanowires were photoexcited non-resonantly at a photon energy of 1.68 eV and the PL emission was monitored near the bandgap energy of the WZ phase (1.43 eV at room temperature). The photoexcitation densities were kept at $1.4\times10^{18}\,\mathrm{cm}^{-3}$ (high density) and $0.7\times10^{18}\,\mathrm{cm}^{-3}$ (low density).

Fig. 6.4 shows the PL dynamics observed in these nanowires. The PL recombination is independent on the injection densities used in this study and exhibits rapid quenching within the 200 ps observation window. The PL decay constants were extracted quantitatively from the sum of two exponential fits. The decay constants of the fast components were found to be 12 ps and 33 ps for 50 nm-InP NWs and 160 nm-InP NWs, respectively. The decay constants of the slow components, on the other hand, were found to be 70 ps and 104 ps for 50 nm-InP NWs and 160 nm-InP NWs, respectively. Transient photoconductivity of carriers in these nanowires was measured by optical-pump terahertz-probe (OPTP) spectroscopy in conjunction with the PL measurements. For InP nanowires, the photoconductivity is dominated by the injected electrons due to their smaller effective mass, as compared with holes [292]. Hence, the THz photoconductivity provides useful information for the recombination dynamics of *all* photoelectrons injected into the nanowires. Fig. 6.4 shows that the photoconductivity decay lifetime of carriers exceeds 1 ns and shows negligible dependence on the diameter of nanowires. The absence of diameter-dependent electron recombination dynamics over the nanosecond time scale indicates that carrier trapping at the surface states of nanowires is not responsible for the ultrafast PL quenching observed within 200 ps. Since the PL intensity is proportional to the product of the electron and hole density distribution at the same **k** space, and the presence of energetic offset across the WZ-ZB type-II heterojunctions provides efficient channels for the electron-hole pairs separation, this plot therefore confirms that the ultrafast PL decay measured at the bandgap of WZ is dominated by the electron injection from the conduction band of WZ into the energetically lower-lying electronic states of ZB in the nanowires, even at room temperature. Furthermore, the PL decay in the 50 nm-InP NWs is faster than that observed in the 160 nm-InP NWs. This is matched by the broader PL spectral linewidth observed in the 50 nm-InP NWs, as seen in

Fig. 6.3, which was attributed to the higher density of unsaturated defect states arising from the stacking faults in the 50 nm-InP NWs to give faster spatial separation of electron-hole pairs across the WZ-ZB heterojunctions, as compared with that in the 160 nm-InP NWs.

6.3.3 Hot-carrier Cooling Dynamics in InP Nanowires

To monitor the intraband carrier relaxation after non-resonant photoexcitation, time-resolved PL spectral measurements were performed at room temperature. Fig. 6.5a shows the representative transient PL spectra of 50 nm-InP NWs measured at different time delays at charge injection density of $1.4\times10^{18}\,\mathrm{cm}^{-3}$. The PL spectra quickly center near the bandgap of the WZ phase within 300 fs, which suggests that hot-carrier thermalization occurs on a time scale that is shorter than the temporal resolution of the measurement setup (≈ 200 fs). This is matched by a rapid rise in transient PL intensity probed at the WZ band edge, as shown in Fig. 6.4. The emission peak energy also reduces gradually by ≈ 15 meV within the 20 ps shortly after the photoexcitation, which suggests the quasi-Fermi level is reduced [29], as the PL is quenched by the injection of electrons from the WZ segments to ZB segments of the nanowires. The high energy edge of the PL spectra is directly proportional to the carrier distribution and can be well-approximated by the Maxwellian-distribution [49, 51, 59], where the slope of the high energy edge is related to the carrier density n via $n \approx \exp(\text{-}\hbar\omega/k_\mathrm{b}T_\mathrm{c})$, where k_b is the Boltzmann's constant, $\hbar\omega$ is the photon energy, and T_c is the carrier temperature. Hence, T_c can be extracted from the slope of the high-energy tail of the PL spectra, as illustrated in the inset of Fig. 6.5a. A progressive increase of the high-energy slope of the PL spectra with time after non-resonant excitation therefore reflects the decrease of carrier temperature after non-resonant photoexcitation.

Fig. 6.5b plots the carrier temperature evolution for both nanowires at different excitation densities extracted in this manner. The intraband carrier relaxation can be characterized by a fast and slow decay component. Here, the initial ultrafast carrier cooling (time delay < 2 ps) can be attributed to the strong coupling between LO-phonons and charge carriers, while the later slow cooling processes (time delay > 2 ps) can be attributed to the acoustic phonon

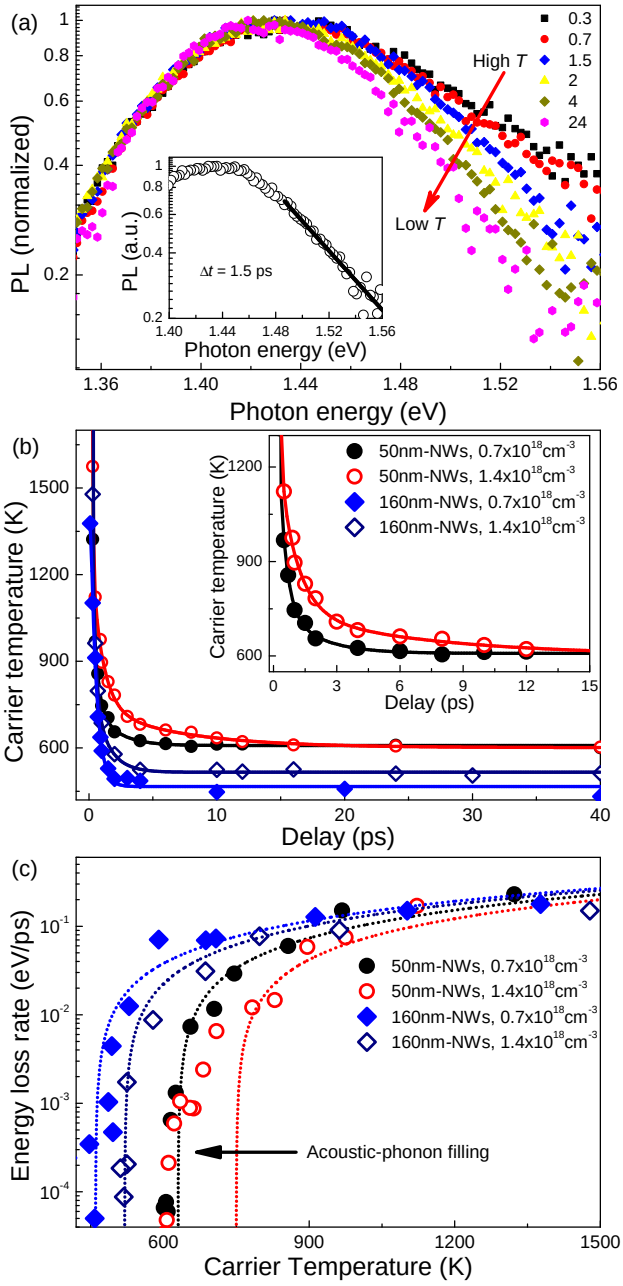

Figure 6.5: (a) Transient PL spectra of 50 nm-InP NWs measured at different time delays after photoexcitation at density of 1.4×10^{18} cm^{-3}. The inset shows an example of an exponential fit (line) to the high-energy tail of the PL spectrum (dots) measured at time delay of 1.5 ps after the excitation. (b) The carrier temperature plotted as a function of time delay for 50 nm-InP NWs (circle) and 160 nm-InP NWs (diamond). The inset shows the carrier temperature of 50 nm-InP NWs at excitation densities of 1.4×10^{18} cm^{-3} and 0.7×10^{18} cm^{-3} during the first 15 ps. The solid lines are guide-to-the eyes. (c) Energy loss rate of hot-carriers plotted as a function of carrier temperature. The energy loss rate of carrier is extracted from the cooling curves in (b) for 50 nm-NWs (circle) and 160 nm-NWs (diamond). The solid and empty symbols shows the energy loss rate obtained at excitation density of 1.4×10^{18} cm^{-3} and 0.7×10^{18} cm^{-3}, respectively. The dotted lines are fits based on Eq. 6.2.

bottleneck effect in bulk semiconductor [57, 59]. By increasing the excitation density, the T_c at time delay > 2 ps also increases, which suggests the increase of non-equilibrium phonon population, as generally observed in other bulk semiconductors at excitation densities in excess of $10^{18}\,\mathrm{cm}^{-3}$ [57, 62, 290]. Interestingly, the T_c at time-delay > 2 ps in 50 nm-InP NWs is higher than the T_c observed in 160 nm-InP NWs, even at lower excitation density. At high injection density, the T_c in 50 nm-InP NWs reduces slowly from ≈ 900 K to 650 K and remains comparable to the T_c observed at low injection density, as seen in the inset of Fig. 6.5b.

Fig. 6.5c summarizes the energy loss rate of hot carriers as a function of carrier temperature. The initial energy loss-rate ($\epsilon_r = \frac{dE}{dt}$) is approximately 0.2 eV/ps in both nanowires and independent on the injection density. It stays nearly constant until the carrier temperature is reduced to ≈ 750 K, which is followed by a sharp decrease over several order-of-magnitudes. Such cooling behavior is similar to that observed in bulk semiconductors where the initial rapid cooling is attributed to the strong carrier-LO phonon coupling that are in equilibrium with each other and cool together via interactions with acoustic phonons [57, 59]. The temperature dependence of the carrier cooling rate in bulk semiconductor can be modelled from the following rate equation, which accounts for the carrier cooling via LO-phonon interactions and acoustic phonon filling [57]:

$$\epsilon_{\mathrm{r}} = \frac{d1.5T_c}{d\mathrm{t}} = \frac{3}{2}\frac{\hbar\omega_\circ}{\tau_{\mathrm{LO}}}\left(\exp^{\hbar\omega_\circ/k_{\mathrm{b}}T_{\mathrm{a}}} - \exp^{\hbar\omega_\circ/k_{\mathrm{b}}T_{\mathrm{c}}}\right)\frac{N_{\mathrm{LO}}(T_{\mathrm{a}})}{N_{\mathrm{LO}}(T_{\mathrm{c}})}\left(\frac{k_{\mathrm{b}}T_{\mathrm{c}}}{\hbar\omega_\circ}\right)^2 \exp^{-\hbar\omega_\circ/k_{\mathrm{b}}T_{\mathrm{c}}}, \qquad (6.2)$$

in which τ_{LO} is the LO-phonon decay rate, T_{a} is the acoustic-phonon temperature and $\hbar\omega_\circ$ is the LO-phonon energy. $N_{\mathrm{LO}}(\mathrm{T})$ is the LO-phonon occupation number at temperature T. Fig. 6.5c shows the output of the fittings from equation 6.2. The measured cooling rate in 160 nm-InP NWs can be accurately described by equation 6.2 by setting $\tau_{\mathrm{LO}} = 0.45$ ps, and $T_{\mathrm{a}} = 460$ K and 530 K for low and high injection densities, respectively. This confirms that the carrier cooling in the nanowires is dominated by the bulk-like LO-phonon coupling

mechanism. The sharp decrease of cooling rate, as T_c is reduced to $\approx 550\,K$, indicates the cooling process is slowed down by the filling of non-equilibrium acoustic phonons, where the carrier cooling is controlled by the decay of the acoustic phonons (acoustic phonon bottleneck) [56, 57, 59, 62, 290]. Such phonon-interaction related energy relaxation of hot-carriers is also observed in 50 nm-InP NWs under low excitation density. However, the T_a is further increased to 600 K, which is much higher than the T_a found in 160 nm-InP NWs under identical excitation conditions. The higher T_a observed in 50 nm-InP NWs indicates the faster buildup of non-equilibrium acoustic modes in the nanowires and hence significantly increases the role of the acoustic-phonon-bottleneck on the carrier cooling. At high injection density, the temperature dependence of the carrier cooling rate in 50 nm-InP NWs deviates significantly from the model predicted from equation 6.2, as seen in Fig. 6.5c. Specifically, the cooling rate reduces steadily over $T_c \approx 900\,K$ – 650 K, instead of the sharp drop, until the final temperature is reached (≈620 K). Morever, the energy loss-rate of the hot carriers in the 50 nm-InP NWs is also much lower than that observed in the 160 nm-InP NWs, as the T_c falls below 900 K. For example, under high excitation density situation, the carrier cooling rate at $T_c = 690\,K$ is approximately $0.0024\,eVps^{-1}$ in the 50 nm-InP NWs whereas it is approximately $0.03\,eVps^{-1}$ in the 160 nm-InP NWs. This plot clearly shows that the carrier cooling observed in the 50 nm-InP NWs is much slower than that found in the 160 nm-InP NWs, due to the sizeable buildup of non-equilibrium phonon population in the nanowires.

6.3.4 Discussion

The slow carrier cooling in bulk semiconductors has been widely attributed to the acoustic phonon bottleneck effect [46, 56, 57, 62]. The decay of acoustic modes, on the other hand, is mainly controlled by the heat-diffusion limited interaction with the environment and, hence, depends on the dimension of the semiconductor [56, 293]. For semiconductor nanostructures, the decay time constant of acoustic modes (τ_D) follows $\tau_D = \frac{C_p \rho_p R^2}{9 C_m \rho_m \Lambda}$ [56, 293], where, for the particle (p) and matrix (m), R is the radius, C is the specific heat, ρ is the density, and Λ is linear thermal conductivity. For the nanowires dispersed on quartz substrate, τ_D of $\approx 470\,ps$

and 4800 ps were estimated for the 50nm-InP NWs and 160nm-InP NWs, respectively (based on established parameters [31]: $C_{InP} = 45.4\,Jmol^{-1}K^{-1}$, $C_{quartz} = 45.3\,Jmol^{-1}K^{-1}$, $\rho_{InP} = 4.81\,gcm^{-3}$, $\rho_{quartz} = 2.20\,gcm^{-3}$, $\Lambda_{quartz} = 0.013\,Jcm^{-1}K^{-1}s^{-1}$). Hence, the decay of acoustic phonon in the 50 nm-InP NWs is nearly 10 times faster than that in the 160 nm-InP NWs, due to their smaller diameter. It is therefore expected that overheating of the acoustic modes and charge carriers, following the non-resonant excitation, may be more significant in the 160 nm-InP NWs than that in the 50 nm-InP NWs, due to the slower acoustic phonon cooling in the 160 nm-InP NWs. However, the opposite trends were observed from the experimental results show in Fig. 6.5. The carrier temperature T_c in the 50 nm-InP NWs appears to be higher than that in the 160 nm-InP NWs at time delay > 2 ps, and the energy loss-rate of hot carriers in the 50 nm-InP NWs is much lower than that found in the 160 nm-InP NWs, even at lower excitation density. Obviously, these observations cannot be explained by the slow decay of acoustic phonon modes alone and suggests the existence of other active mechanisms involved in the slow carrier cooling processes.

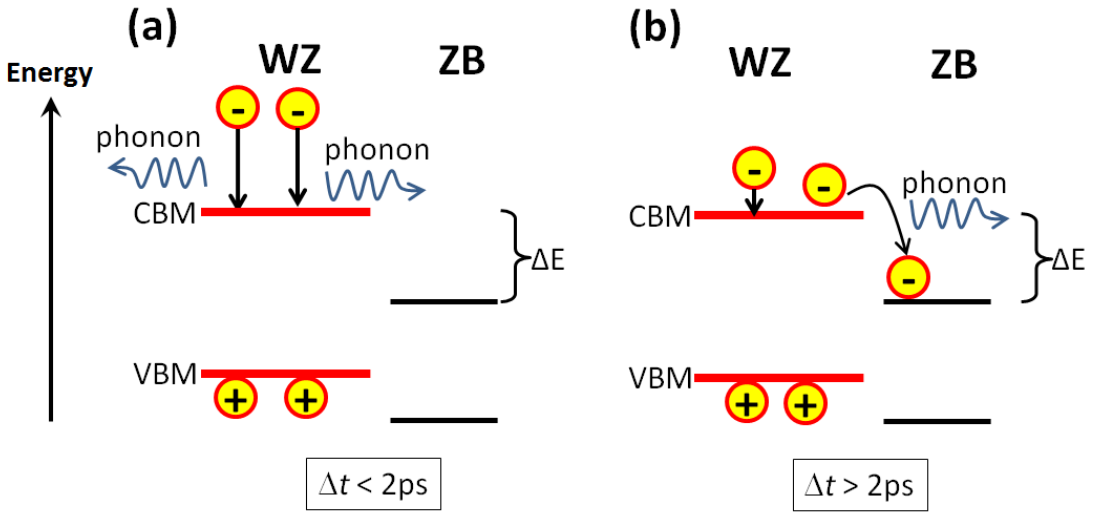

Figure 6.6: Schematic representation of the carrier cooling in semiconductor type-II nanostructures: (a) The initial carrier cooling via LO-phonon couplings at time delay $\Delta t < 2$ ps after the photoexcitation. (b) At $\Delta t > 2$ ps after the photoexcitation, charge transfer across the WZ-ZB type-II interface releases the excess energy comparable to the energetic offset across the heterojunction (ΔE) via the emission of phonons.

The complex intraband relaxation of hot-carriers observed in these rotationally twinned InP nanowires can be attributed to the fast buildup of non-equilibrium phonon population by

the spatial charge transfer across the WZ-ZB type-II heterojunctions where the excess energy of the charge-carrier is released to the lattice via the phonon emissions. Fig. 6.6a,b illustrate the model used to explain the intraband relaxation processes observed in the nanowires. During the early time delay (time delay $< 2\,\mathrm{ps}$ after photoexcitation), the carrier cooling is mainly dominated by LO-phonon coupling to transfer the excess energy of the hot-carriers gained from the non-resonant photoexcitation to the lattice, where the cooling rate depends critically on the carrier temperature and shows negligible dependence on the injection density, as seen in Fig. 6.5. As the carrier temperature is reduced, the emission of LO-phonon via the hot-carrier relaxation ceases, and the LO-phonon decays into the acoustic phonons, where the cooling process becomes dominated by the acoustic-phonon-bottleneck and persists over long time-delay. Such a slow decay of acoustic modes can eventually result in a situation for which $T_\mathrm{c} \approx T_\mathrm{a}$. In bulk semiconductors, the long-term carrier cooling rate can be further reduced at high injection density situation, as a result of the non-equilibrium filling of phonon states [57, 62, 290]. In these nanowires, the non-equilibrium phonon population can be further increased by the spatial charge-transfer across the WZ-ZB type-II heterojunction. Here, the carrier relaxation from the conduction band of WZ to the energetically lower-lying electronic states of ZB is similar to the intersubband transition in quantum wells, where the excess energy is released via the emission of phonons, as schematically shown in Fig. 6.6b [294–297]. Fig. 6.4 shows that the dynamics of PL in these nanowires are dominated by the charge-transfer across the WZ-ZB type-II heterojunctions and independent on the injection density. The PL decay dynamics can therefore be characterized by a charge-transfer rate constant k_CT: $\frac{dn_\mathrm{WZ}}{dt} = n_\mathrm{WZ} k_\mathrm{CT}$, where n_WZ is the remaining carrier density in the WZ. Since the electronic states in the ZB remain highly unsaturated under current excitation conditions, the excess energy associated with the charge-transfer can be assumed to be identical in both nanowires. The corresponding energy release rate (ϵ_h) is therefore proportional to the injection carrier density from the WZ to the ZB (n_WZ), and the charge-transfer rate (k_CT): $\epsilon_\mathrm{h} \propto n_\mathrm{WZ} k_\mathrm{CT}$. Furthermore, the decay of the acoustic modes in both nanowires is shorter than the duration between the laser pulses excited on the nanowires ($\approx 12\,\mathrm{ns}$), the heating of acoustic modes can therefore be accounted for in the linear approximation: $T_\mathrm{a} - T_\mathrm{L} \propto n_\mathrm{WZ}$. This implies

that, under the same excitation density situation, the buildup of non-equilibrium phonon population will be faster in the nanowires where the charge-transfer rate is higher. Since the carrier cooling rate decreases with increasing the population of non-equilibrium phonons [57, 62, 290], the carrier cooling will be slower in the nanowires where the charge-transfer rate is higher.

This scenario is consistent with the experimental observations. Fig. 6.4 reveals that the fast component decay rate of the PL in the 50 nm-InP NWs is nearly 3 times higher than that in the 160 nm-InP NWs. Assuming that the excess energy release during the spatial charge transfer across the WZ-ZB type-II heterojunction is identical in both 50 nm-InP NWs and 160 nm-InP NWs, the faster charge-transfer observed in the 50 nm-InP NWs would imply the higher filling of non-equilibrium phonon states in these nanowires. As a result, the long-term carrier cooling in the 50 nm-InP NWs will be slower than that in the in the 160 nm-InP NWs. Consistently, it was found that, the long-term (time delay > 2 ps) carrier temperature in the 50 nm-InP NWs is much higher than that found in the 160 nm-InP NWs, as seen in Fig. 6.5b. Furthermore, the carrier cooling rate at $T_c < 900$ K is also much lower in the 50 nm-InP NWs, as compared with the carrier cooling rate observed in the 160 nm-InP NWs, as seen in Fig. 6.5c. Hence, these results clearly demonstrate that the carrier cooling in these InP nanowires is closely related to the heating induced by the spatial charge-transfer across the WZ-ZB type-II heterojunction.

To further access the effects of spatial charge-transfer on the carrier cooling, Fig. 6.7 summarizes the carrier temperature in both nanowires observed at time delay $\Delta t = 2$ ps and 10 ps, after the photoexcitation, during which the PL dynamics are dominated by the spatial charge-transfer across the WZ-ZB heterojunctions (Fig. 6.4) and the intraband carrier cooling is mainly due to the acoustic-phonon-bottleneck (Fig. 6.5b). The corresponding carrier temperature values are plotted as a function of the product of $n_{WZ}(t)k_{CT}$, which is proportional to the energy release rate during the spatial charge transfer across the type-II heterojunction. Since the transient PL decay curves measured at the emission energy near the band gap of WZ is dominated by the spatial electron-transfer from the WZ to the ZB,

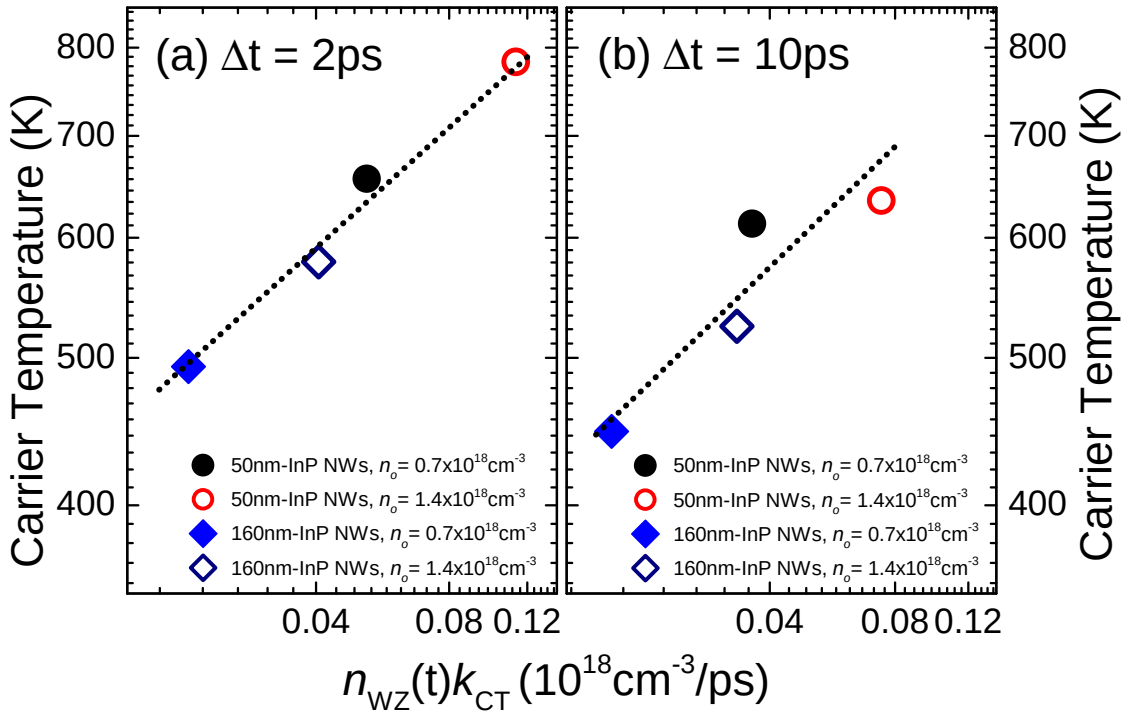

Figure 6.7: The carrier temperature in both 50 nm-InP NWs (circles) and 160 nm-InP NWs (diamonds) at time delay $\Delta t = 2$ ps (a) and 10 ps (b) after the photoexcitation at density of 0.7×10^{18} cm^{-3} (full symbols) and 1.4×10^{18} cm^{-3} (empty symbols). The carrier temperature values are plotted as a function of $n_{WZ}(t)k_{CT}$, where $n_{WZ}(t)$ is the carrier density remains in WZ at time delay t and k_{CT} is the spatial charge-transfer rate. The dotted lines are guide to the eyes.

as seen in Fig. 6.4, the $n_{WZ}(t)$ was calculated by multiplying the PL intensity at time delay t in Fig. 6.4 with the initial injection density n_o. The fast component decay rate of the PL delay curve in Fig. 6.4 therefore represents the k_{CT}. Fig. 6.7 clearly shows that the carrier temperature increases linearly with the product of $n_{WZ}(t)k_{CT}$, which further confirms the notion that the carrier cooling is controlled by the spatial charge-transfer dynamics. These plots reveal that during the slow carrier cooling process, as dominated by the acoustic-phonon-bottleneck, the cooling rate is dominated by the heating of acoustic modes arising from the spatial charge-transfer across the WZ-ZB type-II heterojunction in the nanowires. The fact that the carrier temperature increases proportionally with increasing the product of $n_{WZ}(t)k_{CT}$ further suggests that the decay of acoustic phonon modes is much slower than their buildup arises from the spatial charge transfer. This is further supported by the observation in Fig. 6.5b, where the long-term carrier temperature decreases marginally only.

Moreover, Fig. 6.5b shows that the carrier temperature in the 50 nm-InP NWs decreases slowly from 900 K to 620 K under the high injection density situation, which can be attributed to the excessive filling of non-equilibrium phonon states arising from the spatial charge-transfer in the nanowires that retards the decay of LO phonons [57]. Obviously, a quantitative modeling of the phonon dynamics will require comprehensive knowledge not only the non-equilibrium occupation of both LO and acoustic phonon modes but also of the carrier-phonon coupling strength, and the energy and momentum conservation. Such a quantum-mechanical description exceeds the scope of the current study and will be considered in the future. However, these results provide direct evidence for the effects of spatial charge-transfer across the type-II heterojunctions on the hot carrier cooling dynamics in semiconductor nanowires.

6.4 Conclusion

In conclusion, this Chapter provides direct evidence for the effects of spatial charge transfer across the WZ-ZB type-II heterojunction on the carrier cooling in InP NWs. Following non-resonant photoexcitation, electron-hole pairs undergo rapid spatial separation in 12 ps – 33 ps. However, the carrier cooling is reduced significantly and the carrier temperature becomes much higher than the nominal lattice temperature. The carrier temperature increases successively as the injection density and spatial charge transfer rate are increased. Such a slow carrier cooling process was attributed to the buildup of non-equilibrium phonon population induced by the charge-transfer across the type-II heterojunctions that releases the excess energy to the lattice via the phonon emissions. Quantitative analysis of the carrier cooling and spatial charge-transfer dynamics reveals that the carrier temperature at time delay > 2 ps increases proportionally with increasing the excitation density and charge-transfer rate. The long-term carrier temperature decreases marginally only and suggests the negligible roles of the diameter of nanowires on the carrier cooling. These results demonstrate for the first time that the carrier cooling in the WZ-ZB type-II InP nanowires is closely related to the dynamics of spatial charge-transfer across the type-II heterojunction.

Chapter 7

Conclusions

7.1 Summary of Key Results

In this thesis, the charge carrier dynamics in III-V semiconductor nanowires with high aspect ratio and their blends with various conjugated polymers and small organic molecules are investigated using ultrafast photoluminescence spectroscopy to understand the ultrafast electronic processes. Such non-contact probing of carrier dynamics provides useful information to understand the origin of carrier trapping, carrier cooling, and charge-transfer processes in the nanowires, which have been widely used as building blocks of hybrid organic photovoltaic (OPV) devices.

The effect of surface passivation on the carrier dynamics in GaAs nanowires are investigated using time-resolved PL spectroscopy at 10 K. Here, the GaAs nanowires were overcoated with AlGaAs/GaAs shell-skin layer. The non-resonant excitation of nearly-defect-free semiconductor nanowires is followed by bimolecular interconversion of the initially generated free electron-hole plasma into an exciton population. An increased excitation fluence leads to faster initial exciton formation, while at long times and low charge-pair densities a reduction of the exciton formation rate presents an obstacle to the system attaining thermal equilibrium. Analysis of the emission lineshape showed that the conducting-to-insulating transition occurs gradually over total electron-hole charge pair density of $2–4\times10^{16}\mathrm{cm}^{-3}$.

The gradual Mott-transition is attributed to the slow carrier cooling during the bimolecular interconversion of free charge carriers into excitons and the presence of chemical-potential fluctuations. Without surface-passivation, both free-charge and exciton dynamics are dominated by rapid trapping at defect sites within a few picoseconds after excitation and thus a clear Mott transition cannot be observed. The surface-to-volume ratio of nanowires is inherently high, which results in optoelectronic properties highly sensitive to the surface defect states. The results presented here show that surface-passivation is essential to enhance the carrier lifetime and fundamental for the application in various optoelectronic devices.

In hybrid OPV devices, surface passivation using thick layers of inorganic semiconductors with high bandgap prevents the interfacial exciton dissociation process, a key process to generate free charge carriers. A new method of surface-passivation using conjugated polymers that establish a type-II heterojunction with the GaAs nanowires is presented. Upon removing the native oxide layer from the surface of the nanowires, strong carrier lifetime enhancement for GaAs NWs overcoated with π-conjugated polymers was clearly observed from time-resolved PL measurements, when the ionization potential of the polymers is lower than the workfunction of the nanowires. This effect is attributed to δ-electron-doping from the HOMO of the polymers into the energetically lower lying surface states of the GaAs NWs, which reduces the unsaturated surface-state density. While the picture that emerges superficially resembles that of a metal-semiconductor Schottky-contact [120], a fundamental difference is the strong localization of passivating dopant carriers near the GaAs/polymer surface: DFT calculations reveal that such doping is predominantly limited to the topmost layers near the surface ($\approx 3\,\text{Å}$) and an interface dipole is formed concomitantly to lower the HOMO level of the π-conjugated polymer until the system attains equilibrium. Hence, when the surface of nanowires is covered by native oxide layer of thickness $\approx 1\,\text{nm}$, such surface doping of the nanowires becomes inhibited. The results demonstrate that in nanowire/conjugated polymers type-II hybrid blends, the polymer can perform the dual function of hole transporter and nanowire surface passivating agent. The removal of native oxide on the surface of the nanowires and the use of polymers with sufficiently small IP are essential in order for effective trap passivation to occur. These findings are important for

the design and implementation of new blend materials for hybrid photovoltaic devices and nanoscale photodetectors.

Finally, the carrier cooling in InP nanowires exhibit high density of wurtzite-zincblende type-II heterojunctions along the growth axis of the nanowires was studied. Following non-resonant photoexcitation, the electron-hole pairs undergo rapid spatial separation in 13 ps – 33 ps. However, the carrier cooling is reduced significantly and the carrier temperature is much higher than the nominal lattice temperature. The carrier temperature increases successively as the injection density and spatial charge transfer rate are increased. The slow carrier cooling process was attributed to the heating induced by the charge-transfer across the type-II heterojunctions that releases the excess energy to the lattice via phonon emissions. The resulting buildup of non-equilibrium phonons from such spatial charge-transfer in the nanowires further reduces the carrier cooling rate sizeably. These results demonstrate that the carrier cooling in semiconductor nanowires with type-II heterojunctions is closely related to the spatial charge transfer dynamics.

7.2 Outlook and Future Work

The work presented in this thesis shows that surface passivation is essential to increase the carrier lifetime. The PL lifetime enhancement observed in GaAs nanowires/polymer type-II heterojunctions suggests that the surface-states of nanowires can be passivated by using semiconducting polymers with suitable work functions. This provides excellent guides for using organic semiconductor as surface-passivating agent, while also acting as active materials in the organic-inorganic hybrid devices. In-particular, reducing the dimension and size of the nanostructures ought to change their electronic structure and give rise to the quantum confinement effects in the nanostructures. As a result, the energy level alignment across the organic-inorganic heterojunctions is also altered. It would be of great interest to blend the semiconductor nanostructures with different controlled size and dimensions with the semiconductor polymer, in-order to study the ultrafast electronic processes, such as in-

terfacial charge-transfer across the organic-inorganic semiconductor heterojunctions, surface passivation effects, and the carrier lifetimes in the organic and inorganic semiconductors.

Recently, Ren *et al.* have shown that the short-circuit currents of hybrid OPV devices using GaAs nanowires and P3HT as active medium can be strongly enhanced, when the surface of GaAs nanowires is passivated by titanium oxide [9]. However, the surface passivation by high band gap semiconductor layer can also reduce the charge transfer efficiency. Chapter 5 shows that the surface passivation using organic semiconductor depends crucially on the energy level alignment across the organic-inorganic heterojunctions. It would be of great interest to passivate the surface states of these nanowires using organic dye-molecules with suitable energetic levels, which also act as photon absorber in the hybrid OPV devices.

An alternative experiment would be to combine PLUCS and OPTP-TDS spectroscopy to investigate how the carrier mobility in the nanowires is affected by the surface-passivation using organic materials. In-particular, the charge-transport in hybrid OPV devices requires the well-ordered alignment of nanowires to conduct the charge carriers to the electrodes. Both PLUCS and OPTP-TDS are polarization sensitive techniques. By aligning the nanowires in the polymer matrix, the conductivity and charge-transfer dynamics can be extracted from these non-contact measurements, providing useful information for the optimization of hybrid OPV devices.

The carrier cooling in semiconductor nanostructures plays an important role for the device performance. For example, capturing hot-carriers has been widely explored in photovoltaics, to reduce the non-radiative energy lost to the lattice. The carrier cooling in bulk semiconductor is generally governed by the efficient LO-phonon coupling, where the carrier temperature is quickly reduced to the value close to the lattice temperature within 2 ps. The results in Chapter 6 show that the carrier cooling in semiconductors involving spatial charge-transfer across type-II heterojunctions can be reduced by order-of-magnitudes, providing an alternative route to capture the hot-carriers. It may be possible to incorporate the inorganic semiconductor nanostructures with type-II heterojunctions into the polymer matrix in order to harvest the hot-carrier transfer across the organic-inorganic interfaces.

Bibliography

[1] International Energy Agency (IEA), Key World Energy Statistics (2011).

[2] E. Kymakis, I. Alexandrou, & G. A. J. Amaratunga, *J. Appl. Phys.*, 93 1764 (2003).

[3] W. U. Huynh, J. J. Dittmer, & A. P. Alivisatos, *Science*, 295 2425 (2002).

[4] S. D. Oosterhout, M. M. Wienk, R. Thiedmann, L. J. A. Koster, J. Gilot *et al.*, *Nat. Mater.*, 8 818 (2009).

[5] M. Law, L. E. Greene, J. C. Johnson, R. Saykally, & P. D. Yang, *Nat. Mater.*, 4 455 (2005).

[6] S. Dayal, N. Kopidakis, D. C. Olson, D. S. Ginley, & G. Rumbles, *Nano Lett.*, 10 239 (2010).

[7] K. Szendrei, F. Cordella, M. V. Kovalenko, M. Boberl, G. Hesser *et al.*, *Adv. Mater.*, 21 683 (2009).

[8] H. J. Snaith & L. Schmidt-Mende, *Adv. Mater.*, 19 3187 (2007).

[9] S. Q. Ren, N. Zhao, S. C. Crawford, M. Tambe, V. Bulovic *et al.*, *Nano Lett.*, 11 408 (2011).

[10] C. W. Tang, *Appl. Phys. Lett.*, 48 183 (1986).

[11] A. J. Heeger, N. S. Sariciftci, & E. B. Namdas, *Semiconducting and Metallic Polymers*, Oxford University Press, first edn. (2010).

[12] C. A. Gueymard, *Sol. Energy*, 71 325 (2001).

[13] N. C. Giebink, G. P. Wiederrecht, M. R. Wasielewski, & S. R. Forrest, *Phys. Rev. B*, 82 155305 (2010).

[14] J. Arranz-Andrés & W. J. Blau, *Carbon*, 46 2067 (2008).

[15] D. S. Ginger & N. C. Greenham, *Phys. Rev. B*, 59 10622 (1999).

[16] N. C. Greenham, X. G. Peng, & A. P. Alivisatos, *Phys. Rev. B*, 54 17628 (1996).

[17] P. Wang, A. Abrusci, H. M. P. Wong, M. Svensson, M. R. Andersson *et al.*, *Nano Lett.*, 6 1789 (2006).

[18] H. Němec, J. Rochford, O. Taratula, E. Galoppini, P. Kužel *et al.*, *Phys. Rev. Lett.*, 104 197401 (2010).

[19] S. Dayal, M. O. Reese, A. J. Ferguson, D. S. Ginley, G. Rumbles *et al.*, *Adv. Funct. Mater.*, 20 2629 (2010).

[20] C. J. Novotny, E. T. Yu, & P. K. L. Yu, *Nano Lett.*, 8 775 (2008).

[21] W. J. E. Beek, M. M. Wienk, & R. A. J. Janssen, *Adv. Funct. Mater.*, 16 1112 (2006).

[22] D. H. Cui, J. Xu, T. Zhu, G. Paradee, S. Ashok *et al.*, *Appl. Phys. Lett.*, 88 183111 (2006).

[23] B. Q. Sun, E. Marx, & N. C. Greenham, *Nano Lett.*, 3 961 (2003).

[24] M. Schierhorn, S. W. Boettcher, J. H. Peet, E. Matioli, G. C. Bazan *et al.*, *ACS Nano*, 4 6132 (2010).

[25] Y. Y. Lin, T. H. Chu, S. S. Li, C. H. Chuang, C. H. Chang *et al.*, *J. Am. Chem. Soc.*, 131 3644 (2009).

[26] P. Parkinson, H. J. Joyce, Q. Gao, H. H. Tan, X. Zhang *et al.*, *Nano Lett.*, 9 3349 (2009).

[27] R. Haight, L. Sekaric, A. Afzali, & D. Newns, *Nano Lett.*, 9 3165 (2009).

[28] O. . Demichel, V. . Calvo, A. . Besson, P. . Noe, B. . Salem *et al.*, *Nano Lett.*, 10 2323 (2010).

[29] C. K. Yong, H. J. Joyce, J. Lloyd-Hughes, Q. Gao, H. H. Tan *et al.*, *Small*, 8 1725 (2012).

[30] S. R. Lunt, G. N. Ryba, P. G. Santangelo, & N. S. Lewis, *J. Appl. Phys.*, 70 7449 (1991).

[31] P. Y. Yu & M. Cardona, *Fundamentals of semiconductors*, Springer-Verlag, Heidelberg (1996).

[32] M. L. Cohen & J. R. Chelikowsky, *Electronic Structure and Optical Properties of Semiconductors*, Springer-Verlag, Berlin, second edn. (1988).

[33] C. Kittel, *Introduction to Solid State Physics*, Springer-Verlag, Berlin, second edn. (1986).

[34] C. Klingshirn, *Semiconductor Optics*, Springer-Verlag, Berlin Heidelberg (1997).

[35] Y. M. Niquet, A. Lherbier, N. H. Quang, M. V. Fernandez-Serra, X. Blase *et al.*, *Phys. Rev. B*, 73 165319 (2006).

[36] P. Redlinski & F. M. Peeters, *Phys. Rev. B*, 77 075329 (2008).

[37] H. E. Ruda & A. Shik, *J. Appl. Phys.*, 100 024314 (2006).

[38] A. Lan, J. Giblin, V. Protasenko, & M. Kuno, *Appl. Phys. Lett.*, 92 183110 (2008).

[39] H. E. Ruda & A. Shik, *Phys. Rev. B*, 72 115308 (2005).

[40] J. F. Wang, M. S. Gudiksen, X. F. Duan, Y. Cui, & C. M. Lieber, *Science*, 293 1455 (2001).

[41] I. Robel, B. A. Bunker, P. V. Kamat, & M. Kuno, *Nano Lett.*, 6 1344 (2006).

[42] L. V. Titova, T. B. Hoang, H. E. Jackson, L. M. Smith, J. M. Yarrison-Rice *et al.*, *Appl. Phys. Lett.*, 89 173126 (2006).

[43] E. A. Muljarov, E. A. Zhukov, V. S. Dneprovskii, & Y. Masumoto, *Phys. Rev. B*, 62 7420 (2000).

[44] O. L. Muskens, J. G. Rivas, R. E. Algra, E. P. A. M. Bakkers, & A. Lagendijk, *Nano Lett.*, 8 2638 (2008).

[45] A. Leitenstorfer, A. Lohner, T. Elsaesser, S. Haas, F. Rossi *et al.*, *Phys. Rev. Lett.*, 73 1687 (1994).

[46] J. Shah, *Ultrafast Spectroscopy of Semiconductors and Semiconductor Nanostructures*, Springer, first edn. (1996).

[47] A. Othonos, *J. Appl. Phys.*, 83 1789 (1998).

[48] A. Leitenstorfer, C. Furst, A. Laubereau, W. Kaiser, G. Trankle *et al.*, *Phys. Rev. Lett.*, 76 1545 (1996).

[49] D. W. Snoke, W. W. Ruhle, Y. C. Lu, & E. Bauser, *Phys. Rev. Lett.*, 68 990 (1992).

[50] W. H. Knox, D. S. Chemla, G. Livescu, J. E. Cunningham, & J. E. Henry, *Phys. Rev. Lett.*, 61 1290 (1988).

[51] T. Elsaesser, J. Shah, L. Rota, & P. Lugli, *Phys. Rev. Lett.*, 66 1757 (1991).

[52] U. Hohenester, P. Supancic, P. Kocevar, X. Q. Zhou, W. Ktt *et al.*, *Phys. Rev. B*, 47 13233 (1993).

[53] S. Hunsche, H. Heesel, A. Ewertz, & H. Kurz, *Phys. Rev. B*, 48 17818 (1993).

[54] W. H. Knox, C. Hirlimann, D. A. B. Miller, J. Shah, D. S. Chemla *et al.*, *Phys. Rev. Lett.*, 56 1191 (1986).

[55] J. Shah & R. C. C. Leite, *Phys. Rev. Lett.*, 22 1304 (1969).

[56] M. Achermann, A. P. bartko, J. A. Hollingsworth, & V. I. Klimov, *Nat. Phys.*, 2 557 (2006).

[57] V. Klimov, P. H. Bolivar, & H. Kurz, *Phys. Rev. B*, 52 4728 (1995).

[58] J. F. Ryan, R. A. Taylor, A. J. Turberfield, A. Maciel, J. M. Worlock *et al.*, *Phys. Rev. Lett.*, 53 1841 (1984).

[59] H. W. Yoon, D. R. Wake, & J. P. Wolfe, *Phys. Rev. B*, 54 2763 (1996).

[60] E. O. Goebel & O. Hildebrand, *Phys. Status Solidi B*, 88 645 (1978).

[61] J. Shah, A. Pinczuk, A. C. Gossard, & W. Wiegmann, *Phys. Rev. Lett.*, 54 2045 (1985).

[62] P. Lugli & S. M. Goodnick, *Phys. Rev. Lett.*, 59 716 (1987).

[63] G. Rupper, N. H. Kwong, & R. Binder, *Phys. Rev. Lett.*, 97 (11) 117401 (2006).

[64] J. S. Im, A. Moritz, F. Steuber, V. Harle, F. Scholz *et al.*, *Appl. Phys. Lett.*, 70 (5) 631 (1997).

[65] A. Liu & Y. Rosenwaks, *J. Appl. Phys.*, 86 430 (1999).

[66] Y. P. Varshni, *Phys. Status Solidi*, 19 (2) 459 (1967).

[67] L. V. Titova, T. B. Hoang, J. M. Yarrison-rice, H. E. Jackson, Y. Kim *et al.*, *Nano Lett.*, 7 3383 (2007).

[68] M. Fox, *Optical Properties of Solids*, Oxford University Press, first edn. (2001).

[69] J. Szczytko, L. Kappei, J. Berney, F. Morier-Genoud, M. T. Portella-Oberli *et al.*, *Phys. Rev. Lett.*, 93 (13) 137401 (2004).

[70] R. J. Elliott, *Phys. Rev.*, 108 1384 (1957).

[71] J. Shah, R. F. Leheny, & W. Wiegmann, *Phys. Rev. B*, 16 1577 (1977).

[72] S. M. Ryvkin & Y. V. Shmartser, *Proceedings of the International Conference on the Physics of Semiconductors,*, Nauka, Leningrad, Russia (1968).

[73] N. F. Mott, *Proc. Phys. Soc. London*, 62 416 (1949).

[74] J. Shah, M. Combescot, & A. H. Dayem, *Phys. Rev. Lett.*, 38 (25) 1497 (1977).

[75] L. Kappei, J. Szczytko, F. Morier-Genoud, & B. Deveaud, *Phys. Rev. Lett.*, 94 (14) 147403 (2005).

[76] J. Szczytko, L. Kappei, J. Berney, F. Morier-Genoud, M. T. Portella-Oberli *et al.*, *Phys. Rev. B*, 71 (19) 195313 (2005).

[77] L. M. Smith & J. P. Wolfe, *Phys. Rev. Lett.*, 57 (18) 2314 (1986).

[78] G. W. Fehrenbach, W. Schafer, J. Treusch, & R. G. Ulbrich, *Phys. Rev. Lett.*, 49 (17) 1281 (1982).

[79] A. Honold, L. Schultheis, J. Kuhl, & C. W. Tu, *Phys. Rev. B*, 40 (9) 6442 (1989).

[80] N. Peyghambarian, H. M. Gibbs, J. L. Jewell, A. Antonetti, A. Migus *et al.*, *Phys. Rev. Lett.*, 53 (25) 2433 (1984).

[81] D. Hulin, A. Mysyrowicz, A. Antonetti, A. Migus, W. T. Masselink *et al.*, *Phys. Rev. B*, 33 4389 (1986).

[82] W. H. Knox, R. L. Fork, M. C. Downer, D. A. B. Miller, D. S. Chemla *et al.*, *Phys. Rev. Lett.*, 54 1306 (1985).

[83] S. Schmitt-Rink, D. S. Chemla, & D. A. B. Miller, *Phys. Rev. B*, 32 (10) 6601 (1985).

[84] D. S. Chemla & D. A. B. Miller, *J. Opt. Soc. Am. B*, 2 (7) 1155 (1985).

[85] A. H. Simon, S. J. Kirch, & J. P. Wolfe, *Phys. Rev. B*, 46 (16) 10098 (1992).

[86] H. W. Yoon, M. D. Sturge, & L. N. Pfeiffer, *Solid State Commun.*, 104 (5) 287 (1997).

[87] D. L. Smith, D. S. Pan, & T. C. McGill, *Phys. Rev. B*, 12 4360 (1975).

[88] R. Ambigapathy, I. Bar-Joseph, D. Y. Oberli, S. Haacke, M. J. Brasil *et al.*, *Phys. Rev. Lett.*, 97 3579 (1997).

[89] R. A. Kaindl, D. Hägele, M. A. Carnahan, & D. S. Chemla, *Phys. Rev. B*, 79 045320 (2009).

[90] R. A. Kaindl, M. A. Carnahan, D. Hägele, R. Lövenich, & D. S. Chemla, *Nature*, 423 734 (2003).

[91] S. Schmitt-Rink, C. Ell, & H. Haug, *Phys. Rev. B*, 33 1183 (1986).

[92] G. Trankle, H. Leier, A. Forchel, H. Haug, C. Ell *et al.*, *Phys. Rev. Lett.*, 58 (4) 419 (1987).

[93] G. Trnkle, E. Lach, A. Forchel, F. Scholz, C. Ell *et al.*, *Phys. Rev. B*, 36 6712 (1987).

[94] P. Vashishta & R. K. Kalia, *Phys. Rev. B*, 25 (10) 6492 (1982).

[95] H. Schweizer, A. Forchel, A. Hangleiter, S. Schmittrink, J. P. Lowenau *et al.*, *Phys. Rev. Lett.*, 51 (8) 698 (1983).

[96] V. I. Klimov, A. A. Mikhailovsky, D. W. McBranch, C. A. Leatherdale, & M. G. Bawendi, *Science*, 287 1011 (2000).

[97] H. Htoon, J. A. Hollingsworth, R. Dickerson, & V. I. Klimov, *Phys. Rev. Lett.*, 91 227401 (2003).

[98] J. A. Czaban, D. A. Thompson, & R. R. Lapierre, *Nano Lett.*, 9 148 (2009).

[99] E. C. Garnett & P. Yang, *J.Am. Chem. Soc.*, 130 9224 (2008).

[100] H. Pettersson, J. Tragardh, A. I. Persson, L. Landin, D. Hessman *et al.*, *Nano Lett.*, 6 229 (2006).

[101] F. Qian, S. Gradecak, Y. Li, C.-Y. Wen, & C. Lieber, *Nano Lett.*, 5 2287 (2005).

[102] E. D. Minot, F. Kelkensberg, M. van Kouwen, J. A. van Dam adn L. P. Kouwenhoven, M. T. B. V. Zwiller *et al.*, *Nano Lett.*, 7 367 (2007).

[103] M. H. Huang, S. Mao, H. Feick, H. Yan, Y. Wu *et al.*, *Science*, 292 1897 (2001).

[104] X. F. Duan, Y. Huang, R. Agarwal, & C. M. Lieber, *Nature*, 421 241 (2003).

[105] F. Qian, Y. Li, Gradečak, H. G. Park, Y. Dong *et al.*, *Nat. Mater.*, 7 701 (2008).

[106] H. A. Nilsson, T. Duty, S. Abay, C.Wilson, J. B.Wagner *et al.*, *Nano Lett.*, 8 872 (2008).

[107] C. Thelander, T. Martensson, M. T. Bjork, B. J. Ohlsson, M. W. Larsson *et al.*, *Appl. Phys. Lett.*, 83 2052 (2003).

[108] Y. Cui, Q. Wei, H. Park, & C. M. Lieber, *Science*, 293 1289 (2001).

[109] J. Hahm & C. M. Lieber, *Nano Lett.*, 4 51 (2004).

[110] M. Law, J. Goldberger, & P. D. Yang, *Ann. Rev. Mater. Res.*, 34 83 (2004).

[111] van Vugt, S. J. Veen, E. P. A. M. Bakkers, A. L. Roest, & D. Vanmaekelbergh, *J. Am. Chem. Soc.*, 127 12357 (2005).

[112] R. P. Prasankumar, S. Choi, S. A. Trugman, S. T. Picraux, & A. J. Taylor, *Nano Lett.*, 8 1619 (2008).

[113] P. Parkinson, J. Lloyd-Hughes, Q. Gao, H. H. Tan, C. Jagadish *et al.*, *Nano Lett.*, 7 2162 (2007).

[114] M. H. Sun, H. J. Joyce, Q. Gao, H. H. Tan, C. Jagadish *et al.*, *Nano Lett.*, 12 3378 (2012).

[115] J. Bardeen, *Phys. Rev.*, 71 717 (1947).

[116] R. Calarco, M. Marso, T. Richter, A. L. Aykanat, R. Meijers *et al.*, *Nano Lett.*, 5 981 (2005).

[117] M. H. M. van Weert, O. Wunnicke, A. L. Roest, T. J. Eijkemans, A. Y. Silov *et al.*, *Appl. Phys. Lett.*, 88 043109 (2006).

[118] W. Shockley & W. T. Read, *Phys. Rev.*, 87 835 (1952).

[119] M. V. Lebedev, *Prog. Surf. Sci.*, 70 153 (2002).

[120] W. E. Spicer, Z. Lilientalweber, E. Weber, N. Newman, T. Kendelewicz *et al.*, *J. Vac. Sci. Technol. B*, 6 1245 (1988).

[121] R. W. Grant, J. R. Waldrop, S. P. Kowalczyk, & E. A. Kraut, *J. Vac. Sci. Technol.*, 19 477 (1981).

[122] M. D. Pashley & K. W. Haberern, *Phys. Rev. Lett.*, 67 2697 (1991).

[123] M. D. Pashley, K. W. Haberern, R. M. Feenstra, & P. D. Kirchner, *Phys. Rev. B*, 48 4612 (1993).

[124] R. Cohen, L. Kronik, A. Shanzer, D. Cahen, A. Liu *et al.*, *J. Am. Chem. Soc.*, 121 10545 (1999).

[125] M. C. Traub, J. S. Biteen, B. S. Brunschwig, & N. S. Lewis, *J. Am. Chem. Soc.*, 130 955 (2008).

[126] H. Haick, M. Ambrico, T. Ligonzo, R. T. Tung, & D. Cahen, *J. Am. Chem. Soc.*, 128 6854 (2006).

[127] K. E. knowles, D. B. Tice, E. A. Mcarthur, G. C. Solomon, & E. A. Weiss, *J. Am. Chem. Soc.*, 132 1041 (2010).

[128] J. Sun, D. J. Seo, W. L. OBrien, F. J. Himpsel, A. B. Ellis *et al.*, *J. Appl. Phys.*, 85 969 (1999).

[129] T. He, J. He, M. Lu, H. Pang, W. F. Reus *et al.*, *J. Am. Chem. Soc.*, 128 14537 (2006).

[130] W. P. Su, J. R. Schrieffer, & A. J. Heeger, *Phys. Rev. Lett.*, 42 1698 (1979).

[131] G. W. C. Kaye & T. H. Laby, *Tables of Physical and Chemical Constants*, Longman, sixteenth edn. (1995).

[132] U. Rauscher, H. Bässler, D. D. C. Bradley, & M. Hennecke, *Phys. Rev. B*, 42 9830 (1990).

[133] J. L. Brédas, J. Cornil, & A. J. Heeger, *Adv. Mater.*, 8 447 (1996).

[134] T. W. Hagler, K. Pakbaz, K. F. Voss, & A. J. Heeger, *Phys. Rev. B*, 44 8652 (1991).

[135] G. D. Scholes & G. Rumbles, *Nat. Mater.*, 5 683 (2006).

[136] K. Fesser, A. R. Bishop, & D. K. Campbell, *Phys. Rev. B*, 27 4804 (1983).

[137] J. L. Brédas, D. Beljonne, V. Coropceanu, & J. Cornil, *Chem. Rev.*, 104 4971 (2004).

[138] G. Rumbles, I. D. W. Samuel, L. Magnani, K. A. Murray, A. J. Demello *et al.*, *Synth. Met.*, 76 47 (1996).

[139] M. Kasha, *Radiat. Res.*, 20 55 (1963).

[140] S. Siddiqui & F. C. Spano, *Chem. Phys. Lett.*, 308 99 (1999).

[141] F. C. Spano, *J. Chem. Phys.*, 122 234701 (2005).

[142] J. Clark, C. Silva, R. H. Friend, & F. C. Spano, *Phys. Rev. Lett.*, 98 206406 (2007).

[143] T. A. Chen, X. M. Wu, & R. D. Rieke, *J. Am. Chem. Soc.*, 117 233 (1995).

[144] P. Parkinson, C. Müller, N. Stingelin, M. B. Johnston, & L. M. Herz, *J. Phys. Chem. Lett.*, 1 2788 (2010).

[145] P. K. H. Ho, L. L. Chua, M. Dipankar, X. Y. Gao, D. C. Qi *et al.*, *Adv. Mater.*, 19 215 (2007).

[146] G. Li, Y. Yao, H. Yang, V. Shrotriya, G. Yang *et al.*, *Adv. Funct. Mater.*, 17 1636 (2007).

[147] J. Clark, J. F. Chang, F. C. Spano, R. H. Friend, & C. Silva, *Appl. Phys. Lett.*, 94 163306 (2009).

[148] F. C. Spano, J. Clark, C. Silva, & R. H. Friend, *J. Chem. Phys.*, 130 074904 (2009).

[149] N. F. COLANERI, D. D. C. Bradley, R. H. FRIEND, P. L. Burn, A. B. Holmes *et al.*, *Phys. Rev. B*, 42 11670 (1990).

[150] R. Österbacka, C. P. An, X. M. Jiang, & Z. V. Vardeny, *Science*, 287 839 (2000).

[151] H. Sirringhaus, N. Tessler, & R. H. Friend, *Science*, 280 1741 (1998).

[152] M. H. Chang, M. J. Frampton, H. L. Anderson, & L. M. Herz, *Phys. Rev. Lett.*, 98 (2) 027402 (2007).

[153] J. Müller, U. Lemmer, G. Raschke, M. Anni, U. Scherf *et al.*, *Phys. Rev. Lett.*, 91 267403 (2003).

[154] T. Förster, *Discuss. Faraday Soc.*, 27 7 (1959).

[155] A. E. Cohen & S. Mukamel, *J. Phys. Chem. A*, 107 3633 (2003).

[156] D. Beljonne, C. Curutchet, G. D. Scholes, & R. J. Silbey, *J. Phys. Chem. B*, 113 6583 (2009).

[157] D. L. Dexter, *J. Chem. Phys.*, 21 836 (1953).

[158] P. F. Barbara, T. J. Meyer, & M. A. Ratner, *J. Phys. Chem.*, 100 13148 (1996).

[159] J. Jortner, *J. Chem. Phys.*, 64 4860 (1976).

[160] C. Deibel, T. Strobel, & V. Dyakonov, *Adv. Mater.*, 22 4097 (2010).

[161] D. R. Stranks, *Discuss. Faraday Soc.*, 29 73 (1960).

[162] P. A. van Hal, S. C. J. Meskers, & R. A. J. Janssen, *Appl. Phys. A: Mater.*, 79 41 (2004).

[163] P. Piotrowiak, *Chem. Soc. Rev.*, 28 143 (1999).

[164] G. L. Closs, L. T. Calcaterra, N. J. Green, K. W. Penfield, & J. R. Miller, *J. Phys. Chem.*, 90 3673 (1986).

[165] A. Petrella, J. Cremer, L. D. Cola, P. Buerle, & R. M. Williams, *J. Phys. Chem. A*, 109 11687 (2005).

[166] A. C. Morteani, A. S. Dhoot, J. S. Kim, C. Silva, N. C. Greenham *et al.*, *Adv. Mater.*, 15 1708 (2003).

[167] S. Westenhoff, I. A. Howard, J. M. Hodgkiss, K. R. Kirov, H. A. Bronstein *et al.*, *J. Am. Chem. Soc.*, 130 13653 (2008).

[168] I. A. Howard, J. M. Hodgkiss, X. Zhang, K. R. Kirov, H. A. Bronstein *et al.*, *J. Am. Chem. Soc.*, 132 328 (2009).

[169] A. A. Bakulin, A. Rao, V. G. Pavelyev, P. H. M. van Loosdrecht, M. S. Pshenichnikov *et al.*, *Science*, 335 1340 (2012).

[170] L. Onsager, *Phys. Rev.*, 54 554 (1938).

[171] C. L. Braun, *J. Chem. Phys.*, 80 4157 (1984).

[172] M. Tachiya, *J. Chem. Phys.*, 89 6929 (1988).

[173] H. Ohkita, S. Cook, Y. Astuti, W. Duffy, S. Tierney *et al.*, *J. Am. Chem. Soc.*, 130 3030 (2008).

[174] T. Clarke, A. Ballantyne, F. Jamieson, C. Brabec, J. Nelson *et al.*, *Chem. Commun.*, 1 89 (2009).

[175] H. Kallmann & M. Pope, *J. Chem. Phys.*, 30 585 (1959).

[176] J. J. M. Halls, K. Pichler, R. H. Friend, S. C. Moratti, & A. B. Holmes, *Appl. Phys. Lett.*, 68 3120 (1996).

[177] P. Peumans, A. Yakimov, & S. R. Forrest, *J. Appl. Phys.*, 93 3693 (2003).

[178] N. S. Sariciftci, L. Smilowitz, A. J. Heeger, & F. Wudl, *Science*, 258 1474 (1992).

[179] G. Yu, J. Gao, J. C. Hummelen, F. Wudl, & A. J. Heeger, *Science*, 270 1789 (1995).

[180] S. E. Shaheen, C. J. Brabec, N. S. Sariciftci, F. Padinger, T. Fromherz *et al.*, *Appl. Phys. Lett.*, 78 841 (2001).

[181] Y. Kim, S. Cook, S. M. Tuladhar, S. A. Choulis, J. Nelson *et al.*, *Nat. Mater.*, 5 197 (2006).

[182] M. Campoy-quiles, T. Ferenczi, T. Agostinelli, P. G. Etchegoin, Y. Kim *et al.*, *Nat. Mater.*, 7 158 (2008).

[183] C. J. Brabec, S. Gowrisanker, J. J. M. Halls, D. Laird, S. J. Jia *et al.*, *Adv. Mater.*, 22 3839 (2010).

[184] P. Peumans, S. Uchida, & S. R. Forrest, *Nature*, 425 158 (2003).

[185] R. F. Salzman, J. G. Xue, B. P. Rand, A. Alexander, M. E. Thompson *et al.*, *Org. Electron.*, 6 242 (2005).

[186] Y. Y. Liang, Z. Xu, J. B. Xia, S. T. Tsai, Y. Wu *et al.*, *Adv. Mater.*, 22 E135 (2010).

[187] J. Peet, J. Y. Kim, N. E. Coates, W. L. Ma, D. Moses *et al.*, *Nat. Mater.*, 6 497 (2007).

[188] S. H. Park, A. Roy, S. Beaupre, S. Cho, N. Coates *et al.*, *Nat. Photonics*, 3 297 (2009).

[189] D. Veldman, O. Ipek, S. C. J. Meskers, J. Sweelssen, M. M. Koetse *et al.*, *J. Am. Chem. Soc.*, 130 7721 (2008).

[190] C. Deibel, T. Strobel, & V. Dyakonov, *Phys. Rev. Lett.*, 103 036402 (2009).

[191] C. R. McNeill, A. Abrusci, I. Hwang, M. A. Ruderer, P. Muller-buschbaum *et al.*, *Adv. Funct. Mater.*, 19 3103 (2009).

[192] T. Salim, S. Y. Sun, L. H. Wong, L. F. Xi, Y. L. Foo *et al.*, *J. Phys. Chem. C*, 114 9459 (2010).

[193] S. Swaraj, C. Wang, H. P. Yan, B. Watts, L. N. Jan *et al.*, *Nano Lett.*, 10 2863 (2010).

[194] C. R. McNeill & N. C. Greenham, *Adv. Mater.*, 21 3840 (2009).

[195] D. C. Olson, J. Pirisa, R. T. Collinsb, S. E. Shaheena, & D. S. Ginley, *Thin Solid Films*, 496 26 (2006).

[196] K. Takanezawa, K. Tajima, & K. Hashimoto, *Appl. Phys. Lett.*, 93 063308 (2008).

[197] P. E. Shaw, A. Ruseckas, & I. D. W. Samuel, *Adv. Mater.*, 20 3516 (2008).

[198] D. Herrmann, S. Niesar, C. Scharsich, A. Khler, M. Stutzmann *et al.*, *J. Am. Chem. Soc.*, 133 18220 (2011).

[199] P. Parkinson, C. Dodson, H. J. Joyce, K. A. Bertness, N. A. Sanford *et al.*, *Nano Lett.*, 12 4600 (2012).

[200] L. E. Greene, M. Law, B. D. Yuhas, & P. Yang, *J. Phys. Chem. C*, 111 18451 (2007).

[201] A. M. Peiro, P. Ravirajan, K. Govender, D. S. Boyle, P. O'Brien *et al.*, *J. Mater. Chem*, 16 2088 (2006).

[202] B. Sun, H. J. Snaith, A. S. Dhoot, S. Westenhoff, & N. C. Greenham, *J. Appl. Lett.*, 97 014914 (2005).

[203] Y. Kanai & J. C. Grossman, *Nano Lett.*, 7 1967 (2007).

[204] R. Pacios, J. Nelson, D. D. C. Bradley, T. Virgili, G. Lanzani *et al.*, *J. Phys.: Condens. Matter*, 16 8105 (2004).

[205] C. J. Brabec, G. Zerza, G. Cerullo, S. Luzzati, J. C. Hummelen *et al.*, *Chem. Phys. Lett.*, 340 232 (2001).

[206] W. U. Huynh, J. J. Dittmer, W. C. Libby, G. L. Whiting, & A. P. Alivisatos, *Adv. Funct. Mater.*, 13 73 (2003).

[207] C. Anghel, V. Derycke, A. Filoramo, S. Lenfant, B. Giffard *et al.*, *Nano Lett.*, 8 3619 (2008).

[208] H. J. Snaith, A. C. Arias, A. C. Morteani, C. Silva, & R. H. Friend, *Nano Lett.*, 2 1353 (2002).

[209] P. Ravirajan, A. M. Peiro, M. K. Nazeeruddin, M. Graetzel, D. D. C. Bradley *et al.*, *J. Phys. Chem. B*, 110 7635 (2006).

[210] P. Tiwana, P. Docampo, M. B. Johnston, H. J. Snaith, & L. M. Herz, *ACS Nano*, 5 5158 (2011).

[211] S. Ardo, Y. Sun, A. Staniszewski, F. N. Castellano, & G. J. Meyer, *J. Am. Chem. Soc.*, 132 6696 (2010).

[212] Y. Vaynzof, A. A. Bakulin, S. Glinas, & R. H. Friend, *Phys. Rev. Lett.*, 108 246605 (2012).

[213] A. Y. Anderson, P. R. F. Barnes, J. R. Durrant, & B. C. ORegan, *J. Phys. Chem. C*, 114 1953 (2010).

[214] Y. Vaynzof, D. Kabra, L. L. Chua, & R. H. Friend, *Appl. Phys. Lett.*, 98 113306 (2011).

[215] M. H. Chang, F. J. M. Hoeben, P. Jonkheijm, A. P. H. J. Schenning, E. W. Meijer *et al.*, *Chem. Phys. Lett.*, 418 196 (2006).

[216] S. D. Stranks, C. Weisspfennig, P. Parkinson, M. B. Johnston, L. M. Herz *et al.*, *Nano Lett.*, 11 66 (2011).

[217] P. W. Parkinson, *Ultrafast Electronic Processes at Nanoscale Organic-Inorganic Semiconductor Interfaces*, Ph.D. thesis, Department of Physics, University of Oxford (2008).

[218] D. N. Nikogosyan, *Appl. Phys. A-Mater. Sci. Process.*, 52 359 (1991).

[219] W. Becker, *Advanced Time-Correlated Single Photon Counting Techniques*, Springer (2005).

[220] L. Ley & M. Cardona, *Photoemission in Solids II*, vol. 27, Springe-Verlagr (1979).

[221] W. Schattke & M. A. V. Hove, *Solid-state photoemission and related methods: theory and experiment*, Wiley-VCH, first edn. (2003).

[222] C. N. Berglund & W. E. Spicer, *Phys. Rev.*, 136 A1030 (1964).

[223] G. Möbus, in *High-resolution imaging and spectrometry of materials*, Springer, first edn. (2003).

[224] R. S. Wagner & W. C. Ellis, *Appl. Phys. Lett.*, 4 89 (1964).

[225] K. Hiruma, M. Yazawa, K. Haraguchi, K. Ogawa, T. Katsuyama *et al.*, *J. Appl. Phys.*, 74 3162 (1993).

[226] H. J. Joyce, Q. Gao, H. H. Tan, C. Jagadish, Y. Kim *et al.*, *Nano Lett.*, 7 921 (2007).

[227] I. Gur, N. A. Fromer, M. L. Geier, & A. P. Alivisatos, *Science*, 310 462 (2005).

[228] M. C. McAlpine, R. S. Friedman, S. Jin, K. H. Lin, W. U. Wang *et al.*, *Nano Lett.*, 3 (11) 1531 (2003).

[229] R. P. Prasankumar, P. C. Upadhya, & A. J. Taylor, *Phys. Status Solidi B-Basic Solid State Phys.*, 246 1973 (2009).

[230] J. Puthussery, A. Lan, T. H. Kosel, & M. Kuno, *ACS Nano*, 2 357 (2008).

[231] R. Kumar, A. S. Vengurlekar, A. V. Gopal, T. Melin, F. Laruelle *et al.*, *Phys. Rev. Lett.*, 81 (12) 2578 (1998).

[232] L. K. van Vugt, S. J. Veen, E. Bakkers, A. L. Roest, & D. Vanmaekelbergh, *J. Am. Chem. Soc.*, 127 12357 (2005).

[233] P. U. Jepsen, W. Schairer, I. H. Libon, U. Lemmer, N. E. Hecker *et al.*, *Appl. Phys. Lett.*, 79 (9) 1291 (2001).

[234] G. Kalyuzhny & R. W. Murray, *J. Phys. Chem. B*, 109 (15) 7012 (2005).

[235] S. Perera, M. A. Fickenscher, H. E. Jackson, L. M. Smith, J. M. Yarrison-Rice *et al.*, *Appl. Phys. Lett.*, 93 (5) 173126 (2008).

[236] D. D. Sell & H. C. Casey, *J. Appl. Phys.*, 45 (2) 800 (1974).

[237] M. D. Sturge, *Phys. Rev.*, 127 (3) 768 (1962).

[238] J. S. Blakemore, *J. Appl. Phys.*, 53 R123 (1982).

[239] C. Piermarocchi, F. Tassone, V. Savona, A. Quattropani, & P. Schwendimann, *Phys. Rev. B*, 55 (3) 1333 (1997).

[240] T. C. Damen, J. Shah, D. Y. Oberli, D. S. Chemla, J. E. Cunningham *et al.*, *Phys. Rev. B*, 42 (12) 7434 (1990).

[241] I. Robel, R. Gresback, U. Kortshagen, R. D. Schaller, & V. I. Klimov, *Phys. Rev. Lett.*, 102 (17) 177404 (2009).

[242] U. Strauss, W. W. Ruhle, & K. Kohler, *Appl. Phys. Lett.*, 62 (1) 55 (1993).

[243] R. Ulbrich, *Phys. Rev. B*, 8 (12) 5719 (1973).

[244] D. Robart, X. Marie, B. Baylac, T. Amand, M. Brousseau *et al.*, *Solid State Commun.*, 95 (5) 287 (1995).

[245] R. T. Phillips, G. C. Nixon, T. Fujita, M. Y. Simmons, & D. A. Ritchie, *Solid State Commun.*, 98 (4) 287 (1996).

[246] A. Chomette, B. Deveaud, A. Regreny, & G. Bastard, *Phys. Rev. Lett.*, 57 1464 (1986).

[247] N. J. Borys, M. J. Walter, J. Huang, D. V. Talapin, & J. M. Lupton, *Science*, 330 1371 (2010).

[248] H. J. Joyce, Q. Gao, H. H. Tan, C. Jagadish, Y. Kim *et al.*, *Prog. Quantum Electron.*, 35 23 (2011).

[249] M. Heeney, C. Bailey, K. Genevičius, M. Shkunov, D. Sparrowe *et al.*, *J. Am. Chem. Soc.*, 127 1078 (2005).

[250] J. Zaumseil, C. L. Donley, J. S. Kim, R. H. Friend, & H. Sirringhaus, *Adv. Mater.*, 18 2708 (2006).

[251] L. L. Chua, J. Zaumseil, J. F. Chang, E. C. W. Ou, P. K. H. Ho *et al.*, *Nature*, 434 194 (2005).

[252] A. L. Briseno, T. W. Holcombe, A. I. Boukai, E. C. Garnett, S. W. Shelton *et al.*, *Nano Lett.*, 10 334 (2010).

[253] C. M. Rodd & R. Agarwal, *Nano Lett.*, 11 3460 (2011).

[254] S. D. Bearden, J. P. Cannon, & S. A. Gold, *Macromolecules*, 44 2200 (2011).

[255] S. Nam, J. Jang, H. Cha, J. Hwang, T. K. An *et al.*, *J. Mater. Chem.*, 22 5543 (2012).

[256] S. H. Chen, A. C. Su, Y. F. Huang, C. H. Su, G. Y. Peng *et al.*, *Macromolecules*, 35 4229 (2002).

[257] D. M. Ceperley & B. J. Alder, *Phys. Rev. Lett.*, 45 566 (1980).

[258] P. Giannozzi, S. Baroni, N. Bonini, M. Calandra, R. Car *et al.*, *J. Phys.-Condes. Matter*, 21 395502 (2009).

[259] D. Vanderbilt, *Phys. Rev. B*, 41 7892 (1990).

[260] N. Troullier & J. L. Martins, *Phys. Rev. B*, 43 1993 (1991).

[261] M. I. McMahon & R. J. Nelmes, *Phys. Rev. Lett.*, 95 215505 (2005).

[262] M. Galicka, M. Bukala, R. Buczko, & P. Kacman, *J. Phys.-Condes. Matter*, 20 454226 (2008).

[263] K. Noori & F. Giustino, *Adv. Funct. Mater.*, 22 5089 (2012).

[264] A. I. Persson, M. W. Larsson, S. Stenstrom, B. J. Ohlsson, L. Samuelson *et al.*, *Nature Mater.*, 3 (10) 677 (2004).

[265] F. Glas, J.-C. Harmand, & G. Patriarche, *Phys. Rev. Lett.*, 99 (14) 146101 (2007).

[266] C. C. Surdu-bob, S. O. Saied, & J. L. Sullivan, *Appl. Surf. Sci.*, 183 126 (2001).

[267] E. A. Kraut, R. W. Grant, J. R. Waldrop, & S. P. Kowalczyk, *Phys. Rev. Lett.*, 44 1620 (1980).

[268] J. Szuber, E. Bergignat, G. Hollinger, A. Polakowska, & P. Koscielniak, *Vacuum*, 67 53 (2002).

[269] G. Lelay, D. Mao, A. Kahn, Y. Hwu, & G. Margaritondo, *Phys. Rev. B, Condens. Matter Mater. Phys. (USA)*, 43 14301 (1991).

[270] G. Grancini, D. Polli, D. Fazzi, J. Cabanilas-gonzalez, G. Cerullo *et al.*, *J. Phys. Chem. Lett.*, 2 1099 (2011).

[271] F. Seker, K. Meeker, T. F. Kuech, & A. B. Ellis, *Chem. Rev.*, 100 2505 (2000).

[272] H. Hasegawa, H. Ishii, T. Sawada, T. Saitoh, S. Konishi *et al.*, *J. Vac. Sci. Technol. B*, 6 1184 (1988).

[273] S. Kobayashi, T. Nishikawa, T. Takenobu, S. Mori, T. Shimoda *et al.*, *Nat. Mater.*, 3 317 (2004).

[274] T. He, D. A. Corley, M. Lu, J. L. He, D. P. Nackashi *et al.*, *J. Am. Chem. Soc.*, 131 10023 (2009).

[275] M. Shalom, S. Ruhle, I. Hod, S. Yahav, & A. Zaban, *J. Am. Chem. Soc.*, 131 9876 (2009).

[276] M. F. Calhoun, J. Sanchez, D. Olaya, M. E. Gershenson, & V. Podzorov, *Nat. Mater.*, 7 84 (2008).

[277] K. Tvrdy, P. A. Frantsuzov, & P. V. Kamat, *Proc. Natl. Acad. Sci. U. S. A.*, 108 29 (2011).

[278] X. F. Duan, Y. Huang, Y. Cui, J. F. Wang, & C. M. Lieber, *Nature*, 409 66 (2001).

[279] X. F. Duan & C. M. Lieber, *Adv. Mater.*, 12 298 (2000).

[280] J. Wallentin, K. Mergenthaler, M. Ek, L. R. Wallenberg, L. Samuelson *et al.*, *Nano Lett.*, 11 2286 (2011).

[281] M. Mattila, T. Hakkarainen, M. Mulot, & H. Lipsanen, *Nanotechnology*, 17 1580 (2006).

[282] K. Ikejiri, Y. Kitauchi, K. Tomioka, J. Motohisa, & T. Fukui, *Nano Lett.*, 11 4314 (2011).

[283] F. Wang, P. J. Reece, S. Paiman, Q. Gao, H. H. Tan *et al.*, *Nano Lett.*, 11 4149 (2011).

[284] K. Pemasiri, M. Montazeri, R. Gass, L. M. Smith, H. E. Jackson *et al.*, *Nano Lett.*, 9 648 (2009).

[285] J. Bao, D. C. Bell, F. Capasso, J. B. Wagner, T. Mårtensson *et al.*, *Nano Lett.*, 8 836 (2008).

[286] L. Zhang, J. Luo, A. Zunger, N. Akopian, V. Zwiller *et al.*, *Nano Lett.*, 10 4055 (2010).

[287] N. Akopian, G. Patriarche, L. Liu, J. C. Harmand, & V. Zwiller, *Nano Lett.*, 10 1198 (2010).

[288] E. Pop, *Nano Res.*, 3 147 (2010).

[289] W. A. Tisdale, K. J. Williams, B. A. Timp, D. J. Norris, E. S. Aydil *et al.*, *Science*, 328 1543 (2010).

[290] J. A. Kash, J. C. Tsang, & J. M. Hvam, *Phys. Rev. Lett.*, 54 2151 (1985).

[291] M. Murayama & T. Nakayama, *Phys. Rev. B*, 49 4710 (1994).

[292] H. J. Joyce, J. Wong-Leung, C. K. Yong, C. J. Docherty, S. Pauman *et al.*, *Nano Lett.*, 12 5325 (2012).

[293] Z. Ge, D. G. Cahill, & P. V. Braun, *J. Phys. chem. B*, 108 18870 (2004).

[294] A. Seilmeier, H. J. Hubner, G. Abstreiter, G. Weimann, & W. Schlapp, *Phys. Rev. Lett.*, 59 1345 (1987).

[295] D. Y. Oberli, D. R. Wake, M. V. Klein, J. Klem, T. Henderson *et al.*, *Phys. Rev. Lett.*, 59 696 (1987).

[296] M. Hartig, S. Haacke, P. E. Selbmann, B. Deveaud, R. A. Taylor *et al.*, *Phys. Rev. Lett.*, 80 1940 (1998).

[297] S. Lutgen, R. A. Kaindl, M. Woerner, T. Elsaesser, A. Hase *et al.*, *Phys. Rev. Lett.*, 77 3657 (1996).

Abbreviations

E_F	Fermi energy
FF	Fill Factor
J_{SC}	Short-Circuit Current
V_{OC}	Open-Circuit Voltage
AlGaAs	aluminum gallium arsenide
AUDM	Advanced unified defect model
BBO	Barium Borate
BCP	Bound charge pair
BGR	Bandgap Renormalization
BGR	Bandgap Renormalization
BHJ	Bulk-heterojunction
CBM	Conduction band minimum
cc	Carrier-carrier
CSS	core-shell-skin
CuPc	copper-phthalocyanine
DFT	Density-functional theory
DOS	Density of states
ELR	Energy Loss Rate
ESCA	Electron Spectroscopy for Chemical Analysis
F8BT	poly[(9,9-di-n-octylfluorenyl-2,7-diyl)-alt-(benzo[2,1,3]thiadiazol-4,8-diyl)]
FESEM	Field Emission Scanning Electron Microscopy

FRET	Förster Resonance Energy Transfer
FWHM	full-width at half-maximum
G2	poly(2,5-bis(3-decylthiophen-2-yl)thieno(2,3-b)thiophene)
GaAs	gallium arsenide
GIXRD	Grazing-angle X-ray diffraction
HH	Heavy-Hole
HMO	Hückel molecular orbital
HOMO	Highest Occupied Molecular Orbital
HRTEM	High Resolution Transmission Electron Microscopy
IMFP	Electron Spectroscopy for Chemical Analysis
IP	Ionization potential
IP	Ionization potential
LDA	local-density approximation
LEDs	Light emitting diodes
LH	Light-Hole
LUMO	Lowest Unoccupied Molecular Orbital
MDMO-PPV	Poly(2-methoxy-5-(3,7-dimethyloctyloxy)-p-phenylene vinylene)
MEH-PPV	poly(2-methoxy-5-(2-ethyl-hexyloxy)-1,4-phenylene-vinylene)
MOCVD	metal-organic chemical vapour deposition
NEXAFS	Grazing-angle X-ray diffraction
NWs	nanowires
OPTP-TDS	optical-pump terahertz-probe time-domain spectroscopy
OPVs	Organic Photovoltaics
P3HT	Poly(3-hexylthiophene)
PCBA	phenyl-C61-butyric acid
PCBM	Phenyl-C_{61}-butyric acid methyl ester
PCE	power conversion efficiency
PEDOT-PSS	poly(3,4-ethylenedioxythiophene)-poly(styrenesulfonate)

PEDOT:PSS	Poly(3,4-ethylenedioxythiophene):Poly(styrenesulfonate)
PIA	Photoinduced absorption
PL	photoluminescence
PLUC	photoluminescence up-conversion
PMMA	Poly(methyl methacrylate)
PMT	Photon Multiplier Tube
QD	Quantum Dot
QW	Quantum Well
QWR	Quantum Wire
SCU	Scan-control unit
SEM	Scanning Electron Microscopy
STM	Scanning tunneling microscopy
TB	Tight-Binding
TCSPC	time-correlated single-photon counting
TEM	transmission electron microscopy
TIPL	Time-integrated PL
TRPL	Time-Resolved PL
UHV	Ultrahigh vacuum
UHV	Ultrahigh vacuum
VBM	valence band maximum
VLS	Vapor-liquid-solid
XPS	X-ray photoemission spectroscopy
XPS	X-ray photoemission spectroscopy
XRD	X-ray diffraction